Development of high-throughput screening assays for oral peptide drug delivery

Larsen, Nanna Wichmann

Publication date:
2022

Document Version
Publisher's PDF, also known as Version of record

DTU Health Tech
Department of Health Technology

Development of high-throughput screening assays for oral peptide drug delivery

PhD Thesis

October 2022

Nanna Wichmann Larsen

Supervisors:
Niels Bent Larsen (Professor, Technical University of Denmark)
Thomas Lars Andresen (Professor, Technical University of Denmark)
Jens Bæk Simonsen (Associate Professor, Technical University of Denmark)
Kasper Kristensen (Researcher, Technical University of Denmark)

Development of high-throughput screening assays for oral peptide drug delivery

PhD Thesis
2022

By
Nanna Wichmann Larsen

Supervisors:
Professor Niels Bent Larsen, Department of Health Technology, DTU (main supervisor)
Professor Thomas Lars Andresen, Department of Health Technology, DTU (co-supervisor)
Associate Professor Jens Bæk Simonsen, Department of Health Technology, DTU (co-supervisor)
Researcher Kasper Kristensen, Department of Health Technology, DTU (co-supervisor)

Published by: DTU, Department of Health Technology, Produktionstorvet, Building 423, 2800 Kgs. Lyngby, Denmarkwww.healthtech.dtu.dk

Preface

This PhD thesis is submitted as part of the requirements for obtaining a Doctor of Philosophy (PhD) degree at the Department of Health Technology at the Technical University of Denmark (DTU Health Tech). The research work presented in this thesis was conducted between December 2018 and September 2022 in the Center for Intestinal Absorption and Transport of Biopharmaceuticals (CitBIO) and in the Colloids and Biological Interfaces (CBIO) group. The work was carried out under the supervision of Professor Thomas Lars Andresen, Professor Niels Bent Larsen, Associate Professor Jens Bæk Simonsen, and Dr. Kasper Kristensen. The project was funded by the Novo Nordisk Foundation's Challenge Programme.

Thank you to my supervisors Thomas Lars Andresen, Niels Bent Larsen, Jens Bæk Simonsen, and Kasper Kristensen. Thanks to Thomas Lars Andresen, Jens Bæk Simonsen, and Kasper Kristensen for giving me the opportunity to join this group and undertake this PhD project. Thanks to Niels Bent Larsen for stepping in as a supervisor when a new main supervisor was needed. Thanks to Niels Bent Larsen, Jens Bæk Simonsen, and Kasper Kristensen for inspirational, encouraging, and empowering supervision, collaboration and feedback. A special thank you to Kasper Kristensen for always being there to help, guide, and discuss the project.

Thank you to Henrik Jensen and Morten Enghave Pedersen from FIDAbio for the opportunity to test the FIDAbio-technology and practical assisting me with the testing.
Thank you to Bente Rotbøl from the flow cytometer core-facility for introducing me to the flow cytometer.

Thank you to the members of the Center for Intestinal Absorption and Transport of Biopharmaceuticals, especially to the members of the journal club for inspiration, feedback, and fun, Kasper for always providing me with great input, Arjen for helping me with the cell studies, Anka for helping me with the HPLC, and Philip and Jannik for the collaboration.

Thank you to the members of the CBIO group and people in the building for providing a fun and helpful work environment. Thank you to Katrine, Rasmus, Elisabeth, Dennis, Sergin, Mia, Philip and Grace for a fun, help, and sweets in the office. Thank you to Michelle and Clara for helping me out practically when my time came short. Thank you to Lene, Lotte, and Ole for making things around the project run smoothly.

Thank you to Jannik, Philip, and Grace for feedback on my thesis.

Thank you to my mother for allocating time to help make ends meet at home during the last part of this PhD.

Thank you to my husband for endless supplies of chocolate, and together with our children underline that interactions are what matter.

Nanna Wichmann Larsen

October 2022

Abstract

Due to non-invasiveness and patient compliance, the oral route is the preferred route of drug delivery. One class of drugs with a great potential is peptides due to their high specificity, high potency, and low toxicity. However, oral delivery of peptide drugs usually result in low bioavailability. This is in part due to the low membrane permeability of peptides which makes it difficult for the peptides to cross the cell membrane of epithelial cells. The membrane impermeability to peptides is so extreme that it constitutes a challenge for peptide uptake despite the very large surface area of the upper part of the small intestine where most substances are absorbed.

The success in delivering peptide drugs orally is limited with the bioavailability of clinically tested oral peptide drugs typically being a few percent or less, Co-formulating drugs with permeation enhancers have in some cases increased their bioavailability.Still, only one linear polypeptide drug has ma been commercialized.

Most permeation enhancers are membrane active and interact with the cell membrane either in a way that increases the permeability of the membrane through fluidization or solubilization of the membrane, or in a way that enhances the peptide's ability to translocate across the lipid bilayer. Also, some peptides are inherently membrane active either as pore-forming antimicrobial peptides or as cell-penetrating peptides. By studying membrane activity, it is possible to obtain information that can lead to increased bioavailability of oral peptide drugs.

Some permeation enhancers require direct interaction with the peptide drug to enhance permeation, and many permeation enhancers are fat-soluble and have been shown to interact with the bile acids and phospholipids present in the upper part of the small intestine. It has also been shown for at least one combination of permeation enhancer and peptide drug that the presence of bile acids and phospholipids influence the interaction between permeation enhancer and peptide drug. However, how such interactions affect the membrane activity has not previously been reported.

In this PhD thesis it is studied how interactions between permeation enhancers, peptide drugs, and bile components influence the membrane activity of the permeation enhancers, and a method is developed to study membrane activity in a high-throughput manner on individual lipid membranes. The latter part enables that information on subpopulations can be obtained.

In project one, the membrane active permeation enhancers and peptides C10, sodium cholate, dodecyl maltoside, sodium dodecyl sulfate, salcaprozate sodium, melittin, and penetratin are studied with respect to their membrane perturbation, their interactions with the peptide drugs insulin and salmon calcitonin, their interactions with the bile components taurocholate and phospholipids, and how these interactions influence the membrane perturbation. The membrane perturbations was studied using a calcein release assay and dynamic light scattering-based size measurements of liposomes, and the interactions were studied using dynamic light scattering and a hydrophobicity assay, the Nile Red assay. The study thus also underlines the possibility of performing such studies in the presence of bile components by the use of POPC:Cholesterol (9:1 molar ratio)-liposomes. Three distinct mechanisms of actions were identified for the membrane active species, with dodecyl maltoside perturbating the lipid membrane in a two-state mechanism, eventually leading to solubilization. Interactions between several permeation enhancers and peptide drugs were identified, and particularly for C10 these interactions increased the membrane perturbation though the effect seemed to be limited by the presence of bile components. Contrary, the membrane perturbation of sodium dodecyl sulfate was generally limited upon interactions with other species. In summary, this project highlights the importance of carrying out mechanistic studies of permeation enhancers in the presence of peptide drugs and bile components, and choosing the combination of peptide drug and permeation enhancer carefully.

In project two a flow cytometry based method was developed allowing the determination of the mode of action for membrane active peptides in a high-througput label free manner. It was established that

POPC:POPS liposomes membrane-labeled with DOPE-Atto655 and encapsulating Alexa488 could be detected using flow cytometry. The mode of action for the membrane active peptides penetratin, Tat magainin-2, macrolittin-70, LL-37, and melittin could be determined to be non-membrane perturbating, membrane perturbating without or membrane perturbating with solubilization. Also, the aggregation of liposomes could be detected using this method. The method was applicable to study single liposomes, and thereby study the simultaneity of the effects. The method was also shown to be suitable to distinguish between modes of actions for liposomes with different charges. The method has potential to be further developed to distinguish between different subpopulations of a sample or to include membrane association of peptides in the study by fluorophore labeling of the peptide. The method developed in this project thus provides a mean to perform high-throughput mechanistic studies of membrane activity contributing to the understanding of permeation enhancement.

Together, this thesis provides insight into the mechanisms of membrane activity and a high-throughput method to study such mechanisms on a single liposome basis. The outcome of this thesis hence provide a basis for faster and more relevant understanding and screening of factors governing permeation enhancement across lipid membranes in a setting relevant for oral drug delivery of peptide.

Dansk resumé

Det foretrækkes ofte at lægemidler administreres oralt, da dette giver en høj patient compliance og er minimalt invasivt. Peptider som klasse har et stort potentiale som lægemidler på grund af deres høje specificitet og potencitet samt deres lave toksisitet. Imidlertid resulterer oral administration af peptidlægemidler sædvanligvis også i lav biotilgængelighed. Dette skyldes hovedsageligt peptidernes lave membranpermeabilitet, der gør det vanskeligt for peptiderne at krydse cellemembranen i epitelceller. Membranens uigennemtrængelighed for peptider er så ekstrem, at den udgør en udfordring for peptidoptagelsen på trods af det meget store overfladeareal af den øverste del af tyndtarmen, hvor de fleste stoffer ellers optages.

Der er begrænset succces med orale peptidlægemidler. For eksempel er biotilgængeligheden af klinisk testede orale peptidlægemidler typisk kun på få procent Co-formulering af lægemidler med permeationsforstærkere har i nogle tilfælde øget deres biotilgængelighed. Alligevel er kun et lineært oralt polypeptidlægemiddel blevet kommercialiseret. .

De fleste permeationsforstærkere er membranaktive og interagerer med cellemembranen på en måde, der enten øger membranens permeabilitet gennem fluidisering eller solubilisering membranen, eller øger peptidets evne til at translokere over lipid-dobbeltlaget. Nogle peptider er også naturligt membranaktive enten som poredannende antimikrobielle peptider eller som cellepenetrerende peptider. Ved at studere membranaktivitet er det muligt, at der kan opnås information, der kan føre til øget biotilgængelighed af orale peptidlægemidler.

For nogle permeationsforstærkere er det nødvendigt at de interagerer direkte med peptidlægemidlet for at øge dets permeation. Desuden er mange permeationsforstærkere fedtopløselige, og flere permeations-forstærkere har vist sig at interagere med galdesyrer og fosfolipider. Disse mødes særligt i den øvre del af tyndtarmen. Det er også blevet vist for mindst én kombination af permeationsforstærker og peptidlægemiddel, at tilstedeværelsen af galdesyrer og phospholipider påvirker interaktionen mellem permeationsforstærker og peptidlægemiddel. Det er imidlertid ikke tidligere blevet rapporteret hvordan sådanne interaktioner påvirker membranaktiviteten.

I denne ph.d.-afhandling studeres det, hvordan vekselvirkninger mellem permeationsforstærker, peptidlægemiddel og galdekomponenter påvirker permeationsforstærkernes membranaktivitetn, og der udvikles en metode til at studere membranaktivitet på en high-throughput måde på individuelle lipidmembraner. Sidstnævnte muliggør at der kan opnås information om delpopulationer.

I projekt 1 studeres de membranaktive permeationsforstærkere og peptider C10, natriumcholat, dodecylmaltosid, natriumdodecylsulfat, salcaprozatnatrium, melittin og penetratin med hensyn til deres membranperturbering, deres interaktioner med peptidlægemidlerne lakse-calcitonin og insulin, deres interaktioner med galdekomponenterne taurocholat og fosfolipider, og hvordan disse interaktioner påvirker membranperturberingen. Membranperturberingen blev undersøgt ved hjælp af et calceinfrigivelsesassay og dynamisk lysspredningsbaserede størrelsesmålinger af liposomer, og interaktionerne blev undersøgt ved hjælp af dynamisk lysspredning og et hydrofobicitetsassay, Nile Red-assayet. Undersøgelsen understreger således også muligheden for at udføre sådanne undersøgelser i nærvær af galdekomponenter ved anvendelse af POPC:kolesterol (9:1 molforhold)-liposomer. Tre forskellige virkningsmekanismer blev identificeret for permeationsforstærkerne. Dodecylmaltosid forstyrrer lipidmembranen i en to-trins mekanisme, der endeligt fører til solubilisering. Interaktioner mellem flere permeationsforstærkere og peptidlægemidler blev identificeret, og især for C10 øgede disse interaktioner membranperturberingen, selvom effekten syntes at blive begrænset af tilstedeværelsen af galdekomponenter. I modsætning hertil blev membranpertuberingen af natriumdodecylsulfat begrænset

ved interaktioner med andre stoffer. Tilsammen fremhæver data i dette projekt vigtigheden af at udføre mekanistiske undersøgelser af permeationsforstærkere i nærvær af peptidlægemidler og galdekomponenter, og at vælge kombinationen af peptidlægemiddel og permeationsforstærker omhyggeligt.

I projekt to blev der udviklet en flowcytometri-baseret metode, som muliggjorde bestemmelsen af, hvordan virkningsmåden for membranaktive peptider kunne bestemmes på en høj-throughput-mærkefri måde. Det blev vist, at POPC:POPS liposomer membranmærket med DOPE-Atto655 og indkapslende Alexa488 kunne påvises ved hjælp af flowcytometri. For de membranaktive peptider penetratin, Tat magainin-2, makrolittin 70, LL-37 og melittin kunne det vises om virkningsmåden var ikke-membranforstyrrende eller membranforstyrrende med eller uden opløsning af membranen. Desuden kunne aggregeringen af liposomer påvises ved anvendelse af denne metode. Metoden var anvendelig til at studere enkelte liposomer og derved studere samtidigheden af virkningerne. Metoden viste sig også at være egnet til at skelne mellem virkningsmåder for liposomer med forskellige ladninger.

Metoden har potentiale til at blive videreudviklet til at skelne mellem forskellige subpopulationer af en prøve eller til at inkludere membranassociering af peptider i undersøgelsen ved at mærke peptidet med en fluorophore. Metoden udviklet i dette projekt giver således et middel til at udføre high-throughput mekanistiske undersøgelser af membranaktivitet, der bidrager til forståelsen af permeationsforbedring.

Tilsammen giver denne afhandling indsigt i mekanismerne for membranaktivitet og en high-throughput metode til at studere sådanne mekanismer på enkelt-liposom basis. Resultatet af denne afhandling giver derfor et grundlag for hurtigere og mere relevant forståelse og screening af hvilke faktorer, der styrer permeationsforstærkningen på tværs af lipidmembraner i en kontekst, der er relevant for oral lægemiddellevering af peptid.

Publications

Publications:

I. **Nanna Wichmann Larsen**, Serhii Kostrikov, Morten B. Hansen, Claudia U. Hjørringgaard, Niels B. Larsen, Thomas L. Andresen, Kasper Kristensen
Biophysical investigation of permeation enhancers and peptide drugs in intestinal environments. In preparation

II. **Nanna Wichmann**, Philip M. Lund, Morten B. Hansen, Claudia U. Hjørringgaard, Jannik B. Larsen, Kasper Kristensen, Thomas L. Andresen, Jens B. Simonsen
Applying flow cytometry to identify the modes of action of membrane-active peptides in a label-free and high-throughput fashion. Biochimica et Biophysica Acta (BBA) - Biomembranes. 2022 Feb 1;1864(2):183820, DOI: 10.1016/j.bbamem.2021.183820

III. Jannik Bruun Larsen, Nayere Taebnia, Alireza Dolatshahi-Pirouz, Anne Zebitz Eriksen, Claudia Hjørringgaard, Kasper Kristensen, **Nanna Wichmann Larsen**, Niels Bent Larsen, Rodolphe Marie, Ann-Kathrin Mündler, Ladan Parhamifar, Andrew James Urquhart, Arjen Weller, Kim I. Mortensen, Henrik Flyvbjerg and Thomas Lars Andresen
Imaging therapeutic peptide transport across intestinal barriers. RSC Chem. Biol. 2021;2,1115–43. DOI: 10.1039/D1CB00024A

List of abbreviations

Alexa488: Alexa Fluor 488 hydrazide
AMP: antimicrobial peptide
Arg: arginine
Asp: aspartic acid
AU: arbitrary 'membrane fluorescence intenisty' units
BSA: bovine serum albumin
C10: caprate
CBIO: Colloids and Biological Interfaces (CBIO) group.
CitBIO: Center for Intestinal Absorption and Transport of Biopharmaceuticals
cLV: calcein-containing LV
CMC: critical micelle concentration
CPP: cell penetrating peptide
DCM: dichloromethane
DDM: dodecyl maltoside
DIC: N,N'-Diisopropylcarbodiimide
DLS: dynamic light scattering
DMF: dimethyl formamide
DMSO: dimethylsulfoxide
DOPE: 1,2-dioleoyl-*sn*-glycero-3-phosphoethanolamine
DTU Health Tech: Department of Health Technology at the Technical University of Denmark
ELSD: evaporative light scattering detector
ESI: electrospray ionization
FaSSIF: fasted state simulated intestinal fluid
FDA: U.S. Food and Drug Administration
Fmoc: fluorenylmethyloxycarbonyl
Glu: glutamic acid
GRAS: generally recognized as safe
GUV: giant unilamellar vesicle
HFIP: hexafluoroisopropanol
I_2: iodine
ICP-MS: inductively coupled plasma-mass spectrometry
Insulin: insulin desB30
LC: liquid chromatography
Leu: leucine
LV: large vesicle
MAP: membrane active peptide
MAP: membrane active peptides
Me: methyl
MeCN: acetonitrile
membrane MFI: membrane-fluorophore fluorescence
MFI: median fluorescence intensity
minSIF: minimum simulated intestinal fluid
MS: mass spectrometry
NaC: sodium cholate
NaCl: sodium chloride
NTA: nanoparticle tracking analysis

OtBu: butyl ester
Oxyma: ethyl cyanohydroxyiminoacetate
Pbf: 2,2,4,6,7,-pentamethyl dihydrobenzofuran-5-sulfonyl
PBS: phosphate buffered saline
PDB: Protein Data Bank
PhD: Doctor of Philosophy
POPC: 1-palmitoyl-2-oleoyl-*sn*-glycero-3-phosphocholine
POPS: 1-palmitoyl-2-oleoyl-*sn*-glycero-3-phospho-L-serine (sodium salt)
Pro: proline
QTOF: quadripole time-of-flight
sCT: salmon calcitonin
SD: standard deviation
SDS: sodium dodecyl sulfate
Ser: serine
SI: supplementary information
SNAC: salcaprozate sodium
TAT: transacting activator of transcription
Tat: transacting activator of transcription-derived peptide
TFA: trifluoroacetic acid
TIPS: triisopropylsilane
AA: amino acid

Table of Contents

Chapter 1: Introduction

Oral delivery is the most common route for drug administration (1). Oral formulations represent approximately 90 % of the total market share of all pharmaceutical formulations [1]. It has many advantages, including mimic of physiological metabolism, ease of ingestion, non-invasiveness and high patient compliance making it a convenient route for drug delivery. Despite its many advantages, many obstacles need to be overcome in the development of oral formulations to ensure sufficient bioavailability to obtain the desired effect [2]. The obstacles are mainly attributed to the harsh environment of the oral route in combination with the physicochemical properties of the drugs, including their membrane permeability [1].

1.1 Thesis objective

The focus of this PhD thesis is mechanisms and properties governing membrane activity in relation to oral peptide drug delivery.

The results presented within this thesis aim to present a novel perspective of permeation enhancement of peptide drugs in intestinal-mimicking fluids, and the development and characterization of methods for this.

The main objectives of the PhD thesis are:

I. The elucidation of the interplay between permeation enhancers, peptide drug, bile components and the importance hereof in relation to the membrane activity of the permeation enhancers.
II. The development of a high throughput method to study the mode of action of membrane active peptides.

1.2 Oral drug delivery

1.2.1 The oral route

The oral route is the route an orally administered formulation has to pass through (Figure 1.1). The oral route starts in the mouth, and continues through the stomach to the intestinal tract (Figure 1.1, left), where most nutrients and drugs are absorbed [1], [3]. From the mouth, both buccal and sublingual drug delivery can take place [4], [5]. Drugs can also be absorbed through the stomach [6]. However, neither the buccal and sublingual routes nor absorption through the stomach will be discussed in this chapter. The focus will be on the intestinal tract, particularly the small intestine. After being absorbed, drugs are either transported through the hepatic portal vein to the liver, from where it enters systemic circulation, which is typical for hydrophilic compounds, or is uptaken directly into the lymphatics, bypassing the liver [1] which is typical for lipophilic compounds.

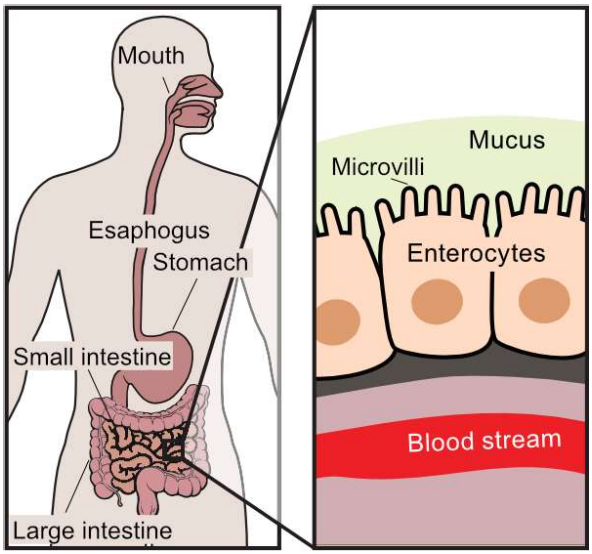

Figure 1.1: The oral route. Left: The oral route starts at the mouth, continues through the esophagus and the stomach to the small instestines and the large intestine, and ends at the rectum. Right: Substances absorbed through in small intestine must pass through the mucus layer and the layer of enterocytes to reach the blood stream. The surface of the enterocytes are increased by the presence of microvilli on the luminal side. The figure is adapted from the manuscript in Chapter 3.

1.2.1.1 The intestinal tract

The intestinal tract is divided into the small and the large intestine. The small intestine consists of the duodenum, jejunum, and ileum, and the large intestine of the cecum, colon, and rectum [1]. The luminal surface is lined with epithelial cells covered by a mucus layer (Figure 1.1 right), constituting a barrier for drugs in reaching the epithelial cells [7]. The mucus layer is thinner in the small intestines than in the stomach and the colon [1]. The surface area of the small intestines is greatly increased through villi structures, particularly in the duodenum and the jejunum [8]. For most substances, absorption mainly occurs through the absorptive cells, the enterocytes, present on the villi. On the apical side (the side facing the lumen) of each enterocyte, a large number of microvilli are present (Figure 1.1 right), which further enlarges the surface. The microvilli has a width of 100-200 nm and a height of approximately 1 µm. The cell membrane is composed of proteins, neutral lipids, phospholipids, and glycolipids, with a high number of proteins having transport properties [7]. Together, these factors contribute to the upper part of the small intestine being a major place for drugs absorption [9].

1.2.1.1.1 The intestinal lumen

Many factors influence the solubility, degradation, and absorption of nutrients and drugs in the intestines, including the physico-chemical environment and bile [10]. In the intestinal lumen, the physico-chemical environment is highly variable; even in the fasted state [11] where chyme from the stomach is also present [12]. The pH generally increases through the small intestines [13], with a mean of pH 6.3-6.5 in the duodenum [11], [14], pH 6.8 in the jejunum [11], and pH 7.4 in the terminal ileum [13]. In the fasted state, the mean osmolality in the duodenum is just below 200 mOsmol/kg [11], [14], 264 mOsmol/kg in the jejunum [11], and 60 mOsmol/kg in the ileum [11], [14].. The pH is increased from the very acidic pH of the stomach by the presence of bile salts [15]. Bile is led from the liver and gall bladder through the common bile duct into the intestine in the second part of the duodenum [16], and is absorbed in the ileum (12). The main components of bile are cholesterol, bile acids, phospholipids, and bilirubin [11], [16]. The

presence of the three first-mentioned components lead to the formation of mixed micellar carriers, which assist in solubilizing fats and fat-soluble substances [11], [17]. The mean concentration of bile acids in the fasted state is reported to be around 3.3 mM in the duodenum, and around 3 mM in the jejunum (8). The main bile acid is taurocholate. It should be noted however, that also bile concentrations and compositions are highly variable, both on an interindividual and an intraindividual basis [11]. The last-mentioned variation may in part be due to intake and timing [11].

Absorption of nutrients and drugs are also influenced by the exposure time of the substance to be absorbed towards the epithelium. The transit time is generally considered to be 3-4 hours for the small intestines, and two to four days for the colon [1].

1.2.1.2 The way of drugs into the blood stream

For orally administered drugs intended for systemic delivery (as opposed to the gastro-intestinal tract itself being the target), has to reach the blood stream. Generally, absorbed drugs are transported through the hepatic portal veins to the liver, from where they enter systemic circulation. In the liver, the drugs are exposed to the hepatic enzymes, and may be subjected to first-pass hepatic metabolism [18]. First-pass hepatic metabolism potentially reduces the bioavailability of the drug before entering the systemic circulation. Lipophilic drugs may instead be absorbed by the intestinal lymphatics, and be delivered directly to systemic circulation, thereby bypass the liver and first-pass hepatic metabolism [19]. When the systemic circulation is reached, the oral route is completed.

1.2.2 Uptake pathways

In order to be absorbed systemically, an orally delivered drug must cross the epithelium. As written above, this is often the epithelium of the duodenum and jejunum. The ability to cross the epithelium and the mechanism by which this is done is determined by many factors, particularly the physicochemical factors of the drug. Figure 1.2 shows different mechanistic possibilities for transport of drugs from the apical side to the basolateral side of the epithelium.

Overall, the transport mechanism can be passive, active, or vesicular [20]. Passive transport is energy-independent transport across the epithelium, driven by a concentration gradient. It can be further divided into paracellular (Figure 1.2a) and transcellular transport (Figure 1.2b). Passive paracellular transport is transport across the epithelium in the gap between the cells, through the gaps between specialized proteins forming tight junctions. The paracellular route is favored by small, hydrophilic drugs. Passive transcellular transport is diffusion across the apical cell membrane, through the cell, and across the basal cell membrane into the blood stream. The mechanism is mainly favored by small, membrane-permeabilizing drugs, typically adhering to 'Lipinski's rule of 5'. 'Lipinski's rule of 5' is a rule consisting of four physicochemical parameter ranges which molecules predicted to be intestinal permeable do not violate more than one of. The parameter ranges are ≤ 5 hydrogen bonds, ≤ 10 hydrogen bond acceptors, molecular weight ≤ 500 Da, and log(P) ≤ 5 [21]. Nonetheless, also lipophilic peptides have been shown to penetrate the lipophilic bilayer of intestinal cells [22], [23]. Due to the large surface area of the enterocytes, the majority of drugs being absorbed without transporters are absorbed by this mechanism. Passive transcellular transport is therefore a target mechanism of many drug studies [7], [23], [24].

In active transcellular transport, molecules are being transported into the cell in an energy-dependent manner, by the use of transporters embedded in the membrane. Transporters cover both influx transporters mediating uptake of e.g. oligopeptides from the apical side, and efflux transporters actively transporting substances out of the cell. Transporters can be placed both in the apical membrane and basolateral membrane, and typically transport hydrophilic molecules recognized as substrates alongside nutrients [25].

Vesicular transcellular transport, also called transcytosis, is transport where the substance is taken up into a vesicle by endocytosis, transported across the cell in the vesicle, and released into the bloodstream by exocytosis.

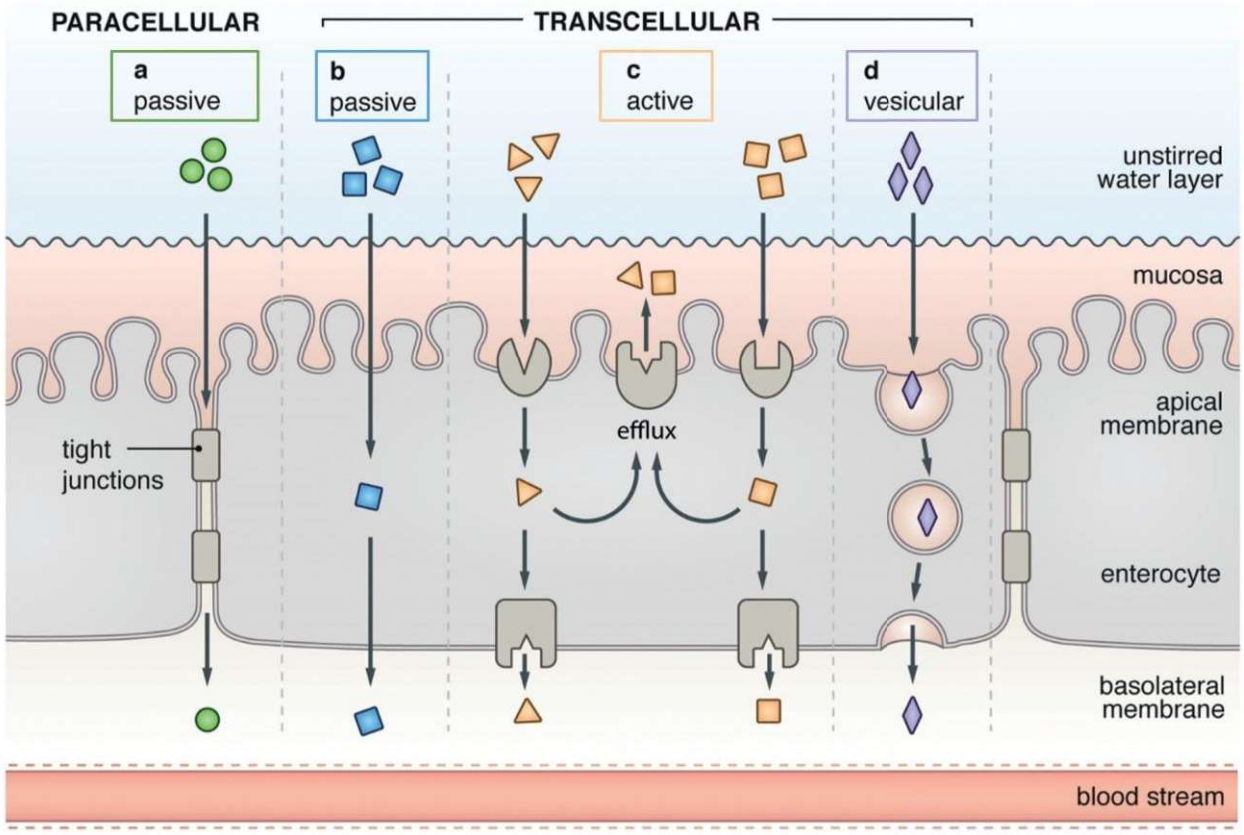

Figure 1.2: Mechanisms of drug absorption through the epithelium to the blood stream. Shown is here transport of molecules across enterocytes, from intestinal lumen on the apical side to the blood stream on the basolateral side. Transport across the epithelium can be a) passive paracellular through the tight junctions that join the cells, b) passive transcellular by diffusion across the cell membrane and the cell, c) active transcellular by transporter-mediated absorption. Transporters can be both influx transporter, transporting molecules into the cell, or efflux transporters, transporting molecules out of the cell, d) vesicular transcellular, by uptake by endocytosis, transport by transcytosis in vesicles, and release by exocytosis. Also the unstirred water layer and mucosa which covers the epithelium are shown here. Both are factors restraining diffusion of large molecules and hence potentially decreasing drug absorption. The figure is adapted from [20] *with permission from John Wiley and Sons.*

1.3 Oral drug delivery of peptides

From the above, it should be clear that some of the challenges in oral drug delivery are highly dependent on the molecular and physicochemical properties of the respective class of drug to be orally administered, including their size and hydrophobicity. Other challenges arise from enzymatic degradation [26] and

entrapment of large, or charged drugs in the mucus layer [27]. From here on, the focus will be on topics related to oral delivery of peptides.

1.3.1 Peptides as orally delivered drugs

Peptides are short chains of amino acids, historically considered to be up to around 50 amino acid residues [28]. Peptides adopt various degrees of specific secondary structure, but contrary to proteins, generally lack tertiary and quaternary structure. Their role in biology and biotechnology are vast, as they function as hormones, neurotransmitters, growth factors, and antibacterial agents [28]. From an oral delivery perspective, their biological and physicochemical properties optimized for their physiological roles, are both the largest strengths and the largest weaknesses of potential peptide drugs.

Due to their individual amino acid sequence and corresponding specifically adopted ensemble of secondary structures, peptides are very distinct molecules. This enables peptides to bind to specific receptors with high specificity and high potency [29], making them the ideal drug candidate for targeting specific receptors in many cases [28]. Due to their lack of higher order structure, peptides are quickly degraded in a predictable manner, typically into non-toxic di- and tripeptides [30]. The fast degradation is an advantage for naturally occurring peptides when functioning as receptor agonists activating e.g. a signal pathway, as this enables a tight regulation of the effect of the peptide. The predictable degradation into non-toxic metabolites is also an advantage of peptide as drug [29]. However, the inherent biological instability of peptides often leads to low bioavailability of peptide drugs.

Naturally, occurring peptides are generally hydrophilic and have a high molecular weight, which generally render them intrinsically membrane impermeable [31]. Also, the paracellular route is generally not an option due to their high molecular weight. Since their biological target is often a cell surface receptor [28], membrane permeability is not a prerequisite for the natural biological function of peptides. However, from an oral peptide drug perspective, membrane impermeability of peptides is highly disadvantageous, as peptides that are to be systemically absorbed need to cross the intestinal epithelium. The membrane impermeability thus greatly lowers the bioavailability of peptide drugs.

Many of the inherent obstacles of oral peptide drug delivery can be overcome by modifying the primary peptide structure or the sidechains of the peptides. This is feasible, as peptides can be synthesized fast and cost-efficient using solid phase peptide synthesis. However, in many cases even small modifications of peptides can greatly decrease their stability, affinity to, and specificity of receptor binding [20]. This demonstrates the difficulties of balancing the peptide bioavailability with their activity.

Thus, while the properties of peptides is what makes them interesting as drug candidates, the same properties decreases the oral bioavailability of peptides and thereby complexating oral peptide drug development.

1.3.2 Possibilities to increase the bioavailability of peptides

As previously stated, many delivery barriers and microenvironmental challenges limit the bioavailability of orally delivered peptide drugs, with the major limitation being the general inability of peptides to cross the epithelium. Nonetheless this is a requirement for peptide drugs to be orally administered for systemic delivery, as desired. Many strategies have been employed to enhance the bioavailability of peptides drugs, several of which focus on minimizing loss and enhancing the local concentration and exposure time of the active peptide drug to the site of absorption [32]. In this thesis, the focus will be on possibilities of

enhancing the absorption of the peptide drugs present at the surface of the epithelial cells, after having passed through the mucus.

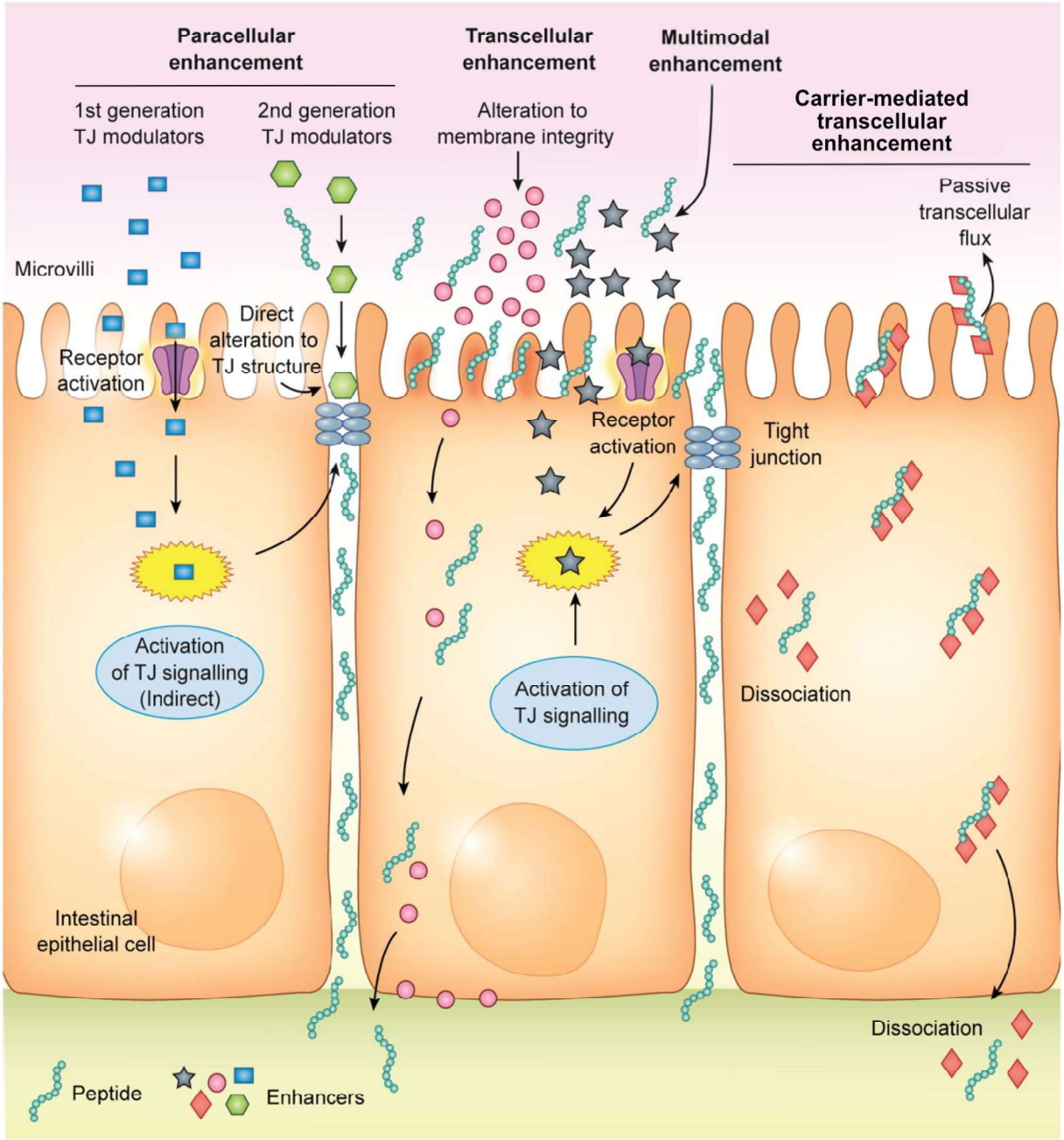

Figure 1.3: Modes of action of permeation enhancer: Paracellular permeation enhancers lead to opening of tight junctions (TJ), and are categorized as 1st or 2nd generation paracellular permeation enhancers. 1st generation paracellular permeation enhancers function indirectly through cell signaling. 2nd generation paracellular permeation enhancers directly target the physical disruption of TJ. Transcellular permeation enhancers act via alteration of the membrane integrity or carrier-mediated enhancement of the passive transcellular flux of the peptide. Some permeation enhancers exhibit both paracellular and transcellular enhancement. These permeation enhancers are referred to as multimodal permeation enhancers. The figure is adapted from [32] *with permission from Elsevier.*

Strategies to increase the absorption of the peptide drugs present at the surface of the epithelial cells generally evolve around the use of helper molecules or helper moieties [32]. Here, both molecules and covalently attached molecular moieties included to enhance the permeation of the drug across the epithelial cell layer are categorized as permeation enhancers.

As mentioned above, uptake pathways can be paracellular or transcellular. The use of permeation enhancers can thus, logically, aim at increasing the paracellular pathway, the transcellular pathway, or both pathways [32]. Paracellular permeation enhancers are permeation enhancers that lead to the opening of the tight junctions, thereby enabling the passage of the peptide drug through the tight junctions. Paracellular permeation enhancers can be grouped into 1st and 2nd generation paracellular permeation enhancers. 1st generation paracellular permeation enhancers translocate across the cell membrane, passively or actively, and activate intracellular signaling involved in disbandment of the tight junctions, thereby opening the tight junctions. 2nd generation paracellular permeation enhancers open the tight junctions directly by disrupting the interactions at cell adhesion recognition sequences. Most paracellular permeation enhancers are of the 1st generation type [32]. Transcellular permeation enhancement can be achieved by altering the membrane integrity, e.g. by fluidizing the membrane, thus making the membrane more permeable. Many permeation enhancers affect both the paracellular and the transcellular transport; these are called multimodal permeation enhancers [32]. Another mean of enhancing transcellular permeation is by altering the ability of the peptide drug to translocate across the lipid bilayer. This can be done by adding a molecule or moiety (here called a carrier) that increases the passive transcellular flux of the peptide drug. The carrier can be added either by covalent attachment (e.g. of lipophilic moieties such as acyl chains) [22], [23] or physical complexation (through electrostatic interactions, hydrophobic ion pairing or non-ionic interactions) [33]–[35]. Most permeation enhancers are transcellular and function by interacting with the plasma membrane [32]; they are membrane active. Below will be elaborated on the modes of action for these permeation enhancers, as well as on peptides exhibiting membrane activity potentially relevant for permeation enhancement

1.3.2.1 Permeation enhancement by alteration of membrane integrity

The majority of transcellular permeation enhancers are surfactants that function by alteration of membrane integrity functions as detergents [32]. Surfactants are surface (membrane) active amphiphiles. They are thus composed of a hydrophilic ‘head’ group, and a hydrophobic ‘tail’ [36]. It has been proposed that surfactant monomers first adsorb to the outer lipid bilayer, then insert into the lipid bilayer, and flipflop into the inner layer of the phospholipid bilayer [37]. The insertion of the surfactant alters the packing of the lipids in the bilayer [38], [39]. At sufficiently high concentrations of surfactants the altered packing of the lipids lead to an increase in membrane fluidity; that is how fast the lateral movement of the phospholipids is [40]. This may lead to an increased permeability without solubilization [41]. At higher concentrations of the membrane-inserted surfactant, phospholipids or fragments of the membrane lipid bilayer are extracted into mixed-micelles with the surfactants, thus solubilizing the membrane, hence increasing the membrane permeability (Figure 1.4) [41], [42]. Permeation enhancement by surfactants is thus highly dependent on the permeation enhancer concetnration. Surfactants generally are able to form micelles or vesicles [43], [44] above a critical micelle concentration (CMC). The micelles and vesicles can function as a reservoir of surfactants, keeping the monomer concentration high when surfactant monomers are inserted into the lipid bilayer. Hence, the higher the CMC is, the higher is the potential concentration of the monomer, free to interact. For fatty acids, longer chain lengths results in higher degree of membrane interaction, but also with greater tendency to form micelles or vesicles and hence a

lower potential free monomer concentration [32]. Consequently, for fatty acids as permeation enhancers, the optimum appears to be a length of 10 carbon atoms (the C10) [32], [42]. However, such correlations cannot generally be done as also many other factors, including the type of molecule and their ability to form also influence the permeation enhancement [42].

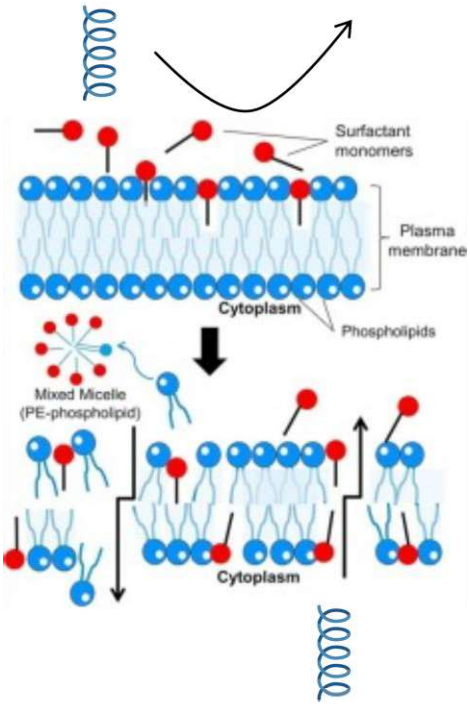

Figure 1.4: Proposed mechanism by which surfactant-based permeation enhancers may alter membrane integrity. Surfactant permeation enhancers insert into the phospholipid bilayer, resulting in altered phospholipid packing. Upon the altered packing of the phospholipids, they and/or membrane fragments can be absorbed into permeation enhancer micelles, leading to the formation of permeation enhancer-phospholipid mixed micelles. The disintegration of the phospholipid bilayer enhances the permeability of the membrane towards peptide drugs. Figure adapted from [42] *with permission from the Elsevier.*

Leading surfactant permeation enhancers include dodecylmaltoside (DDM); sodium dodecyl sulfate (SDS); salts of fatty acids, such as sodium caprate (C10); and bile salts, such as sodium cholate (NaC). As these will also be used in the thesis, these permeation enhancers will be described in more detail below.

1.3.2.1.1 C10

C10 is the sodium salt of the medium chain fatty acid capric acid, and is one of the most well studied permeation enhancer. It has a long history of use in man, is used as food additive, and has been used in Phase II studies to improve intestinal permeation insulin [45]. In the ionized form of C10, C10 form colloidal structures only at high concentrations [44], leaving a high monomeric concentration free to function as a surfactant in permeation enhancement, yet this equilibrium is highly environment-dependent [46]. Furthermore, it is evident that C10 also has an effect as first generation paracellular permeation enhancer. Many mechanisms for this have been proposed, including a pathway that stimulates the intracellular calcium concentration [47], leads to contraction of perijunctional actomyosin ring, and thereby permit increased tight junction permeability [48]. The paracellular permeation enhancer effect of C10 may be attributed to its membrane fluidizing properties [47], and it is clear that the permeation enhancement and mechanism of such is highly concentration dependent [46].

1.3.2.1.2 Bile salts

Bile salts are naturally present in the intestinal lumen and aid at solubilizing fatty compounds, transporting lipids, and enhancing lipid absorption [49]. They are ionic amphiphilic compounds with a steroid skeleton. Generally, bile acids are able to form small, primary micelles on their own [43] but also form secondary micelles where multiple primary micelles aggregate through hydrophobic interactions [49]. Bile acids are known to form mixed-micelles with phospholipids [50], and can fluidize and extract membrane lipids as other surfactants used for permeation enhancement [51]. Nonetheless, many bile acids appear also to affect the tight junctions and thereby lead to enhanced paracellular permeability. The paracellular mechanisms of actions are highly variable, and include the generation of reactive oxidative species [52], EGF receptor autophosphorylation [53], and binding of the calcium near the tight junctions [49]. The multimodal permeation enhancement appears to be general for bile acids; at least NaC [54], sodium taurocholate [32], and sodium deoxycholate [32] have been shown to have a multimodal mode of action.

1.3.2.1.3 DDM

DDM is an alkyl maltoside with the polar head group being a disaccharide (maltose) and the hydrophobic group being an alkyl chain. It was developed to be a solubilizing agent for membrane proteins [55]. DDM is known to have a very low CMC. The formed micelles are 6-7 nm in diameter [56], leaving only a small monomeric concentration free for permeation enhancement. Yet, DDM is also known to be permeation enhancing at lower concentrations than eg. sodium cholate and C10 [32], [54], [57]. DDM has been shown to have a multimodal mode of action, primarily through increase of the membrane fluidity [32] and solubilization of the membrane [54]. Yet, it has also been indicated that DDM enhance permeation through direct interactions with tight junction proteins [58].

1.3.2.1.4 SDS

SDS is a classical surfactant, and the most prominent alkyl sulfate tested in oral peptide delivery. It is approved as an excipient in drugs [59] and as a food additive [60] by the FDA. SDS form distinct micelles on its own, are known to form membrane protein:SDS complexes and mixed membrane lipid:SDS micelles [61]. While it has a classical transcellular surfactant mode of action in permeation enhancement [32], it differs from other surfactant permeation enhancers, as it is strongly protein denaturing [61], [62]. The denaturation might constitute a challenge for delivery of peptides, if the denaturation is not reversible.

Of the four mentioned permeation enhancers, only SDS is considered to be exclusively a transcellular permeation enhancers, the three others are multimodal permeation enhancers, functioning both paracellular and transcellular [32]. Yet even for the transcellular effect, it is difficult to correlate permeation enhancement to physiochemical properties [32]. This may be because soluble surfactants can be further categorized into two sub-groups based on whether (subgroup 1) or not (subgroup 2) they are able to form higher order liquid crystal structures [32], with fatty acids such as C10 and bile acids, such as cholate being placed in subgroup 1 and 2, respectively.

1.3.2.2 Carrier-mediated permeation enhancement

Carrier-mediated permeation enhancement is, as mentioned above, the utilization of another compound to enhance the ability of the peptide drug to translocate across the lipid bilayer. Many carriers, such as Salcaprozate Sodium (SNAC) has a lipophilic moiety, and enhances the lipophilic surface area of the peptide drug complex. In addition, other means of membrane-interactions can be utilized to enhance the translocation properties of a peptide drug, and another group of molecules mediating permeation enhancement as a carrier, is the group of cell penetrating peptides. A short introduction to permeation enhancers with a carrier function used in this thesis, SNAC, and the cell-penetrating peptides (CPPs) Tat and penetratin will be given below.

1.3.2.2.1 SNAC

SNAC is a synthetic N-acetylated amino acid derivate of salicylic acid. It was discovered in a screen for molecules enhancing the absorption of salmon calcitonin (sCT) [63], and is part of the Eligen ®-carrier library, which contains proprietary carriers that physically interact with a wide range of drugs to enhance passive permeation across the intestinal epithelium [32]. SNAC has status of 'generally recognized as safe' (GRAS) by the U.S. Food and Drug Administration (FDA) [46], and is used as permeation enhancer for oral semaglutide (Rybelsus), the only linear polypeptide drug being approved for oral delivery by the FDA [64]. In Rybelsys, SNAC enhances permeation in the stomach through multiple actions. SNAC showed a local buffering effect, thereby reducing peptide cleavage by pepsin, and increased membrane fluidity in a surfactant-like manner, but as a carrier, SNAC shifted semaglutide towards a monomeric state better suited for translocation across the epithelium into the blood stream [6]. SNAC has also been shown to increase the lipophilic surface area of insulin through non-covalent bonding and/or conformational changes to the peptide [32].

1.3.2.2.2 Cell penetrating peptides

The first CPPs to be discovered was a peptide derived from the human immuno-deficiency virus-1 transacting activator of transcription protein TAT) (The peptide is hereafter denoted Tat), which was able to translocate across the cell membrane [65]. Tat has been shown to act as a carrier permeation enhancer, by translocating proteins to which it is conjugated, into the cell through pinocytosis [66]. The second CPP discovered was a peptide derived from the third helix of the DNA-binding transcription factor *Drosophila* Antennapedia homeodomain, called penetratin [67]. Both Tat and penetratin are, as many other CPPs, short cationic peptides.

Penetratin is able to translocate across the cell plasma membrane alone, but has also been shown *in vivo* to be able to function as a carrier for cargo, including insulin (43). Penetratin has been used as a carrier, often covalently coupled to its cargo, but has also been shown to enhance the absorption of insulin when being physically complexed with insulin through electrostatic interactions (28). Penetratin appears to translocate across the lipid bilayer by means of various mechanisms, depending on multiple factors, including concentration and cell line (44), with the energy-dependent uptake mechanism of endocytosis being favored for high concentrations and energy-independent translocation mechanisms being favored for low concentrations (44). Energy-independent translocation of penetratin has been assigned to all of the common energy-independent translocation mechanism, formation of inverted micelles (44), mechanisms that can be explained by the carpet model and the barrel stave pore model (45), as well as the toroidal pore model (46) (Figure 1.5). The mechanisms will be elaborated below in section 1.3.2.3.1.

Overall, the mechanisms all require some degree of lipid reorganization, albeit to various degrees, and studies deviate as to whether the membrane is perturbated upon the translocation of penetratin (47). Yet, generally for CPPs, the mechanism may also very well depend on the cargo-complexation (45), with larger cargo favoring endocytic uptake (44).

Overall, permeation enhancement by the use of CPPs appears to require the CPP functioning as a carrier [68], and the use of CPPs as permeation enhancers are thus much more specific than for surfactants. In their favor, CPPs therefore require much lower permeation enhancer concentrations than surfactants as typical permeation enhancing concentration *in situ* for penetratin are around 0.5 mM , whereas for surfactant two-digit mM concentrations are common [32]).

1.3.2.3 Membrane active peptides

While peptides do generally not interact with the lipid membrane, a few peptides, the CPPs, are able to translocate across the lipid membrane. In a drug delivery perspective, CPPs are interesting both as vehicles to transport cargo-peptide drugs across the epithelial membrane, but also to study in the quest to enhance the inherent translocation properties of the peptide drug itself. Overall, a broad range of translocation mechanisms have been proposed, and even for the individual CPPs the mechanism of translocation appears to be multiplex [69]. The range of mechanisms include both energy-independent and energy dependent (endocytic) mechanisms. Here, the focus will be on the energy-independent mechanisms of translocation. The proposed energy-independent mechanisms cover formation of inverted micelles, formation of pores, and the carpet model (Figure 1.5) [70]. Common for the translocation mechanisms of CPPs are that they all exert some membrane activity (see below in section 1.3.2.3.1).

1.3.2.3.1 Mechanisms of energy-independent CPP translocation

The proposed mechanisms of energy-independent CPP translocation that will be covered here are the formation of inverted micelles, two versions of the carpet model, and translocation involving pore-formation.

For translocation through the formation of inverted micelles, the CPP is translocated across the lipid bilayer, entrapped in an inverted micelle that provides a hydrophilic environment for the CPP. The inverted micelle is formed as a result of changes in the membrane curvature mediated by electrostatic CPP:lipid interactions. This mechanism is considered to favor transport of hydrophilic compounds covalently attached to the CPP [69].

In the carpet model, the CPP self-associate in a carpet-like manner while being associated with the membrane surface due to electrostatic interactions. Upon accumulation above a certain threshold, hydrophobic sites of the CPP then embed in the lipid region of the membrane, leading to a reorganization of the lipids, and ultimately micellization and disruption of the membrane, similar to the mechanisms of surfactants [70], as well as internalization of the CPP [69]. An alternative to the carpet model is the membrane-thinning effect. Here, rather than the vertical insertion of the hydrophobic CPP moieties into the lipid bilayer, the cationic groups of the CPP interacts with the negatively charged lipids and inserts into the head group region of the membrane in a surface aligned manner. This requires an expansion of the head group area, and is usually accompanied by a reduction of the acyl chain layer thickness [71], [72]. The thinning and a concurrent reduction of the local surface tension allows for intercalation of the CPP within the membrane [69].

The translocation mechanisms involving pore-formation are in general proposed as mechanisms used by primary amphipathic peptides [69]. In the barrel-stave model, CPPs aggregate on the membrane and insert into the membrane bilayer forming a well-defined pore with inwardly facing hydrophilic surfaces and interactions between the outwardly facing hydrophobic residues and the lipid tails of the membrane [69], [70]. In the toroidal model, the CPPs form α-helices upon the interaction with the membrane and cause the lipid monolayer to bend into the interior, thereby forming a hydrophilic gap in the membrane [69].

From the insertion into the membrane, the CPP may dissociate into the interior of the cell, thereby being translocated [73].

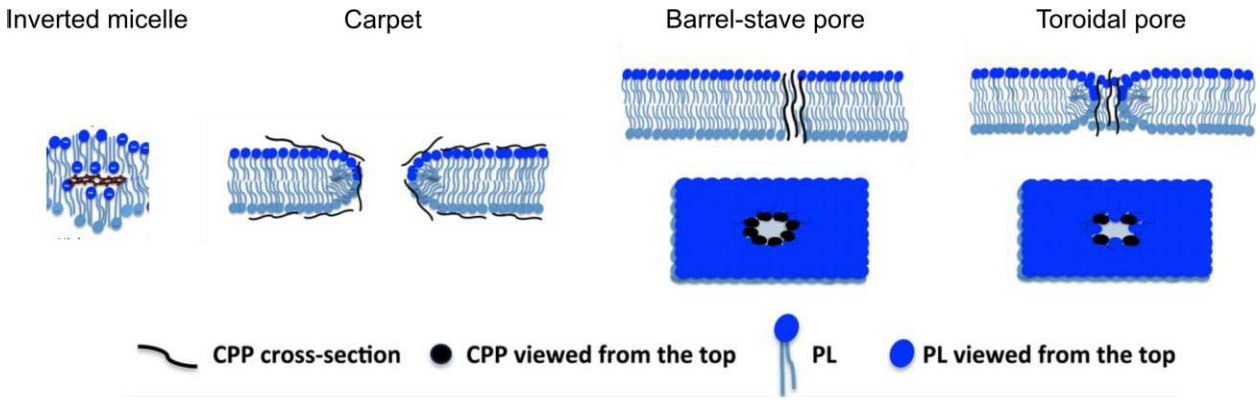

Figure 1.5: Proposed energy-independent translocation mechanisms for cell penetrating peptides (CPPs). PL: phospholipids. Adapted with permission from [69], [70]*. Copyright 2022 American Chemical Society.*

1.3.2.3.2 Antimicrobial and pore-forming peptides

Other peptides, such as many antimicrobial peptides (AMPs) are also membrane active, functioning by some of the same mechanism as CPPs [74], and sharing some of the properties of CPPs, such as their short length and commonly being positively charged. A major difference between CPPs and AMPs are their ability to keep the membrane intact or be membrane disrupting, respectively [75]. This difference may be due to the stability of the defects (transient vs. permanent), and in their native form, AMPs are therefore not suited as permeation enhancers [32]. Yet insight into membrane activity mechanisms of AMPs may contribute to the general insight of (peptide) membrane activity, both as a permeation enhancer and for insight into modifying peptide drugs into being self-translocating. Studies of the mechanisms of AMPs and pore-forming peptides may thereby contribute to the journey towards increasing the bioavailability of peptide drugs. Below, a small selection of antimicrobial and pore-forming peptides will be introduced.

Melittin is an amphiphatic, cationic AMP and the main component of bee venom. It specifically induce lysis of the red blood cells. Melittin form α-helices upon the binding to lipid membranes [76], and, depending on the orientation, may insert into the lipid bilayer forming a toroidal pore [77]. Interesting from a drug delivery perspective, some of the melittin may be translocated across the lipid bilayer upon disintegration of the pore [73]. For anionic lipids, melittin has been reported to rather function in a detergent-like manner as for surfactants [78]. Melittin has been studied as a permeation enhancer, and was shown to unspecifically increase the permeation across various cell layers as a paracellular permeation enhancer [79], [80] in a reversible manner [80]. Yet, its inherent toxicity due to its membrane activity limits its use as a permeation enhancer [81].

Magainin-2 is a cationic, amphipathic AMP found in the skin of the frog *Xenopus laevis*. It has a specificity towards bacterial membranes [82]. Similar to melittin, Magainin-2 is α-helical and known to form toroidal pores [83], from which it can translocate across a lipid bilayer upon disintegration of the pore [84]. Magainin-2 has also been proposed to act through the membrane-thinning mechanism [71].

Macrolittin-70 is a synthetic peptide developed from the sequence of melittin. Yet, contrary to most AMPs, macrolittin-70 has an overall anionic charge. Macrolittin-70 was developed to form large pores as opposed to many pore-forming peptides, and has a multifaceted and destructive effect on the lipid bilayer structure, and a potent membrane permeabilization activity [85].

LL-37 is an AMP from human cathelicidin. It is amphipathic, cationically charged, and 37 amino acid residues long. Contrary to other AMPs, LL-37 form fibril-like structures in solution, and in the membrane, it forms a narrow channel by the use of an LL-37 tetramer, but also appears to function in a detergent-like manner, revealing a complex, and not well-resolved mechanism of action for LL-37 [86].

1.3.3 Safety and other thoughts on the way to the clinic

Overall, providing drugs as oral formulations rather than by parenteral administration, should, among other things, increase the safety of the drug use. Yet several factors regarding safety should be considered. At the site of absorption, concerns include the disruption of the epithelium [87], usually required for peptide absorption, namely the membrane perturbating effect of e.g. surfactant permeation and pore formation by pore-forming peptides, and the opening of the tight junctions. Several studies with permeation enhancers have shown a decrease in transepithelial electrical resistance, cytotoxicity and mucosal damage [42], [87]–[89]. Permeation enhancers often have high toxicity, in for example Caco-2 cells, and the toxicity even appears to be related to the permeation enhancement [87], [90]. Yet, an optimum with permeation enhancement concurrently with rapid recovery can sometimes be found – the so-called 'therapeutic window' [87], [90]. Also in isolated rat intestines were C10 and SNAC [91], and SDS [89] shown to cause mild damage. Yet, the toxicity in vivo appears to be limited as all three of these permeation enhancers are approved by the FDA as food additive [60], [92]. The lack of toxicity in humans may be due to the fast recovery observed for more complex models [93], but can also be attributed to the unlikeliness that the intestinal epithelium is exposed to high permeation enhancer concentrations for a prolonged period of time due to short transit times, spreading, dilutions, and absorption [32]. Obviously, safety is a very important factor in getting the drug to the clinic. However, the focus of this thesis is on understanding the mechanisms of permeation enhancement and membrane activity, and safety will thus not be further considered here.

The lack of long exposure time of high concentrations of permeation enhancers, however also enhances the requirements of the permeation enhancers, and may increase the necessary permeation enhancer dose for the desired effect. Finally, even for state-of-the-art of orally delivered peptides, the bioavailability is not increased to more than 1-2 % of the dosed drug [6], [94]. Oral delivery of peptides thus requires high concentrations of both peptide drugs and their permeation enhancer, which may contribute to adherent side effects and will inevitably lead to higher production cost, which may limit orally delivered peptide drugs in 'going to the market' [95].

1.4 Studying oral drug delivery of peptide drugs

Many factors influence oral delivery of peptide drugs, and thus many aspects of oral peptide drug delivery are relevant to study. Naturally, only clinical studies will show if a drug formulation has the desired effect. However, clinical studies provide little information about the mechanisms occurring in the body. To get a better understanding of the mechanisms guarding oral peptide drug delivery, model systems can thus be applied. The model systems ranges from humans, over animals and cells, to synthetic lipid membranes (Figure 1.6). Obviously, the different model systems require different methods, and each model provides different levels of mechanistic detail [64]. The mechanistic detail is, however, often a trade-off for the biological relevance and feasibility of the studies, and the methods and model systems should thus be used to supplement each other, to screen for relevant drugs or formulations, to elucidate mechanisms of peptide drug delivery, and to validate if the desired drug formulation has an effect. Many of these model systems are discussed with respect to their ability to provide mechanistic information about peptide drug absorption in the article 'Imaging therapeutic peptide transport across intestinal barriers' [64] included as the appendix. Below will be a brief note on some of the models and methods, followed by a short discussion of the use of lipid vesicles to study mechanisms of peptide translocation across lipid bilayers, and finally a presentation the aim of this thesis.

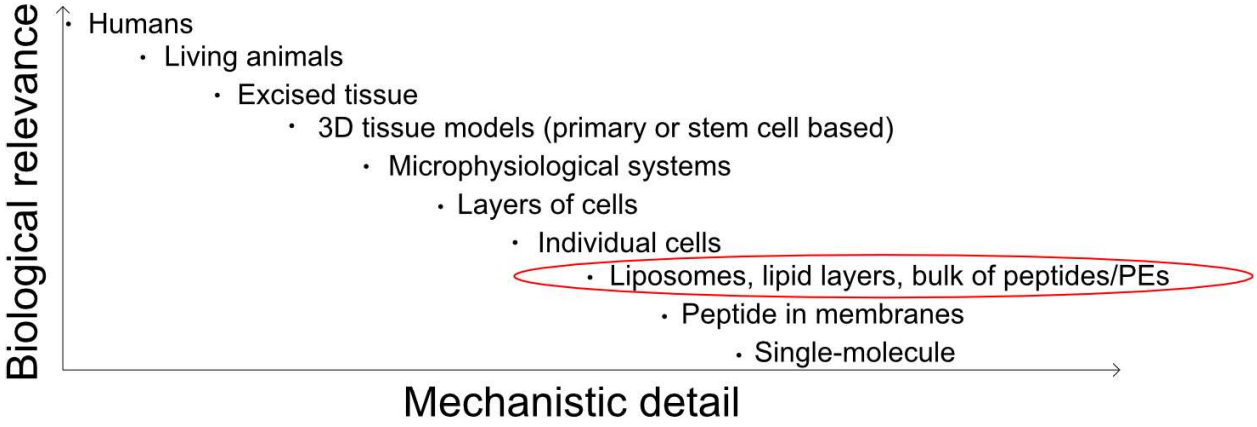

Figure 1.6: Mechanistic detail and biological relevance is a trade-off. Here a range of model systems is ranked with respect to biological relevance and mechanistic detail.

1.4.1 Models and methods

In studies in human, the physiological effect of oral administration of peptide drug formulation can be studied, e.g. by investigating if the glucose level in blood samples is decreased as a response to oral administration of insulin [96]. For more direct studies of the pathway by which peptides can be taken up in the body, advanced intravital microscopy has been used on living animals to locate fluorescently labelled ovalbumin to goblet cell-associated pathways upon per-oral administration [97]. This method, however, requires highly specialized training and equipment. Models that are more feasible are *ex vivo* models, such as Ussing chambers equipped with intestinal human or animal epithelium, and *in vitro* models, such as transwell studies with a cell layer where the complexity can be varied. These model systems allows for the detection of peptide translocation, and enables quantification of the amount of peptide translocated across the epithelium or the cell layer over time [98], [99]. By including marker molecules and barrier resistance measurements, these types of models can further provide information about whether the translocation occurs paracellularly or transcellularly [98], [99]. More detailed mechanistic studies of the translocation are often obtained by the use of microscopy on cells or artificial

lipid membranes, such as giant unilamellar vesicles (GUVs), and require the use of fluorescent entities. For cells, studies can provide information about location of the peptide in the cell, and thus indicate if peptide drugs are taken up by e.g. endocytosis or direct translocations [100]. For GUVs, studies can further provide information on the kinetics of fluorescently labelled drugs, as well as whether a translocation is coupled with loss of membrane integrity and thereby provide information about the translocation mechanism [101]. Artificial lipid vesicles are in general often used to study the effect of peptides on membrane integrity [102], [103], and have furthermore been used to study the orientation of peptides in membranes, thereby enabling differentiation between various types of pore-forming mechanisms [77]. Studies of artificial lipid membranes integrity are also often used to screen for membrane-active peptides [104]. The use of lipid vesicles as a model system will be further elaborated below. Finally, peptide structures in solution and in surfactants mimicking the membrane can provide information about the initial steps of peptides associating, such as pore-formation by oligomerization of peptides [86]. It is important to note, that many non-microscopy studies of peptide drugs using artificial lipid membranes do not provide information about the peptide drug translocation across the membranes. Rather the studies provide information about peptide associating with the lipids or the lipid bilayer, and how the peptides interact with and influence the lipid membranes; that is, their membrane activity. For the rest of this thesis, the focus will be on peptides, and membrane activity.

1.4.1.1 Lipid vesicles as a model system

Lipid vesicles are useful for studying the mechanisms of peptide membrane translocation and membrane interactions [105]. Advantages of liposomes include the opportunity to modulate the membranes to the purpose of the studies, such as the use of species-specific lipids [106], inclusion of charged lipids to include charge-driven membrane association [107], and inclusion of cholesterol to increase the 'stiffness' of the lipid bilayer [108]. Furthermore, fluorophores can be included, embedded specifically or unspecifically in the membrane or entrapped in the vesicle, enabling a great variety of studies not possible otherwise. The methods to study lipid vesicles are versatile and cover both bulk assays [102], [109], [110], assays measuring the coherence of single events [111], [112] as well as studies of individual vesicles [101], [113].

For peptide drug delivery, the major constituent of lipid vesicles used for studying membrane interactions is often 1-palmitoyl-2-oleoyl-sn-glycero-3-phosphocholine (POPC) [78], [98], [106], [114], which is representative of the abundant glycrophosphocholine, a common lipid of human plasma membranes [115]. Other typical components include anionic lipids for charge modulation [106] and cholesterol to enhance the stability of the lipid vesicles [116]. It is important to keep in mind that naturally occurring membranes are constituted of many components, varying both by species [117] , membrane type[115], and within the membranes [118]. Many considerations with regards to choice and complexity of lipid compositions can thus be relevant, but are often kept simple with one to three components [78], [98], [106], [114]. Peptide induced membrane permeability of lipid vesicles with POPC as the major constituent has, at least for sCT with various degrees of lipidations, been shown to correlate with the degree of peptide translocation across Caco-2 cell layers [22].

1.4.2 Studying oral drug delivery of peptides in this thesis

With an outset in oral peptide drug delivery, targeting transcellular absorption through the upper part of the small intestines, the focus of this thesis is the study of membrane activity and properties guarding membrane activity for peptides and permeation enhancers. It is important to note that the studies carried

out, do not provide any measures for peptide translocation or peptide absorption. The membrane activity studies will be carried out on POPC-based lipid vesicles due to the previously mentioned correlation between membrane permeation and peptide translocation across a layer of Caco-2 cells, which is used as a functional model for the small intestines. Additional lipid components are included to fit the study and will be further justified for each sub-project (Chapter 3 and chapter 4). Studies will be carried out in solutions with pH 6.7 and an osmolality of around 200 mOsmol, similar to the simplest simulated intestinal fluids used by Fuchs et al., as this should represent an average pH and osmolality of the duodenum and jejunum in fasted state [119]. While taking medications in fed state may be more convenient than in fasted state, the components of the bile present in the fasted state are also present at the fed state, albeit at a higher concentration in the fed state [14], why studies in fasted state simulated intestinal fluids may provide general information about membrane activity. In Chapter 3, the solution therefore included 2.7 mM taurocholate and 0.7 mM phospholipids as representative for bile components as compromise between that suggested by Fuchs et. al [119] and the BioRelevant fasted state simulated intestinal fluid (FaSSIF) [120]. The time span used in this thesis for the studies is 30-60 min, as this is the typical transit time of the upper part of the small intestine. It may be a little long as the exposure time would thus typically be smaller. Yet for Caco-2 transwell studied, the exposure time is typically up to two hours, and thus 30-60 minutes appears to be a proper time to study various effects. [71]

1.5 Thesis outline

This PhD thesis is outlined into 5 chapters as follows:

Chapter 1 provides a general introduction to the oral route, particularly focusing on the intestine, oral peptide drug delivery and possibilities to increase the bioavailabilites of peptide drugs and the mechanisms of this. In addition, it introduces some of the common model systems to study various aspects of oral peptide drug delivery.

Chapter 2 provides an introduction to the most commonly used methodologies in this thesis, including a discussion about advantages and limitations of the methods.

Chapter 3 contains manuscript I*: Biophysical investigation of permeation enhancers and peptide drugs in intestinal environments.* In this manuscript, a study is presented in which the membrane activity of seven permeation enhancers or membrane active peptides are studied in the absence and presence of peptide drugs and/or bile components. The study highlights the importance of including the peptide drug in the presence of bile components to elucidate mechanism of permeation enhancement.

Chapter 4 contains published paper I: Applying flow cytometry to identify the modes of action of membrane-active peptides in a label-free and high-throughput fashion. In this paper, the modes of action of six membrane active peptides are identified. The study presents a new flow-cytometry based method to identify such modes of action, allowing for concurrent investigation of membrane perturbation and membrane solubilization on a single vesicle base.

Chapter 5 summarizes the results of this thesis, highlights the novelty of the results, and comment on future perspectives.

Appendix contains the published review I: Imaging therapeutic peptide transport across intestinal barriers. In this review, fluorescence imaging techniques and models for the investigation of oral peptide drugs and their transport across the intestinal barrier in the early stage of drug development are review.

1.6 References

[1] M. S. Alqahtani, M. Kazi, M. A. Alsenaidy, and M. Z. Ahmad, "Advances in Oral Drug Delivery," *Front Pharmacol*, vol. 12, p. 62, Feb. 2021, doi: 10.3389/FPHAR.2021.618411/BIBTEX.

[2] N. Günday Türeli and A. E. Türeli, "Industrial perspectives and future of oral drug delivery," *Nanotechnology for Oral Drug Delivery: From Concept to Applications*, pp. 483–502, Jan. 2020, doi: 10.1016/B978-0-12-818038-9.00016-8.

[3] J. Kim and O. de Jesus, *Medication Routes of Administration*. StatPearls Publishing, 2022. Accessed: Aug. 27, 2022. [Online]. Available: https://www.ncbi.nlm.nih.gov/books/NBK568677/

[4] R. Anders, H. P. Merkle, W. Schurr, and R. Ziegler, "Buccal absorption of protirelin: An effective way to stimulate thyrotropin and prolactin," *J Pharm Sci*, vol. 72, no. 12, pp. 1481–1483, 1983, doi: 10.1002/JPS.2600721231.

[5] A. L. Paris *et al.*, "Sublingual protein delivery by a mucoadhesive patch made of natural polymers," *Acta Biomater*, vol. 128, pp. 222–235, Jul. 2021, doi: 10.1016/J.ACTBIO.2021.04.024.

[6] S. T. Buckley *et al.*, "Transcellular stomach absorption of a derivatized glucagon-like peptide-1 receptor agonist," *Sci Transl Med*, vol. 10, no. 467, p. eaar7047, Nov. 2018, doi: 10.1126/scitranslmed.aar7047.

[7] G. Patel and A. Misra, "Oral Delivery of Proteins and Peptides: Concepts and Applications," *Challenges in Delivery of Therapeutic Genomics and Proteomics*, pp. 481–529, Jan. 2011, doi: 10.1016/B978-0-12-384964-9.00010-4.

[8] J. E. Hall and M. E. Hall, "Digestion and Absorption in the Gastrointestinal Tract - ClinicalKey," in *Guyton and Hall Textbook of Medical Physiology*, 14th ed., Elsevier, 2021, pp. 823–832. Accessed: Aug. 29, 2022. [Online]. Available: https://www.clinicalkey.com/#!/content/book/3-s2.0-B9780323597128000667

[9] T. Murakami, "Expert Opinion on Drug Discovery Absorption sites of orally administered drugs in the small intestine Absorption sites of orally administered drugs in the small intestine," 2017, doi: 10.1080/17460441.2017.1378176.

[10] D. Sahoo *et al.*, "Oral drug delivery of nanomedicine," *Theory and Applications of Nonparenteral Nanomedicines*, pp. 181–207, Jan. 2021, doi: 10.1016/B978-0-12-820466-5.00009-0.

[11] A. Fuchs and J. B. Dressman, "Composition and physicochemical properties of fasted-state human duodenal and jejunal fluid: a critical evaluation of the available data," *J Pharm Sci*, vol. 103, no. 11, pp. 3398–3411, Oct. 2014, doi: 10.1002/JPS.24183.

[12] A. Gräns and C. Olsson, "Integrated function and control of the gut | Gut Motility," *Encyclopedia of Fish Physiology*, vol. 2, pp. 1292–1300, 2011, doi: 10.1016/B978-0-12-374553-8.00073-3.

[13] J. Fallingborg, "Intraluminal pH of the human gastrointestinal tract," *Dan Med Bull*, vol. 46, no. 3, pp. 183–196, 1999.

[14] D. Dahlgren *et al.*, "Fasted and fed state human duodenal fluids: Characterization, drug solubility, and comparison to simulated fluids and with human bioavailability," *European Journal of Pharmaceutics and Biopharmaceutics*, vol. 163, pp. 240–251, Jun. 2021, doi: 10.1016/J.EJPB.2021.04.005.

[15] A. N. Almajid and K. Sugumar, "Physiology, Bile," *StatPearls*, Sep. 2021, Accessed: Sep. 26, 2022. [Online]. Available: https://www.ncbi.nlm.nih.gov/books/NBK542254/

[16] M. Hundt, C. Y. Wu, and M. Young, “Anatomy, Abdomen and Pelvis, Biliary Ducts,” *StatPearls*, Aug. 2021, Accessed: Aug. 29, 2022. [Online]. Available: https://www.ncbi.nlm.nih.gov/books/NBK459246/

[17] B. L. Schneider, “Intestinal bile acid transport: biology, physiology, and pathophysiology,” *J Pediatr Gastroenterol Nutr*, vol. 32, no. 4, pp. 407–417, Apr. 2001, doi: 10.1097/00005176-200104000-00002.

[18] B. N. Singh, “Drug Delivery: Oral Route,” *Encyclopedia of Pharmaceutical Science and Technology, Fourth Edition*, pp. 1122–1149, Jul. 2013, doi: 10.1081/E-EPT4-120050250.

[19] J. A. Yáñez, S. W. J. Wang, I. W. Knemeyer, M. A. Wirth, and K. B. Alton, “Intestinal lymphatic transport for drug delivery,” *Adv Drug Deliv Rev*, vol. 63, no. 10, p. 923, Sep. 2011, doi: 10.1016/J.ADDR.2011.05.019.

[20] A. F. B. Räder *et al.*, “Orally Active Peptides: Is There a Magic Bullet?,” *Angewandte Chemie International Edition*, vol. 57, no. 44, pp. 14414–14438, Oct. 2018, doi: 10.1002/anie.201807298.

[21] C. A. Lipinski, F. Lombardo, B. W. Dominy, and P. J. Feeney, “Experimental and computational approaches to estimate solubility and permeability in drug discovery and development settings,” *Adv Drug Deliv Rev*, vol. 64, no. SUPPL., pp. 4–17, Dec. 2012, doi: 10.1016/J.ADDR.2012.09.019.

[22] S. Trier, L. Linderoth, S. Bjerregaard, H. M. Strauss, U. L. Rahbek, and T. L. Andresen, “Acylation of salmon calcitonin modulates in vitro intestinal peptide flux through membrane permeability enhancement,” *European Journal of Pharmaceutics and Biopharmaceutics*, vol. 96, pp. 329–337, Oct. 2015, doi: 10.1016/j.ejpb.2015.09.001.

[23] S. Trier, L. Linderoth, S. Bjerregaard, T. L. Andresen, and U. L. Rahbek, “Acylation of Glucagon-Like Peptide-2: Interaction with Lipid Membranes and In Vitro Intestinal Permeability,” *PLoS One*, vol. 9, no. 10, p. e109939, Oct. 2014, doi: 10.1371/journal.pone.0109939.

[24] B. Homayun, X. Lin, and H. J. Choi, “Challenges and Recent Progress in Oral Drug Delivery Systems for Biopharmaceuticals,” *Pharmaceutics*, vol. 11, no. 3, Mar. 2019, doi: 10.3390/PHARMACEUTICS11030129.

[25] R. A. Fearn and B. H. Hirst, “Predicting oral drug absorption and hepatobiliary clearance: Human intestinal and hepatic in vitro cell models,” *Environ Toxicol Pharmacol*, vol. 21, no. 2, pp. 168–178, Feb. 2006, doi: 10.1016/J.ETAP.2005.06.002.

[26] G. Chen, W. Kang, W. Li, S. Chen, and Y. Gao, “Oral delivery of protein and peptide drugs: from non-specific formulation approaches to intestinal cell targeting strategies,” *Theranostics*, vol. 12, no. 3, pp. 1419–1439, 2022, doi: 10.7150/THNO.61747.

[27] M. Boegh and H. M. Nielsen, “Mucus as a Barrier to Drug Delivery – Understanding and Mimicking the Barrier Properties,” *Basic Clin Pharmacol Toxicol*, vol. 116, no. 3, pp. 179–186, Mar. 2015, doi: 10.1111/BCPT.12342.

[28] A. Henninot, J. C. Collins, and J. M. Nuss, “The Current State of Peptide Drug Discovery: Back to the Future?,” 2017, doi: 10.1021/acs.jmedchem.7b00318.

[29] M. Erak, K. Bellmann-Sickert, S. Els-Heindl, and A. G. Beck-Sickinger, “Peptide chemistry toolbox – Transforming natural peptides into peptide therapeutics,” *Bioorg Med Chem*, vol. 26, no. 10, pp. 2759–2765, Jun. 2018, doi: 10.1016/J.BMC.2018.01.012.

[30] C. S. Brian Chia, "A Review on the Metabolism of 25 Peptide Drugs," *International Journal of Peptide Research and Therapeutics 2021 27:2*, vol. 27, no. 2, pp. 1397–1418, Feb. 2021, doi: 10.1007/S10989-021-10177-0.

[31] O. Zupančič and A. Bernkop-Schnürch, "Lipophilic peptide character - What oral barriers fear the most," *J Control Release*, vol. 255, pp. 242–257, Jun. 2017, doi: 10.1016/J.JCONREL.2017.04.038.

[32] S. Maher, R. J. Mrsny, and D. J. Brayden, "Intestinal permeation enhancers for oral peptide delivery," *Adv Drug Deliv Rev*, vol. 106, pp. 277–319, Nov. 2016, doi: 10.1016/j.addr.2016.06.005.

[33] M. Kristensen *et al.*, "Penetratin-Mediated Transepithelial Insulin Permeation: Importance of Cationic Residues and pH for Complexation and Permeation," *AAPS Journal*, vol. 17, no. 5, pp. 1200–1209, Sep. 2015, doi: 10.1208/s12248-015-9747-3.

[34] A. Leone-Bay *et al.*, "Acylated non-α-amino acids as novel agents for the oral delivery of heparin sodium, USP," *Journal of Controlled Release*, vol. 50, no. 1–3, pp. 41–49, Jan. 1998, doi: 10.1016/S0168-3659(97)00101-6.

[35] P. O. Hegg, "Precipitation of egg white proteins below their isoelectric points by sodium dodecyl sulphate and temperature," *BBA - Protein Structure*, vol. 579, no. 1, pp. 73–87, Jul. 1979, doi: 10.1016/0005-2795(79)90088-6.

[36] N. Dan, "Core–shell drug carriers: liposomes, polymersomes, and niosomes," *Nanostructures for Drug Delivery*, pp. 63–105, Jan. 2017, doi: 10.1016/B978-0-323-46143-6.00002-6.

[37] M. L. Rogerson, B. H. Robinson, S. Bucak, and P. Walde, "Kinetic studies of the interaction of fatty acids with phosphatidylcholine vesicles (liposomes)," *Colloids Surf B Biointerfaces*, vol. 48, no. 1, pp. 24–34, Mar. 2006, doi: 10.1016/J.COLSURFB.2006.01.001.

[38] M. Tomita, M. Hayashi, T. Horie, T. Ishizawa, and S. Awazu, "Enhancement of Colonic Drug Absorption by the Transcellular Permeation Route," *Pharmaceutical Research 1988 5:12*, vol. 5, no. 12, pp. 786–789, 1988, doi: 10.1023/A:1015992819290.

[39] P. Sharma, M. V. S. Varma, H. P. S. Chawla, and R. Panchagnula, "Absorption enhancement, mechanistic and toxicity studies of medium chain fatty acids, cyclodextrins and bile salts as peroral absorption enhancers," *Farmaco*, vol. 60, no. 11–12, pp. 884–893, Nov. 2005, doi: 10.1016/J.FARMAC.2005.08.008.

[40] M. L. Jackson, C. F. Schmidt, D. Lichtenberg, B. J. Litman, and A. D. Albert8, "Solubilization of Phosphatidylcholine Bilayers by Octyl Glucoside," *Biochemistry*, vol. 21, pp. 4576–4582, 1982.

[41] D. Lichtenberg, Y. Zilberman, P. Greenzaid, and S. Zamir, "Structural and Kinetic Studies on the Solubilization of Lecithin by Sodium Deoxycholate," *Biochemistry*, vol. 18, pp. 3517–3525, 1979, doi: 10.1021/bi00583a013.

[42] S. Maher, J. Heade, F. McCartney, S. Waters, S. B. Bleiel, and D. J. Brayden, "Effects of surfactant-based permeation enhancers on mannitol permeability, histology, and electrogenic ion transport responses in excised rat colonic mucosae," *Int J Pharm*, vol. 539, no. 1–2, pp. 11–22, Mar. 2018, doi: 10.1016/J.IJPHARM.2018.01.008.

[43] D. M. Small, "A Classification of Biologic Lipids Based upon Their Interaction in Aqueous Systems," *J Am Oil Chem Soc*, vol. 45, no. 3, pp. 108–119, 1968, doi: 10.1007/BF02915334.

[44] T. Namani and P. Walde, "From Decanoate Micelles to Decanoic Acid/ Dodecylbenzenesulfonate Vesicles," 2005, doi: 10.1021/la047028z.

[45] I. B. Halberg, K. Lyby, K. Wassermann, T. Heise, E. Zijlstra, and L. Plum-Mörschel, “Efficacy and safety of oral basal insulin versus subcutaneous insulin glargine in type 2 diabetes: a randomised, double-blind, phase 2 trial,” *Lancet Diabetes Endocrinol*, vol. 7, no. 3, pp. 179–188, Mar. 2019, doi: 10.1016/S2213-8587(18)30372-3.

[46] C. Twarog, S. Fattah, J. Heade, S. Maher, E. Fattal, and D. J. Brayden, “Intestinal permeation enhancers for oral delivery of macromolecules: A comparison between salcaprozate sodium (SNAC) and sodium caprate (c10),” *Pharmaceutics*, vol. 11, no. 2. MDPI AG, Feb. 01, 2019. doi: 10.3390/pharmaceutics11020078.

[47] M. Tomita, M. Hayashi, and S. Awazu, “Absorption-Enhancing Mechanism of EDTA, Caprate, and Decanoylcarnitine in Caco-2 Cells,” *J Pharm Sci*, vol. 85, no. 6, pp. 608–611, Jun. 1996, doi: 10.1021/JS9504604.

[48] T. Shimaz Aki, M. T. Mita, S. Sadahiro, M. Hayashi, and S. Awazu, “Absorption-Enhancing Effects of Sodium Caprate and Palmitoyl Carnitine in Rat and Human Colons,” *Dig Dis Sci.*, vol. 43, no. 3, pp. 641–645, 1998, doi: 10.1023/a:1018835829643.

[49] E. Moghimipour, A. Ameri, and S. Handali, “Absorption-Enhancing Effects of Bile Salts,” *Molecules*, vol. 20, no. 8, p. 14451, Aug. 2015, doi: 10.3390/MOLECULES200814451.

[50] J. M. Barrios and L. M. Lichtenberger, “Role of biliary phosphatidylcholine in bile acid protection and nsaid injury of the lleal mucosa in rats,” *Gastroenterology*, vol. 118, no. 6, pp. 1179–1186, 2000, doi: 10.1016/S0016-5085(00)70371-4.

[51] E. J. Dial, S. H. M. Rooijakkers, R. L. Darling, J. J. Romero, and L. M. Lichtenberger, “Role of phosphatidylcholine saturation in preventing bile salt toxicity to gastrointestinal epithelia and membranes,” *J Gastroenterol Hepatol*, vol. 23, no. 3, pp. 430–436, Mar. 2008, doi: 10.1111/J.1440-1746.2007.05153.X.

[52] Y. Araki *et al.*, “Bile acid modulates transepithelial permeability via the generation of reactive oxygen species in the Caco-2 cell line,” *Free Radic Biol Med*, vol. 39, no. 6, pp. 769–780, Sep. 2005, doi: 10.1016/J.FREERADBIOMED.2005.04.026.

[53] F. Raimondi *et al.*, “Bile acids modulate tight junction structure and barrier function of Caco-2 monolayers via EGFR activation,” *Am J Physiol Gastrointest Liver Physiol*, vol. 294, no. 4, pp. 906–913, Apr. 2008, doi: 10.1152/AJPGI.00043.2007/ASSET/IMAGES/LARGE/ZH30040850480009.JPEG.

[54] E. Michael Danielsen and G. H. Hansen, “Probing the Action of Permeation Enhancers Sodium Cholate and N-dodecyl-β-D-maltoside in a Porcine Jejunal Mucosal Explant System,” *Pharmaceutics*, vol. 10, no. 4, Dec. 2018, doi: 10.3390/PHARMACEUTICS10040172.

[55] P. Rosevear, T. VanAken, J. Baxter, and S. Ferguson-Miller, “Alkyl Glycoside Detergents: A Simpler Synthesis and Their Effects on Kinetic and Physical Properties of Cytochrome c Oxidase,” *Biochemistry*, vol. 19, no. 17, pp. 4108–4115, 1980, doi: 10.1021/bi00558a032.

[56] T. Vanaken, S. Foxall-Vanaken, S. Castleman, and S. Ferguson-Miller, “[3] Alkyl glycoside detergents: Synthesis and applications to the study of membrane proteins,” *Methods Enzymol*, vol. 125, no. C, pp. 27–35, Jan. 1986, doi: 10.1016/S0076-6879(86)25005-3.

[57] X. Wang, S. Maher, and D. J. Brayden, “Restoration of rat colonic epithelium after in situ intestinal instillation of the absorption promoter, sodium caprate,” *Ther Deliv*, vol. 1, no. 1, pp. 75–82, Jul. 2010, doi: 10.4155/TDE.10.5.

[58] K. Gradauer *et al.*, "Dodecylmaltoside Modulates Bicellular Tight Junction Contacts To Promote Enhanced Permeability," 2017, doi: 10.1021/acs.molpharmaceut.7b00297.

[59] FDA, "Inactive Ingredient Search for Approved Drug Products." https://www.accessdata.fda.gov/scripts/cder/iig/index.cfm (accessed Sep. 27, 2022).

[60] "Food Additive Status List | FDA." https://www.fda.gov/food/food-additives-petitions/food-additive-status-list (accessed Sep. 13, 2022).

[61] M. N. Jones, "Surfactants in membrane solubilisation," *Int J Pharm*, vol. 177, no. 2, pp. 137–159, Jan. 1999, doi: 10.1016/S0378-5173(98)00345-7.

[62] A. K. Bhuyan, "On the Mechanism of SDS-Induced Protein Denaturation," 2009, doi: 10.1002/bip.21318.

[63] A. Leone-Bay *et al.*, "N-Acylated-Amino Acids as Novel Oral Delivery Agents for Proteins," *J. Med. Chem*, vol. 38, pp. 4263–4269, 1995, doi: 10.1021/jm00021a015.

[64] J. B. Larsen *et al.*, "Imaging therapeutic peptide transport across intestinal barriers," *RSC Chem Biol*, vol. 2, no. 4, pp. 1115–1143, Aug. 2021, doi: 10.1039/D1CB00024A.

[65] E. Vivès, P. Brodin, and B. Lebleu, "A Truncated HIV-1 Tat Protein Basic Domain Rapidly Translocates through the Plasma Membrane and Accumulates in the Cell Nucleus," *Journal of Biological Chemistry*, vol. 272, no. 25, pp. 16010–16017, Jun. 1997, doi: 10.1074/JBC.272.25.16010.

[66] J. S. Wadia, R. v. Stan, and S. F. Dowdy, "Transducible TAT-HA fusogenic peptide enhances escape of TAT-fusion proteins after lipid raft macropinocytosis," *Nat Med*, vol. 10, no. 3, pp. 310–315, Mar. 2004, doi: 10.1038/NM996.

[67] D. Derossi, S. Calvet, A. Trembleau, A. Brunissen, G. Chassaing, and A. Prochiantz, "Cell internalization of the third helix of the antennapedia homeodomain is receptor-independent," *Journal of Biological Chemistry*, vol. 271, no. 30, pp. 18188–18193, 1996, doi: 10.1074/jbc.271.30.18188.

[68] N. Kamei, M. Morishita, and K. Takayama, "Importance of intermolecular interaction on the improvement of intestinal therapeutic peptide/protein absorption using cell-penetrating peptides," *Journal of Controlled Release*, vol. 136, no. 3, pp. 179–186, Jun. 2009, doi: 10.1016/J.JCONREL.2009.02.015.

[69] I. Ruseska and A. Zimmer, "Internalization mechanisms of cell-penetrating peptides," *Beilstein J. Nanotechnol*, vol. 2020, pp. 101–123, 2020, doi: 10.3762/bjnano.11.10.

[70] M. di Pisa, G. Chassaing, and J.-M. Swiecicki, "Translocation Mechanism(s) of Cell-Penetrating Peptides: Biophysical Studies Using Artificial Membrane Bilayers," *Biochemistry*, vol. 54, no. 2, pp. 194–207, Jan. 2015, doi: 10.1021/bi501392n.

[71] S. Ludtke, K. He, and H. Huang, "Membrane thinning caused by magainin 2," *Biochemistry*, vol. 34, no. 51, pp. 16764–16769, 1995, doi: 10.1021/BI00051A026.

[72] S. Afonin, S. Kara, G. Buth, and A. S. Ulrich, "Membrane Thinning and Thickening Induced by Membrane-Active Amphipathic Peptides. Front," *Cell Dev. Biol*, vol. 4, p. 65, 2016, doi: 10.3389/fcell.2016.00065.

[73] K. Matsuzaki, S. Yoneyama, and K. Miyajima, "Pore formation and translocation of melittin," *Biophys J*, vol. 73, no. 2, pp. 831–838, Aug. 1997, doi: 10.1016/S0006-3495(97)78115-3.

[74] S. T. Henriques, M. N. Melo, and M. A. R. B. Castanho, “Cell-penetrating peptides and antimicrobial peptides: how different are they?,” *Biochemical Journal*, vol. 399, no. 1, pp. 1–7, Oct. 2006, doi: 10.1042/BJ20061100.

[75] N. Röckendorf, C. Nehls, and T. Gutsmann, “Design of Membrane Active Peptides Considering Multi-Objective Optimization for Biomedical Application,” *Membranes 2022, Vol. 12, Page 180*, vol. 12, no. 2, p. 180, Feb. 2022, doi: 10.3390/MEMBRANES12020180.

[76] G. van den Bogaart, J. V. Guzmán, J. T. Mika, and B. Poolman, “On the Mechanism of Pore Formation by Melittin,” *J Biol Chem*, vol. 283, no. 49, p. 33854, Dec. 2008, doi: 10.1074/JBC.M805171200.

[77] L. Yang, T. A. Harroun, T. M. Weiss, L. Ding, and H. W. Huang, “Barrel-Stave Model or Toroidal Model? A Case Study on Melittin Pores,” *Biophys J*, vol. 81, no. 3, pp. 1475–1485, Sep. 2001, doi: 10.1016/S0006-3495(01)75802-X.

[78] A. S. Ladokhin and S. H. White, “‘Detergent-like’ permeabilization of anionic lipid vesicles by melittin,” *Biochim Biophys Acta Biomembr*, vol. 1514, no. 2, pp. 253–260, Oct. 2001, doi: 10.1016/S0005-2736(01)00382-0.

[79] S. Maher, X. Wang, V. Bzik, S. McClean, and D. J. Brayden, “Evaluation of intestinal absorption and mucosal toxicity using two promoters. II. Rat instillation and perfusion studies,” *Eur J Pharm Sci*, vol. 38, no. 4, pp. 301–311, Nov. 2009, doi: 10.1016/J.EJPS.2009.07.011.

[80] S. Maher *et al.*, “Evaluation of intestinal absorption enhancement and local mucosal toxicity of two promoters. I. Studies in isolated rat and human colonic mucosae,” *European Journal of Pharmaceutical Sciences*, vol. 38, no. 4, pp. 291–300, Nov. 2009, doi: 10.1016/j.ejps.2009.09.001.

[81] S. Maher, M. Devocelle, S. Ryan, S. McClean, and D. J. Brayden, “Impact of amino acid replacements on in vitro permeation enhancement and cytotoxicity of the intestinal absorption promoter, melittin,” *Int J Pharm*, vol. 387, no. 1–2, pp. 154–160, Mar. 2010, doi: 10.1016/j.ijpharm.2009.12.022.

[82] Y. Imura, N. Choda, and K. Matsuzaki, “Magainin 2 in Action: Distinct Modes of Membrane Permeabilization in Living Bacterial and Mammalian Cells,” *Biophys J*, vol. 95, no. 12, p. 5757, Dec. 2008, doi: 10.1529/BIOPHYSJ.108.133488.

[83] S. J. Ludtke, K. He, W. T. Heller, T. A. Harroun, L. Yang, and H. W. Huang, “Membrane Pores Induced by Magainin,” *Biochemistry*, vol. 35, no. 43, pp. 13723–13728, 1996, doi: 10.1021/bi9620621.

[84] K. Matsuzaki, O. Murase, N. Fujii, and K. Miyajima, “Translocation of a Channel-Forming Antimicrobial Peptide, Magainin 2, across Lipid Bilayers by Forming a Pore,” *Biochemistry*, vol. 34, pp. 6521–6526, 1995, doi: 10.1021/bi00019a033.

[85] S. Li, S. Y. Kim, A. E. Pittman, G. M. King, W. C. Wimley, and K. Hristova, “Potent Macromolecule-Sized Poration of Lipid Bilayers by the Macrolittins, A Synthetically Evolved Family of Pore-Forming Peptides,” *J Am Chem Soc*, vol. 140, no. 20, pp. 6441–6447, May 2018, doi: 10.1021/jacs.8b03026.

[86] E. Sancho-Vaello *et al.*, “Structural remodeling and oligomerization of human cathelicidin on membranes suggest fibril-like structures as active species,” *Sci Rep*, vol. 7, no. 1, Dec. 2017, doi: 10.1038/s41598-017-14206-1.

[87] K. Whitehead, N. Karr, and S. Mitragotri, “Safe and Effective Permeation Enhancers for Oral Drug Delivery”, doi: 10.1007/s11095-007-9488-9.

[88] U. Werner, T. Kissel, and M. Reers, “Effects of permeation enhancers on the transport of a peptidomimetic thrombin inhibitor (CRC 220) in a human intestinal cell line (Caco-2),” *Pharm Res*, vol. 13, no. 8, pp. 1219–1227, 1996, doi: 10.1023/a:1016020505313.

[89] E. S. Swenson, W. B. Milisen, and W. Curatolo, “Intestinal permeability enhancement: efficacy, acute local toxicity, and reversibility,” *Pharm Res*, vol. 11, pp. 1132–1142, 1994, doi: 10.1023/A:1018984731584.

[90] C. Twarog *et al.*, “A head-to-head Caco-2 assay comparison of the mechanisms of action of the intestinal permeation enhancers: SNAC and sodium caprate (C10),” *European Journal of Pharmaceutics and Biopharmaceutics*, vol. 152, pp. 95–107, Jul. 2020, doi: 10.1016/j.ejpb.2020.04.023.

[91] C. Twarog, F. McCartney, S. M. Harrison, B. Illel, E. Fattal, and D. J. Brayden, “Comparison of the effects of the intestinal permeation enhancers, SNAC and sodium caprate (C10): Isolated rat intestinal mucosae and sacs,” *European Journal of Pharmaceutical Sciences*, vol. 158, p. 105685, Mar. 2021, doi: 10.1016/J.EJPS.2020.105685.

[92] fda and cder, “RYBELSUS (semaglutide) tablets, for oral use .” 2017. Accessed: Sep. 13, 2022. [Online]. Available: https://www.accessdata.fda.gov/drugsatfda_docs/label/2019/213051s000lbl.pdf

[93] A. T. Blikslager, A. J. Moeser, J. L. Gookin, S. L. Jones, and J. Odle, “Restoration of barrier function in injured intestinal mucosa,” *Physiol Rev*, vol. 87, no. 2, pp. 545–564, Apr. 2007, doi: 10.1152/PHYSREV.00012.2006/ASSET/IMAGES/LARGE/Z9J0020724330008.JPEG.

[94] D. J. Brayden and S. Maher, “Transient Permeation Enhancer® (TPE®) technology for oral delivery of octreotide: a technological evaluation,” *Expert Opin Drug Deliv*, vol. 18, no. 10, pp. 1501–1512, 2021, doi: 10.1080/17425247.2021.1942838.

[95] A. Abramson, F. Halperin, J. Kim, and G. Traverso, “Quantifying the value of orally delivered biologic therapies: A cost-effectiveness analysis of oral semaglutide HHS Public Access,” *J Pharm Sci*, vol. 108, no. 9, pp. 3138–3145, 2019, doi: 10.1016/j.xphs.2019.04.022.

[96] ClinicalTrials. gov National Institutes of Health, “A Study to Evaluate the Efficacy and Safety of ORMD-0801 (Oral Insulin) in Patients With Type 2 Diabetes Mellitus - Full Text View - ClinicalTrials.gov.” https://clinicaltrials.gov/ct2/show/NCT03467932?id=NCT03467932&draw=2&rank=1&load=cart (accessed Sep. 15, 2022).

[97] S. E. Howe, D. J. Lickteig, K. N. Plunkett, J. S. Ryerse, and V. Konjufca, “The Uptake of Soluble and Particulate Antigens by Epithelial Cells in the Mouse Small Intestine,” *PLoS One*, vol. 9, no. 1, p. e86656, Jan. 2014, doi: 10.1371/JOURNAL.PONE.0086656.

[98] R. G. Diedrichsen *et al.*, “Revealing the importance of carrier-cargo association in delivery of insulin and lipidated insulin,” *Journal of Controlled Release*, vol. 338, pp. 8–21, Oct. 2021, doi: 10.1016/J.JCONREL.2021.07.030.

[99] S. Fattah *et al.*, “Salcaprozate sodium (SNAC) enhances permeability of octreotide across isolated rat and human intestinal epithelial mucosae in Ussing chambers,” *European Journal of Pharmaceutical Sciences*, vol. 154, p. 105509, Nov. 2020, doi: 10.1016/J.EJPS.2020.105509.

[100] H. L. Åmand, K. Fant, B. Nordén, and E. K. Esbjörner, “Stimulated endocytosis in penetratin uptake: Effect of arginine and lysine,” *Biochem Biophys Res Commun*, vol. 371, no. 4, pp. 621–625, Jul. 2008, doi: 10.1016/J.BBRC.2008.04.039.

[101] Md. M. R. Moghal, Md. Z. Islam, S. Sharmin, V. Levadnyy, Md. Moniruzzaman, and M. Yamazaki, “Continuous detection of entry of cell-penetrating peptide transportan 10 into single vesicles,” *Chem Phys Lipids*, vol. 212, pp. 120–129, May 2018, doi: 10.1016/j.chemphyslip.2018.02.001.

[102] C. Kayalar and N. Düzgüneç, “Membrane action of colicin E1: detection by the release of carboxyfluorescein and calcein from liposomes,” *BBA - Biomembranes*, vol. 860, no. 1, pp. 51–56, 1986, doi: 10.1016/0005-2736(86)90497-9.

[103] S. F. Hedegaard *et al.*, “Fluorophore labeling of a cell-penetrating peptide significantly alters the mode and degree of biomembrane interaction,” *Sci Rep*, vol. 8, no. 1, pp. 1–14, 2018, doi: 10.1038/s41598-018-24154-z.

[104] J. R. Marks, J. Placone, K. Hristova, and W. C. Wimley, “Spontaneous Membrane-Translocating Peptides by Orthogonal High-Throughput Screening,” *J Am Chem Soc*, vol. 133, no. 23, pp. 8995–9004, Jun. 2011, doi: 10.1021/ja2017416.

[105] R. M. Epand and R. F. Epand, “Liposomes as Models for Antimicrobial Peptides,” *Methods Enzymol*, vol. 372, pp. 124–133, Jan. 2003, doi: 10.1016/S0076-6879(03)72007-2.

[106] A. L. Russell, A. M. Kennedy, A. M. Spuches, D. Venugopal, J. B. Bhonsle, and R. P. Hicks, “Spectroscopic and thermodynamic evidence for antimicrobial peptide membrane selectivity,” *Chem Phys Lipids*, vol. 163, no. 6, pp. 488–497, Jun. 2010, doi: 10.1016/J.CHEMPHYSLIP.2010.03.009.

[107] Y. Pouny, D. Rapaport, A. Mor, P. Nicolas, and Y. Shai, “Interaction of Antimicrobial Dermaseptin and Its Fluorescently Labeled Analogues with Phospholipid Membranes1,” *Biochemistry*, vol. 31, pp. 12416–12423, 1992, doi: 10.1021/bi00164a017.

[108] G. Szabo, “Dual mechanism for the action of cholesterol on membrane permeability,” *Nature*, vol. 252, pp. 47–49, 1974, doi: 10.1038/252047a0.

[109] T. Etzerodt, J. R. Henriksen, P. Rasmussen, M. H. Clausen, and T. L. Andresen, “Selective Acylation Enhances Membrane Charge Sensitivity of the Antimicrobial Peptide Mastoparan-X,” *Biophys J*, vol. 100, no. 2, p. 399, Jan. 2011, doi: 10.1016/J.BPJ.2010.11.040.

[110] S. A. Spinella, R. B. Nelson, and D. E. Elmore, “Measuring peptide translocation into large unilamellar vesicles.,” *J Vis Exp*, no. 59, p. e3571, Jan. 2012, doi: 10.3791/3571.

[111] N. Wichmann *et al.*, “Applying flow cytometry to identify the modes of action of membrane-active peptides in a label-free and high-throughput fashion,” *Biochimica et Biophysica Acta (BBA) - Biomembranes*, vol. 1864, no. 2, p. 183820, Feb. 2022, doi: 10.1016/J.BBAMEM.2021.183820.

[112] K. Temmerman and W. Nickel, “A novel flow cytometric assay to quantify interactions between proteins and membrane lipids,” *J Lipid Res*, vol. 50, no. 6, pp. 1245–1254, Jun. 2009, doi: 10.1194/jlr.D800043-JLR200.

[113] Per E. G. Thorén, Daniel Persson, Elin K. Esbjörner, Mattias Goksör, Per Lincoln, and B. Nordén, “Membrane Binding and Translocation of Cell-Penetrating Peptides,” *Biochemistry*, vol. 43, no. 12, pp. 3471–3489, 2004, doi: 10.1021/BI0360049.

[114] T. Benachir and M. Lafleur, “Study of vesicle leakage induced by melittin,” *Biochim Biophys Acta*, vol. 1235, no. 2, pp. 452–460, May 1995, doi: 10.1016/0005-2736(95)80035-E.

[115] G. van Meer and A. I. P. M. de Kroon, “Lipid map of the mammalian cell,” *J Cell Sci*, vol. 124, no. 1, pp. 5–8, Jan. 2011, doi: 10.1242/JCS.071233.

[116] M. L. Briuglia, C. Rotella, A. McFarlane, and D. A. Lamprou, “Influence of cholesterol on liposome stability and on in vitro drug release,” *Drug Deliv Transl Res*, vol. 5, no. 3, pp. 231–242, Jun. 2015, doi: 10.1007/S13346-015-0220-8/FIGURES/11.

[117] D. Casares, P. v. Escribá, and C. A. Rosselló, “Membrane Lipid Composition: Effect on Membrane and Organelle Structure, Function and Compartmentalization and Therapeutic Avenues,” *Int J Mol Sci*, vol. 20, no. 9, May 2019, doi: 10.3390/IJMS20092167.

[118] D. A. Brown, “Lipid Rafts,” *Encyclopedia of Biological Chemistry: Second Edition*, pp. 741–744, Jan. 2013, doi: 10.1016/B978-0-12-378630-2.00185-7.

[119] A. Fuchs, M. Leigh, B. Kloefer, and J. B. Dressman, “Advances in the design of fasted state simulating intestinal fluids: FaSSIF-V3,” *European Journal of Pharmaceutics and Biopharmaceutics*, vol. 94, pp. 229–240, Aug. 2015, doi: 10.1016/j.ejpb.2015.05.015.

[120] Biorelevant, “What is FaSSIF (Fasted State Simulated Intestinal Fluid)?” https://biorelevant.com/learning_center/what-is-fassif/ (accessed Sep. 28, 2022).

Chapter 2: Methodology

The main methods in this thesis will be based on fluorescence and light scattering. Here, a brief introduction to the physical phenomena of fluorescence and light scattering will be given, focusing on aspects relevant to the methods used. In addition, an introduction will be given to the principles of the main methods of this thesis. Finally, the advantages and limitations of the methods will be discussed.

2.1 Fluorescence

2.1.1 Basic introduction to fluorescence

The following is based on the third edition of Principles of Fluorescence Spectroscopy by J.R. Lakowicz (1) where nothing else is stated.

Electrons in a molecule can be assigned to an energy state and will over time return to the ground level. An electron can be excited by the absorption of one or more photons, typically in the form of light, with an energy corresponding to the energy difference between the current energy of the electron and the energy of an excited state (Figure 2.1). Molecules that are able to re-emit this energy as light, are called fluorophores. At the excited state, the fluorophore can exist in a number of vibrational states (0,1,2, Figure 2.1). Excitation will typically occur to a higher vibrational level than the lowest vibrational state of the energy state in question. Upon excitation, the electron will, generally, quickly decay to the lowest vibrational level of the first excited energy state (S_1, Figure 2.1) through internal conversion, typically through the release of heat. From the excited state, fluorophores will return to the ground state (S_0, Figure 2.1) through the emission of a photon. This is what is called fluorescence. The fluorescence typically occur to a higher vibrational level than the ground vibrational state, from where thermal equilibrium is reached.

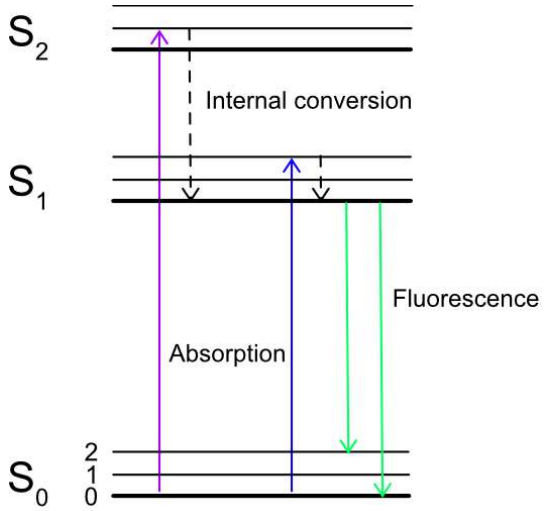

Figure 2.1: A simple form of a Jablonski diagram. The diagram depicts the singlet ground (S_0), first (S_1), and second (S_2) electronic state of a fluorophore. Vibrational energy levels of each electronic state are depicted as 0,1, and 2. Transitions between energy states are depicted as vertical lines. Transitions due to thermal equilibration are depicted as dashed lines.

Taking the vibrational relaxation into consideration, the energy difference for fluorescence is typically lower than that of excitation. Accordingly, fluorescence emission is usually measured at a lower energy, hence at longer wavelength, than excitation. This difference in absorption and fluorescence emission is called a Stoke's shift. The variations of vibrational levels to which a fluorophore decays results in a small variation in the energy of the photons emitted and thereby a broadening of the fluorescence signal.

2.1.1.1 Solvent polarity and fluorescence maximum

The emission from many fluorophores are highly dependent on various properties of the surroundings, particularly the polarity of the solvent [1]. Here, a short overview of the theory of general solvents effect is presented. In this theory, many assumptions are made, and many minor effects are furthermore left out in this description, yet it provides a way of explaining effects on the fluorescence observed for fluorophores in solvents of various polarity. In this theory, the fluorophore is considered to be a dipole, and the solvent a medium with a uniform dielectric constant. Interaction between the fluorophore and the solvent will lead to a change, typically decrease, in the energy difference between the excited state and the ground state, thereby leading to a redshift of the emitted fluorescence. The effect mainly driving this change is a change in the dielectric constant caused by a reorientation of the dipoles of the solvent around the fluorophore. The reorientation of the solvent, called solvent relaxation, stabilizes the excited state, thereby lowering the energy of the excited state. Furthermore, the dipoles of the solvent are no longer oriented around the ground state, and the ground state is thus destabilized, increasing the energy of the ground state. Together, the change in dipole moment due to reorientation, generally, leads to fluorescence at lower energy and longer wavelength in polar solvents than in non-polar solvents, with the effect additionally being most pronounced for polar fluorophores.

2.1.1.2 Fluorescence quenching

In general, the total fluorescence emission of a sample in a specific environment correlates linearly with the number of fluorophores in that specific environment at a particular wavelength. This is frequently used for quantification [2]–[4]. However, many factors can decrease the fluorescence, commonly referred to as quenching. Quenching is generally divided into two types of quenching, static quenching and collisional quenching. Static quenching is typically a result of complexation of the fluorophore in the ground state, and will not be described further in this chapter. When a fluorophore undergoes collisional quenching, it decays to the ground state without the emission of a photon upon contact with the quencher. This can occur by transfer of energy from the excited fluorophore to the quencher whereby the fluorophore is decayed to the ground state and the quencher is excited and decays in a non-fluorescent manner. The transfer of energy requires that the emission energy spectra of the fluorophore and the excitation energy of the quencher overlap, and then this common amount of required energy is what is transferred. For some fluorophores, like fluorescein and calcein, the Stoke's shift is small, and the energy transfer can occur between the fluorophores with the fluorophores acting both as donor and quencher. This transfer of energy requires the close proximity of the fluorophores, and typically takes place when at high fluorophore concentrations or when multiple fluorophores are coupled to the same molecule, bringing them in close proximity of each other. This is called self-quenching. For carboxyfluorescein it has been shown that it dimerizes into a non-fluorescent dimer, and that the dimerization as well as energy transfer to the dimer also contributes to self-quenching [5]. Self-quenching can be exploited to investigate protein folding [6] or protein dimerization [7], but also in calcein release assays and alike (Section 2.1.3).

2.1.2 Nile Red

Nile Red is commonly used as a hydrophobicity marker [8]–[10] Nile Red is a hydrophobic fluorophore, which easily partitions into hydrophobic regions [9]. It has an excitation wavelength around 549 nm and is unaffected by changes in pH between 4.5 and 8.5. Nile Red can thus be used at a range of pH-values and without interference of the absorption from proteins and peptides, which absorb around 205 nm,

215 nm, and 280 nm. The fluorescence of Nile Red is highly dependent on the solvent polarity. At decreased polarity, the fluorescence maxima is blue shifted and the intensity increased (2). In aqueous solutions, the fluorescence of Nile Red is quenched (3). Nile Red has been used to detect CMCs of a broad range of surfactants [11] and the oligomerization of melittin (2). Nile Red has a low solubility in aqueous solutions and is therefore preferable dissolved in non-polar solvents, typically dimethyl sulfoxide (DMSO) [12]. This is a drawback when using Nile Red as a hydrophobicity marker of particles in aqueous solutions as DMSO may disrupt e.g. lipid membranes [13]. This effect can, nonetheless, be minimized by adding very small volumes of the dissolved Nile Red to the solution of interest. While small volumes are more prone to have a higher fraction of uncertainty, the fluorescence quantum yield of Nile Red is high, and even small hydrophobic regions or changes in hydrophobic areas can be detected as changes in the Nile Red fluorescence [9].

2.1.3 The calcein release assay

The calcein release assay is a frequently used assay to measure membrane perturbation [14]–[17]. It is made possible based on the fluorescent properties of calcein. This, together with the principle of the calcein release assay, and advantages and disadvantages or attention points of the calcein release assay will be explained in detail below.

2.1.3.1 Properties of calcein

Calcein is a water-soluble fluorescein fluorophore. It is widely used as an extrinsic label, and has the advantage of being insensitive to the solvent polarity [1]. The fluorescence of calcein is insensitive to pH in the region of pH 6.4-8.4, outside which the fluorescence decreases [18]. The fluorescence intensity of calcein, like for other fluoresceins [1], correlate linearly with fluorophore concentration at low concentrations, but are self-quenching at higher concentrations [19], [20]. In a HEPES buffer at pH 7.4 calcein fluorescence intensity was reported to correlate linearly with calcein concentration ranging from 0-2 mM and reach its maximum at 3.1 mM calcein, whereafter the fluorescence intensity decreased due to self-quenching. In another study, the fluorescence of calcein was shown to be 99 % self-quenched at calcein concentration of 50 mM [20]. A similar pattern of linearity was observed in our studies where a linear correlation was observed up to approximately 7 mM calcein in 10 mM phosphate buffer, 100 mM NaCl, pH 6.7 (Figure 2.2).

2.1.3.2 The calcein release assay in practice

The water-soluble, pH-insensitive, selv-quenching properties of calcein is frequently utilized to measure the membrane permeability of liposomes in a calcein release assay [14], [21]–[23], and is also used as such in this thesis. In the calcein release assay, calcein is encapsulated at a high, self-quenching concentration. When calcein escapes the liposomes, e.g. upon the exposure to a permeater, the calcein is spread into the entire solution, and the calcein is thereby heavily diluted to a non-self-quenching concentration. Furthermore, to quantify the release, the fluorescence intensity upon treatment must be compared to the fluorescence at full release. The fluorescence intensity at full release is usually defined as the fluorescence intensity from the liposomes in the presence of the surfactant Triton X-100 [17], [21], [22], [24], [25]. The addition of the right amount of Triton X-100 leads to the complete disintegration of the liposomes, and hence to full release [26]. Triton X-100 is then added to the solution at the end of the experiment, or to a separate liposome solution measured simultaneously [17], [27]. Finally, a blank sample

of the liposomes in the absence of permeaters is usually also included. The calcein release is then typically calculated as:

$$Calcein\ release = \frac{F - F_0}{F_{max} - F_0} \cdot 100\%$$

where F is the fluorescence of the sample of which the calcein release is to be measured, F_0 is the fluorescence of the blank sample, and F_{max} is the fluorescence of the Triton X-100-exposed sample.

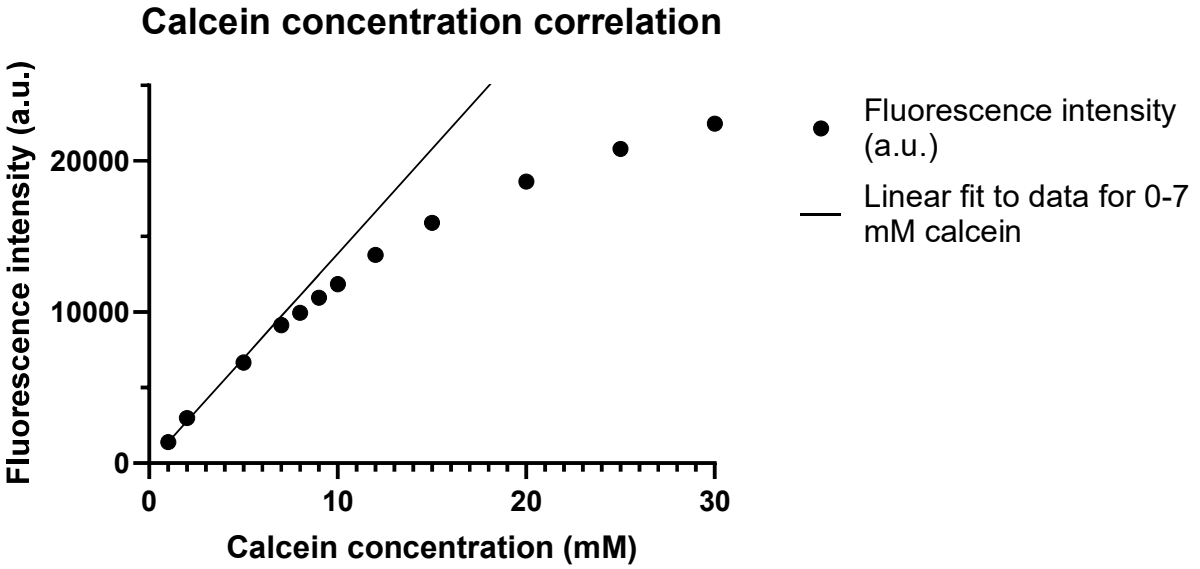

Figure 2.2: Calcein fluorescence correlation with concentration showing self-quanching at concentration above approximately 7 mM calcein. Stock solution of calcein (60 mM calcein 10 mM phosphate buffer, pH 6.7) was diluted to the desired concentration in buffer (10 mM phosphate, 100 mM NaCl, pH 6.7) and measured Ex/Em: 491/514 nm in a Tecan plate-reader.

2.1.3.3 Limitations of the calcein release assay as a method

The calcein release assay requires that calcein is encapsulated at a sufficiently high self-quenching concentration, and that the concentration of calcein upon complete release is not affected by self-quenching. Furthermore, it is assumed that calcein does not permeate the liposomes in the absence of a permeater (including a prospective drug, a permeation enhancer, Triton-X or alike), and that the permeater does not affect the calcein fluorescent signal. These experimental considerations will be elaborated below.

Calcein almost completely self-quenches at concentrations above 50 mM, and the typical concentrations used in the calcein release assay are thus 50-130 mM. However, a study shows that calcein encapsulation is lipid dependent. For the lipid compositions tested, including pure POPC liposomes, the calcein encapsulation efficiency was between 54 and 71 % [28]. Through inclusion of the blank measurement, minor deviations from complete self-quenching do not affect the results as long as it does not lead to the fluorescence of the full release exceeding the linear range of the calcein fluorescence.

An assumption of the assay is that the calcein fluorescence is not affected by the permeaters. Yet this is not always the case. Major deviations from this assumption occurs if the permeaters lead to a change in the pH to be outside of the pH independent region of calcein fluorescence. This is likely the case for C10

(Figure 2.3A), which resulted in a pH above 8.5 at concentrations above 5-20 g/L (Figure 2.3A insert). For the majority of the measurements with C10 in this thesis, the C10 concentration did not exceed 22 g/L. C10 was thus considered not to decrease the signal from the calcein at these concentrations. In the presence of 40 g/L C10, the calcein signal was decreased with approximately 10 %. By limiting the number of measurements where the concentration were larger than 22 g/L, the influence of C10 on the calcein signal was neglected. If a higher C10 concentration had been desired, F_{max} could have been corrected for the effect of the C10 on the calcein signal. Also other effects may affect the calcein fluorescence. For our set-up, a decrease of around 20-25 % in calcein fluorescence intensity for 5 µM calcein was observed when adding either sodium cholate, SDS, melittin, or Triton X-100, whereas the calcein signal appeared not to be affected by DDM at the concentrations used (Figure 2.3B). As the signal also appeared to decrease over time for calcein-encapsulating liposomes exposed to Triton X-100 (Figure 2.3C) it is possible that the decrease in signal is due to calcein adsorbing to the well over time. This naturally present some uncertainties in the quantifications and may in part be overcome by systematic timing, and potentially concentration-dependent corrections.

Another factor that may influence the signal at full release is self-quenching, if the calcein concentration is not sufficiently decreased upon release. This however, is easily checked by measuring the signal of a range of concentrations of Triton X-100 treated liposomes.

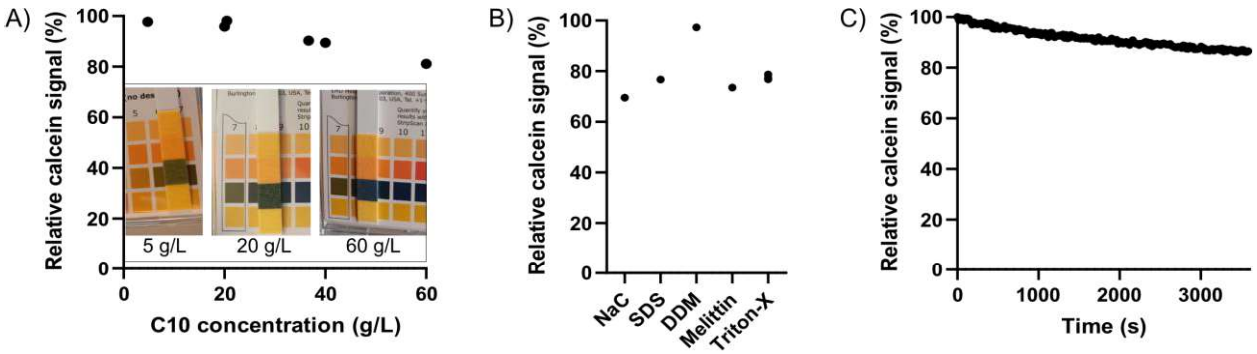

Figure 2.3: Fluorescent signal of 5 mM calcein (diluted from the stock concentration in the buffer and measured as stated in Figure 2.2) under various conditions. A) Fluorescent signal of 5 mM calcein in the presence of various concentrations of C10 relative to that of 5 mM calcein in the presence of 0.5 % (V/V) Triton X-100. The insert shows pH strips exposed to 5, 20, or 60 g/L C10. B) Fluorescent signal of 5 mM calcein 1 g/L NaC, 0.6 g/L SDS, 0.08 g/L DDM, 0.9 mg/L melittin, or 0.5 % (V/V) Triton X-100 with the fluorescent signals being relative to the signal of 5 mM calcein in the absence of permeation enhancers. C) Fluorescent signal of 0.6 nM calcein-encapsulating liposomes exposed to 0.5 % (V/V) Triton X-100 over time, relative to the signal immediately after addition of Triton X-100.

Another assumption of the calcein release assay is that calcein does not permeate the liposomes in the absence of a permeater. It has been shown that this is not completely the case for many liposome compositions [18]. However, for pure POPC liposomes with a diameter of 117 nm at pH 7.4 around 1 % calcein appears to be released within the first two hours [18], and in this set-up, calcein release not caused by a permeation will thus have a limited effect on the results. As measurements of a blank sample is furthermore carried out, leakage in the absence of a permeation enhancer does not influence the conclusions drawn from the calcein release assays presented in this thesis.

It is important to note that the calcein release assay in itself does not tell anything about the mechanism of membrane perturbation, e.g. by pore-formation, membrane thinning, membrane fluidization, or membrane solubilization, nor whether the calcein is released gradually or by an all-or-none mechanism with all the calcein from each liposome being released all of a sudden. Neither does the assay provide information about the permeability for other substances than calcein, though it may in part correlate [29].

Despite these considerations and drawbacks, the calcein release assay is frequently used to study membrane permeability in bulk, and has the advantages of being an easy high-throughput method which enables quantification with a time resolution as fast as one can pipette and the measurements can be performed.

2.1.4 Flow cytometry

Flow cytometry is a method used to analyze characteristics of cells, compounds or particles (hereafter commonly denoted as particles) one by one in suspension by the means of fluorescence and scattering. It is most frequently used to investigate cells [30]–[32], but has also been used to measure on extracellular vesicles and liposomes [4], [33], [34]. In the following, the concept of flow cytometry will be presented and flow cytometry as a method will be discussed with a focus on matters relevant for flow cytometry of liposomes.

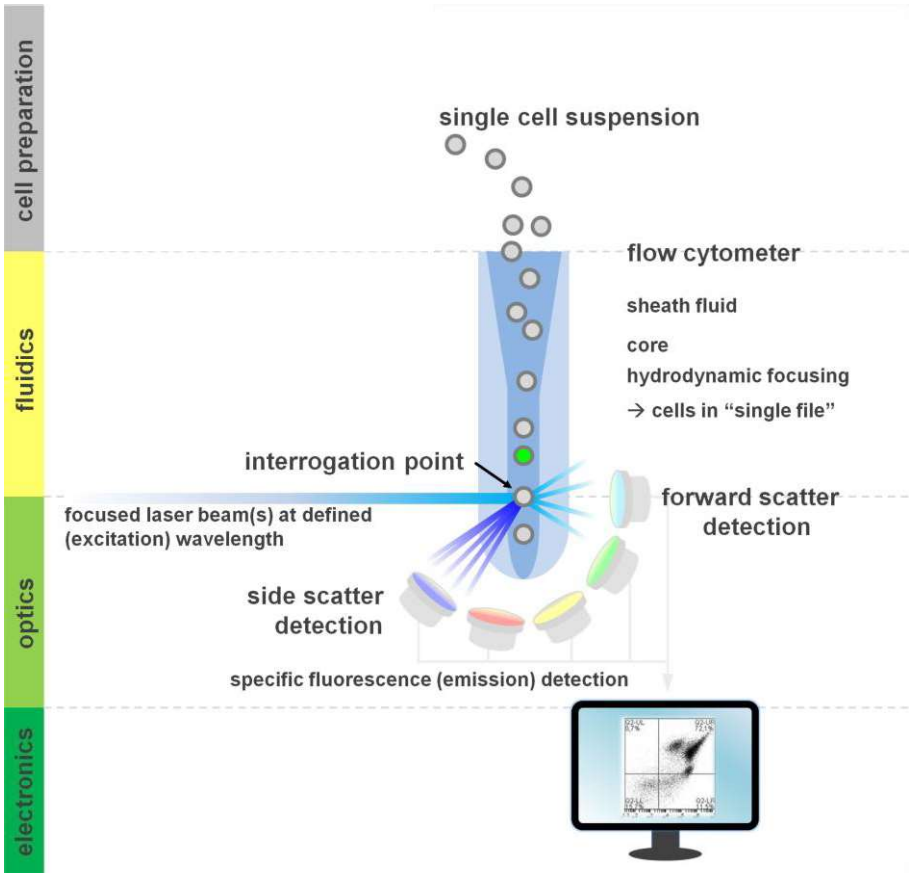

Figure 2.4: Flow cytometry consists of sample (cell) preparation, fluidics, optics, and electronics. Sheath fluid is used to hydrodymanically focus the single cells/particles in suspension to cells/particles in 'single files'. The particles are excited at the interrogation point, forward scatter and emission is measured, and the detected light is converted to electronic signals. The figure is adapted from [43] *with permission from JoVE.*

2.1.4.1 The flow cytometry set-up

A flow cytometer is a microfluidic system [35]. It consists of three parts, fluidics, optics, and electronics (Figure 2.4). The sample should be prepared to consist of single particles. The sample is injected into the center core of a flow of sheath fluid thereby hydrodynamically focusing the particles of the sample, ideally into a line of separated single particles. A laser at a specific wavelength is focused on the interrogation point, where particles containing the proper fluorophore is excited upon passing by. The particles scatter light depending on their size (See section 2.2.1). This is recorded as forward scatter. Fluorescence from the particle is emitted isotropically, and can be detected at any angle. The flow cytometer has a sequence of lasers, and multiple different fluorophores on the same particle can thus be excited and detected with respect to forward scatter and fluorescence intensity. The light signals detected are converted to electronic signals, processed by a computer and visualized on a monitor for data analysis. A particle is detected and recorded as an event only when the forward scatter or fluorescence intensity at one chosen wavelength exceeds a set trigger threshold value. The fluorescence intensity at other wavelengths for that event can be recorded with no set lower intensity limit.

2.1.4.2 Discussion of flow cytometry as a method

A great advantage of flow cytometry is that a single particle can be detected at a time, enabling the detection of inhomogeneity in a sample, providing the opportunity to investigate heterogeneity of samples [36]. In the ideal world, the hydrodynamic focusing ensures good separation of every single particle, causing one particle at a time to pass the interrogation point. This is usually the case for e.g. cells as the hydrodynamic focusing can be adjusted to fit just one particle [35]. However, there is a lower boundery of how narrow the interrogation point can be. This presents a risk for particles below this size to pass as multiple particles. This problem may be overcome by lowering the concentration. A linear correlation between the mean fluorescence intensity and the concentration will verify the overall single-particle detection [34].

Another major advantage of flow cytometry is the detection of fluorescence at multiple wavelengths, concurrently on the same particle [35]. Together, these advantages allow the identification of different subpopulations in the sample [37] and thereby enable the monitoring of e.g. how a treatment alters specific subpopulations.

Finally, flow cytometry is a high-throughput method, typically measuring on thousands of particles every second. This not only lowers the time required to study a suspension, but also enables some degree of kinetic studies, either within the sample [38] or with a lower time resolution by running multiple samples shortly after each other.

A limitation of flow cytometry, particularly with respect to small particles, is the need for a trigger threshold value. For large particles this generally does not present a problem, as the trigger threshold is often chosen based on the forward scatter, as larger particles scatter light more in the forward direction. For small particles, however, the forward scatter is too low for sufficient detection, and instead an event is triggered on the fluorescence intensity of a set wavelength [39]. To exceed the trigger threshold fluorescence, the fluorophore must be present at a certain amount. To ensure a sufficiently large fluorescence signal, the concentration of the fluorophore in or on the particle may be increased if this does not induce self-quenching (Section 2.1.1.2). As for other studies utilizing fluorophores, inclusion of

fluorophores, and particularly a larger fraction of the fluorophores, may represent an issue as fluorophores may alter the properties of the particles to be studied, e.g. the stability of the liposomes [40] or the membrane-activity of peptides [24]. It is thus important to keep in mind, that conclusions drawn from experiments with fluorophores in the membrane or conjugated to the molecule of interest, cannot necessarily rightfully transferred to the corresponding system without fluorophores. A practical aspect of detecting fluorescent signals is naturally to have a good signal to-noise ratio. This requires a certain concentration of fluorophores in the sample to be detected, and a limitation of e.g. free fluorophores in the surrounding solution. This is particularly important when the signals are low, and more difficult to obtain for some 'sticky' materials.

Another limitation of flow cytometry compared to e.g. microscopy, is that the location of the fluorophore within the particle cannot be detected, and it is thus not possible to detect if a fluorescently labeled particle is associated to a membrane or internalized. This may be overcome by the use of the combination of microscopy and flow cytometry in imaging flow cytometry [41]. This method, however, is more advanced and not used in this study and will therefore not be explained further here.

Multiple fluorophores may be included in a sample in flow cytometry. This enables the study of more complex contexts. However, the use of multiple fluorophores may lead to spectral overlap and thus requires careful choice of the panel of fluorophores and potentially the use of compensation beads [42]. This will however not be relevant for the studies presented in this thesis and will thus not be elaborated.

All together, flow cytometry is a versatile method to study effects of e.g. various treatments on cells or liposomes. Using flow cytometry, it is possible to detect how fluorescence from multiple fluorophores. For flow cytometry, the use of fluorophores is both what gives rise to both its largest assets and the largest drawback.

2.2 Light scattering

The following is based on the introductions to light scattering by Lars Øgendal where nothing else is stated (6,7).

2.2.1 Basics of (dynamic) light scattering

When photons interact with a material, they are generally absorbed or scattered. Particles much smaller than the wavelength of light causes Rayleigh scattering with significant levels of scattering in all directions. The larger the particle is, relative to the wavelength of the incoming light, the more forward scattering will be favored over equal scattering in all directions. The light will thus be scattered with various intensity at various angles depending on the particle size. Thus, how the intensity of the scattered light changes as a function of the angle contains information about the size of the particles scattering light.

The many photons undergoing quasielastic scattering of different scatterers interfere to produce a given phase and thereby intensity at the detector at a given time point. A little later, the scatterers will have moved to new positions due to Brownian motions. This will give rise to a new combined phase, and thereby intensity, at the detector. If the particles diffuse quickly, the rate of change in intensity over time is faster than if the scatterers diffuse more slowly. All particles in a solution move by Brownian motions, and when there are many molecules, their position relative to each other changes all the time. This gives rise to fluctuations in the intensity. These fluctuations are what is measured in dynamic light scattering (DLS) as a technique. The rate of the fluctuations depends on the rate of the movements, which again depends inversely on the viscosity of the solvent and the size of the particle. Thus, the larger the particle, the slower its motion will be, which will give rise to slower fluctuations. This can be utilized to obtain

information about the movement of particles in solutions, and thereby indicate their size. How movement and size correlate will be further elaborated below in section 2.2.2 and how this information is practically obtained by measuring the fluctuating intensities will be elaborated below in section 2.2.3.

2.2.2 Diffusion coefficients, hydrodynamic radius and size

How fast a particle move is usually described by the diffusion coefficient, D. The diffusion coefficient of a particle depends on the temperature, T, and inversely on the friction of the solution on the particle. The friction of the solution increases with increasing viscosity of the solution and with increasing size of the particle. For spherical particles, the diffusion coefficient can be calculated as:

$$D = \frac{kT}{6\pi\eta r}$$

where k is the Boltzmann's constant, T is the temperature of the solution, η is the viscosity of the solution, and r is the hydrodynamic radius of the particle. The volume of a non-spherical particle and a spherical particle with the same hydrodynamic radius is approximately the same, as long as the particles are not very long or wide and flat. As a rule of thumb, the hydrodynamic radius is approximately 6 % larger than the radius of a spherical particle when the axial ratio is increased by one.

2.2.3 The autocorrelation function

Practically, the information gained from DLS is obtained by measuring the fluctuating intensities. To measure the fluctuations of the intensities, the intensity of the scattered light at a fixed angle is measured at discrete times, measured very shortly after each other. The intensities are measured for a small volume where a few, but random, number of particles are present. Unless the particles are very large and settle (typically above 1 µm, in which case they are not suited for DLS analysis), the particles move randomly in and out of the volume from which the intensities are measured. The scattered light from the different particles interfere with each other, creating interference maxima and minimum, and it is the number of these maxima that are detected for very short time periods, recorded as the intensity. Small changes in position or velocity of the particles will only change this scattering intensity slightly. However, over time, the change in position and velocity will increase, and the intensity will therefore change until it no longer is correlated to the original intensity. The smaller the particles are, the faster they will move, and thus the faster the intensity will no longer be correlated to the original intensity. The correlation of intensities over time is called an autocorrelation function. The autocorrelation function is measured at discrete times. If the measurements are done on particles of the same size and shape, the autocorrelation function, $g_2(\tau)$ can be written as:

$$g_2(\tau) = (A \cdot e^{-B\tau})^2 + 1$$

where τ is the time between intensity measurements, and A and B are constants. B is related to the diffusion coefficient. The autocorrelation curve decreases, ideally from close to 1 to 0 [44], and for monodisperse samples in an inverse sigmoidal manner when plotted on a log-time scale. The larger the particles measured are, the longer will the initial lag phase be, and the more polydisperse a sample is, the steeper the decay will be. Data can be analyzed from the fitting of the autocorrelation function, assuming a monomodal (cumulant analysis) or non-monomodal (distribution analysis) distribution. When assuming non-monomodal distributions, more terms are included in the autocorrelation function, which is then fitted to multiple decays [45]. The first order result from the fitted autocorrelation function is an intensity distribution of particle sizes [44]. The intensity distribution is weighted according to the scattering

intensity of the group of particles giving rise to the specific hydrodynamic radius. The intensity distribution is presented as peaks on an intensity vs log(size) plot, with one symmetric peak typically interpreted as one population (though it may be more populations with approximately the same hydrodynamic radius).

2.2.4 Discussion of DLS as a method

DLS is an easy method to use to obtain information about sizes. It can be done without the need of labelling and without affecting the material. For large particles, the required sample concentration is low. DLS is often used to measure the size of liposomes [18], [46] and aggregation, and can also be used to detect interactions [47], [48]. However, it is important to keep in mind that DLS only provides information about the hydrodynamic radius. For polydisperse samples and samples with little scattering, it may be difficult to fit the autocorrelation function. More terms, corresponding to the presence of more populations, may be included in the autocorrelation function to get a good fit. However, in the quest to get a good fit, too many terms may be included. This will result in the term not being meaningful included for another set of measurements on an identical sample. According to Øgendal, no more than three populations can reliably be fitted to the data. Furthermore, hydrodynamic radii of the different populations in a non-monomodal sample separated by less than a factor of four are, according to Øgendal, poorly defined. Importantly for this thesis, small particles are poor scatterers (for particles much smaller than the wavelength of the incoming light (633 nm in this thesis), the intensity is proportional to r^6, where r is the hydrodynamic radius [49]). Their contribution to the decay is therefore small and can easily be masked by the noise or the contribution of the large scatterers. In an intensity based size distribution analysis, populations of small particles may therefore not be detected, or give rise to very small peaks. If the fitting to the autocorrelation curve consistently include a term for a populations with the same small hydrodynamic radius, it is likely that this, by number, is a major specie in the solution, as the signal from the population with the small size would otherwise be easily masked by the signal from larger particles.

Another factor that can be used to evaluate and interpret the data is the count rate and the attenuation factor. The DLS instrument simply detects photons over time. The count rate is the number of photons per second as measured over the entire measurement time (typically 60-120 s), and it needs to be above some minimum value for the data to be suitable for data analysis. However, the detector can be saturated if the rate of detected photons is too high. To avoid this, an attenuator is used to reduce the detected intensity [49]. The attenuator can be between 6 and 11, with as much light as possible being detected when the attenuator is 11. When compared with the size distributions, the attenuator (and count rate) can thus provide relative indications about the number of particles with the given size present. Namely, if the intensity size distribution gives rise to a peak with a large hydrodynamic radius (which is assumed to be a result of particles which are large and thus scatter a lot), but the attenuator is set to let as much light in as possible (which is the case when the scatter intensity is low), the apparent peak may be a result of dust present or overfitting to ‘no signal’.

All together, DLS is a method useful to determine the hydrodynamic radius of particles in a solution when the number of subpopulations are maximum three, and the size distributions are well defined and well separated.

2.3 References

[1] J. R. Lakowicz, *Principles of fluorescence spectroscopy*, 3rd ed. Springer, 2006. doi: 10.1007/978-0-387-46312-4/COVER.

[2] F. Illien *et al.*, "Quantitative fluorescence spectroscopy and flow cytometry analyses of cell-penetrating peptides internalization pathways: optimization, pitfalls, comparison with mass spectrometry quantification," *Scientific Reports 2016 6:1*, vol. 6, no. 1, pp. 1–13, Nov. 2016, doi: 10.1038/srep36938.

[3] M. E. Díaz-García and R. Badía-Laíño, "FLUORESCENCE | Overview," *Encyclopedia of Analytical Science: Second Edition*, pp. 97–106, Jan. 2005, doi: 10.1016/B0-12-369397-7/00161-8.

[4] J. B. Simonsen, J. B. Larsen, C. Hempel, N. Eng, A. Fossum, and T. L. Andresen, "Unique Calibrators Derived from Fluorescence-Activated Nanoparticle Sorting for Flow Cytometric Size Estimation of Artificial Vesicles: Possibilities and Limitations," *Cytometry Part A*, vol. 95, no. 8, pp. 917–924, 2019, doi: 10.1002/cyto.a.23797.

[5] R. F. Chen and J. R. Knutson, "Mechanism of fluorescence concentration quenching of carboxyfluorescein in liposomes: energy transfer to nonfluorescent dimers," *Anal Biochem*, vol. 172, no. 1, pp. 61–77, 1988, doi: 10.1016/0003-2697(88)90412-5.

[6] X. Zhuang, T. Ha, H. D. Kim, T. Centner, S. Labeit, and S. Chu, "Fluorescence quenching: A tool for single-molecule protein-folding study," *Proc Natl Acad Sci U S A*, vol. 97, no. 26, pp. 14241–14244, Dec. 2000, doi: 10.1073/PNAS.97.26.14241/ASSET/F1ACC66D-E641-4578-8608-BF50CB05B863/ASSETS/GRAPHIC/PQ0115181004.JPEG.

[7] L. W. Runnels and S. F. Scarlata, "Theory and application of fluorescence homotransfer to melittin oligomerization," *Biophys J*, vol. 69, no. 4, pp. 1569–1583, Oct. 1995, doi: 10.1016/S0006-3495(95)80030-5.

[8] K. Goodling, K. Johnson, L. Lefkowitz, and B. W. Willuams, "Luminescent Characterization of Sodium Dodecyl Sulfate Micellar Solution Properties," *J Chem Educ*, vol. 71, no. 1, pp. A8–A12, 1994, doi: 10.1021/ed071pA8.

[9] D. L. Sackett and J. Wolff, "Nile red as a polarity-sensitive fluorescent probe of hydrophobic protein surfaces," *Anal Biochem*, vol. 167, no. 2, pp. 228–234, Dec. 1987, doi: 10.1016/0003-2697(87)90157-6.

[10] P. Greenspan and S. D. Fowler, "Spectrofluorometric studies of the lipid probe, nile red.," *J Lipid Res*, vol. 26, no. 7, pp. 781–789, Jul. 1985, doi: 10.1016/S0022-2275(20)34307-8.

[11] N. Scholz, T. Behnke, and U. Resch-Genger, "Determination of the Critical Micelle Concentration of Neutral and Ionic Surfactants with Fluorometry, Conductometry, and Surface Tension-A Method Comparison," *J Fluoresc*, vol. 28, no. 1, pp. 465–476, Jan. 2018, doi: 10.1007/S10895-018-2209-4.

[12] "Nile Red (ultra pure) - ENZ-52551 - Enzo Life Sciences." https://www.enzolifesciences.com/ENZ-52551/nile-red-ultra-pure/ (accessed Oct. 05, 2022).

[13] M. A. de Ménorval, L. M. Mir, M. L. Fernández, and R. Reigada, "Effects of dimethyl sulfoxide in cholesterol-containing lipid membranes: a comparative study of experiments in silico and with cells," *PLoS One*, vol. 7, no. 7, Jul. 2012, doi: 10.1371/JOURNAL.PONE.0041733.

[14] C. Kayalar and N. Düzgüneç, "Membrane action of colicin E1: detection by the release of carboxyfluorescein and calcein from liposomes," *BBA - Biomembranes*, vol. 860, no. 1, pp. 51–56, 1986, doi: 10.1016/0005-2736(86)90497-9.

[15] G. van den Bogaart, J. T. Mika, V. Krasnikov, and B. Poolman, “The lipid dependence of melittin action investigated by dual-color fluorescence burst analysis,” *Biophys J*, vol. 93, no. 1, pp. 154–163, Jul. 2007, doi: 10.1529/biophysj.107.106005.

[16] R. M. Epand and R. F. Epand, “Liposomes as Models for Antimicrobial Peptides,” *Methods Enzymol*, vol. 372, pp. 124–133, Jan. 2003, doi: 10.1016/S0076-6879(03)72007-2.

[17] A. L. Russell, A. M. Kennedy, A. M. Spuches, D. Venugopal, J. B. Bhonsle, and R. P. Hicks, “Spectroscopic and thermodynamic evidence for antimicrobial peptide membrane selectivity,” *Chem Phys Lipids*, vol. 163, no. 6, pp. 488–497, Jun. 2010, doi: 10.1016/J.CHEMPHYSLIP.2010.03.009.

[18] B. Maherani, E. Arab-Tehrany, A. Kheirolomoom, D. Geny, and M. Linder, “Calcein release behavior from liposomal bilayer; influence of physicochemical/mechanical/structural properties of lipids,” *Biochimie*, vol. 95, no. 11, pp. 2018–2033, Nov. 2013, doi: 10.1016/J.BIOCHI.2013.07.006.

[19] S. Hamann, J. F. Kiilgaard, T. Litman, F. J. Alvarez-Leefmans, B. R. Winther, and T. Zeuthen, “Measurement of Cell Volume Changes by Fluorescence Self-Quenching,” *J Fluoresc*, vol. 12, no. 2, 2002.

[20] W. Bae, T. Y. Yoon, and C. Jeong, “Direct evaluation of self-quenching behavior of fluorophores at high concentrations using an evanescent field,” *PLoS One*, vol. 16, no. 2, p. e0247326, Feb. 2021, doi: 10.1371/JOURNAL.PONE.0247326.

[21] T. Benachir and M. Lafleur, “Study of vesicle leakage induced by melittin,” *Biochim Biophys Acta*, vol. 1235, no. 2, pp. 452–460, May 1995, doi: 10.1016/0005-2736(95)80035-E.

[22] N. Wichmann *et al.*, “Applying flow cytometry to identify the modes of action of membrane-active peptides in a label-free and high-throughput fashion,” *Biochimica et Biophysica Acta (BBA) - Biomembranes*, vol. 1864, no. 2, p. 183820, Feb. 2022, doi: 10.1016/J.BBAMEM.2021.183820.

[23] T. M. Allen and L. G. Cleland, “Serum-induced leakage of liposome contents,” *Biochim Biophys Acta*, vol. 597, no. 2, pp. 418–426, Apr. 1980, doi: 10.1016/0005-2736(80)90118-2.

[24] S. F. Hedegaard *et al.*, “Fluorophore labeling of a cell-penetrating peptide significantly alters the mode and degree of biomembrane interaction,” *Sci Rep*, vol. 8, no. 1, pp. 1–14, 2018, doi: 10.1038/s41598-018-24154-z.

[25] S. Trier, L. Linderoth, S. Bjerregaard, H. M. Strauss, U. L. Rahbek, and T. L. Andresen, “Acylation of salmon calcitonin modulates in vitro intestinal peptide flux through membrane permeability enhancement,” *European Journal of Pharmaceutics and Biopharmaceutics*, vol. 96, pp. 329–337, Oct. 2015, doi: 10.1016/j.ejpb.2015.09.001.

[26] G. Weissmann, G. Sessa, and S. Weissmann, “Effect of Steroids and ‘Triton X-100’ on Glucose-Filled Phospholipid/cholesterol Structures,” *Nature 1965 208:5011*, vol. 208, no. 5011, pp. 649–651, 1965, doi: 10.1038/208649a0.

[27] Z. Qian *et al.*, “Discovery and Mechanism of Highly Efficient Cyclic Cell-Penetrating Peptides,” *Biochemistry*, vol. 55, no. 18, pp. 2601–2612, May 2016, doi: 10.1021/acs.biochem.6b00226.

[28] L. M. Were, B. D. Bruce, P. M. Davidson, and J. Weiss, “Size, Stability, and Entrapment Efficiency of Phospholipid Nanocapsules Containing Polypeptide Antimicrobials,” *J Agric Food Chem*, vol. 51, no. 27, pp. 8073–8079, Dec. 2003, doi: 10.1021/JF0348368/SUPPL_FILE/JF0348368SI20031001_121928.TIF.

[29] S. Trier, L. Linderoth, S. Bjerregaard, T. L. Andresen, and U. L. Rahbek, “Acylation of Glucagon-Like Peptide-2: Interaction with Lipid Membranes and In Vitro Intestinal Permeability,” *PLoS One*, vol. 9, no. 10, p. e109939, Oct. 2014, doi: 10.1371/journal.pone.0109939.

[30] H. M. Shapiro, “Practical Flow Cytometry,” *Practical Flow Cytometry*, Jun. 2003, doi: 10.1002/0471722731.

[31] J. M. Freire, D. Gaspar, B. G. de La Torre, A. S. Veiga, D. Andreu, and M. A. R. B. Castanho, “Monitoring antibacterial permeabilization in real time using time-resolved flow cytometry,” *Biochimica et Biophysica Acta (BBA) - Biomembranes*, vol. 1848, no. 2, pp. 554–560, Feb. 2015, doi: 10.1016/J.BBAMEM.2014.11.001.

[32] G. Patel *et al.*, “Cell-penetrating peptide sequence and modification dependent uptake and subcellular distribution of green florescent protein in different cell lines”, doi: 10.1038/s41598-019-42456-8.

[33] K. Temmerman and W. Nickel, “A novel flow cytometric assay to quantify interactions between proteins and membrane lipids,” *J Lipid Res*, vol. 50, no. 6, pp. 1245–1254, Jun. 2009, doi: 10.1194/jlr.D800043-JLR200.

[34] J. B. Simonsen, “A liposome-based size calibration method for measuring microvesicles by flow cytometry,” *Journal of Thrombosis and Haemostasis*, vol. 14, no. 1, pp. 186–190, Jan. 2016, doi: 10.1111/jth.13176.

[35] BD Biosciences, Ed., *Introduction to Flow Cytometry - A Learning Guide*. Becton, Dickinson and Company, 2002.

[36] A. L. Heins *et al.*, “Quantitative flow cytometry to understand population heterogeneity in response to changes in substrate availability in escherichia coli and saccharomyces cerevisiae chemostats,” *Front Bioeng Biotechnol*, vol. 7, no. AUG, p. 187, 2019, doi: 10.3389/FBIOE.2019.00187/BIBTEX.

[37] S. A. Stoner *et al.*, “High sensitivity flow cytometry of membrane vesicles,” *Cytometry Part A*, vol. 89, no. 2, pp. 196–206, Feb. 2016, doi: 10.1002/cyto.a.22787.

[38] G. Mészáros, B. Szalay, G. Toldi, A. Kaposi, B. Vásárhelyi, and A. Treszl, “Kinetic Measurements Using Flow Cytometry: New Methods for Monitoring Intracellular Processes,” *Assay Drug Dev Technol*, vol. 10, no. 1, p. 97, Feb. 2012, doi: 10.1089/ADT.2011.0368.

[39] J. P. Nolan and S. A. Stoner, “A trigger channel threshold artifact in nanoparticle analysis,” *Cytometry Part A*, vol. 83A, no. 3, pp. 301–305, Mar. 2013, doi: 10.1002/CYTO.A.22255.

[40] J. Cauzzo, M. Nystad, A. M. Holsaeter, P. Basnet, and N. Škalko-Basnet, “Following the Fate of Dye-Containing Liposomes In Vitro,” *International Journal of Molecular Sciences Article*, doi: 10.3390/ijms21144847.

[41] D. A. Basiji, W. E. Ortyn, L. Liang, V. Venkatachalam, and P. Morrissey, “Cellular Image Analysis and Imaging by Flow Cytometry,” *Clin Lab Med.*, vol. 27, no. 3, pp. 653–670, 2007, doi: 10.1016/j.cll.2007.05.008.

[42] “Fluorescent Compensation - Flow Cytometry Guide | Bio-Rad.” https://www.bio-rad-antibodies.com/flow-cytometry-fluorescence-compensation.html (accessed Oct. 06, 2022).

[43] V. Menon, R. Thomas, A. R. Ghale, C. Reinhard, and J. Pruszak, “Flow cytometry protocols for surface and intracellular antigen analyses of neural cell types,” *Journal of Visualized Experiments*, no. 94, Dec. 2014, doi: 10.3791/52241.

[44] “Dynamic Light Scattering (DLS) | Common Terms Defined | Malvern Panalytical.” https://www.malvernpanalytical.com/en/learn/knowledge-center/whitepapers/wp111214dlstermsdefined (accessed Sep. 24, 2022).

[45] P. M. Carvalho, M. R. Felício, N. C. Santos, S. Gonçalves, and M. M. Domingues, “Application of light scattering techniques to nanoparticle characterization and development,” *Front Chem*, vol. 6, p. 237, Jun. 2018, doi: 10.3389/FCHEM.2018.00237/BIBTEX.

[46] S. Rex, “Pore formation induced by the peptide melittin in different lipid vesicle membranes,” *Biophys Chem*, vol. 58, no. 1–2, pp. 75–85, Jan. 1996, doi: 10.1016/0301-4622(95)00087-9.

[47] R. G. Diedrichsen *et al.*, “Revealing the importance of carrier-cargo association in delivery of insulin and lipidated insulin,” *J Control Release*, vol. 338, pp. 8–21, Oct. 2021, doi: 10.1016/J.JCONREL.2021.07.030.

[48] M. Kristensen *et al.*, “Penetratin-Mediated Transepithelial Insulin Permeation: Importance of Cationic Residues and pH for Complexation and Permeation,” *AAPS Journal*, vol. 17, no. 5, pp. 1200–1209, Sep. 2015, doi: 10.1208/s12248-015-9747-3.

[49] “Dynamic Light Scattering: An Introduction in 30 Minutes.” Accessed: Sep. 24, 2022. [Online]. Available: https://warwick.ac.uk/fac/cross_fac/sciencecity/programmes/internal/themes/am2/booking/particlesize/intro_to_dls.pdf

Chapter 3: Manuscript in preparation: Biophysical investigation of permeation enhancers and peptide drugs in intestinal environments

As mentioned in the introduction, many ways of enhancing the bioavailability of orally delivered peptide drugs are continuously explored, and particularly the transcellular translocation through the epithelium appears to bear a great potential for increasing the bioavailability. Currently, the use of permeation enhancers show the greatest potential for increasing the bioavailability of orally delivered polypeptide drugs. While permeation enhancers with a carrier function is known to directly interact with the peptide drug and thereby influence the ability of the peptide drug to permeate the membrane, the interaction between peptide drugs and permeation enhancers not acting as carriers, are only recently becoming a studied topic [1]. For permeation enhancers with a surfactant mode of action, multiple studies have studied the interaction with and behavior in bile components [1], [2], and there is an increasing awareness of the importance of studying permeation enhancement in more biological relevant solutions, containing bile components [3]. Both interactions with peptide drugs and bile components may mutual influence their interaction with permeation enhancers. Recently, one such study of permeation enhancer interactions with peptide drugs in simulated intestinal fluid was published. The study showed a reduced affinity of exenatide towards the permeation enhancers C10 and SNAC in biorelevant intestinal media [1]. Here we present a functional study of how the membrane activity of a range of permeation enhancers is affected by interactions with the oppositely charged peptide drugs sCT and insulin, in phosphate buffer and in fasted state simulated intestinal fluid. This was done to investigate the importance of permeation enhancer-peptide drug interactions, how they are affected by bile components, and if such functional studies can be performed in fasted state simulated intestinal fluid.

The membrane perturbation studies were carried out as calcein release studies on liposomes consisting of 90 mole % POPC and 10 mole % cholesterol. Cholesterol was included to ensure a sufficient degree of liposome stability as the bile component taurocholate is known to be able to form mixed micelles with lipids such as POPC. Such a formation of mixed micelles would destabilize the liposomes and we had found that for pure POPC liposomes, the permeability of the liposomes would have markedly increased somewhere between 2 and 18 hrs after incubation with fasted state simulated intestinal fluid (Figure 3.1A). By increasing the cholesterol concentration to 30 % cholesterol however, the liposomes were stabilized to such a degree, that SDS 6.7 g/L only resulted in 40 % release over an hour (Figure 3.1B). POPC:Cholesterol (7:3 mol%)-liposomes were thus considered too stable. Instead, it was decided to use 10 % Cholesterol, as these liposomes gave rise to a detectable calcein release for the majority of the permeation enhancers at 6 g/L within 30 min (Figure 4A in the manuscript). The 6 g/L was chosen as this concentration is well above the concentration of C10 which gave rise to detergent-based perturbation of Caco-2 monolayers [4], and calcein release from the liposomes were thus expected at this concentration. To decide the concentration of POPC:Cholesterol (9:1 mol%)-liposomes to use, a range of concentrations of the liposomes were incubated for 30 min with 0.5 % (V/V) Triton-X to obtain full-release signal (Figure 3.1C). Except for an apparent outlier at 0.6 nM liposomes, the fluorescence intensity corresponding to the fluorescence from calcein, appeared to be linear from 0-1 nM liposomes. For calcein-release assay historical reasons, 0.6 nM liposomes (50 µM lipids) were thus chosen.

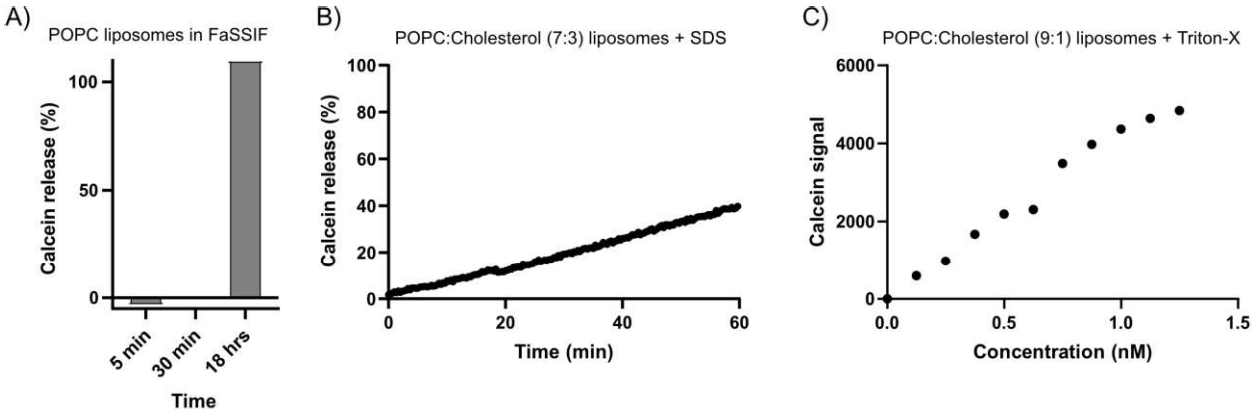

Figure 3.1: Deciding on lipid composition and liposome concentration. Ex/Em: 491 nm/514 nm

1 References

[1] C. Twarog *et al.*, "Characterization of the physicochemical interactions between exenatide and two intestinal permeation enhancers: Sodium caprate (C10) and salcaprozate sodium (SNAC)," *Int J Pharm*, vol. 626, p. 122131, Oct. 2022, doi: 10.1016/J.IJPHARM.2022.122131.

[2] S. Hossain *et al.*, "Influence of Bile Composition on Membrane Incorporation of Transient Permeability Enhancers," *Mol Pharm*, vol. 17, no. 11, pp. 4226–4240, Nov. 2020, doi: 10.1021/ACS.MOLPHARMACEUT.0C00668/ASSET/IMAGES/LARGE/MP0C00668_0010.JPEG.

[3] S. Maher, D. J. Brayden, L. Casettari, and L. Illum, "Application of Permeation Enhancers in Oral Delivery of Macromolecules: An Update," *Pharmaceutics*, vol. 11, no. 1, Jan. 2019, doi: 10.3390/PHARMACEUTICS11010041.

[4] D. J. Brayden, S. Maher, B. Bahar, and E. Walsh, "Sodium caprate-induced increases in intestinal permeability and epithelial damage are prevented by misoprostol," *European Journal of Pharmaceutics and Biopharmaceutics*, vol. 94, no. 1, pp. 194–206, 2015, doi: 10.1016/J.EJPB.2015.05.013.

Biophysical investigation of permeation enhancers and peptide drugs in intestinal environments

Authors: Nanna Wichmann Larsen, Serhii Kostrikov, Morten B. Hansen, Claudia U. Hjørringgaard, Niels B. Larsen, Thomas L. Andresen, Kasper Kristensen

Abstract

Oral administration is the preferred route of drug administration. Yet for peptide drugs this is not trivial. On the road towards this being feasible, permeation enhancers that induce membrane perturbations or cell penetrating peptides is often used to increase the translocation of peptide drugs across the lipid bilayer of the cells lining the epithelium. Many factors may influence such permeation enhancement, including the bile acids and phospholipids present in the intestinal fluid. Yet, how the presence of the actual peptide drug influence the permeation enhancers' mechanism of action is rarely studied. We hypothesized that the peptide drugs and permeation enhancers mutually affect each other, and that the equilibrium of these interactions is influenced by the presence of bile acids and phospholipids. We therefore investigated the ability of the permeation enhancers caprate, sodium cholate, dodecyl maltoside, sodium dodecyl sulfate, salcaprozate sodium, melittin, and penetratin to permeate membranes membrane. The study was done in the absence and presence of the peptide drugs insulin and salmon calcitonin. We focused on how the presence of these drugs and fasted state simulated intestinal fluid influenced intermolecular interactions and membrane interactions of permeation enhancers. We established that POPC:Cholesterol membranes were a suitable model system for biophysical work in fasted state simulated intestinal fluid. We show that some permeation enhancers and peptide drugs do indeed affect each other, just as permeation enhancers and fasted state simulated intestinal fluid components affect each other, but also that bile acids can interact with salmon calcitonin, leading to an intrinsice membrane activity of salmon calcitonin. Finally, we show that these interactions all changes the equilibria governing the membrane perturbation of lipid membranes, with the effect of fasted state simulated intestinal fluid interactions often dominating that of the peptide drug. Together this highlights the importance of testing permeation enhancement in more complex solutions such as fasted state simulated intestinal fluid and to carefully choose a permeation enhancer with the specific drug in mind.

1 Introduction

The oral route is generally considered to be the most attractive route of drug administration [1]. Yet, most peptide drugs are administered by injection due to low oral bioavailability [2].

When oral drugs are swallowed they eventually enter the stomach, and potentially the gastrointestinal tract, where drugs can be absorbed by crossing the cells lining the gastrointestinal tract (Figure 1A). However, the size and hydrophilic nature of peptide drugs generally prevent them from diffusing across the lipid bilayer into the cells, thereby to be absorbed through transcellular peptide transport. This is one of the main obstacles for increasing the oral bioavailability. To enhance this, permeation enhancers either affecting the membrane or the translocation properties of the peptide drug can be used.

In the present study, we focus on the interplay between permeation enhancers and the peptide drug for which the permeation should be enhanced and the influence of bile acids on this interplay.

Two out of three completed phase III studies completed for oral formulations of linear polypeptides (Rybelsus, an oral formulation of semaglutide, and a formulation of salmon calcitonin (sCT)) as well as

many prospect orally administered peptide drugs, utilize permeation enhancers [3]. Semaglutide and sCT are coformulated with the Eligen®-based permeation enhancers salcaprozate sodium (SNAC) [4] and 8-(N-2-hydroxy-5-chloro-benzoyl)-amino-caprylic acid also known as 5-CNAC [5], respectively. In addition, insulin has been successfully tested in Phase II studies with the fatty acid permeation enhancer, C10 [6]. However, the required insulin dose were too high for the product to be commercially viable [7].

In Rybelsus, semaglutide is co-formulated with the permeation enhancer SNAC. Buckley et al. demonstrated that semaglutide is absorbed in the stomach of dogs where SNAC reduces its degradation by peptidase and shifts semaglutide towards a monomeric state, which is better suited for transport [8]. The study furthermore indicate that SNAC also enhances the transcellular transport of semaglutide [8].

Together with SNAC, sodium caprate (C10) is the permeation enhancer tested most extensively in humans [9]. Mechanistic studies confirm that C10 increases membrane fluidity [10], leading to an inherent enhanced membrane permeability, which influence transcellular transport. Paracellular transport is also, indirectly affected as tight junctions are opened by a membrane perturbation-mediated alteration in the cellular Ca^{2+} levels [3], [9].

Similar to C10, many of the transcellular permeation enhancers function by insertion of the permeation enhancer monomer into the membrane, thereby fluidizing the membranes [3]. However, many other components are present in the intestines, such as bile acids and phospholipids, with which the permeation enhancers can interact. As shown by coarse grain simulations, the permeation enhancers may form mixed micelles with these components, thereby changing the prerequisites for permeation enhancement [11]. While drug studies done in simulated intestinal fluids have been a topic at least since 1966 [12], the literature with intestinal permeation enhancers in (simulated) intestinal fluid is still scarce. Yet, it is clear that there is a growing awareness of the benefits of testing this [13].

Some transcellular permeation enhancers function by affecting or interacting with the peptide drug. Penetratin, as an example, is a cell-penetrating peptide that without perforation of the membrane passes through the membrane [14]. While penetratin typically is used as a permeation enhancer in a covalently attached form [15], it has been shown *in vivo* that a non-covalent complex between penetratin and insulin enhances insulin permeation too [16], [17].

Regardless of the differences found for SNAC and C10, the choice of one permeation enhancer over another is often based on formulation, manufacturing, and commercial considerations rather than e.g. than considerations about the peptide drug [2], [9]. Comparisons are continuously carried out, typically focusing on two permeation enhancers, sometimes in the presence of a macromolecule such as dextran [18]–[21]. Despite interactions between some pairs of permeation enhancer and peptide drugs being crucial for permeation enhancement, the peptide drug is rarely included in such comparisons [8], [16].

In the present study, we focus on properties of permeation enhancers with respect to their enhancement of peptide drug permeation across the lipid bilayer of the epithelial cells lining the gastrointestinal tract. We investigated seven different permeation enhancers that functioned transcellular and/or had a membrane perturbating function. The permeation enhancers were studied in the absence or presence of either of the peptide drugs insulin or sCT to illuminate how permeation enhancer:peptide drug interaction

may affect the desired permeation enhancement. The experiments were carried out in two different buffers of different biological complexity; one with pH and osmolality matching the intestinal fluid, the other also containing a bile salt and phospholipids to further shed light on how these components of the intestinal fluid may affect the desired permeation enhancement.

We used liposomes as a model system to study membrane perturbation by the permeation enhancers using a calcein release assay (Figure 1B). The underlying mechanism was further elucidated by studying the liposome integrity with respect to size using dynamic light scattering (DLS). The mechanisms were correlated to the self-assembly properties of the permeation enhancers as determined using the hydrophobicity marker Nile Red and DLS. Having characterized the permeation enhancers, we measured the membrane perturbation in the presence of insulin or sCT, and compared deviations to permeation enhancer-peptide drug interactions as determined by size and hydrophobicity. Finally, we established that the model system was sufficiently stable to be suitable for studies in FaSSIF and measured the membrane perturbation by the permeation enhancers in the absence and presence of the peptide drugs therein.

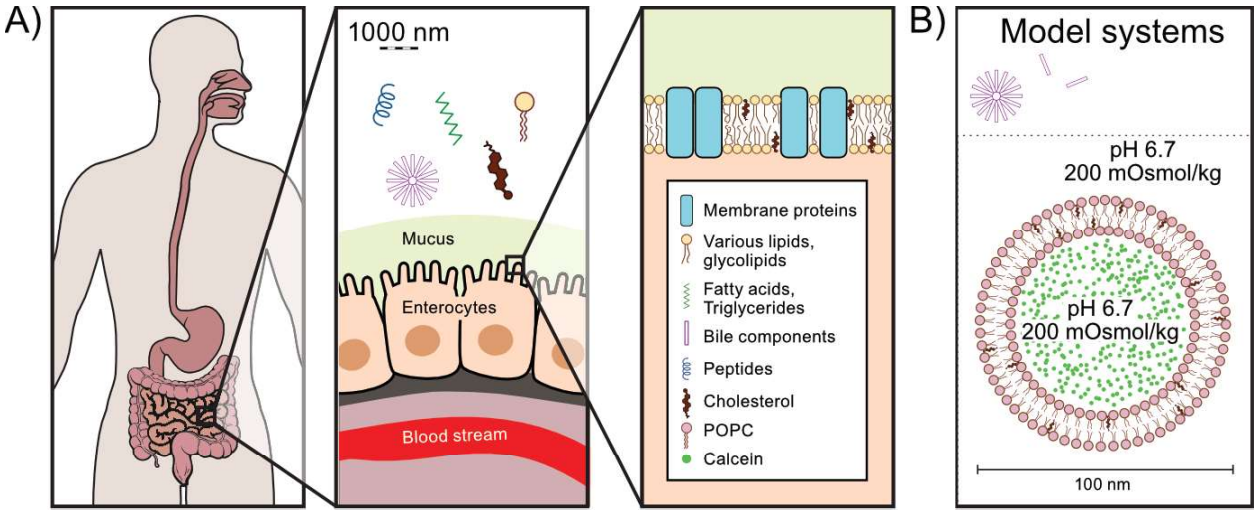

Figure 1: Overview figure: A) Biological context: For the drugs of an orally swallowed tablet (left) to be absorbed in the gastrointestinal tract, the drugs should cross the epithelial cells lining the gastrointestinal tract (middle). For transcellular transport, the drug should enter the cell by translocating across the lipid bilayer. The lipid bilayer is complex, containing multiple different lipids, glycolipids, and membrane proteins (right). B) The model system: POPC:Cholesterol (9:1) liposomes containing calcein in a self-quenching concentration were used as a model system. Experiments were carried out in two simulated intestinal fluids, one with pH and osmolality matching the intestinal fluid, and another where also bile acids and phospholipid similar to the intestinal fluid, were included.

2 Materials and methods

2.1 Materials

Calcein, sodium dihydrogen phosphate, sodium chloride (NaCl), Triton X-100, sodium dodecyl sulfate (SDS), N-Dodecyl-β-Maltoside (DDM), sodium cholate hydrate (NaC), sodium caprate (C10), tert-butanol, and dimethylsulfoxide (DMSO) were purchased from Sigma-Aldrich

1-Palmitoyl-2-oleoyl-sn-glycero-3-phosphocholine (POPC) and cholesterol (ovine wool) were purchased from Avanti Polar Lipids (Alabaster, AL, USA).

Insulin desB30 (Insulin) was kindly provided by Novo Nordisk A/S. SNAC was purchased from VulcanChem.

Slurry for preparing Sepharose CL-4B columns was purchased from GE Healthcare (Little Chalfont, UK). Econo-Column glass chromatography column (dimensions 1.5 × 20 cm) was purchased from Bio-Rad

(Hercules, CA, USA). Q-Max syringe filters with 0.22-µm cellulose acetate filtration membranes were purchased from Frisenette (Knebel, Denmark). Black, untreated flatbottomed Nunc F96 MicroWell™ polystyrene plates were purchased from Thermo Scientific™.

2.2 Synthesis and purification of melittin, penetratin, and sCT

Melittin, penetratin, and sCT were synthesized using standard solid phase peptide synthesis. Melittin and penetratin were synthesized and purified as in [22]. In short were all peptides synthesized on a resin that was Fmoc-deprotected and subject to repeating cycles of draining and washing, coupling by adding amino acid solution, and washing. sCT were furthermore subject to formation of disulfide on the resin by adding an iodine solution to the resin. Upon synthesis and disulphide formation (for sCT), the peptide was cleaved of the resin and purified and analyzed using reversed-phase-high performance liquid chromatography (RP-HPLC) with C18 columns. The final purities were 99 % for melittin, 93 % for penetratin, and 98 % for sCT as determined by HPLC. For further details, see supplementary information.

2.3 Solutions

Three solutions were used within this paper, Minimum Simulated Intestinal Fluid (minSIF), 60 mM Calcein solution, and Fasted State Simulated Intestinal Fluid (FaSSIF). minSIF consisted of 10 mM phosphate and 100 mM NaCl, was adjusted to pH 6.7 using NaOH, and had an osmolality of 190±5 mOsmol/kg. The calcein solution consisted of 60 mM calcein and 10 mM phosphate, was pH adjusted to pH 6.7 using NaOH, and had an osmolality of 190±5 mOsmol/kg. The calcein solution was prepared with milli-Q water and NaOH solutions filtered through a 0.22 µm sterile filter prior to use. FaSSIF was prepared by dissolving FaSSIF powder from Biorelevant in minSIF in a ratio of 2.016 g:900 mL, resulting in a final composition of 3 mM taurocholate, 0.75 mM phospholipids, 10 mM phosphate, and 100 mM NaCl, with pH 6.7, and an osmolality of 200±2 mOsmol/kg. The solution was left to equilibrate for at least two hours, and was used within 48 hrs from preparation as stated in the instructions.

2.4 Liposome preparation

The liposomes were prepared by dissolving POPC and Cholesterol in tert-butanol:mQ (9:1) and mixing them in a 9:1 molar ratio. The tert-butanol:mQ was removed by lyophilization overnight.

60 mM calcein was added to the lyophilized lipid mixture. The resulting lipid suspension was vortexed gently seven times with 5 minutes between each time and then subjected to five freeze-thaw cycles (alternating between submersion into a 70˚C water bath and into a liquid nitrogen bath). Subsequently, the lipid suspension was extruded 21 times through a 100 nm polycarbonate membrane (Whatman, GE Healthcare) using a mini-extruder (Avanti Polar Lipids). Non-encapsulated calcein was removed and exchanged to minSIF by size-exclusion chromatography using a Sepharose CL-4B column (dimensions 1.5 × 20 cm) and elusion with minSIF at a flow rate of 1 mL/min. The eluted liposomes were added to an Amicon Ultra-4 30 kDa centrifugal filter unit (Merck, Darmstadt, Germany) and concentrated by centrifuging at 2000 ×*g*. The lipid concentration of the samples were determined via RP-HPLC (See below), and the liposome size was verified using DLS (See below). All dilutions were done in minSIF. Two independent batches of liposomes were prepared, and were used within 2 months after preparation. The liposomes were kept at 5 ˚C when not in use.

2.5 Determining lipid concentration in liposome samples

The POPC concentration of the liposome samples were determined via RP-HPLC using a Shimadzu Nexera i-series HPLC equipped with a PDA and an evaporative light scattering detector (ELSD) SEDEX LT-ELSD 100LT together with a Waters XTerra C8 column with a flow rate of 1 mL/min. The used mobile phases were milli-Q water containing 0.1 % Trifluoroacetic acid (TFA) and 5 % Acetonitrile (MeCN) (V/V/V) and MeCN containing 0.1 % TFA (V/V). The area under the curve ELSD signal was compared to a POPC standard curve. The total lipid concentration of the liposome stocks were calculated as the $c_{lipids_{total}} = \frac{c_{POPC}}{0.9}$, to include the 10 % cholesterol.

2.6 Estimating liposome concentration

The liposome concentrations were estimated based on the lipid concentrations. It was assumed that the liposomes were unilamellar with a thickness of the bilayer membrane of 5 nm, and that all lipids had a head group area of 0.71 nm^2, like POPC [23]. Furthermore, it was also assumed that all liposome had a diameter of 105 nm, as this is the diameter of the majority of the liposomes, as determined when performing a number-based size distribution analysis of the dynamic light scattering measurements of the liposomes (See below). With these assumptions, the number of lipids per liposomes were calculated as

$$N_{total} = \frac{4\pi}{0.71\ nm}(r^2 + (r - 5\ nm)^2 \frac{lipids}{liposome} = 88848 \frac{lipids}{liposome}$$

2.7 Handling of permeation enhancers and peptide drugs

Lyophilized melittin, penetratin, insulin, and sCT were adjusted to room temperature, and minSIF filtered through at least 0.4 µm sterile filter or FaSSIF filtered through a 0.4 µm sterile filter was added to dissolve the peptides to stock solutions. The solutions were vortexed gently for 10 s. The absorption spectra were measured using a NanoDrop 2000c spectrophotometer, and the concentrations of the stock solutions were calculated using Lambert-Beer's Law and extinction coefficients calculated to be 5500 $M^{-1}cm^{-1}$ for melittin, 11000 $M^{-1}cm^{-1}$ for penetratin, 6335 $M^{-1}cm^{-1}$ for insulin, and 1615 $M^{-1}cm^{-1}$ for sCT, all at 280 nm, using the work by Pace et al. [24]

For stock solutions of C10, DDM, NaC, and SDS, at least 2.0 mg powder were weighed. The powders were dissolved in an exact volume of either filtered minSIF or filtered FaSSIF to obtain a known concentration of the stock solution of at least 5 g/L. Dilutions were done in the respective solution of dissolution.

2.8 Calcein Release assay

With the solutions of interest being the permeation enhancers at various, set, concentrations, with or without peptide drugs, in minSIF or FaSSIF, the solutions of interest were added to a 96-well plate.

The solutions of interest and the liposomes were preheated at 37 ˚C. Liposomes were added to the solutions of interest to a final liposome concentration of 0.6 nM and a final volume of 150 µL using a multipipette. The fluorescence intensity, F, was measured continuously for 30-60 minutes using a Spark multimode microplate reader (Tecan, Männedorf, Switzerland) with an excitation wavelength of 491 nm and an emission wavelength of 514 nm.

For kinetic measurements, suspensions in all wells were handled simultaneously, and measurements initiated within less than 20 s from the liposomes were added. For all other measurements, the measurements were initiated within three minutes after the liposomes were added to the first wells.

The fluorescence intensity of the intact liposomes, F_0, was measured using liposomes added to minSIF or FaSSIF corresponding to that of the solution of interest. The maximum fluorescence intensity, F_{max}, was measured using liposomes added to Triton X-100 diluted in minSIF or FaSSIF corresponding to that of the solution of interest and a final concentration of Triton X-100 of 0.5 V/V %.

The calcein release was calculated using the equation

$$Calcein\ Release = \frac{F - F_0}{F_{max} - F_0} \cdot 100\ \%$$

Measurements of calcein release in minSIF were carried out at least in triplicates, on two independent batches of liposomes, Measurements of calcein release in FaSSIF were generally carried out at least in triplicates, except for C10 at EC95 and C10 at EC50 in the presence of sCT which were carried out in duplicates.

2.9 Obtaining EC50 and EC95 values

For each permeation enhancer, the percentage of calcein released from liposomes upon exposure to a range of concentrations of permeation enhancer for 30 min was determined. The calcein release was determined in triplicate, two of which were on the same batch of liposomes. The calcein release was plotted towards the permeation enhancer concentrations in GraphPad Prism 9.4.0, and a curve was fitted to the data using a dose-response non-linear regression, fitting to ECAnything where the model is

$$EC50 = \frac{ECF}{\left(\frac{F}{100 - F}\right)^{\frac{1}{HillSlope}}}, Y = Bottom + \frac{Top - Bottom}{1 + \left(\frac{EC50}{X}\right)^{HillSlope}}$$

Here, ECF is the permeation enhancer concentration that gives a response F percent of the way between Bottom and Top plateau, EC50 is the ECF at 50 %, Hillslope is the steepness of the family of curves, and Top and Bottom are plateaus in the units of the Y-axis [25]. F was set to 50 to extract EC50 values, and to 95 to extract EC95 values, each as a concentration with a 95 % confidence interval. For DDM and C10, the EC50 value used was manually chosen to be slightly different (< 3 %) than the EC50 value given by GraphPad Prism, but still within the confidence interval.

2.10 DLS

To determine the size and homogeneity of the liposomes, the concentrated liposomes were diluted in minSIF to approximately 0.5 nM liposomes and DLS was measured at room temperature.

For all other DLS measurements were solutions preheated separately for 20 min at 37 ˚C, mixed, and then incubated for approximately 30 min, before investigation by DLS at 37 ˚C. For determining the effect of permeation enhancers on the size of liposomes, liposomes and permeation enhancers were mixed to a final liposome concentration of 0.6 nM and a final permeation enhancer concentration at the EC95 value. For DLS measurements of permeation enhancers in FaSSIF and in minSIF without liposomes, the final permeation enhancer concentration was the EC50 value. For DLS measurements with permeation enhancer and peptide drugs combined, EC50s were used as the final permeation enhancer concentration, and 300 mg/L as the final peptide drug concentration.

All investigations by DLS were performed by using a Zetasizer Nano ZS (Malvern, Worcestershire, UK). Three technical measurements were carried out on each of two independent replicates. The number of

runs per measurement were adjusted automatically by the Zetasizer. Where nothing else is stated, intensity-based size distribution analysis was carried out using the Malvern Zetasizer software 7.13. Listed sizes are the sizes ± standard deviations as obtained from an average of the six measurements by the Malvern Zetasizer software 7.13.

2.11 Nile Red measurements

The solutions of interest were the permeation enhancers at various, set, concentrations, the permeation enhancers at their EC50 with or without 300 mg/L of the peptide drugs, insulin and sCT, and a blank run with minSIF.

The solutions of interest were mixed in a 96-well plate to a final volume of 100 µL. 2 µL of 1.5 mM Nile red in DMSO was added to each of the solutions of interest to a final concentration of Nile Red of 29 µM. The solutions were mixed, and incubated at 37 ˚C for at least 30 min before transfer to a Spark multimode microplate reader (Tecan, Männedorf, Switzerland) heated to 37 ˚C. The Nile Red fluorescence emission intensity of the samples at 633 nm was measured using an excitation wavelength of 550 nm. Nile Red measurements were carried out in duplicates.

2.12 Statistical analysis

Statistical significance was measured by two-tailed t-tests with Welch's correction using GraphPad Prism 9® software and was designated at the level of $P < 0.05$.

3 Results and discussion

We hypothesized that interactions between permeation enhancers and peptide drugs or bile components could influence the membrane activity of the permeation enhancers. We therefore did a biophysical investigation of seven membrane interacting permeation enhancers in the absence and presence of two peptide drugs. The permeation enhancers were characterized with respect to their membrane perturbation, self-association, and peptide drug interactions. Experiments were carried out in a minimum simulated intestinal fluid (minSIF) and in fasted state simulated intestinal fluid (FaSSIF), both with a pH of 6.7 and an osmolality of around 200 mOsmol/kg. The FaSSIF additionally contained the bile acid taurocholate and phospholipids.

The permeation enhancers chosen are the five small molecule permeation enhancers C10, DDM, NaC, SDS, and SNAC, and the two peptide permeation enhancers melittin and penetratin [3], [26] (Figure 2A). The peptide drugs chosen were insulin desB30 (hereafter denoted insulin) and sCT (Figure 2B). At pH 6.7 as used here, insulin has an overall negative charge of -1.7, and sCT an overall positive charge of +3.1.

3.1 Establishing a model system

First, we needed to ensure that we had a system, in which membrane perturbation could be tested. We tested the membrane perturbation of the permeation enhancers using a calcein release assay (Figure 3A). Here, we used calcein fluorescence after a certain time to measure the calcein released from liposomes with calcein encapsulated in an otherwise self-quenching concentration.

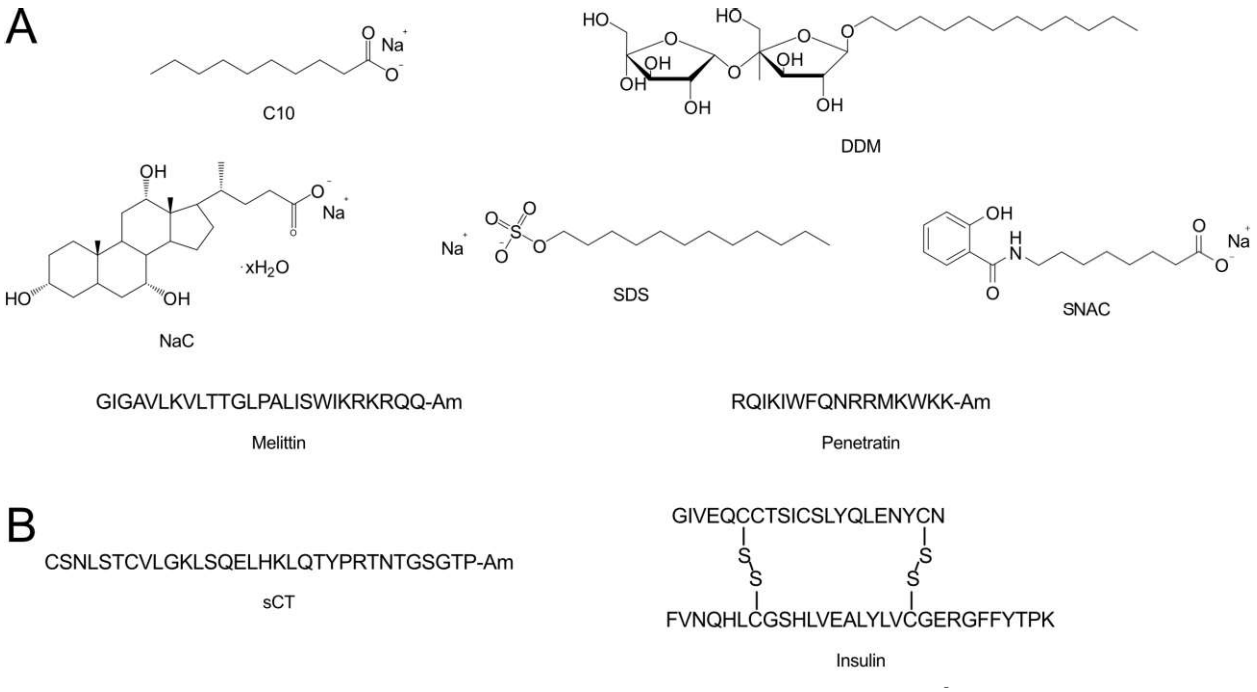

Figure 2: Structures of compounds. A) Permeation enhancers. B) Peptide drugs. The chemical permeation enhancers are shown as chemical structures and the peptides are shown by one-letter abbreviations of the amino acid residues. Amidation of the peptides are indicated by –Am.

We measured the calcein release from 0.6 nM POPC:Cholesterol (9:1) liposomes with a range of concentrations of each of the permeation enhancers. After 30 min, calcein release was observed for all the permeation enhancers, but not for penetratin, measured for up to 500 mg/L) (To further characterize the model system, the calcein release kinetics were measured for each of the permeation enhancers at their EC95 and their EC50 (Figure 4C). For the permeation enhancers at their EC95, a plateau of close to full release had logically been reached within 30 min. It was evident that for melittin, and NaC, this plateau was reached almost instantaneously whereas for C10, DDM and SDS, it took longer time to reach this plateau. The calcein release exceeding 100 % for C10 appear odd. As it was not consistently observed, we assume that it was due to some technical uncertainties, such as a slightly larger liposome concentration in the C10 sample than for the other samples. The higher signal, however, shoul not affect the kinetic profile. More interesting is that for melittin, NaC, and C10 at their EC50, an almost steady level of around 50 % calcein release was reached within 20 min, whereas for SDS and DDM the reaction continued, reaching close to full release within an hour. Some degree of uncertainty is observed for melittin and DDM around 40 and 50 % calcein release, respectively. This is assumed to be due to the large rate of increase in calcein release around its EC50.

With the above, we have determined that SNAC, C10, NaC, SDS, DDM, and melittin, but not penetratin, are membrane perturbating in our set-up, with the concentrations required for membrane perturbation decreasing in the listed order. Furthermore, we showed that SDS and DDM was slower in their membrane perturbation than the rest of the permeation enhancers, and that DDM had a markedly different kinetic profile of the membrane perturbation than any of the other permeation enhancers. In the gastrointestinal tract, dilution of the permeation enhancers will inevitably take place, and it may thus be useful to take the slow kinetics into consideration when choosing a permeation enhancer concentration.

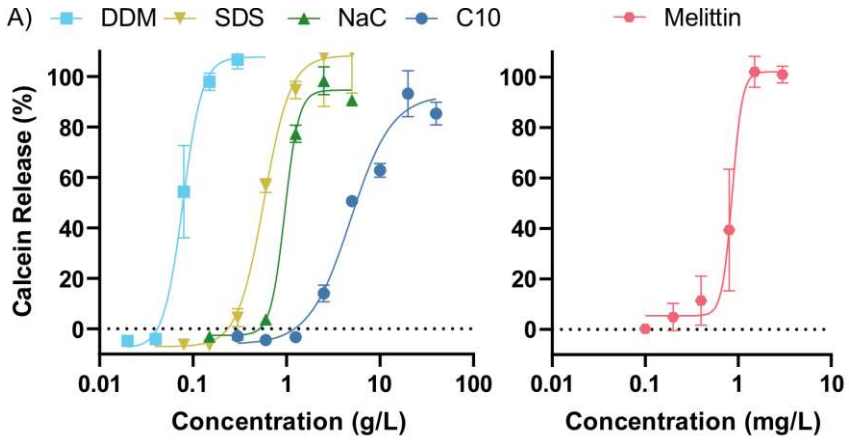

B)

Permeation enhancer	EC50 (95 % CI)	EC95 (95 % CI)
C10 (g/L)	5.0 (4.0-6.0)	22 (13-44)
DDM (g/L)	0.076 (0.070-0.087)	0.16 (N/A-0.23)
NaC (g/L)	0.95 (0.89-1.07)	1.6 (1.4-1.8)
SDS (g/L)	0.57 (0.50-0.66)	1.5 (1.0-2.5)
Melittin (g/L)	$8.6 \cdot 10^{-3}$ ($N/A-1.0 \cdot 10^{-3}$)	$1.2 \cdot 10^{-3}$ ($N/A-2.6 \cdot 10^{-3}$)
Penetratin (mg/L)	-	-

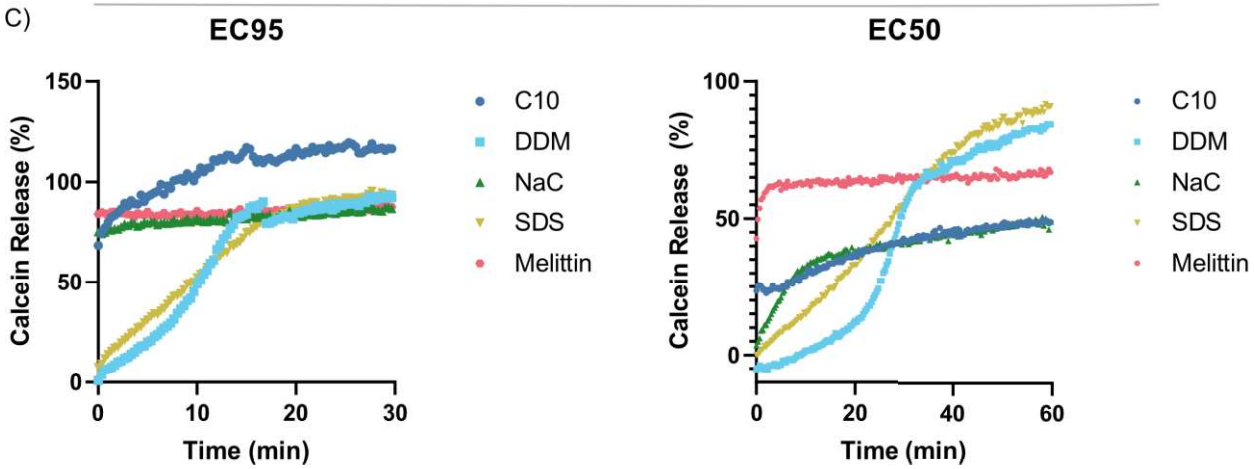

Figure 4A, Supplementary figure 1). The calcein release increased with increasing permeation enhancer concentration in a non-linear manner with a top plateau at full release. SNAC required very high concentrations to give rise to calcein release. While SNAC were indeed soluble at concentrations well above this concentration, it precipitated within the time course of the handling of the permeation enhancers, and SNAC was therefore not included in the further investigations. We have thus established a system that is suitable for comparing the effect of permeation enhancers under various conditions.

For later analyses and comparisons, we used the permeation enhancer concentrations that gave rise to 50 % (EC50) and 95 % (EC95) of the maximum calcein signal for each permeation enhancer. These concentrations were extracted from a non-linear fit to the calcein release per concentration (Figure 4A,B).

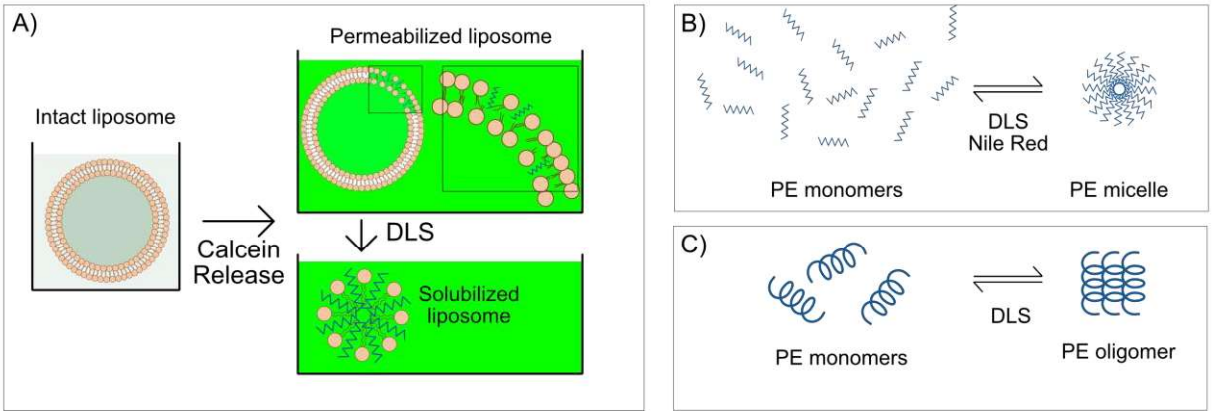

Figure 3: Possible interactions and methods used to study them. A) Principle of Calcein release: Left: intact liposome. Right: liposomes with pores (top), liposomes with PEs inserted -> solubilized liposomes (liposomes). Indications of calcein release used to study membrane permeabilization, DLS used to discriminate membrane perforation and solubilization. B) Permeation enhancers forming micelles. Indication of this being studied using DLS and Nile Red. C) Peptides forming oligomers.

To further characterize the model system, the calcein release kinetics were measured for each of the permeation enhancers at their EC95 and their EC50 (Figure 4C). For the permeation enhancers at their EC95, a plateau of close to full release had logically been reached within 30 min. It was evident that for melittin, and NaC, this plateau was reached almost instantaneously whereas for C10, DDM and SDS, it took longer time to reach this plateau. The calcein release exceeding 100 % for C10 appear odd. As it was not consistently observed, we assume that it was due to some technical uncertainties, such as a slightly larger liposome concentration in the C10 sample than for the other samples. The higher signal, however, shoul not affect the kinetic profile. More interesting is that for melittin, NaC, and C10 at their EC50, an almost steady level of around 50 % calcein release was reached within 20 min, whereas for SDS and DDM the reaction continued, reaching close to full release within an hour. Some degree of uncertainty is observed for melittin and DDM around 40 and 50 % calcein release, respectively. This is assumed to be due to the large rate of increase in calcein release around its EC50.

With the above, we have determined that SNAC, C10, NaC, SDS, DDM, and melittin, but not penetratin, are membrane perturbating in our set-up, with the concentrations required for membrane perturbation decreasing in the listed order. Furthermore, we showed that SDS and DDM was slower in their membrane perturbation than the rest of the permeation enhancers, and that DDM had a markedly different kinetic profile of the membrane perturbation than any of the other permeation enhancers. In the gastrointestinal tract, dilution of the permeation enhancers will inevitably take place, and it may thus be useful to take the slow kinetics into consideration when choosing a permeation enhancer concentration.

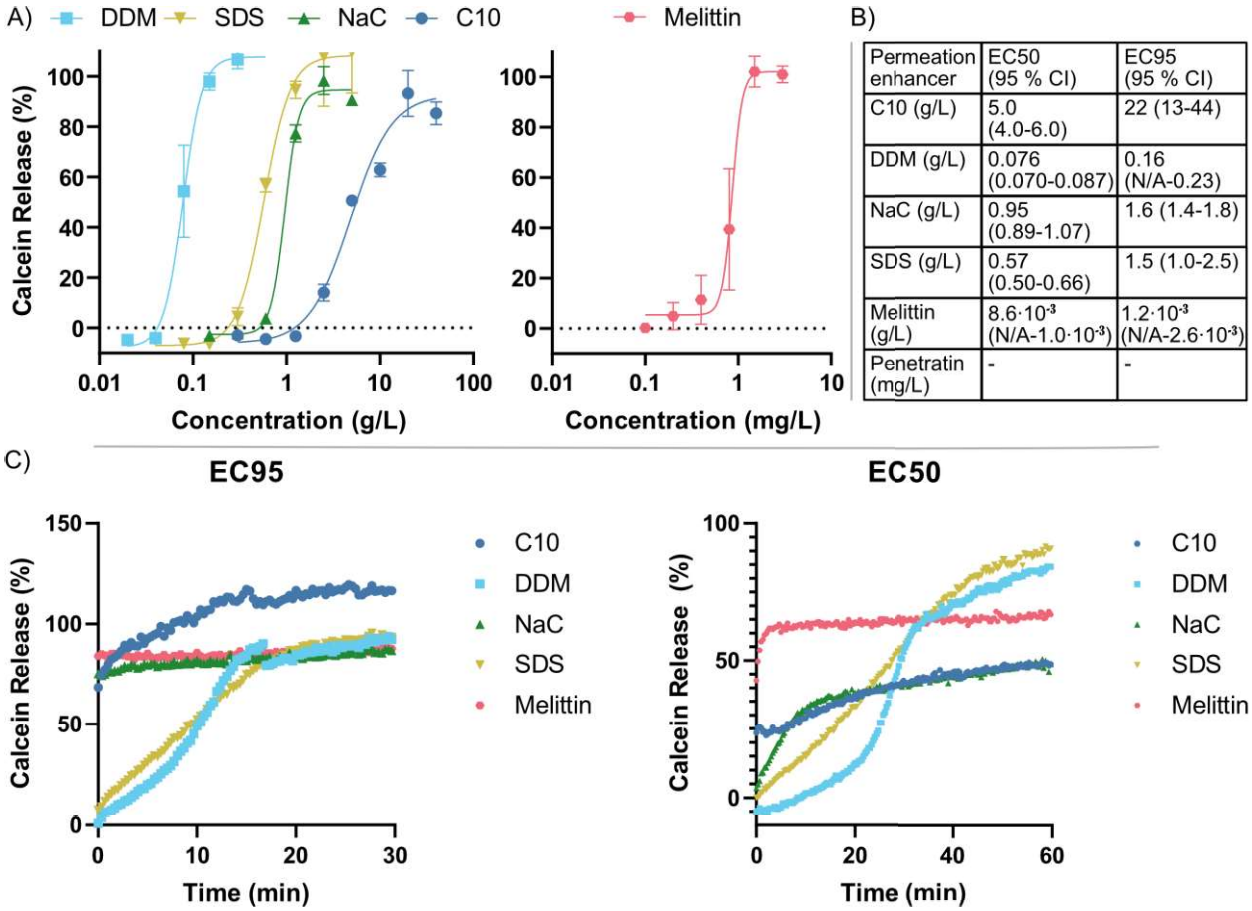

Permeation enhancer	EC50 (95 % CI)	EC95 (95 % CI)
C10 (g/L)	5.0 (4.0-6.0)	22 (13-44)
DDM (g/L)	0.076 (0.070-0.087)	0.16 (N/A-0.23)
NaC (g/L)	0.95 (0.89-1.07)	1.6 (1.4-1.8)
SDS (g/L)	0.57 (0.50-0.66)	1.5 (1.0-2.5)
Melittin (g/L)	$8.6 \cdot 10^{-3}$ ($N/A-1.0 \cdot 10^{-3}$)	$1.2 \cdot 10^{-3}$ ($N/A-2.6 \cdot 10^{-3}$)
Penetratin (mg/L)	-	-

Figure 4: Membrane perturbation by permeation enhancers. A) Degree of membrane perturbation of 0.6 nM liposomes by various small molecule permeations enhancers (left) and peptide permeation enhancer melittin (right) at a range of concentrations as detected by a calcein release assay after 30 min. A non-linear fit is shown (line) for each of the permeation enhancers. Shown are the average calcein release ± standard deviation (SD) for each permeation enhancer, with n≥3 B) Table of the EC50 and EC95 values used in this article, and their corresponding 95 % confidence interval (CI). C) Time dependent membrane perturbation. Degree of membrane perturbation of 0.6 nM liposomes by various permeation enhancers at the EC95 concentration (left) and the EC50 concentration (right) of the permeation enhancers over time as measured by calcein release. The signal was measured every 20 s. The graphs show one, representative, measurement of the calcein release kinetics for each permeation enhancer. For C10 the 'EC95' concentration was 21 g/L instead of 22 g/L.

3.2 Peptide drugs can influence the membrane activity of permeation enhancers

To investigate potential effects of coadministrating permeation enhancer and peptide drug, we biophysically characterized the permeation enhancers at their EC50 in the absence and presence of 300 mg/L of either of the peptide drugs.

We measured the calcein release from liposomes after 30 min incubation with a combination of 300 mg/L of peptide drug and permeation enhancer at their EC50 (Figure 5). Under these conditions, the peptide drugs on their own did not give rise to calcein release (Supplementary figure 2).

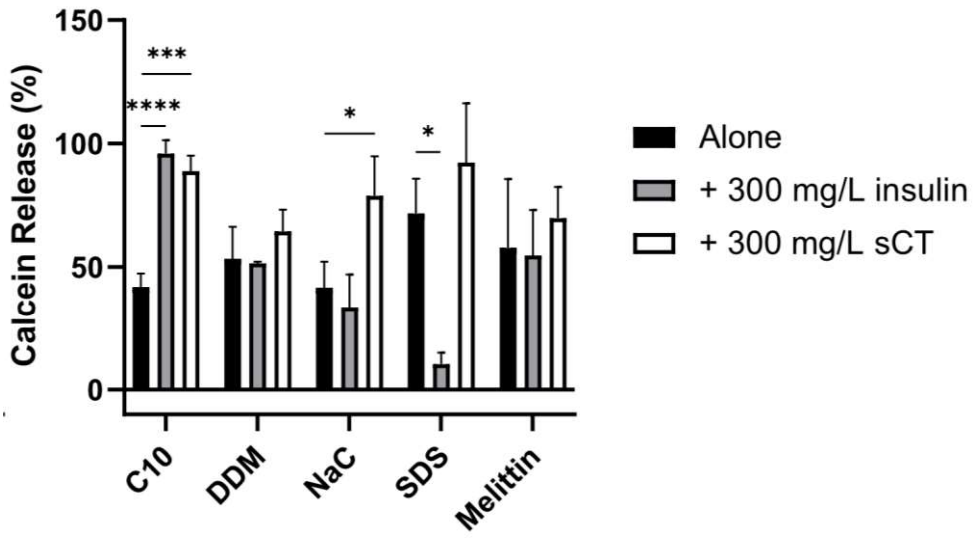

Figure 5: Membrane perturbation by peptide drugs:permeation enhancer combinations. Degree of Membrane perturbation of 0.6 nM liposomes by various peptide drug:permeation enhancer combinations at EC50 of the permeation enhancers after 30 min as detected by a calcein release assay. Significance levels were determined for the permeation enhancers with peptide drug relative to the permeation enhancers alone. ∗:p<0.05, ∗∗:p<0.01, ∗∗∗:p<0.001, ∗∗∗∗:p<0.0001. Shown are the average calcein release ± sd, with n≥3

For NaC with sCT and for C10 with each of the peptide drugs, the calcein release increased to the double. Oppositely, for SDS, hardly any calcein release was observed when incubated with insulin. For SDS alone and with sCT the calcein release is well above 50 % and subject to some uncertainty even though using the EC50. This may be a result of the calcein release reaction not being at steady state. Altogether, it is obvious that the effect of permeation enhancers can be influenced by the presence of the peptide drug desired to get across the lipid membrane.

3.3 Permeation enhancer self-association

Permeation enhancers often have a hydrophobic part which can lead to a hydrophobic driven self-association forming larger structures, e.g. micelles or vesicles (Figure 3B) [13], [27], or lead to interaction with the hydrophobic part of lipid membranes. As part of elucidating the mechanism behind the observed effect of the presence of peptide drugs on the membrane perturbation by permeation enhancers, we therefore characterized the permeation enhancers with respect to hydrophobic driven self-association and mechanism of membrane perturbation under the conditions used here.

Nile Red is a hydrophobicity marker, which fluoresce upon binding to hydrophobic regions [28]. It has been used to detect the formation of micelles by binding to the hydrophobic core of the micelles, hence to determine the critical micelle concentration (CMC) [29]. In a permeation enhancer perspective, the CMC provides information about the maximum concentration of free (non-micellar) monomers. It is generally considered to be the monomer that interacts with the membranes [3], and the micelles are considered to function as a reservoir, from which monomers inserted into the lipid membrane can be replaced, keeping the monomer concentration at the maximum concentration even upon insertion of monomers into the lipid membrane. Nile Red was added to a range of permeation enhancer

concentrations (Figure 6A). For the small molecule permeation enhancers, a large Nile Red fluorescence intensity signal was observed for C10, DDM, and SDS. The Nile Red fluorescence intensity increased with increasing permeation enhancer concentrations, starting just above EC50 (DDM, above 0.08 g/L) or just below EC50 (C10, around 2.5 g/L and SDS, above 0.15 g/L). For NaC, however, the increase in Nile Red fluorescence was only observed for the highest concentration (5 g/L), which is well above EC95 (1.6 g/L) for NaC. Self-assembly above a certain threshold for C10, DDM, SDS, and NaC can thus be inferred from the increase in Nile Red fluorescence intensity. For melittin and penetratin, no increase in Nile Red fluorescence intensity was observed. Thus, at EC50 the permeation enhancers with an acyl chain self-assemble into larger structures.

To further characterize the self-assembled structures for C10 and SDS, and to be aware of any non-hydrophobically driven structures, DLS was measured for each of the permeation enhancers at their respective EC50 (Figure 6B, Supplementary figure 3, and Figure 7A).

It became evident that C10 formed large, heterogeneous structures. The majority of these (from a number-based size distribution analysis) had a size of 71 nm, corresponding to medium-sized vesicles. Other studies have likewise found C10 to form heterogeneous vesicles above a critical vesicle concentration in the same range for similar conditions [27], [30]. SDS formed well-defined structures of around 5 nm, which shows that in this set-up SDS forms micellular structures that are similar in size to a previous report for SDS in aqueous buffer [31]. The micelle formation initiate at concentrations (0.15 g/L), which is a bit below the CMC of 0.3 g/L for SDS in 125 mM NaCl reported elsewhere [29]. DDM formed larger structures, the majority of around 29 nm, which could be either a micelle or a vesicle. The formation of large DDM structures at concentrations above 0.08 g/L in the minSIF buffer is consistent with the CMC in water being 0.09 g/L [32]. The size of the DDM structures, however, is much larger than the sizes reported in the literature for DDM which are around 7 nm in buffers with pH and osmolality in the same range [33], [34]. Taking the low EC50 of DDM into account, the discrepancy may be due to the concentration dependent difficulty of detecting small species when using DLS. Thus, while it may be the case that DDM form very different structures in minSIF than in a variety of other aqueous solutions, the discrepancy may rather be due to a lack of detection and that two populations with different sizes (2.9 nm and 29 nm) are present.

For penetratin, a small, but consistent signal corresponding to structures of 1.0 nm was observed (A). This is consistent with penetratin being on monomeric form (Protein Data Bank (PDB) structure 1KZ0). No signal for NaC and melittin was detected at their EC50, which implies that they were too small for detection using DLS at the given concentrations. Consistent with the Nile Red data, which report NaC to form very small micelles consisting of just 3-8 molecules [35], NaC thus appears not to be self-assembling into larger structures at EC50 and EC95. For melittin, a monomeric state or small oligomeric state is consistent with literature, as melittin has been reported to exist as monomers under similar conditions as these [36].

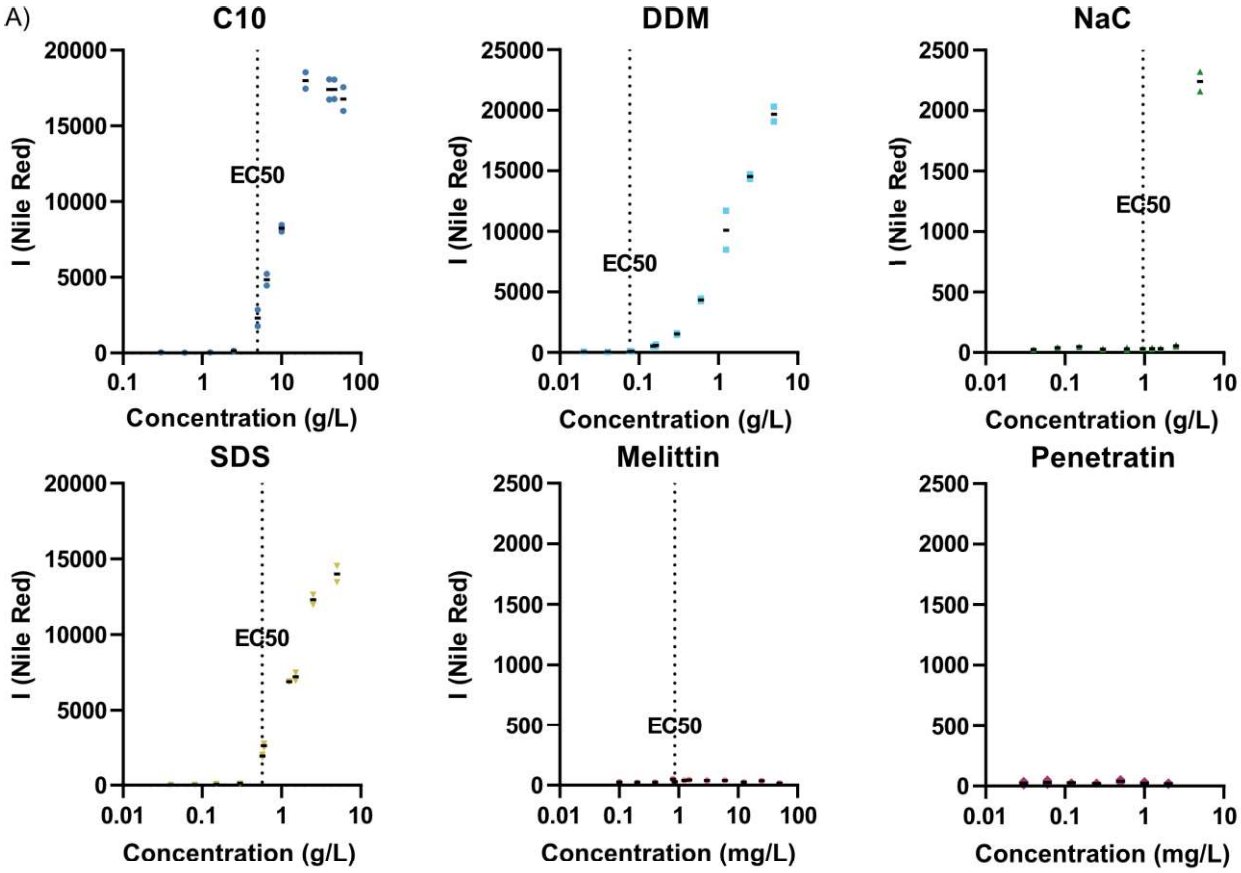

B)

Permeation enhancer	Size ± SD
C10	371 ± 253 nm
DDM	29 ± 6 nm 231 ± 97 nm
NaC	-
SDS	5 ± 1
Melittin	627 ± 153 nm
Penetratin	1 ± 0.2 nm

C)

Permeation enhancer	Liposomes Size
No	134 ± 32 nm
C10	4 ± 1 nm 223 ± 68 nm
DDM	44 ± 23 nm 158 ± 67 nm
NaC	137 ± 44 nm
SDS	142 ± 42 nm 5 ± 1 nm
Melittin	133 ± 34 nm
Penetratin	138 ± 39 nm

Figure 6: Characterization of permeation enhancers. A) Fluorescence of the hydrophobicity marker Nile Red, in the presence of various permeation enhancer concentrations. EC50 of each permeation enhancer is indicated with a dotted line. The measurements were carried out in duplicates, and the intensity for each measurement is shown B) The size ± SD of permeation enhancers as determined by DLS using the intensity based distribution analysis. Sizes corresponding to the signal observed from the buffer are not listed here. The data is shown in Supplementary figure 3. C) The size of the liposomes alone and in the presence of permeation enhancers at a permeation enhancer concentration of EC95 as determined by DLS using the intensity based distribution analysis (See Supplementary figure 4). For DLS, three technical replicates were carried out on a duplicate of samples.

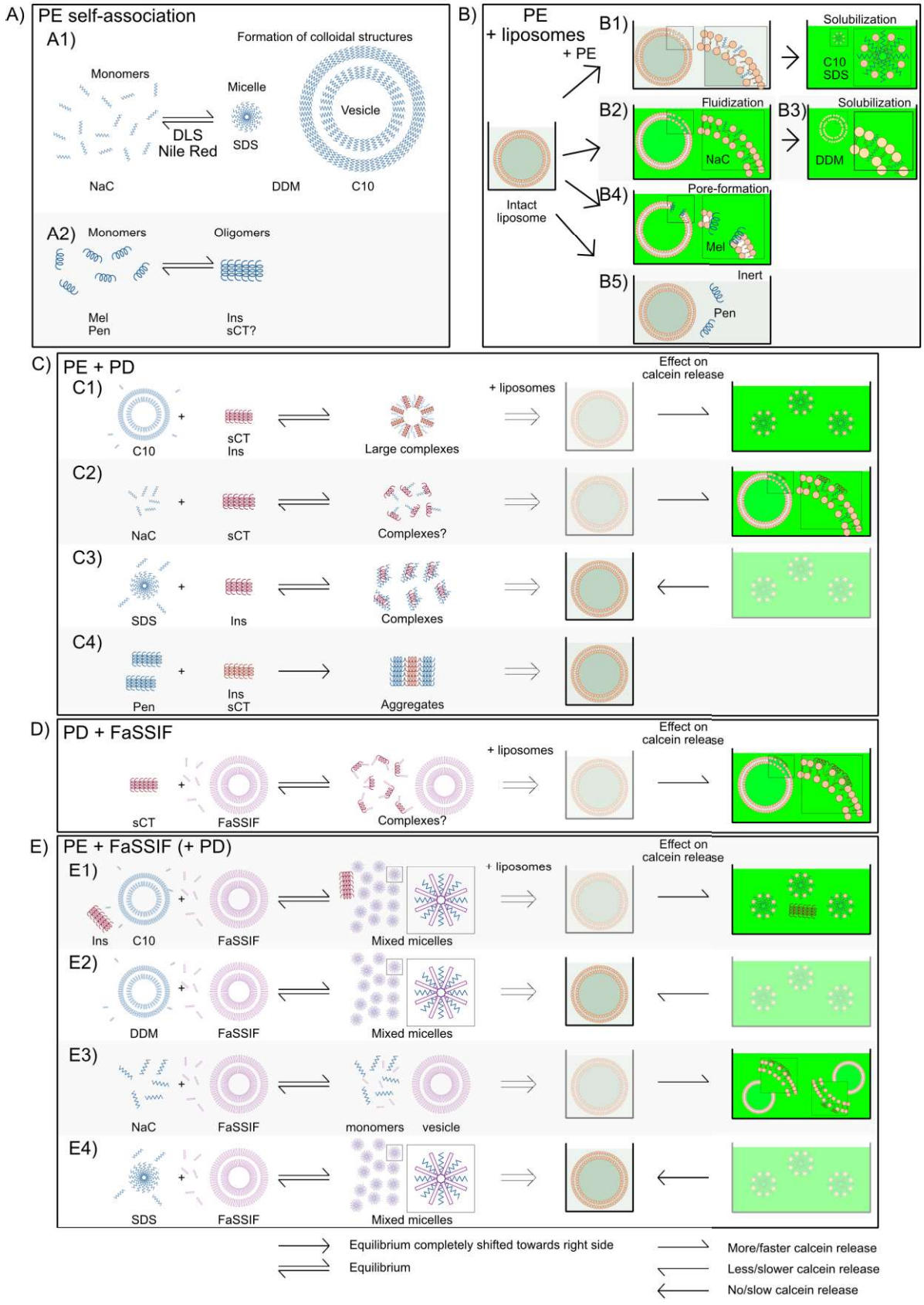
A)
PE self-association
A1)
Formation of colloidal structures
Monomers
Micelle
Vesicle
DLS
Nile Red
SDS
NaC
DDM
C10
A2)
Monomers
Oligomers
Mel
Pen
Ins
sCT?
B)
PE
+ liposomes
+ PE
B1)
Solubilization
C10
SDS
B2)
Fluidization
NaC
B3)
Solubilization
DDM
Intact
liposome
B4)
Pore-formation
Mel
B5)
Inert
Pen
C)
PE + PD
C1)
C10
sCT
Ins
Large complexes
+ liposomes
Effect on
calcein release
C2)
NaC
sCT
Complexes?
C3)
SDS
Ins
Complexes
C4)
Pen
Ins
sCT
Aggregates
D)
PD + FaSSIF
sCT
FaSSIF
Complexes?
+ liposomes
Effect on
calcein release
E)
PE + FaSSIF (+ PD)
E1)
Ins
C10
FaSSIF
Mixed micelles
+ liposomes
Effect on
calcein release
E2)
DDM
FaSSIF
Mixed micelles
E3)
NaC
FaSSIF
monomers
vesicle
E4)
SDS
FaSSIF
Mixed micelles
Equilibrium completely shifted towards right side
Equilibrium
More/faster calcein release
Less/slower calcein release
No/slow calcein release

Figure 7: Overview figure of what happens. A: Self-association at EC50: A1: Self-association of permeation enhancers can lead to micelles or vesicles, A2: Self-association of peptides can lead to formation of oligomers. Indicated are the proposed state of each permeation enhancer at EC50. B: Proposed permeation enhancer interactions with liposomes: B1: C10 and SDS insert into the lipid bilayer and lead to calcein release upon solubilization, B2): DDM inserts into the lipid bilayer and further solubilizes the liposomes. Both processes lead to calcein release, B3: NaC leads to calcein release upon insertion into the lipid bilayer, B4: melittin leads to calcein release upon insertion into lipid bilayer as pores, B5: penetratin does not influence the liposomes (liposome + penetratin as is). C: Proposed permeation enhancer-peptide drugs interactions and their influence on membrane perturbation: C1: C10 changes colloidal structure in the presence of sCT or insulin, and form vesicles with the peptide drug inserted, from which an increased amount of C10 is inserted into the lipid bilayer. This leads to slightly increased calcein release, C2: NaC and sCT form a complex which inserts into the lipid bilayer leading to increased calcein release, C3: SDS and insulin form a complex from which SDS is not inserted into the lipid bilayer and does thus not lead to calcein release, C4: Penetratin form large aggregates with insulin and sCT, none of which lead to calcein release. D: Proposed interactions of peptide drugs in FaSSIF: sCT and taurocholate form a complex which inserts in the lipid bilayer leading to calcein release. E: Proposed interactions of permeation enhancers in FaSSIF: E1: C10 and FaSSIF components form mixed micelles, both in the absence and presence of insulin. From these micelles more C10 is inserted into the lipid bilayer, and thereby enhances the degree of solubilization of and calcein release from liposomes, E2: DDM and FaSSIF components form mixed vesicles from which DDM do not insert into the lipid bilayer and thus do not lead to calcein release, E3: NaC and taurocholate both inserts into the lipid bilayer, leading to an additive effect of membrane perturbation. E4: SDS and FaSSIF components form mixed micelles from which SDS do not insert into the lipid bilayer and thus do not lead to calcein release.

3.4 Permeation enhancer interactions with lipid membrane

Multiple mechanisms of action exist for membrane perturbation by permeation enhancers including pore formation [37], and functioning as detergents [3]. Detergents insert as monomers into the lipid bilayer until the liposomes are saturated, above which concentration mixed phospholipid-detergent micelles will begin to form, thereby solubilizing the membrane [38] (Figure 3A, left).

To investigate the integrity of the liposomes (with respect to size), we measured DLS of the liposomes in the presence of each of the permeation enhancers (Figure 6C, Supplementary figure 4). To focus on the species subsequent to the reaction, permeation enhancer were added at their respective EC95.

Incubation of the liposomes with NaC, melittin, and penetratin did not give rise to any change in the signal. Two sizes were calculated from the measurements of liposomes in the presence of SDS. These did not differ from the size of liposomes and SDS alone. Nonetheless did the overall signal decrease for liposomes in the presence of SDS compared to that for liposomes alone (Supplementary figure 4), clearly indicating a decrease in the number of intact liposomes. The size of the major number of species for liposomes in the presence of C10 and DDM changed dramatically from 134 nm for bare liposomes to 4.2 nm for C10 and to an average of 44 nm for DDM, albeit the reacted solution was very heterogeneous for liposomes in the presence of DDM.

The decrease in the number of liposomes together with rather long time for the plateau of calcein release to be reached for C10, DDM, and SDS (compared to for NaC and melittin), clearly indicate that C10, DDM, and SDS solubilize the liposomes; for C10 and SDS forming small, distinct structures and for DDM forming larger, yet clearly reorganized, structures. The overall structure of the liposomes are unaffected and thus considered intact for NaC, melittin, and penetratin.

3.4.1 Solubilizing permeation enhancers

The permeation enhancers that self-assemble forming hydrophobic interactions, also solubilize the lipid membranes of the liposomes. Inspection of overlays of the Nile Red signal with the calcein release (Supplementary figure 5) further reveals that for C10 and SDS, concentration dependence of the calcein release correlates with the concentration dependence of the self-assembly. The membrane perturbation

thereby appears to be highly dependent on a consistently high monomer concentration. With the plateau of calcein release in mind, it can thus be inferred that insertion of C10 and SDS in itself do not lead to membrane perturbation, but rather that solubilization is a requirement for membrane perturbation (Figure 7B1), and that this solubilization occurs only at high monomer concentrations. This is consistent with literature for C10, which shows that C10 increase membrane fluidity only above CMC (6), and consistent with a few liposomes being left intact in the presence of SDS.

For DDM, taking the sigmoidal curve of the release kinetics into consideration, it appears that the membrane perturbation by DDM has a different nature than for C10 and SDS. It may be that insertion of DDM monomers into the lipid bilayer leads to a membrane perturbating, calcein releasing, local rearrangement of the lipids (the initial phase with a slow, steady increase in calcein release). Subsequently, at sufficiently high concentrations, DDM may then solubilize the liposomes (the later phase with a fast increase in calcein release) (Figure 7B3). The calcein release in the initial phase would thus correlate to the monomer release from the DDM vesicles, rather than on the concentration of DDM inserted required for solubilization. Inspection of the Nile Red and calcein release overlay reveals that calcein release and self-assembly occurs above the same, low, concentration. Yet, an increase in calcein release at lower concentrations than the concentrations that led to increasing self-assembly into large structures was observed. This may be explained by a lower CMC value for DDM:phospholipid vesicles than for pure DDM vesicles, shifting the equilibrium between free DDM and vesicle-bound DDM towards more free DDM upon the formation of mixed DDM:phospholipid vesicles.

3.4.2 Non-solubilizing permeation enhancers

NaC do not form large micelles at the relevant concentrations, nor solubilize the lipid membrane. Yet, NaC is known to fluidize the membrane [3], and it thus indicates that the insertion of NaC into the membrane leads to a membrane perturbating local rearrangement of the lipids, resulting in calcein release (Figure 7B2). The lack of solubilization for melittin is consistent with melittin being known from the literature to form pores [37]. The lack of solubilization by penetratin is not surprising taking the lack of membrane perturbation into consideration, and this is consistent with the literature, where penetratin is known to translocate across the lipid membrane without perforating the lipid bilayer in some studies [14].

3.5 Permeation enhancer and peptide drug interactions

To elucidate whether the nature of the above found differences in membrane perturbation in the absence and presence of peptide drugs, were due to structurally changing permeation enhancer:peptide drug interactions, we measured the apparent hydrodynamic diameter of the permeation enhancers and peptide drugs in solution using DLS (Figure 7C, Figure 8A). We further investigated whether any complexation was hydrophobically driven, using the Nile Red assay (Figure 8B). Under the conditions used, measured using DLS, sCT had a hydrodynamic diameter of 3.3 nm ± 0.6 nm, as detected using a concentration of 600 mg/L, and insulin a hydrodynamic diameter of 4.9 nm ± 1.5 nm (Supplementary figure 6). For sCT this size correspond to the length of the monomeric structure of sCT (PDB structure 2GLH), but may also represent a small oligomer due to the rod-like shape of the monomer. For insulin, this size correspond to the largest distance in an insulin hexamer (PDB structure 1ZNI). No Nile Red signal above the background noise was detected for sCT, and a small signal was observed for insulin, thereby supporting the characterization using DLS.

3.5.1 C10 with peptide drugs

For C10 with sCT the calcein release was close to 100 %, almost the double of that for C10 alone at EC50 (Figure 5). Inspection of the DLS data revealed smaller structures than for the C10 alone and no structures with a size corresponding to sCT alone (Figure 8A, Supplementary figure 6). The structures for C10 in the presence of sCT appeared more homogeneous, and the intensity was larger than for the C10 vesicles alone, despite the smaller size (Supplementary figure 6). The Nile Red signal was almost double for C10 in the presence of sCT, indicating the presence of a larger hydrophobic area. From this, it can be suggested that sCT led to a hydrophobically driven change of the colloidal structure of C10, possibly by the formation of a mixed C10:sCT structure (Figure 7C1). Recalling that the membrane perturbation appears to be highly dependent on a continuous high monomer concentration, the increased membrane perturbation in the presence of sCT may thus have shifted the equilibrium towards a higher free monomeric concentration.

The colloidal structure of C10 is known to be highly dependent on the ionization state of C10 [27], [39]. Furthermore, it has been proposed that it is the ionized form of C10 that has surfactive, membrane active, properties [30], and the charge at pH 6.7 is negative. Despite the low ratio of sCT to C10 (1 sCT to 430 C10 molecules at EC50 of C10), the change in apparent colloidal structures could be caused by the cationic charge of sCT at the present pH as well as the formation of mixed C10:sCT vesicles. Thus, changes in the colloidal structures of C10 in the presence of sCT may involve electrostatic interactions.

Also for C10 with insulin was the calcein release close to 100 % (Figure 5). Due to the inhomogeneity of the C10 vesicles on their own and overlaps of peaks, made it difficult to deduce any changes in average sizes of C10 when in the presence of insulin from the DLS data. Nonetheless, did the particles present in the sample appear more homogeneous, which may infer some kind of colloidal change (Supplementary figure 6). No sizes corresponding to insulin alone could be extracted, possibly due to the signal being dominated by the intensity from the larger structures (Figure 8, Supplementary figure 6). No difference between the Nile Red signal for C10 in the absence or presence of insulin could be detected (Figure 8B). This suggests that the presence of insulin, as for sCT, influence the colloidal structure of C10, albeit in a different manner that is not driven by a hydrophobicity increase (Figure 7C), Furthermore, the signal corresponding to a structure with a size of around 9 nm indicate that C10 and insulin may form small complexes together. While the mechanism of complexation of C10 and insulin appears not to lead to a higher hydrophobic region, and is thus different from that of C10 and sCT, it may be that the apparent reorganization of C10 accompanying the complexation with insulin, like for C10 with sCT, lead to a higher monomer concentration of C10. This may be due to a higher CMC, or C10 being ‘drawn’ out of the C10 vesicles (Figure 7C).

3.5.2 NaC with peptide drugs

For NaC with sCT the calcein release is close to 100 %, almost the double of that for NaC alone at EC50 (Figure 5). However, inspection of both DLS data and Nile Red signals show no differences from that of NaC and sCT alone (Figure 8). NaC and sCT thus do not form any larger structures. Rather, at 600 mg/L sCT and NaC, at EC50, a fit to the data gives a size of 2.4 nm, rather than the 3.3 nm for 600 mg/L sCT alone (Supplementary figure 6). While this is on the limit of what can reasonably be detected by DLS, it confirms the absence of large complexes, and rather indicates that if any interaction happens, it may break any small sCT oligomer. NaC is negatively charged and sCT has an overall positive charge, it is possible that

NaC and sCT interact in a charge driven manner, forming small distinct complexes (Figure 7C2). This is further enabled by the lack of self-assembly by NaC, leaving it free to react as a monomer. Considering such a complex, we speculate that the NaC:sCT complex function similar to an lipidation of sCT (Figure 7C2). This would explain the higher amount of calcein release as compared to that of NaC alone, as it has been shown that some lipidated sCT permeabilize similar lipid membranes [40].

For NaC and insulin no change in calcein release was observed compared to that for NaC alone (Figure 5), just as the DLS signal and Nile Red signal did not differ from that of the signals for NaC and insulin alone (Figure 8). Thus, we did not detect any interactions between NaC and insulin in our study.

3.5.3 SDS with peptide drugs

For SDS with insulin, hardly any calcein release was observed, as opposed to for SDS alone (Figure 5). Inspection of the DLS data shows that the hydrodynamic diameter for SDS and insulin together is similar to that of SDS and insulin (Figure 8A, Supplementary figure 6). The Nile Red signal was slightly, but significantly ($p=0.03$), larger than for SDS and insulin alone (Figure 8B). Nonetheless, from the lack of calcein release in the presence of insulin, it is clear that the presence of insulin does affect the membrane perturbation of SDS. SDS are known to undergo hydrophobic ion pairing with oppositely charged amino acid side chains [41] and as insulin also has positively charged amino acid residues, this may also be the case for SDS and insulin in this case. Such an SDS:insulin interaction would decrease the availability of SDS for solubilization of the lipid membrane, and thereby explain the observed lack of calcein release.

For SDS with sCT, the calcein release is well above 50 % and subject to some uncertainty, as is it for SDS alone, despite using SDS at EC50 (Figure 5). Inspection of both DLS data and Nile Red signals show no differences from that of SDS alone (Figure 8) (no DLS signal for sCT is observed, but the signal from sCT is easily masked by larger structures such as that from SDS), suggesting that no SDS and sCT complexes are formed. Instead, the slightly higher calcein release for SDS with and without sCT and the high uncertainty is rather considered a result of the calcein release reaction not being at steady state for SDS. It is noteworthy that SDS, contrary to NaC, do not interact with sCT, which underlines that permeation enhancer:peptide drug interactions are not solely due to charges.

3.5.4 Other combinations

For DDM and melittin in the presence of sCT the calcein release there was no significant difference from the calcein release for DDM alone. Still, it appeared slightly higher than for the permeation enhancers alone (Figure 5). The size of DDM and melittin with sCT cannot easily be determined from DLS data, but the signal intensity increased and there was an absence of signal corresponding to sCT (Figure 8, Supplementary figure 6), which can be due to some degree of complexation. For DDM and sCT the Nile Red signal was slightly larger than for each of them alone, further indicating some kind of DDM:sCT complexation. While the DLS data indicates that some complexation between melittin and sCT may have occurred, the Nile Red signal seemingly was unaffected (Figure 8B).

For both DDM and melittin the differences are small and the nature of the complexation difficult to assess. As the effect on the calcein release is likewise insignificant, the potential complexation of DDM and sCT and of melittin and sCT will not be characterized further.

Penetratin did not give rise to calcein release on its own nor in the presence of insulin or sCT (Figure 5). The lack of calcein release by penetratin is consistent with literature [42] and that penetratin functions as a cell-penetrating peptide that without perforation of the membrane passes through the membrane [14]. The size measured for the mixture of penetratin and insulin and the corresponding intensity using DLS were very high, indicating formation of large aggregates (Figure 7C4, Figure 8A). This confirms the results of a similar experiment by Kristensen et al. [16]. The aggregation is only minorly associated with an increase in Nile Red signal (Figure 8B), and thus the hydrophobic area, and the interaction should therefore not be considered to be hydrophobically driven. Rather, as the overall charge of insulin and penetratin in this study has been calculated to be -1.7 and +8.0, respectively, the interaction may be charge driven. To test this, we utilized that insulin at 600 mg/L visually precipitates in the presence of as little as 7 mg/L penetratin. At 1 M NaCl, 10 mM phosphate, no visual precipitation was observed. The data thus clearly indicate a charge-driven interaction, consistent with the findings by Kristensen et al. [16].

For penetratin and sCT, the data could be fitted to two populations, corresponding to both the sCT monomer and a larger complex (Figure 8A), which logically corresponds to a penetratin:sCT complex. As the signal from sCT is easily masked, and decreases in sCT concentration would make its detection even more difficult, it can be inferred from the presence of the sCT signal that the concentration of sCT is not remarkably decreased. It can thus be inferred that only a small fraction of sCT complexate with penetratin. No difference in Nile Red signal from the penetratin and sCT alone is observed for the complex. This may be due to the low degree of complexation, and no information about the driving force of an sCT:penetratin complexation can thus not be deduced. An potential explanation could be aggregation in a charge-driven manner despite the overall charge being positive for both peptides, as sCT does have negative charges. This would, however, be to a lower extend than for penetratin and insulin due to charge-charge repulsions.

No other effects on calcein release or permeation enhancer:peptide drug complexes was identified using the DLS and Nile Red assays.

A)

Permeation enhancer	+ insulin 5 ± 1 nm 22 ± 4 nm	+ sCT 3 ± 1 nm
C10 371 ± 253 nm	179 ± 110 nm 9 ± 2 nm	196 + 108 nm
DDM: 29 ± 6 nm; 231 ± 97 nm	354 ± 124 nm 178 ± 34 nm 20 ± 7 nm	168 ± 65 nm 40 ± 10 nm
NaC N/A	4 ± 1 nm 24 ± 3 nm	3 ± <1 nm 43 ± 8 nm
SDS 5 ± 1 nm	6 ± 1 nm	6 ± 1 nm 220 ± 119 nm
Melittin 627 ± 153	5 ± 1 nm	444 ± 77 856 ± 188
Penetratin 1 ± <1 nm	803 ± 166 nm	41 ± 11 nm 3 ± <1 nm

B)

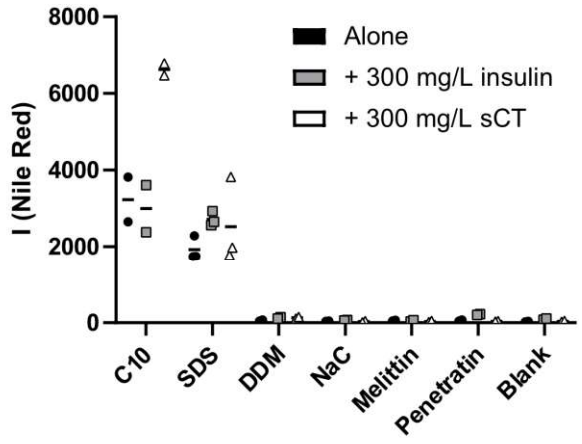

Figure 8: Permeation enhancer:peptide drug interactions. A) Sizes ± SD of permeation enhancer:peptide drug combinations as determined using DLS using an intensity based size distribution. Sizes corresponding to the signal from the buffer are not listed. Three technical replicates were carried out on two duplicate samples. B) Fluorescence of the hydrophobicity marker Nile Red of the permeation enhancers alone and in the presence of the peptide drugs insulin and sCT. The intensity for each measurement is shown, with n≥2.

3.6 Membrane perturbation in fasted state simulated intestinal fluids

The studies above have been carried out in minSIF buffer. However, many components are present in the intestinal buffer, including phospholipids and bile acids. Both bile acids and phospholipids are able to form micelles. As this could potentially have great impact on the interaction between permeation enhancers, peptide drugs and lipid membranes, we here studied the abovementioned interactions in FaSSIF, which contains 3 mM of the bile acid taurocholate and 0.75 mM phospholipids.

Melittin and penetratin both visually precipitated at concentrations to be used to carry out the experiments (around 1 mg/L for melittin and 1.5 mg/L for penetratin). As both melittin and penetratin are highly positively charged at pH 6.7 (+6 and +8, respectively) and taurocholate is negatively charged (-1), the precipitation may be due to charge-charge interactions. Further analysis of melittin and penetratin in FaSSIF were not included in the further work. All other permeation enhancers and peptide drugs remained soluble.

We measured calcein release after 30 min at their respective EC95 and at their respective EC50 for membrane perturbation in minSIF in the absence and presence of the insulin or sCT in FaSSIF (Figure 9). Under these conditions, the liposomes remained intact and did not give rise to any calcein release on their own (Supplementary figure 7). We thus established that it is possible to measure calcein release on POPC:Chol (9:1) liposomes in FaSSIF.

We measured the size of the structures of FaSSIF in the absence and presence of the permeation enhancers at their respective EC50 after 30 min incubation (Figure 9B, Supplementary figure 8). Under these conditions, analysis of the DLS signal for the FaSSIF revealed the presence of very uniform structures with a hydrodynamic diameter of 46 nm ± 10 nm. It thus appears that the taurocholate and the phospholipids form mixed micelles in our set-up.

3.6.1 sCT in FaSSIF

Generally, we found that the amount of calcein release was affected by the presence of bile acids and phospholipids. Firstly, it should be noted that sCT gave rise to calcein release on its own in FaSSIF (Figure 9A). The FaSSIF contains taurocholate, which has a structure similar to that of NaC. The most significant differences are the presence of an amide group and a sulfonate group instead of a carboxylate (Figure 2A and Figure 10). Hence, an obvious explanation for the induced membrane permeability by sCT is that taurocholate interacts with sCT in a manner similar to that of NaC (Figure 7C2, Figure 7D).

3.6.2 C10 in FaSSIF

For C10 at EC95 close to 100 % calcein was released, and no effects could be deduced from this alone (Figure 9A). For C10 in FaSSIF at EC50, the calcein release was just above 50 %, yet, while being a small difference from the amount of calcein released by C10 in minSIF, the difference was significant. DLS measurements of C10 in FaSSIF showed the presence of structures of micellar size (5 nm ± 1 nm) (Figure 9B). The presence of only one population, differing from either of the C10 vesicles and the FaSSIF component vesicles point towards C10 and FaSSIF components forming common mixed micelles . Together with the slight increase in calcein release, this is consistent with the findings by Lapré et al. that

the lytic activity is higher for C10 in mixed micelles with cholate than on its own [43]. The concurrent presence of C10 and FaSSIF components thus changed the colloidal structure of C10, which likely changed the concentration of ionized C10 monomers available for insertion into the lipid bilayer of the liposomes, thereby causing the higher calcein release (Figure 7E1). Furthermore, for C10 and insulin together in FaSSIF, the calcein release was the same as for C10 alone in FaSSIF, contrary to the calcein release in minSIF. This indicates that the C10:insulin structures found upon incubation in minSIF did not form in FaSSIF. A similar weakening of the interaction of C10 with peptide drug in FaSSIF was observed for exenatide [44]. For C10 with sCT the calcein release was close to double of that for C10 alone. Yet it cannot be determined from these data whether this increase was due to the formation of the C10:sCT complex as found in minSIF (Figure 7C1), or if it was an additive effect of C10 and sCT, separately, in FaSSIF (Figure 7D and Figure 7E1).

3.6.3 DDM in FaSSIF

For DDM, the calcein release was lower in FaSSIF than in minSIF at its EC95 (Figure 9A) as well as at its EC50 in the absence and presence of insulin, albeit not significant. From an inspection of the DLS data (Figure 9B, Supplementary figure 8), it was evident that structures larger than each of DDM and FaSSIF components on their own were present. It can thus be inferred that DDM was incorporated into a mixed micelle with the FaSSIF components (Figure 7E2). It is likely that DDM was retained in the mixed micelles and that this was the nature of the lower degree of calcein release. Some calcein is however released, which could very well be due to DDM inserted into the lipid bilayer of the liposome to a lesser extend, thus not leading to the solubilization of the liposomes (Compare Figure 7E2 and Figure 7B3).

DDM with sCT in FaSSIF led to less calcein release than DDM with sCT in minSIF and less than for sCT in FaSSIF alone, but more than for DDM in FaSSIF alone. This points towards less of the sCT:FaSSIF component complexes (Figure 7D) being available for membrane perturbation in the presence of DDM, possibly due the FaSSIF components being associated with DDM instead (Figure 7E2).

3.6.4 SDS in FaSSIF

SDS in FaSSIF did not lead to calcein release, neither at EC95, at EC50, nor in the presence of insulin (Figure 9A). Inspection of the DLS results (Figure 9B, Supplementary figure 8) reveals the presence of structures larger than the SDS micelles, but much smaller than the FaSSIF component micelles, clearly showing that mixed SDS:FaSSIF component micelles had been formed. Assuming these micelles are largely favorable for SDS, this minimizes the SDS available for membrane perturbation (Figure 7E4). Due to the apparent all-or-none membrane perturbation mechanism, minor changes in concentrations can have a great impact on degree of membrane perturbation.

For SDS and sCT, less calcein is released than for the sCT alone. Taking the assumed stability of the SDS:FaSSIF component micelles into considerations, this is most likely due to less FaSSIF components being available to interact with sCT (Figure 7D) as suggested for DDM and sCT.

3.6.5 NaC in FaSSIF

All tested solutions with NaC in FaSSIF gave rise to full calcein release (Figure 9A). An inspection of the DLS results showed that the FaSSIF component micelles were not affected by the presence of NaC (Figure 9B, Supplementary figure 8) with respect to size. However, NaC and the FaSSIF component taurocholate contain the same steroid core structure (Figure 2, Figure 10) and are, consequently, likely to interact in similar manners. A possible explanation of the full calcein release is thus that cholate and taurocholate had an additive effect (Figure 7E3). While the taurocholate and phospholipids on their own do not permeabilize the liposomes at the given concentrations within the given time, the NaC is already at a concentration where membrane perturbation occur, and any minor additions of similar functioning molecules will thus increase the membrane perturbation. It is possible that such a contribution stems from the small amount of non-micellar taurocholate being present due to the inherent equilibrium between monomeric taurocholate and micellar taurocholate.

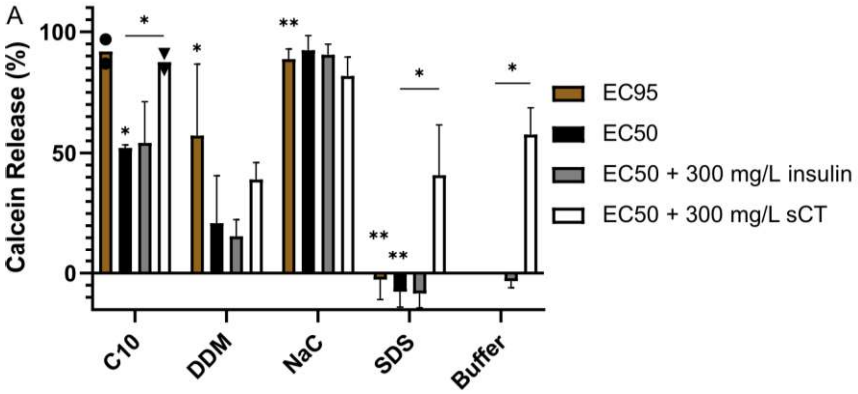

B

Permeation enhancer	FaSSIF Size ± SD
No	46 ± 10 nm
C10 371 ± 253 nm	5 ± 1 nm 484 ± 249 nm
DDM 29 ± 6 nm	66 ± 17 nm
NaC -	49 ± 13 nm
SDS 5 ± 1 nm	7 ± 2 nm

Figure 9: Permeation enhancers in FaSSIF. A) Membrane perturbation of 0.6 nM liposomes in FaSSIF by permeation enhancers at their EC95, their EC50, and their EC50 with the peptide drugs insulin and sCT. Significance levels are shown for the permeation enhancers alone in FaSSIF compared to in minSIF (no line), and for permeation enhancers in the presence of peptide drugs (with line below the significance stars). P-values were determined using unpaired t-test with Welch's correction, ∗ :p<0.05, ∗∗ :p<0.01. For C10, the calcein release for each sample is shown, with n≥2, for all other permeation enhancers, the average calcein release ± SD is shown, with n≥3.. B) Sizes ± SD of main species in FaSSIF without and with permeation enhancers as measured using DLS. The sizes ± SD of the permeation enhancers in minSIF are also stated. DLS measurements were carried out as three technical measurements on a duplicate of samples.

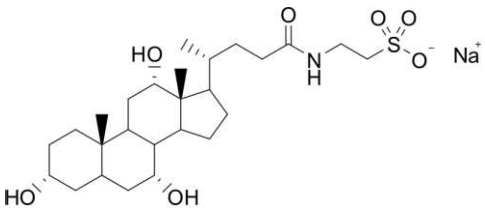

Figure 10: Chemical structure of taurocholate

4 Conclusion and perspectives

Absorption of orally delivery peptide drugs in the gastrointestinal tract is generally hindered by the inability of the peptide drugs to cross the layer of epithelial cells [45], [46]. Many studies utilize permeation enhancers that induce membrane perturbations [3] or cell penetrating peptides that

spontaneous translocate across the lipid bilayer with the peptide drug as cargo [47] to increase the translocation of peptide drugs across the lipid bilayer. Components of the intestinal fluid such as bile acids and phospholipids are known to influence the various equilibria of permeation enhancers with a detergent-like function [11]. While it is known that many factors influence the permeation enhancers, the mechanistic impact of the presence of peptide drugs is rarely studied.

We hypothesized that the peptide drugs and permeation enhancers mutually affect each other, and that the equilibrium of these interactions can be influenced by the presence of bile acids and phospholipids. We therefore investigated the permeation enhancers C10, NaC, DDM, SDS, SNAC, melittin, and penetratin in the absence and presence of the peptide drugs insulin and sCT. We focused on self-assembling and peptide drug interactions of permeation enhancers, how these interactions affected interactions with the membrane, and if such effects were altered in FaSSIF. To do this we established POPC:Cholesterol (9:1 molar ratio) as a model system suitable for the testing membrane perturbations and self-assembley both in minSIF and in FaSSIF.

We show that under the conditions tested here, some permeation enhancers and peptide drugs do indeed mutually affect each other, and we elucidate the underlying mechanisms. For the permeation enhancers studied, at least two different mechanisms of membrane perturbation of POPC:Cholesterol liposomes exist: membrane perturbation by insertion into the lipid bilayer and membrane perturbation concurrent with solubilization. NaC and melittin appeared to enhance membrane perturbation by insertion into the lipid bilayer alone. C10 and SDS required concentrations that also gave rise to self-assembly and solubilization, and solubilizaton thus appeared to be a requirement for their membrane perturbation. Membrane perturbation by DDM appeared to be two-staged, with both of the above mentioned mechanisms playing a role.

We show that the membrane perturbation by C10 and SDS is highly influenced by peptide drug interactions and the accompanying changes in colloidal structures that increase the membrane perturbation for C10 in the presence of peptide drugs, and decrease it for SDS in the presence of insulin. All three solubilizing permeation enhancers interact with FaSSIF components, likely forming mixed micelles or vesicles. For C10 the membrane perturbation is only minorly affected by the formation of mixed C10:FaSSIF micelles but the mixed micelles appears to shield C10 from interactions with peptide drugs. The formation of mixed micelles or vesicles for SDS and DDM decreases the membrane perturbation, more so for SDS than for DDM. The decrease is likely due to retention of SDS and DDM, thereby leading to a lower concentration of available monomer. For SDS this effect is more pronounced for the interaction with FaSSIF components than for insulin.

NaC is a bile acid similar in structure to the bile acid, taurocholate, but where only NaC induces membrane perturbations in the concentrations used here, the presence of taurocholate appears to enhance the effect of NaC, probably by a mechanism similar as that of NaC. Both NaC and taurocholate appears to interact with sCT and form very small complexes, which induces membrane activity of sCT, likely by mimicking lipidation of sCT.

Penetratin form large aggregates with both insulin and sCT in minSIF. It is thus possible that penetratin is able to function as a permeation enhancer for sCT through non-covalent complexation as it is for insulin.

To sum up, we established an easily available system for which biophysical studies can be done in FaSSIF. We show that the effect of permeation enhancers can be greatly influenced by the presence of a peptide drug and FaSSIF components, with the effect of FaSSIF interactions often dominating that of the peptide drug. It will be beneficial to be aware of these effects when choosing a permeation enhancer for a peptide drug, as well as when characterizing permeation enhancement systems.

5 References

[1] M. S. Alqahtani, M. Kazi, M. A. Alsenaidy, and M. Z. Ahmad, "Advances in Oral Drug Delivery," *Front Pharmacol*, vol. 12, p. 62, Feb. 2021, doi: 10.3389/FPHAR.2021.618411/BIBTEX.

[2] D. J. Brayden, T. A. Hill, D. P. Fairlie, S. Maher, and R. J. Mrsny, "Systemic delivery of peptides by the oral route: Formulation and medicinal chemistry approaches," *Adv Drug Deliv Rev*, vol. 157, pp. 2–36, Jan. 2020, doi: 10.1016/J.ADDR.2020.05.007.

[3] S. Maher, R. J. Mrsny, and D. J. Brayden, "Intestinal permeation enhancers for oral peptide delivery," *Adv Drug Deliv Rev*, vol. 106, pp. 277–319, Nov. 2016, doi: 10.1016/j.addr.2016.06.005.

[4] fda and cder, "RYBELSUS (semaglutide) tablets, for oral use ." 2017. Accessed: Sep. 13, 2022. [Online]. Available: https://www.accessdata.fda.gov/drugsatfda_docs/label/2019/213051s000lbl.pdf

[5] K. Henriksen *et al.*, "A randomized, double-blind, multicenter, placebo-controlled study to evaluate the efficacy and safety of oral salmon calcitonin in the treatment of osteoporosis in postmenopausal women taking calcium and vitamin D," *Bone*, vol. 91, pp. 122–129, Oct. 2016, doi: 10.1016/J.BONE.2016.07.019.

[6] I. B. Halberg, K. Lyby, K. Wassermann, T. Heise, E. Zijlstra, and L. Plum-Mörschel, "Efficacy and safety of oral basal insulin versus subcutaneous insulin glargine in type 2 diabetes: a randomised, double-blind, phase 2 trial," *Lancet Diabetes Endocrinol*, vol. 7, no. 3, pp. 179–188, Mar. 2019, doi: 10.1016/S2213-8587(18)30372-3.

[7] A. Abramson, F. Halperin, J. Kim, and G. Traverso, "Quantifying the value of orally delivered biologic therapies: A cost-effectiveness analysis of oral semaglutide HHS Public Access," *J Pharm Sci*, vol. 108, no. 9, pp. 3138–3145, 2019, doi: 10.1016/j.xphs.2019.04.022.

[8] S. T. Buckley *et al.*, "Transcellular stomach absorption of a derivatized glucagon-like peptide-1 receptor agonist," *Sci Transl Med*, vol. 10, no. 467, p. eaar7047, Nov. 2018, doi: 10.1126/scitranslmed.aar7047.

[9] C. Twarog, S. Fattah, J. Heade, S. Maher, E. Fattal, and D. J. Brayden, "Intestinal permeation enhancers for oral delivery of macromolecules: A comparison between salcaprozate sodium (SNAC) and sodium caprate (c10)," *Pharmaceutics*, vol. 11, no. 2. MDPI AG, Feb. 01, 2019. doi: 10.3390/pharmaceutics11020078.

[10] B. K. Yoon, J. A. Jackman, M. C. Kim, T. N. Sut, and N. J. Cho, "Correlating Membrane Morphological Responses with Micellar Aggregation Behavior of Capric Acid and Monocaprin," *Langmuir*, vol. 33, no. 11, pp. 2750–2759, Mar. 2017, doi: 10.1021/ACS.LANGMUIR.6B03944/ASSET/IMAGES/LARGE/LA-2016-039445_0007.JPEG.

[11] S. Hossain *et al.*, "Influence of Bile Composition on Membrane Incorporation of Transient Permeability Enhancers," *Mol Pharm*, vol. 17, no. 11, pp. 4226–4240, Nov. 2020, doi: 10.1021/ACS.MOLPHARMACEUT.0C00668/ASSET/IMAGES/LARGE/MP0C00668_0010.JPEG.

[12] H. E. Huber, L. B. Dale, and G. L. Christenson, "Utilization of Hydrophilic Gums for the Control of Drug Release from Tablet Formulations I. Disintegration and Dissolution Behavior," *J Pharm Sci*, vol. 55, no. 9, pp. 974–976, Sep. 1966, doi: 10.1002/JPS.2600550923.

[13] S. Maher, D. J. Brayden, L. Casettari, and L. Illum, "Application of Permeation Enhancers in Oral Delivery of Macromolecules: An Update," *Pharmaceutics*, vol. 11, no. 1, Jan. 2019, doi: 10.3390/PHARMACEUTICS11010041.

[14] P. E. G. Thorén, D. Persson, M. Karlsson, and B. Nordén, "The Antennapedia peptide penetratin translocates across lipid bilayers – the first direct observation," *FEBS Lett*, vol. 482, no. 3, pp. 265–268, Oct. 2000, doi: 10.1016/S0014-5793(00)02072-X.

[15] E. Dupont, A. Prochiantz, and A. Joliot, "Penetratin Story: An Overview," in *Methods in molecular biology (Clifton, N.J.)*, vol. 1324, 2015, pp. 29–37. doi: 10.1007/978-1-4939-2806-4_2.

[16] M. Kristensen *et al.*, "Penetratin-Mediated Transepithelial Insulin Permeation: Importance of Cationic Residues and pH for Complexation and Permeation," *AAPS Journal*, vol. 17, no. 5, pp. 1200–1209, Sep. 2015, doi: 10.1208/s12248-015-9747-3.

[17] E. J. B. Nielsen *et al.*, "In vivo proof of concept of oral insulin delivery based on a co-administration strategy with the cell-penetrating peptide penetratin.," *J Control Release*, vol. 189, pp. 19–24, Sep. 2014, doi: 10.1016/j.jconrel.2014.06.022.

[18] E. Michael Danielsen and G. H. Hansen, "Probing the Action of Permeation Enhancers Sodium Cholate and N-dodecyl-β-D-maltoside in a Porcine Jejunal Mucosal Explant System," *Pharmaceutics*, vol. 10, no. 4, Dec. 2018, doi: 10.3390/PHARMACEUTICS10040172.

[19] K. C. Fein, J. P. Gleeson, A. N. Newby, and K. A. Whitehead, "Intestinal permeation enhancers enable oral delivery of macromolecules up to 70 kDa in size," *European Journal of Pharmaceutics and Biopharmaceutics*, vol. 170, pp. 70–76, Jan. 2022, doi: 10.1016/J.EJPB.2021.11.010.

[20] S. Maher, X. Wang, V. Bzik, S. McClean, and D. J. Brayden, "Evaluation of intestinal absorption and mucosal toxicity using two promoters. II. Rat instillation and perfusion studies," *Eur J Pharm Sci*, vol. 38, no. 4, pp. 301–311, Nov. 2009, doi: 10.1016/J.EJPS.2009.07.011.

[21] C. Twarog, F. McCartney, S. M. Harrison, B. Illel, E. Fattal, and D. J. Brayden, "Comparison of the effects of the intestinal permeation enhancers, SNAC and sodium caprate (C10): Isolated rat intestinal mucosae and sacs," *European Journal of Pharmaceutical Sciences*, vol. 158, p. 105685, Mar. 2021, doi: 10.1016/J.EJPS.2020.105685.

[22] N. Wichmann *et al.*, "Applying flow cytometry to identify the modes of action of membrane-active peptides in a label-free and high-throughput fashion," *Biochimica et Biophysica Acta (BBA) - Biomembranes*, vol. 1864, no. 2, p. 183820, Feb. 2022, doi: 10.1016/J.BBAMEM.2021.183820.

[23] J. N. Israelachvili and D. J. Mitchell, "A model for the packing of lipids in bilayer membranes," *Biochimica et Biophysica Acta (BBA) - Biomembranes*, vol. 389, no. 1, pp. 13–19, Apr. 1975, doi: 10.1016/0005-2736(75)90381-8.

[24] C. N. Pace, F. Vajdos, L. Fee, G. Grimsley, and T. Gray, "How to measure and predict the molar absorption coefficient of a protein," *Protein Science*, vol. 4, no. 11, pp. 2411–2423, 1995, doi: 10.1002/pro.5560041120.

[25] H. J. Motulsky, “Equation: ECanything,” *GraphPad Curve Fitting Guide*. https://www.graphpad.com/guides/prism/latest/curve-fitting/reg_ecanything_2.htm (accessed Aug. 03, 2022).

[26] G. van den Bogaart, J. V. Guzmán, J. T. Mika, and B. Poolman, “On the Mechanism of Pore Formation by Melittin,” *J Biol Chem*, vol. 283, no. 49, p. 33854, Dec. 2008, doi: 10.1074/JBC.M805171200.

[27] T. Namani and P. Walde, “From Decanoate Micelles to Decanoic Acid/ Dodecylbenzenesulfonate Vesicles,” 2005, doi: 10.1021/la047028z.

[28] D. L. Sackett and J. Wolff, “Nile red as a polarity-sensitive fluorescent probe of hydrophobic protein surfaces,” *Anal Biochem*, vol. 167, no. 2, pp. 228–234, Dec. 1987, doi: 10.1016/0003-2697(87)90157-6.

[29] K. Goodling, K. Johnson, L. Lefkowitz, and B. W. Willuams, “Luminescent Characterization of Sodium Dodecyl Sulfate Micellar Solution Properties,” *J Chem Educ*, vol. 71, no. 1, pp. A8–A12, 1994, doi: 10.1021/ed071pA8.

[30] S. Maher, T. W. Leonard, J. Jacobsen, and D. J. Brayden, “Safety and efficacy of sodium caprate in promoting oral drug absorption: from in vitro to the clinic,” *Adv Drug Deliv Rev*, vol. 61, no. 15, pp. 1427–1449, Dec. 2009, doi: 10.1016/J.ADDR.2009.09.006.

[31] M. Thongngam and D. J. McClements, “Influence of pH, ionic strength, and temperature on self-association and interactions of sodium dodecyl sulfate in the absence and presence of chitosan,” *Langmuir*, vol. 21, no. 1, pp. 79–86, Jan. 2005, doi: 10.1021/LA048711O/ASSET/IMAGES/LARGE/LA048711OF00012.JPEG.

[32] T. Vanaken, S. Foxall-Vanaken, S. Castleman, and S. Ferguson-Miller, “[3] Alkyl glycoside detergents: Synthesis and applications to the study of membrane proteins,” *Methods Enzymol*, vol. 125, no. C, pp. 27–35, Jan. 1986, doi: 10.1016/S0076-6879(86)25005-3.

[33] J. Lipfert, L. Columbus, V. B. Chu, S. A. Lesley, and S. Doniach, “Size and shape of detergent micelles determined by small-angle X-ray scattering,” *Journal of Physical Chemistry B*, vol. 111, no. 43, pp. 12427–12438, Nov. 2007, doi: 10.1021/JP073016L/ASSET/IMAGES/LARGE/JP073016LF00011.JPEG.

[34] P. Rosevear, T. VanAken, J. Baxter, and S. Ferguson-Miller, “Alkyl Glycoside Detergents: A Simpler Synthesis and Their Effects on Kinetic and Physical Properties of Cytochrome c Oxidase* 1",” *Biochemistry*, vol. 19, no. 17, pp. 4108–4116, 1980.

[35] D. M. Small, “A Classification of Biologic Lipids Based upon Their Interaction in Aqueous Systems,” *J Am Oil Chem Soc*, vol. 45, no. 3, pp. 108–119, 1968, doi: 10.1007/BF02915334.

[36] J. C. Talbot, J. Dufourcq, J. de Bony, J. F. Faucon, and C. Lussan, “Conformational change and self association of monomeric melittin,” *FEBS Lett*, vol. 102, no. 1, pp. 191–193, Jun. 1979, doi: 10.1016/0014-5793(79)80957-6.

[37] K. Matsuzaki, S. Yoneyama, and K. Miyajima, “Pore formation and translocation of melittin,” *Biophys J*, vol. 73, no. 2, pp. 831–838, Aug. 1997, doi: 10.1016/S0006-3495(97)78115-3.

[38] M. therese Paternostre, M. Roux, and J. louis Rigaud, “Mechanisms of Membrane Protein Insertion into Liposomes during Reconstitution Procedures Involving the Use of Detergents. 1. Solubilization of Large Unilamellar Liposomes (Prepared by Reverse-Phase Evaporation) by Triton

X-100, Octyl Glucoside, and Sodium Cholate," *Biochemistry*, vol. 27, no. 8, pp. 2668–2677, Apr. 1988, doi: 10.1021/BI00408A006/ASSET/BI00408A006.FP.PNG_V03.

[39] S. Berg *et al.*, "Impact of Intestinal Concentration and Colloidal Structure on the Permeation-Enhancing Efficiency of Sodium Caprate in the Rat," *Mol Pharm*, vol. 19, no. 1, pp. 200–212, Jan. 2022, doi: 10.1021/ACS.MOLPHARMACEUT.1C00724/SUPPL_FILE/MP1C00724_SI_001.PDF.

[40] S. Trier, L. Linderoth, S. Bjerregaard, H. M. Strauss, U. L. Rahbek, and T. L. Andresen, "Acylation of salmon calcitonin modulates in vitro intestinal peptide flux through membrane permeability enhancement," *European Journal of Pharmaceutics and Biopharmaceutics*, vol. 96, pp. 329–337, Oct. 2015, doi: 10.1016/j.ejpb.2015.09.001.

[41] P. O. Hegg, "Precipitation of egg white proteins below their isoelectric points by sodium dodecyl sulphate and temperature," *BBA - Protein Structure*, vol. 579, no. 1, pp. 73–87, Jul. 1979, doi: 10.1016/0005-2795(79)90088-6.

[42] S. F. Hedegaard *et al.*, "Fluorophore labeling of a cell-penetrating peptide significantly alters the mode and degree of biomembrane interaction," *Sci Rep*, vol. 8, no. 1, pp. 1–14, 2018, doi: 10.1038/s41598-018-24154-z.

[43] J. A. Lapre, D. S. M. L. Termont, A. K. Groen, and R. van der Meer, "Lytic effects of mixed micelles of fatty acids and bile acids," *Am J Physiol Gastrointest Liver Physiol*, vol. 263, no. 3 26-3, 1992, doi: 10.1152/AJPGI.1992.263.3.G333.

[44] C. Twarog *et al.*, "Characterization of the physicochemical interactions between exenatide and two intestinal permeation enhancers: Sodium caprate (C10) and salcaprozate sodium (SNAC)," *Int J Pharm*, vol. 626, p. 122131, Oct. 2022, doi: 10.1016/J.IJPHARM.2022.122131.

[45] C. A. Lipinski, F. Lombardo, B. W. Dominy, and P. J. Feeney, "Experimental and computational approaches to estimate solubility and permeability in drug discovery and development settings," *Adv Drug Deliv Rev*, vol. 64, no. SUPPL., pp. 4–17, Dec. 2012, doi: 10.1016/J.ADDR.2012.09.019.

[46] Z. Antosova, M. Mackova, V. Kral, and T. Macek, "Therapeutic application of peptides and proteins: parenteral forever?," *Trends Biotechnol*, vol. 27, no. 11, pp. 628–635, Nov. 2009, doi: 10.1016/J.TIBTECH.2009.07.009.

[47] M. Kristensen and H. M. Nielsen, "Cell-penetrating peptides as tools to enhance non-injectable delivery of biopharmaceuticals," *Tissue Barriers*, vol. 4, no. 2, Apr. 2016, doi: 10.1080/21688370.2016.1178369.

6 Supplementary Information

6.1 Supplementary figures

Supplementary figure 1: Concentration dependent membrane perturbation by SNAC and penetratin

Concentration dependent membrane perturbation by SNAC (left) and penetratin (right). Degree of membrane perturbation of 0.6 nM liposomes by SNAC or penetratin as observed using a calcein release assay. For SNAC, the signal obtained by adding 0.5 % Triton X-100 to liposomes, was corrected by a correction factor for each concentration of SNAC to provide a corrected value of F_{max} for each concentration of SNAC. The correction factor was calculated from the fluorescent signal for 5 µM calcein in the presence, $F_{calcein+SNAC}$, and the absence, $F_{calcein}$,, of SNAC such that: $F_{max\ corrected} = F_{max} \cdot \frac{F_{calcein+c_{SNAC}}}{F_{calcein}}$

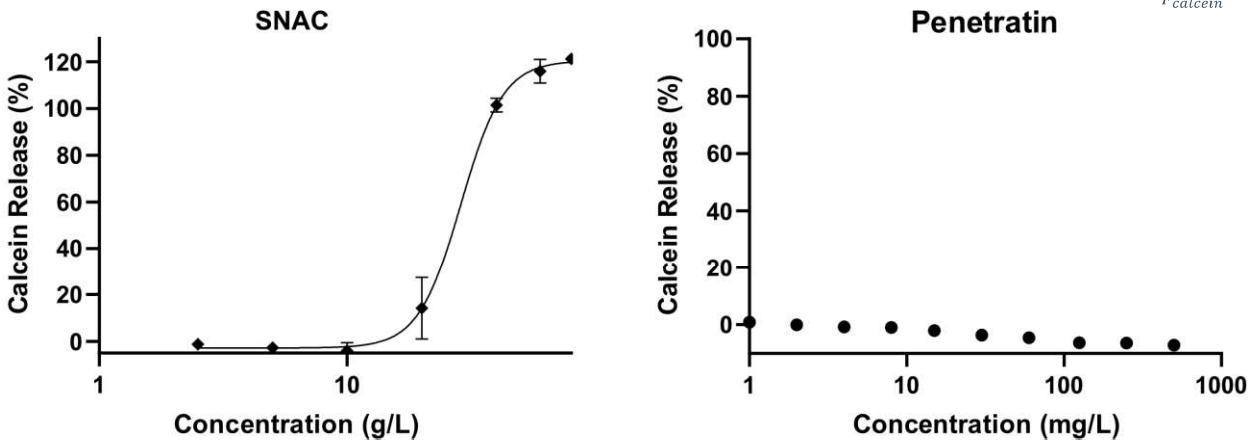

Supplementary figure 2: Membrane perturbation by peptide drugs.

Degree of membrane perturbation of 0.6 nM liposomes by 300 mg/L peptide drug after 30 min as determined by using the calcein release assay. The calcein release by insulin was determined in triplicates, calcein release by sCT determined by a single measurement. In an identical setting, for another batch of sCT also 103 and 343 mg/L sCT did not give rise to calcein release (data not shown).

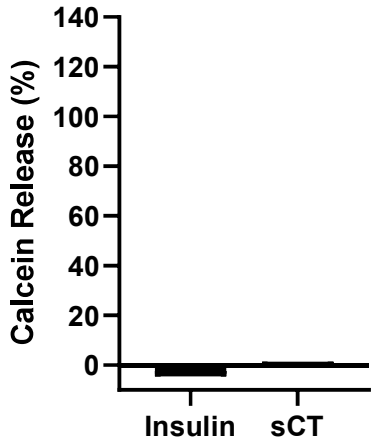

Supplementary figure 3: DLS of permeation enhancers

Intensity based distribution analysis of DLS measurements of the permeation enhancers at their EC50 concentration with respect to their membrane perturbating effect. Shown are the sizes of 1-200 nm. The inserts show the full size range (1-10000 nm) In the table, the hydrodynamic diameters of each of the population giving rise to a peak are listed. Sizes above 1000 nm are not included. In addition, the attenuation factors of the measurements are included. The attenuation factor ranges from 6-11 on the Malvern Zetasizer. A low concentration of small particles will result in a high attenuation factor, and a high concentration of large particles will result in a low attenuation factor. Three technical measurements were carried out on a duplicate of samples.

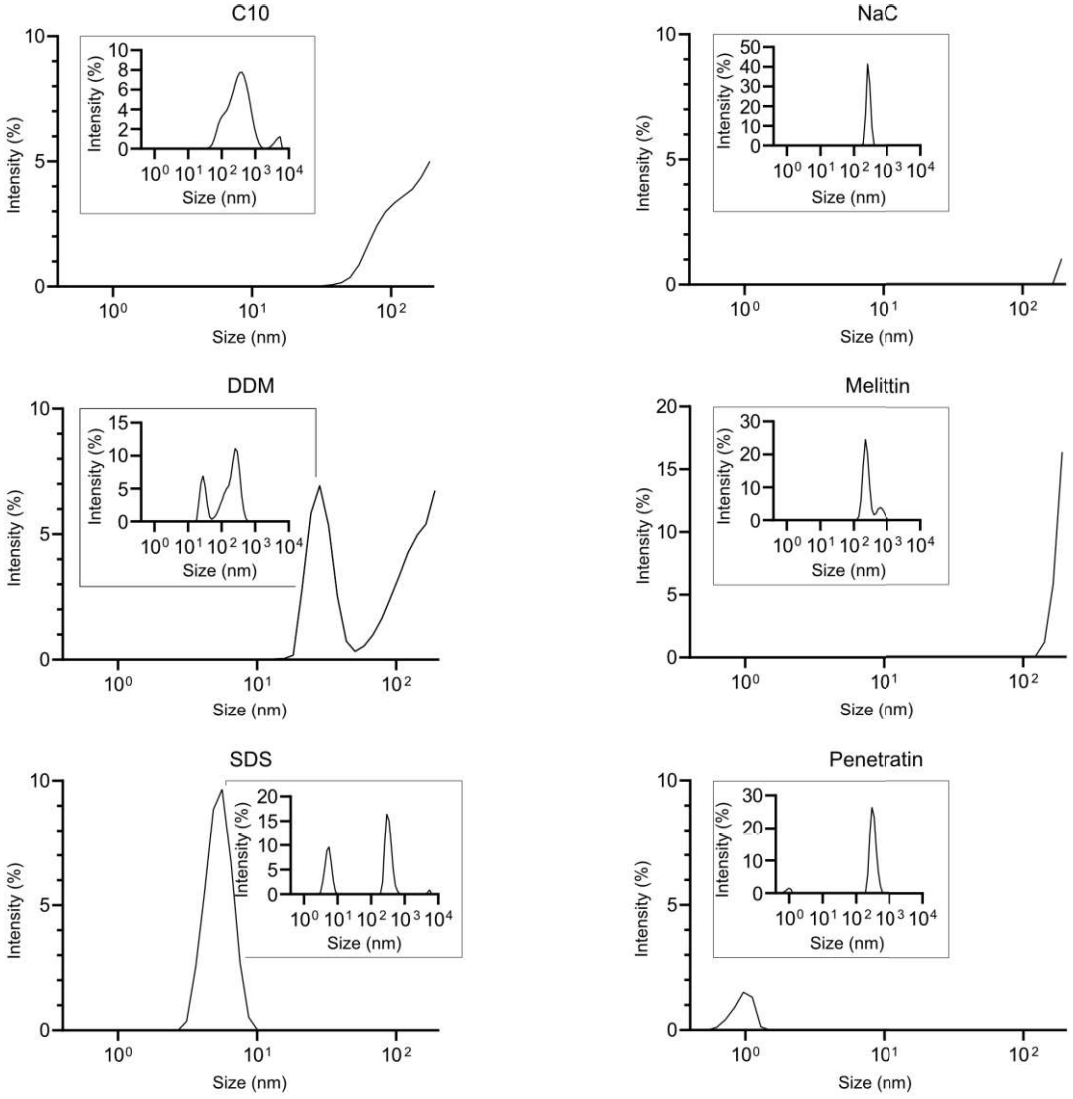

Permeation enhancer	Size ± SD	Attenuation factor
C10	371 ± 253 nm	7
DDM	29 ± 6 nm 231 ± 97 nm	11
NaC	270 ± 37 nm	11
SDS	337 ± 77 nm 5 ± 1	11
Melittin	236 ± 49 nm 627 ± 153 nm	11
Penetratin	325 ± 69 nm 1 ± <1 nm	11
Buffer	394 ± 87 nm	11

Supplementary figure 4: DLS of liposomes in the presence of permeation enhancers

Intensity based distribution analysis of DLS measurements of 0.6 nM liposomes in the absence and presence of the various permeation enhancers, at their EC95 concentrations with respect to their membrane perturbating effect. The graphs are overlayed with the graphs for the permeation enhancers in the absence of liposomes (Supplementary figure 3).) In the table, the hydrodynamic diameters of each of the populations giving rise to a peak are listed. In addition, the attenuation factors of the measurements are listed. The attenuation factor ranges from 6-11 on the Malvern Zetasizer. A low concentration of small particles will result in a high attenuation factor, and a high concentration of large particles will result in a low attenuation factor. Three technical measurements were carried out on a duplicate of samples. Mel: melittin, Pen: penetratin

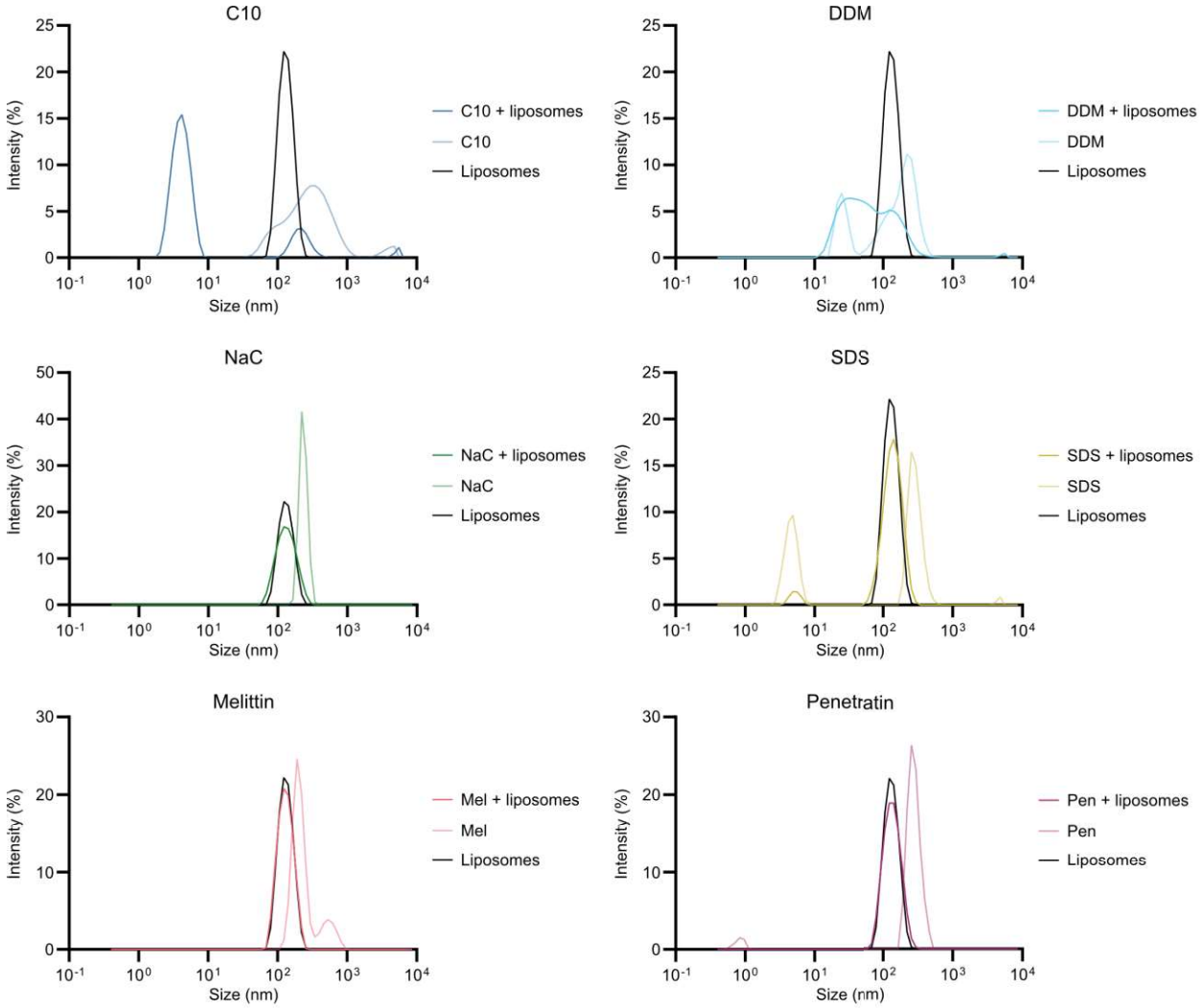

Permeation enhancer	Liposomes Size	Attenuation factor
No	134 ± 32 nm	8
C10	4 ± 1 nm 223 ± 68 nm	11
DDM	44 ± 23 nm 158 ± 67 nm	10
NaC	137 ± 44 nm	8
SDS	142 ± 42 nm 5 ± 1 nm	10
Melittin	133 ± 34 nm	9
Penetratin	138 ± 39 nm	8

Supplementary figure 5: Overlay of NileRed signal (from Figure 6A) and Calcein Release (from Figure 4A) for hydrophobically driven self-assembling permeation enhancers.

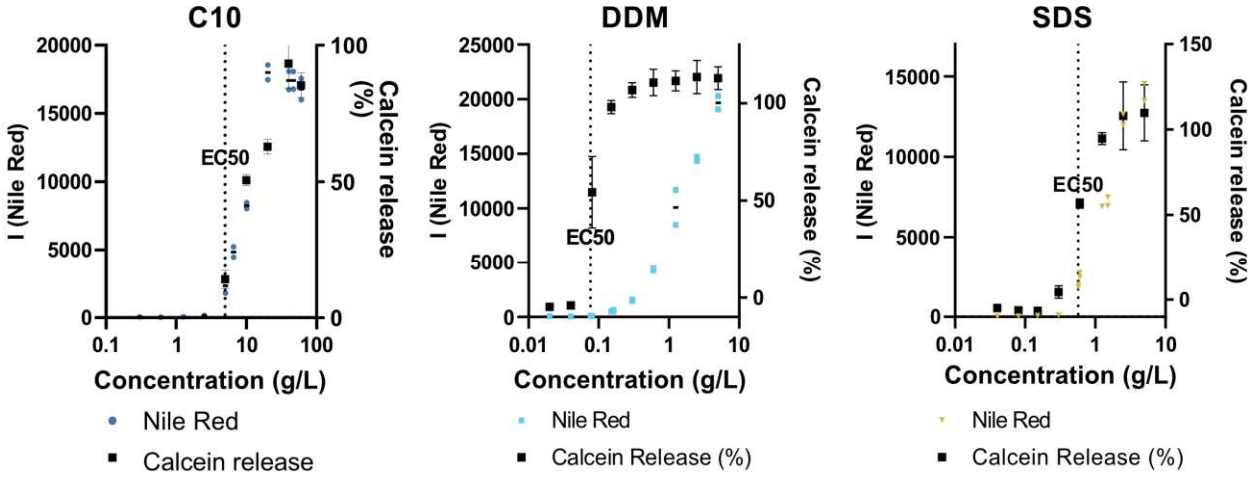

Supplementary figure 6: DLS data for permeation enhancers in the presence of peptide drugs.

Intensity based distribution analysis of DLS measurements of the permeation enhancers at their EC50 concentration with respect to their membrane perturbating effect in the absence and presence of 300 mg/L sCT or insulin. In the inserts, a zoom of the size range of 1-100 nm is shown. In the table, O,, the hydrodynamic diameters of each of the populations giving rise to a peak are listed. Sizes above 1000 nm are not included. The attenuation factors of the measurements are also listed. The attenuation factor ranges from 6-11 on the Malvern Zetasizer. A low concentration of small particles will result in a high attenuation factor, and a high concentration of large particles will result in a low attenuation factor. Three technical measurements were carried out on a duplicate of samples. The sizes of the particles ± SD shown in figure 8, are also included in the table, P.

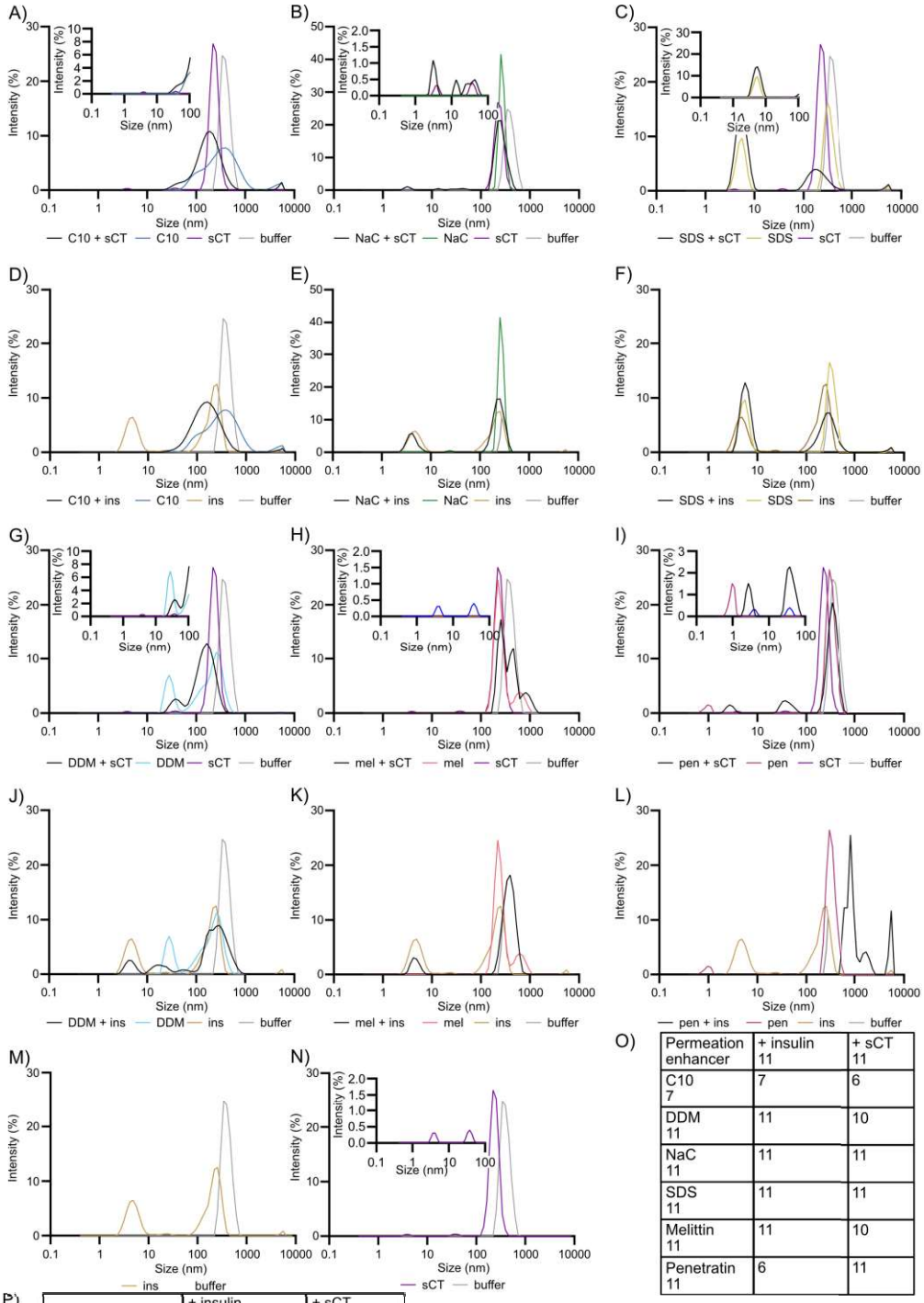

O)

Permeation enhancer	+ insulin 11	+ sCT 11
C10 7	7	6
DDM 11	11	10
NaC 11	11	11
SDS 11	11	11
Melittin 11	11	10
Penetratin 11	6	11

P)

	+ insulin 5 ± 1 nm 22 ± 4 nm	+ sCT 3 ± 1 nm
C10 371 ± 253 nm	179 ± 110 nm 9 ± 2 nm	196 + 108 nm
DDM: 29 ± 6 nm; 231 ± 97 nm	354 ± 124 nm 178 ± 34 nm 20 ± 7 nm	168 ± 65 nm 40 ± 10 nm
NaC N/A	4 ± 1 nm 24 ± 3 nm	3 ± <1 nm 43 ± 8 nm
SDS 5 ± 1 nm	6 ± 1 nm	6 ± 1 nm 220 ± 119 nm
Melittin 627 ± 153	5 ± 1 nm	444 ± 77 856 ± 188
Penetratin 1 ± <1 nm	803 ± 166 nm	41 ± 11 nm 3 ± <1 nm

Supplementary figure 7: Calcein release from liposomes in FaSSIF

Calcein release from 0.6 nM liposomes in the presence of FaSSIF. 0 % calcein release is based on the fluorescence at T=0 min in this case. The shown data points are a representative data set.

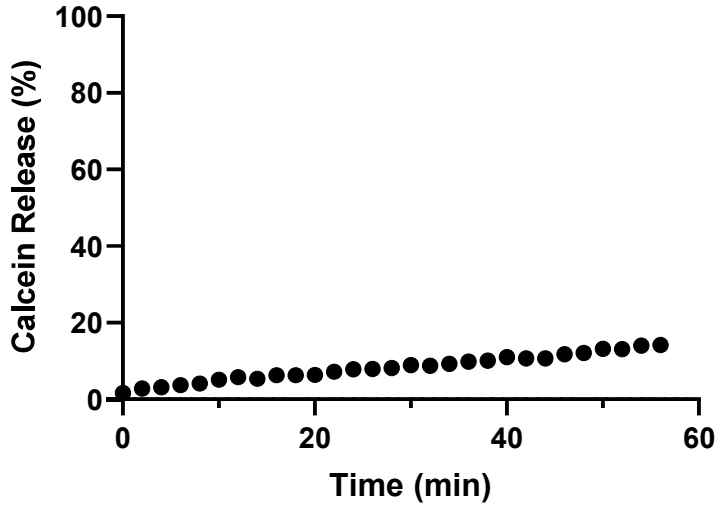

Supplementary figure 8: DLS of permeation enhancers in FaSSIF

Intensity based distribution analysis of DLS measurements of the permeation enhancers at their EC50 concentration with respect to their membrane perturbating effect after approximately 30 min in FaSSIF. The attenuation factors of the measurements are also listed. The attenuation factor ranges from 6-11 on the Malvern Zetasizer. A low concentration of small particles will result in a high attenuation factor, and a high concentration of large particles will result in a low attenuation factor. Three technical measurements were carried out on a duplicate of samples.

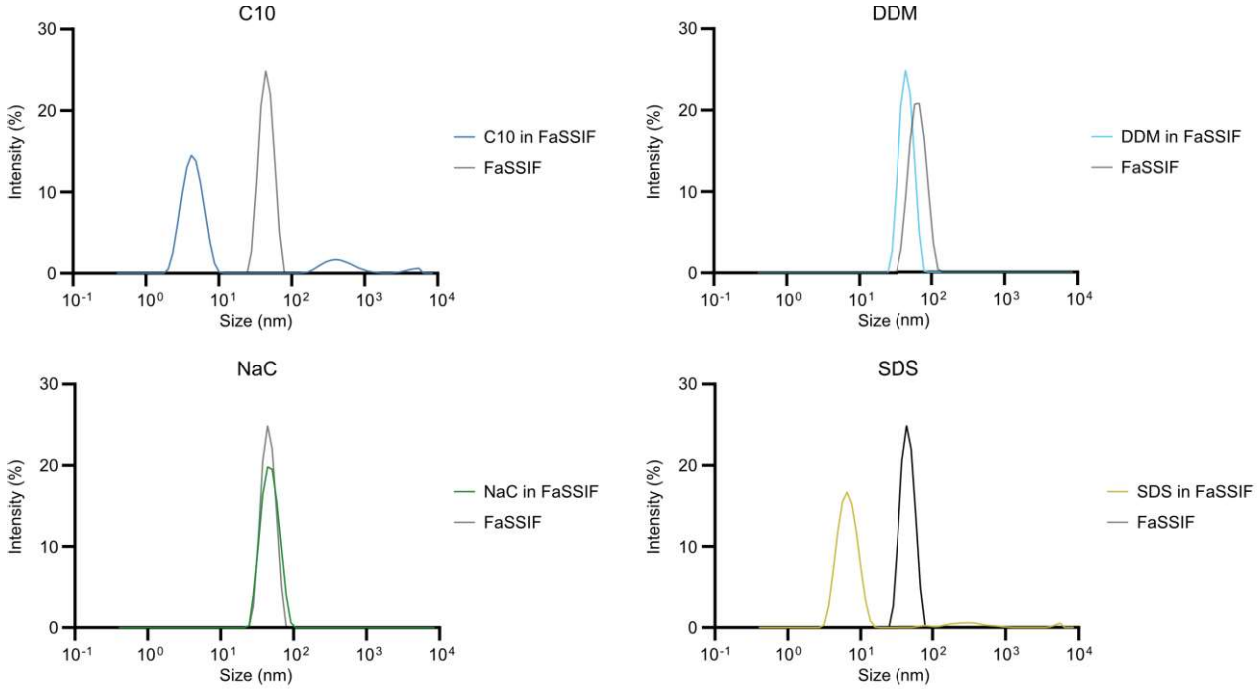

Permeation enhancer	FaSSIF Size ± SD	Attenuation factor
No	46 ± 10 nm	7
C10 371 ± 253 nm	5 ± 1 nm 484 ± 249 nm	11
DDM 29 ± 6 nm	66 ± 17 nm	7
NaC -	49 ± 13 nm	7
SDS 5 ± 1 nm	7 ± 2 nm	11

6.2 Supplementary material and methods

6.2.1 Material and methods

Fmoc-protected amino acids, oxyma and N,N'-Diisopropylcarbodiimide (DIC) were purchased from Iris-Biotech. The resin was purchased from Rapp Polymere. Solvents and all other reagents were purchased from Sigma Aldrich. Special Fmoc amino acids were: Fmoc-L-Leu-L-Ser[PSI(Me, Me)Pro]-OH, Fmoc-L-Glu-OtBu, Fmoc-L-Asp-OtBu.

6.2.2 Synthesis and purification of melittin, penetratin, and sCT

6.2.2.1 Solid phase peptide synthesis of melittin, penetratin, and sCT

Melittin and penetratin were synthesized and purified as in [22]. In short were all peptides synthesized on a Biotage Initiator + Alstra microwave-assisted peptide synthesizer. For sCT it was done in 10 mL fritted syringes on a 0.05 mmol scale. A TentaGel S RAM resin (loading 0.23 mmol/g) was used for sCT and melittin, A Fmoc-PAL-AM resin (loading 0.61 mmol/g) was used for penetratin. Fmoc-deprotection was performed by adding deprotection solution (20% piperidine in dimethyl formamide (DMF), 0.1 M ethyl cyanohydroxyiminoacetate (Oxyma) to the resin at 75 °C, for sCT for 30 sec, for melittin and penetratin for 2 min. Another portion of deprotection solution was added and heated to 75 °C, for sCT for 2 min, for melittin and penetratin for 5 min. Next, the resin was drained and washed five times with DMF. Coupling of amino acids was performed by adding amino acid solution (for sCT 4 eq. of Fmoc-L-amino acid (AA)-OH, 4 eq. Oxyma in DMF, 0.3 M concentration, for melittin and penetratin 5 eq. of Fmoc-L-AA-OH, 5 eq. Oxyma in DMF), DIC solution (2 M DIC in DMF) and heating the mixture to 75 °C, for sCT for 5 min, for melittin and penetratin for 10 min. The solution was drained and the resin was washed once with DMF. The coupling was repeated. After the second coupling the resin was washed 4 times with DMF. For sCT extended coupling times were applied for Fmoc-Arg(Pbf)-OH and Fmoc-L-Leu-L-Ser[PSI(Me, Me)Pro]-OH. These amino acids were coupled at room temperature for 25 min followed by 75 °C for 5 min. Also for sCT the resin was drained, washed 4 times with DMF (5 mL) and the coupling was repeated. Fmoc-removal on Asp residues was performed with 5% piperidine rather than 20%. For melittin and penetratin, the coupling times for arginine residues were 25 min and 5 min. For histidine residues the temperature was lowered to 50 °C.

6.2.2.2 Formation of disulfide on resin for SCT

For sCT after coupling and deprotection of the last amino acid, the resin was washed five times with Dichloromethane (DCM) (5 mL). An iodine solution (5 mL; 1:4 Hexafluoroisopropanol (HFIP)/1% iodine (I2) in DCM) was added to the resin, shaken for exactly 2 min, filtered, and washed once with a 1:1 HFIP/DCM solution. The resin was then left to shake for 15 min with a 1:1 HFIP/DCM solution. The solution was drained, and the resin was washed five times with DCM and five times with DMF. Next, Fmoc was removed by adding 20% piperidine, 0.1% Oxyma in DMF (5 mL), and the tube was shaken for 2x 20 min. The resin was washed with DMF, DCM, DMF, DCM, isopropanol, DCM, and diethyl ether.

6.2.2.3 Peptide cleavage, purification and analysis of melittin, penetratin, and sCT

After disulphide formation (for sCT) or deprotection of the final amino acid residue (for melittin and penetratin), the resin was washed 5 times with of DMF, 5 times with DCM and air-dried. The resin was treated with cleavage cocktail (for sCT 90 % TFA, 5% water, 5 % triisopropylsilane (TIPS), for melittin and penetratin 95 % TFA, 2.5 % water, 2.5 % TIPS) for 4 hrs. The crude peptide was precipitated in cold diethylether, centrifuged, and decanted. For sCT, the residue was air-dried and re-dissolved in 20 % MeCN in MQ. For melittin and penetratin, the peptide-cleavage mixture was triturated (twice). The crude peptide was purified on a Dionex Ultimate 3000 system equipped with a RQ variable wavelength detector and an automated fraction collector, for sCT using a Phenomenex, Gemini NX 5u, C18, 110Å, AXIA, 250 mm x 21 mm column, for melittin and penetratin using a Phenomenex Gemini NX 5u, C18, 110 Å, 250 mm × 30 mm column, both at a 20 mL/min flowrate. RP-HPLC gradients were run using a solvent system consisting of solution A (H2O + 0.1 % TFA) and B (MeCN + 0.1 % TFA). Pure fractions were combined and lyophilized. Peptides were analyzed on a Shimadzu NexeraX2 RP-HPLC system equipped with Shimadzu LC-30AD pumps, a Shimadzu SIL-30AC autosampler, a CTO-20AC column oven and a Shimadzu PDA detector (monitoring at 214 nm, 280 nm and 492 nm) using a Waters XBridge BEH C18, 2.5µm 3.0x150mm XP Column at a flow rate of 0.5 mL/min. RP-HPLC gradients were run using a solvent system consisting of solution A (5% MeCN in H2O + 0.1% TFA) and B (MeCN + 0.1 % TFA). Mass analysis was performed using an electrospray ionization (ESI) micrOTOF-Q III (Bruker Daltonics, Bremen, Germany) for sCT, or a Waters Acquity Ultra Performance UPLC equipped with a QDa detector and an Acquity UPLC BEH C18, 1.7 µm, 2.1 × 50 mm column for melittin and penetratin. The final sCT had a 98 % purity (HPLC) (Supplementary figure 9), (ESI) *m/z*: $[M + 4H]^{4+}$=858.7, $[M + 3H]^{3+}$=1144.9 (Supplementary figure 10). The final melittin had a 99 % purity (HPLC) [22], Liquid chromatography-mass spectrometry (LC-MS) (ESI) *m/z*: = $[M + 6H]^{6+}$ = 475.4, $[M + 5H]^{5+}$ = 569.9, $[M + 4H]^{4+}$ = 712.3, $[M + 3H]^{3+}$ = 949.7[22]. The final penetratin had a 93 % purity (HPLC) [22] and LC-MS (ESI) *m/z*: = $[M + 5H]^{5+}$ = 450.3, $[M + 4H]^{4+}$ = 562.4, $[M + 3H]^{3+}$ = 749.5, $[M + 2H]^{2+}$ = 1123.8[22].

Supplementary figure 9: sCT purity: Analytical HPLC chromatogram

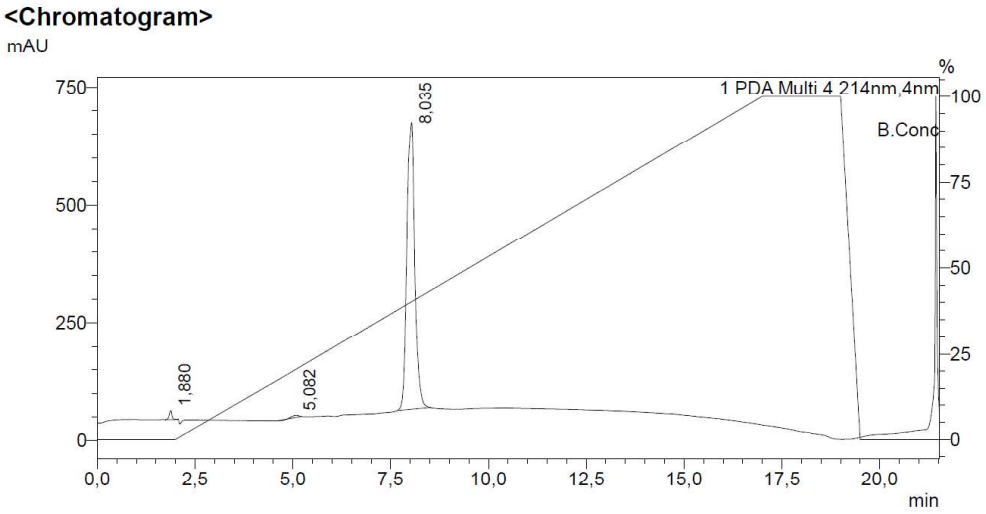

Supplementary figure 10: Identification of sCT. ESI spectrum acquired via quadripole time-of-flight (QTOF)-MS

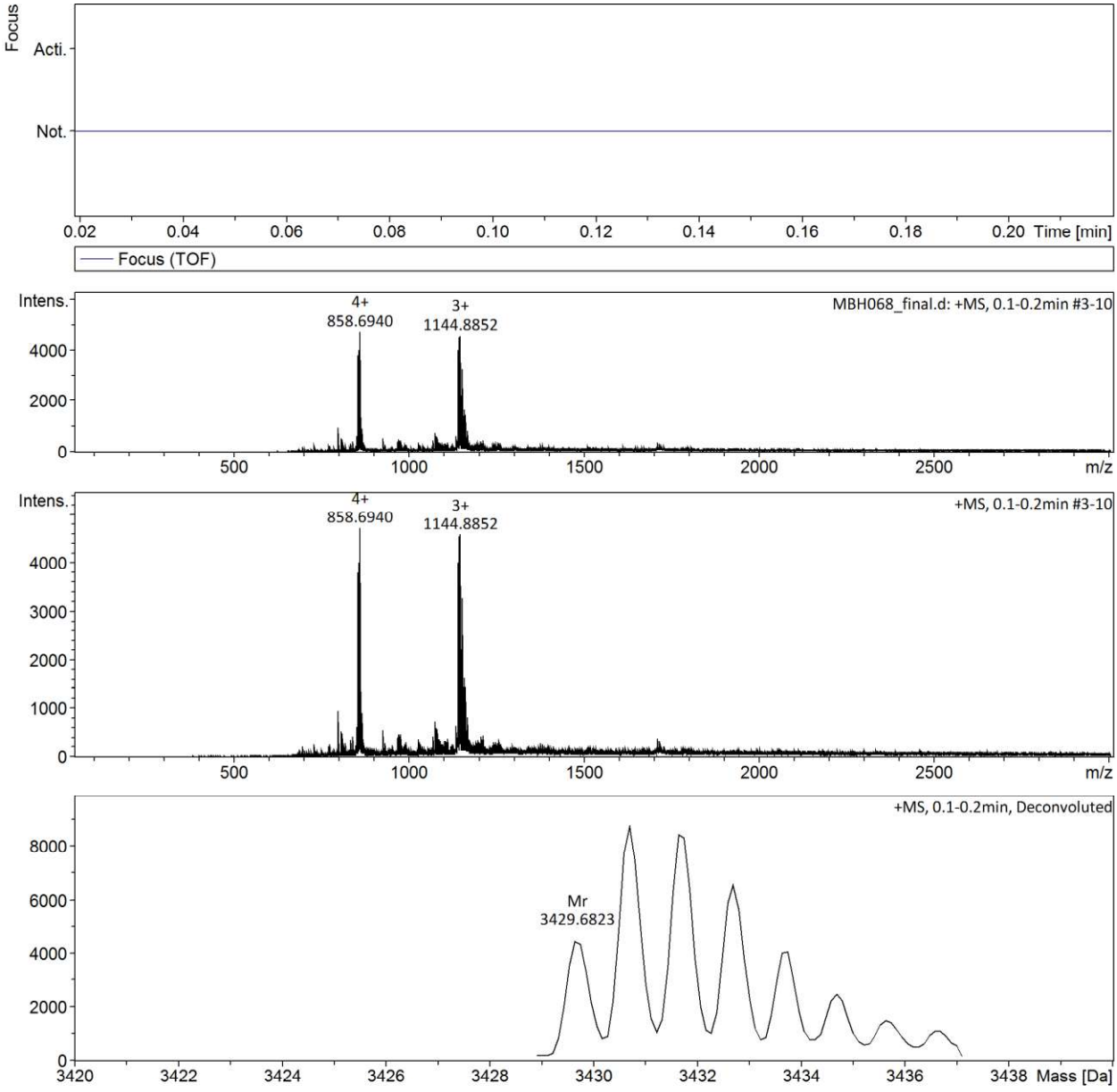

Chapter 4: Article: Applying flow cytometry to identify the modes of action of membrane-active peptides in a label-free and high-throughput fashion

In the manuscript above, two methods, calcein release and dynamic light scattering, was used to study the mode of actions of a range of permeation enhancers and membrane active peptides in a high throughput manner. Often, mechanistic studies of membrane activity of peptides are otherwise performed using microscopy [1]–[6]. Microscopy studies have the advantage of being an integrated platform to study both membrane perturbation and solubilization. However, microscopy is a low throughput method. We wanted to investigate if flow cytometry could be used as an integrated platform to study membrane activity of peptides, and thus be used as an alternative approach to study membrane activity, in a high-throughput manner. If succeeding, it would be possible to study the same effects as observed by calcein release and DLS, albeit at a single liposome level rather than as bulk assays. This would make it possible to distinguish between non-permeated and permeated (sub)populations. Additionally, if flow cytometry could be used as a method to study the membrane activity of peptides, it would make this kind of mechanistic studies accessible for other types of laboratories. Finally, the method would have the potential of further development by including more fluorophores, e.g. on the membrane active peptide, which would enable the study of peptide association with the liposome as well.

We decided to use membrane-labeled liposomes encapsulating another fluorophore to track effects on both lipid membranes and membrane permeability. Considerations prior to the experiments evolved around the use of fluorophores and their proper detection. It was important that the liposomes were large enough to contain enough membrane-fluorophores to be detected, but at an as-low-as-possible concentration to decrease the effects of the fluorophore on interactions between peptides and lipid membranes. Previous studies of liposomes in flow cytometry had showed good detection for 1 mol% of the lipids being fluorophore labelled with atto-fluorophores [7], why this was the chosen concentration. For the encapsulated fluorophores, it was important with high fluorescence from the encapsulated fluorophores. Atto- and alexa-dyes have been shown to have strong fluorescence and to be self-quenching at much higher concentrations than calcein and fluorescein. By measuring the fluorescence from a concentration series of Alexa488 in 10 mM phosphate, 100 mM NaCl, pH 6.7, we found that the fluorescence increased linearly until approximately 20 µM, and continued to increase until approximately 290 µM Figure 4.1. To get sufficient change of fluorescence intensity upon membrane perturbation, we decided to use an encapsulated concentration of 80 µM Alexa488.

We chose to work with POPC liposomes with 20 % 1-palmitoyl-2-oleoyl-sn-glycero-3-phospho-L-serine (POPS). POPS is an anionic lipid found in human plasma membranes, and was chosen to mimic the negatively charged human plasma membrane [8]. An advantage of having negatively charged lipid membranes were furthermore that many membrane active peptides have been shown to have enhanced membrane activity towards negatively charged membrane [9], and were thus expected to provide a larger working span. We are aware that POPS is mainly exposed on the exterior side of the cells under dying conditions [10]. Yet the focus here was on deriving the modes of actions of membrane active peptides,

and the biological relevance were of lesser priority. However, the method proved useful for studying how the modes of actions may differ for lipid membranes with various lipid compositions.

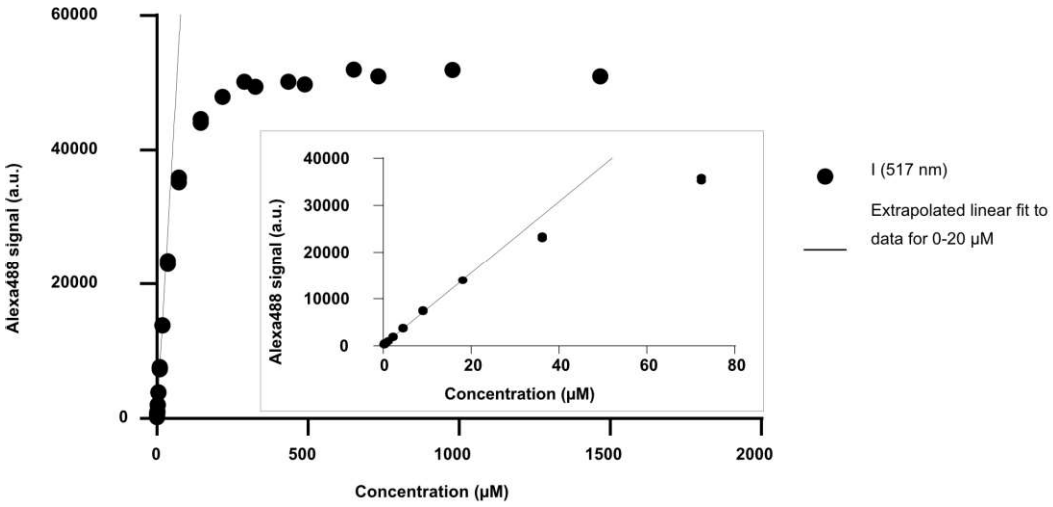

Figure 4.1: Fluorescence intensity of Alexa488 at various concentrations. The inserts show a zoom of the fluorescence signals for concentrations between 0 and 80 μM Alexa488. A linear fit extrapolated from the fluorescence intensities of 0-20 μM Alexa488 is shown to underline the linear increase in fluorescence at these concentrations. Alexa488 was dissolved and diluted in 10 mM phosphate, 100 mM NaCl, pH 6.7. Ex/Em: 488 nm/517 nm.

The work resulted in the published article 'Applying flow cytometry to identify the modes of action of membrane-active peptides in a label-free and high-throughput fashion' [11]. The article is reprinted on the following page with permission from Elsevier.

4.1 References

[1] Y. Imura, N. Choda, and K. Matsuzaki, "Magainin 2 in Action: Distinct Modes of Membrane Permeabilization in Living Bacterial and Mammalian Cells," *Biophys J*, vol. 95, no. 12, p. 5757, Dec. 2008, doi: 10.1529/BIOPHYSJ.108.133488.

[2] Md. Z. Islam, H. Ariyama, J. Md. Alam, and M. Yamazaki, "Entry of Cell-Penetrating Peptide Transportan 10 into a Single Vesicle by Translocating Across Lipid Membrane and Its Induced Pores," *Biochemistry*, vol. 53, no. 2, pp. 386–396, Jan. 2014, doi: 10.1021/bi401406p.

[3] B. Apellániz, J. L. Nieva, P. Schwille, and A. J. García-Sáez, "All-or-None versus Graded: Single-Vesicle Analysis Reveals Lipid Composition Effects on Membrane Permeabilization," *Biophys J*, vol. 99, no. 11, pp. 3619–3628, Dec. 2010, doi: 10.1016/j.bpj.2010.09.027.

[4] J. He, K. Hristova, and W. C. Wimley, "A Highly Charged Voltage-Sensor Helix Spontaneously Translocates across Membranes," *Angewandte Chemie International Edition*, vol. 51, no. 29, pp. 7150–7153, Jul. 2012, doi: 10.1002/anie.201202741.

[5] S. A. Wheaten, F. D. O. Ablan, B. L. Spaller, J. M. Trieu, and P. F. Almeida, "Translocation of Cationic Amphipathic Peptides across the Membranes of Pure Phospholipid Giant Vesicles," *J Am Chem Soc*, vol. 135, no. 44, pp. 16517–16525, Nov. 2013, doi: 10.1021/ja407451c.

[6] J. Pae, L. Liivamägi, D. Lubenets, P. Arukuusk, Ü. Langel, and M. Pooga, "Glycosaminoglycans are required for translocation of amphipathic cell-penetrating peptides across membranes,"

Biochimica et Biophysica Acta (BBA) - Biomembranes, vol. 1858, no. 8, pp. 1860–1867, Aug. 2016, doi: 10.1016/J.BBAMEM.2016.04.010.

[7] J. B. Simonsen, "A liposome-based size calibration method for measuring microvesicles by flow cytometry," *Journal of Thrombosis and Haemostasis*, vol. 14, no. 1, pp. 186–190, Jan. 2016, doi: 10.1111/jth.13176.

[8] M. Pekker and M. N. Shneider, "The surface charge of a cell lipid membrane," *J Phys Chem Biophys*, vol. 5, no. 2, Jan. 2014, doi: 10.4172/2161-0398.1000177.

[9] A. L. Russell, A. M. Kennedy, A. M. Spuches, D. Venugopal, J. B. Bhonsle, and R. P. Hicks, "Spectroscopic and thermodynamic evidence for antimicrobial peptide membrane selectivity," *Chem Phys Lipids*, vol. 163, no. 6, pp. 488–497, Jun. 2010, doi: 10.1016/J.CHEMPHYSLIP.2010.03.009.

[10] S. Nagata, J. Suzuki, K. Segawa, and T. Fujii, "Exposure of phosphatidylserine on the cell surface," *Cell Death Differ*, vol. 23, no. 6, p. 952, Jun. 2016, doi: 10.1038/CDD.2016.7.

[11] N. Wichmann *et al.*, "Applying flow cytometry to identify the modes of action of membrane-active peptides in a label-free and high-throughput fashion," *Biochimica et Biophysica Acta (BBA) - Biomembranes*, vol. 1864, no. 2, p. 183820, Feb. 2022, doi: 10.1016/J.BBAMEM.2021.183820.

BBA - Biomembranes 1864 (2022) 183820

Contents lists available at ScienceDirect

BBA - Biomembranes

journal homepage: www.elsevier.com/locate/bbamem

Applying flow cytometry to identify the modes of action of membrane-active peptides in a label-free and high-throughput fashion

Nanna Wichmann, Philip M. Lund, Morten B. Hansen, Claudia U. Hjørringgaard, Jannik B. Larsen, Kasper Kristensen, Thomas L. Andresen *, Jens B. Simonsen *

Department of Health Technology, Center for Intestinal Absorption and Transport of Biopharmaceuticals, Technical University of Denmark, 2800 Kgs. Lyngby, Denmark

ARTICLEINFO

Keywords:
Membrane-active peptides
Flow cytometry Liposomes
Modes of action
High-throughput
Label-free

ABSTRACT

Membrane-active peptides (MAPs) have several potential therapeutic uses, including as antimicrobial drugs. Many traditional methods used to evaluate the membrane interactions of MAPs have limited applicability. Low- throughput methods, such as microscopy, provide detailed information but often rely on fluorophore-labeled MAPs, and high-throughput assays, such as the calcein release assay, cannot assess the mechanism behind the disruption of vesicular-based lipid membranes. Here we present a flow cytometric assay that provides detailed information about the peptide-lipid membrane interactions on single artificial lipid vesicles while being high- throughput (1000–2000 vesicles/s) and based on label-free MAPs. We synthesized and investigated six MAPs with different modes of action to evaluate the versatility of the assay. The assay is based on the flow cytometric readouts from artificial lipid vesicles, including the fluorescence from membrane-anchored and core- encapsulated fluorophores, and the vesicle concentration. From these parameters, we were able to distinguish between MAPs that induce vesicle solubilization, permeation (pores/membrane distortion), and aggregation or fusion. Our flow cytometry findings have been verified by traditional methods, including the calcein release assay, dynamic light scattering, and fluorescence microscopy on giant unilamellar vesicles. We envision that the presented flow cytometric assay can be used for various types of peptide-lipid membrane studies, e.g. to identify new antibiotics. Moreover, the assay can easily be expanded to derive additional valuable information.

1. Introduction

Membrane-active peptides (MAPs) have potential applications in biotechnology [1,2], particularly within therapeutics [3–5]. Some MAPs are, for example, antimicrobial peptides (AMPs) that show antimicrobial activity through pore formation in lipid membranes [4,6–8]. These AMPs are receiving increased attention, as pathogenic microorganisms are becoming increasingly resistant towards conventional antibiotics [9]. Another interesting therapeutic application of MAPs is their use as cell-penetrating peptides (CPPs). Introducing a CPP moiety to a drug can improve or facilitate drug internalization through biological membrane barriers [10–14]. In general, peptides are interesting from a drug development perspective, because automated solid-phase peptide synthesis allows for high-throughput synthesis of peptides with variations in the amino acid sequence and/or containing amino acid modifications.

To rationally engineer MAPs for therapeutic applications, it is critical to understand the modes by which they interact with lipid membranes. Current approaches often rely on fluorophore-labeled peptides, which, combined with low-throughput fluorescence microscopy, can provide detailed mechanistic information [15]. However, fluorophore-labeling of peptides can dramatically alter the mode of membrane interaction of the peptides [16]. Many traditional fluorophore-labels have been shown to have a significant affinity towards the lipid membranes [17,18]. Further, the evaluation of therapeutic peptides from large peptide libraries can be a rate-limiting factor in the identification of lead drug candidates due to lack of high-throughput evaluation assays. High- throughput methods that rely on label-free peptides are often limited in revealing mechanistic insights about how MAPs interact with membranes. Among high-throughput assays, the calcein release assay is likely the most commonly used to study lipid membrane perturbations, induced by external agents such as MAPs [1,16,19–22]. This assay relies on the appearance of calcein fluorescence after release from the core of artificial (lipid) vesicles (in the following denoted 'vesicles'). As in many other studies, the vesicles represent a simple model system of cell

*Corresponding authors
E-mail addresses: tlan@dtu.dk (T.L. Andresen), jbak@dtu.dk (J.B. Simonsen).
https://doi.org/10.1016/j.bbamem.2021.183820
Received 9 July 2021; Received in revised form 29 October 2021; Accepted 12 November 2021 Available online 20 November 2021

membranes [21,23–26]. However, the calcein release assay falls short in providing mechanistic information, as it cannot distinguish whether MAP-mediated calcein release is due to vesicle solubilization or localized membrane permeabilization. In addition, it provides no information about vesicle fusion and aggregation, two phenomena that potentially also may lead to calcein release independent of the direct membrane perturbations and, thereby, putative biological activity of the peptides [27].

To overcome some of the limitations associated with the most commonly used methods for studying peptide-lipid membrane interactions, we developed a method based on flow cytometry. A flow cytometer is a microfluidic system equipped with several lasers and corresponding detectors that allow for high-throughput multi-parameter analysis of single particles in terms of their light scattering and fluorescence properties. Properties that can be used to phenotype cells by using fluorophore-labeled antibodies against antigens on specific cell types [28]. Flow cytometry has previously been used to investigate the interactions of MAPs with cells, for example, mapping the time course of AMP-induced permeabilization of bacteria using live/dead DNA-probes [29] and the cell-penetration properties of CPPs fused with GFP [30]. In the latter study, additional microscopy studies were needed to verify that the CPP-GFP compounds were able to penetrate into the cell. A general limitation of traditional flow cytometry is its inability to directly assess whether compounds of interest are at the cell surface or inside the cell [31].

Conventional flow cytometers can also be used to study submicron vesicles [32–34]. In this study, we determined how flow cytometry on dual-fluorophore-labeled vesicles (a core- and a membrane–fluorophore) can be used to study the membrane interactions of label-free MAPs. The concept is shown in Fig. 1, and exemplified by a MAP that leads to pore formation in the vesicle membrane. By using the fluorescence intensity from the membrane-fluorophore as an indirect measure of the vesicle size-integrity in combination with an indirect measure of the vesicle concentration, we could determine whether peptide-dependent reduction in the core fluorescent readout was due to localized membrane permeabilization or vesicle solubilization. In the former case, the vesicle concentration and fluorescence intensity from the membrane fluorophore is unchanged, whereas in the latter case, the vesicle concentration and fluorescence intensity from the membrane- fluorophore decreases. Finally, increases in the membrane fluorescence for individual readouts reveal MAP-induced vesicle fusion/aggregation. Based on the above, we present a flow cytometry assay that provides an integrated platform to study the membrane interactions of peptides on a single vesicle level in detail in a label-free and high- throughput manner.

To evaluate the versatility of our flow cytometric assay, we synthesized six MAPs. Five of the MAPs are well-studied with respect to their membrane interactions, and one is the potent pore-forming peptide macrolittin-70 developed recently [3]. The five known MAPs include the three AMPs melittin [35,36], magainin-2 [37,38], and LL-37 [39], and the two highly cationic CPPs penetratin [40,41] and HIV-derived peptide Tat [42,43]. These MAPs are known to exhibit different modes of action, including membrane permeabilization [3] and membrane solubilization [44,45]. Further, we envision that the highly positively charged CPPs could lead to vesicle aggregation or fusion in membrane-assays when negatively charged vesicles are applied [27].

We verified the flow cytometry findings with data from (i) the traditional high-throughput calcein release assay that measures calcein escape from vesicles, (ii) dynamic light scattering (DLS) that measures the apparent size of the vesicles, and (iii) visual-based fluorescence microscopy studies on giant unilamellar vesicles (GUVs).

2. Results and discussion

2.1. Dual-labeled vesicles used as membrane model in the flow cytometry assay

Previous research have shown that vesicles can be studied by flow cytometry when the membrane of the vesicles is fluorophore labeled [32–34,47]. Therefore, in this study, we prepared large vesicles (LVs) containing 1 mol% of a DOPE lipid conjugated to Atto655 as membrane label (membrane-fluorophore), 20 mol% of the negatively charged POPS lipid to prepare vesicles with an overall net negative membrane charge like biological membranes, and 79 mol% POPC (one of the most commonly used lipids in vesicle studies). In order to detect changes in the barrier properties of the vesicle membrane, we encapsulated the small fluorescent dye Alexa488 inside the core of the vesicles (core-fluorophore). We used an appropriate core-fluorophore concentration of 80 μM that was adequate for detection by flow cytometry without eliciting quenching (Fig. S1 in the Supplementary information (SI)).

The LVs were prepared with diameters spanning between 100 and 1000 nm using a standard lipid film rehydration method [48]. In brief, the mixed lipid films were hydrated in a phosphate buffer (10 mM phosphate, 100 mM NaCl, pH 6.7) containing 80 μM core-fluorophore, freeze-thawed five times, and extruded five times through a 400 nm pore filter followed by size-exclusion chromatography to remove the non-encapsulated core-fluorophore. This preparation method was expected to yield a polydisperse sample of LVs. As a negative control for LVs containing the core-fluorophores, we prepared LVs without core- fluorophore by hydrating the lipid film in the bare buffer.

Classical ensemble/bulk-based characterization techniques such as DLS are not well suited for a study of the size distribution of polydisperse samples or samples containing multiple size populations [49–51]. Along this line, it was not possible to obtain reproducible size

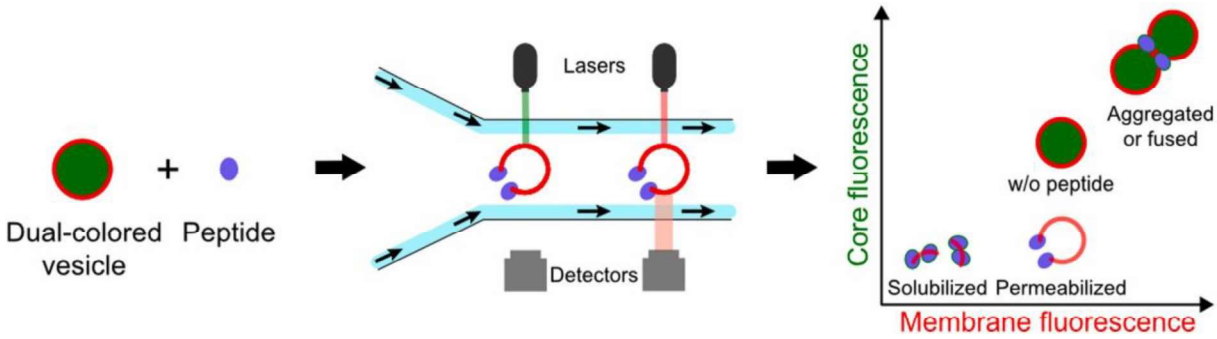

Fig. 1. Concept – applying flow cytometry to identify MAPs' modes of action. The different steps in the peptide-lipid membrane interaction assay. Left: the vesicle-peptide reaction. The red color on the vesicle refers to membrane-anchored fluorophores, and the green color represents the core-fluorophores. Center: The flow cytometry measurement of the reaction mixture. A MAP that induces pore formation in a vesicle is shown – the released core-fluorophore is heavily diluted and thus not shown. Right: The analysis that provides general information on the MAP's mode of action. We can identify the three modes of action: (i) Leakage due to localized membrane permeabilization, (ii) leakage due to membrane solubilization, and (iii) vesicle aggregation/fusion.

populations from DLS measurements (data not shown). Hence, to validate the size distribution of the LVs, we used nanoparticle tracking analysis (NTA), a single-particle characterization tool that tracks the Brownian motion of individual particles in suspension to determine particle size (Fig. 2). Due to its sensitivity and robustness to determine concentration and size distribution of polydisperse, sub-micron particles, NTA has become the gold standard for characterization of the biological vesicles known as extracellular vesicles [52]. With our NTA setup, we were able to track the LVs by one of the following three tracking modes: Light scattering (640 nm), fluorescence from the core-fluorophore (excitation 488 nm, detection >500 nm), and fluorescence from the membrane-fluorophore (excitation 640 nm, detection >660 nm). NTA analysis based on scattering demonstrated that the LVs had a mean diameter of 207 nm and a standard deviation (SD) of the population of 98 nm. The large SD highlights the significant size-heterogeneity of the LV sample. The presence of LV sizes above 400 nm, which is the size of the membrane pores used for extrusion, could be due to defects in some of the pores (we only extruded the LV samples five times) and that larger sized vesicles are modular/flexible and thus able to squeeze through pores smaller than the LVs. Further, studies have shown that LVs formed by rehydration, cycles of freeze-thawing, and extrusion can form LV populations with mean sizes below the pore size of the membrane used for extrusion when the pore size is above 100 nm [33,53]. The size distributions derived from tracking LVs using the membrane-fluorophore fluorescence and core-fluorophore fluorescence overlay well with the scatter- based size distribution, with mean ± SD sizes of 241 nm ± 113 nm and 226 nm ± 90 nm, respectively. The slight discrepancies between the derived mean sizes may be due to different optical sensitivities and settings of the tracking modes. Furthermore, the vesicle concentrations detected by using the three different detection modes are similar ($1.2–2.6 \times 10^7$ particles/mL). Together, the NTA data confirm that we have prepared LVs containing both core-fluorophore and membrane- fluorophore. We also prepared LVs without core-fluorophore. These have a size distribution based on light scattering that was approximately the same (mean ± SD size of 204 ± 90 nm) as the dual-labeled LVs (Fig. 2B). The size distribution based on the membrane-fluorophore fluorescence was slightly larger (mean ± SD size of 281 ± 141 nm). However, in contrast to the dual-labeled LVs, we detected significantly fewer events from the LVs without core-fluorophore when we tracked the LVs using the fluorescence detection used for the core-fluorophore fluorescence, as expected. Together, the NTA data support that we have prepared LVs with sizes and fluorophore-labels that are suitable for flow cytometry.

2.2. Detecting LVs by flow cytometry

To correlate MAP activity with the fluorescence signal in flow cytometry, it was a prerequisite that the dual-labeled LVs could be detected by the flow cytometer and distinguished from the LVs without core-fluorophore. Therefore, we adjusted the vesicle concentration and flow cytometry settings to enable the detection of single LVs by flow cytometry. We triggered the detection of the LV events based on the fluorescence from the membrane-fluorophore in line with previous studies [33]. Using a trigger (threshold) value of 200 arbitrary 'membrane fluorescence intensity' units (AU) gave rise to 800–2300 events per second, of which the bare buffer or non-membrane labeled LVs only accounted for ≤1% of the total count. Therefore, the recorded events for the samples can be considered to be primarily membrane-labeled LVs.

We most likely only detected the largest LVs due to the limited sensitivity of the flow cytometer, and thus, we obtained a membrane-fluorophore fluorescence profile of the LVs (Fig. 3A) that peaks (is cut off) at the threshold value (200 AU). Although we were not able to detect the entire LV population, it is important to note that our assay is not dependent on measuring all LVs. The membrane-fluorophore fluorescence intensity profiles and median fluorescence intensity (MFI) based on the membrane-fluorophore fluorescence (membrane MFI) for the LVs with (membrane MFI = 287 ± 2 AU) and without core-fluorophore (membrane MFI = 293 ± 3 AU) are almost identical, which confirms their similar size distribution derived from NTA (Fig. 2). To ensure that we study individual LVs, we performed an LV dilution series, which is commonly used to optimize the study of individual EVs by flow cytometry [54]. We used an LV lipid concentration (500 nM) that was within the concentration regime that shows a linear correlation between the count rate and the particle concentration, and a constant membrane MFI and fairly constant core MFI (Fig. S2 in SI), and this strongly supported that we mostly detect single LVs [34,54].

We plotted the core-fluorophore fluorescence intensity profiles of LVs with or without core-fluorophore, both triggered by the membrane- fluorophore fluorescence (Fig. 3B). It is clear from the profiles and the corresponding MFI values of the LVs with (104 ± 3 AU) and without core-fluorophore (28 ± 2 AU) that these two different LV samples can be clearly distinguished based on their core MFIs. The symmetric profile of the core-fluorophore fluorescence of the dual-labeled LVs is different from the membrane-fluorophore fluorescence-based profile. The different profiles may in part be due the core fluorescence signal being processed differently to the trigger channel (membrane fluorescence) and some detector variation, and in part due the fact that the membrane fluorescence scales with the area, and the core-fluorescence scales with the volume of the LV. The impact on the triggering strategy was also present when we triggered the LVs on the core-fluorophore; we observed a symmetric membrane-fluorophore fluorescence intensity profile and an asymmetric core-fluorophore fluorescence intensity profile (Fig. S3 in SI). Since we can detect single LVs with and without core-fluorophores, we have the appropriate LV samples and flow cytometry settings in place to study the interaction of MAPs with LV membranes. Importantly, we also tested that the fluorescence readouts from the LVs were constant

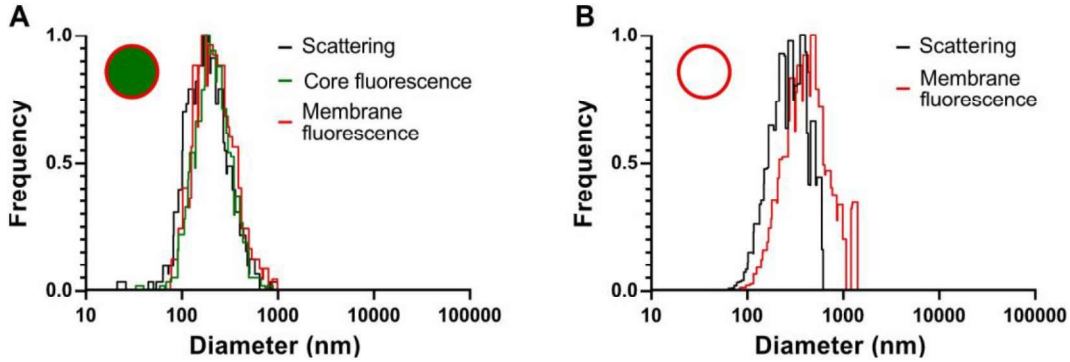

Fig. 2. Size distribution of the LVs. The size distribution of LVs with core-fluorophore (A) and without core-fluorophore (B) derived from NTA measurements. The size distributions are shown for each of the relevant detection modes: Light scattering (black line), core-fluorophore fluorescence (green line), and membrane- fluorophore fluorescence (red line). The inserted circles illustrate the LVs including the position of the fluorophore-labels and their fluorescent colors.

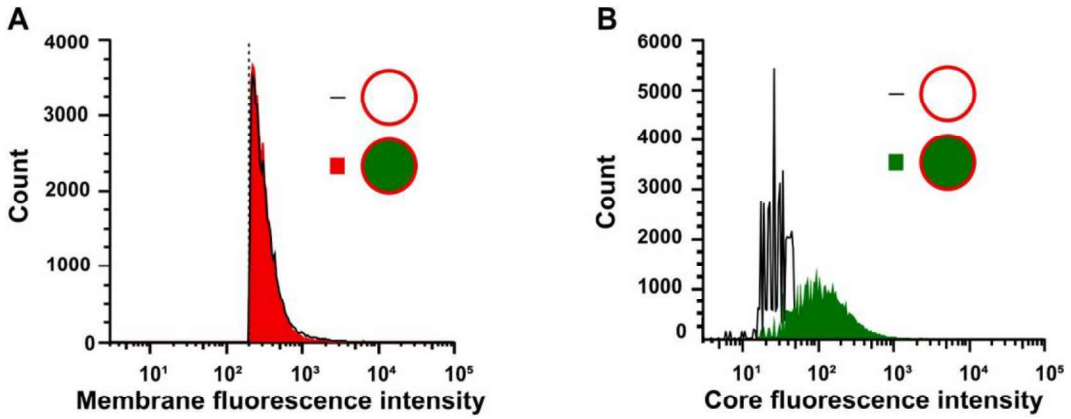

Fig. 3. Flow cytometry data on LVs. Representative histograms based on fluorescence from the membrane-fluorophore triggered at 200 AU (A, membrane fluorescence intensity) and the core-fluorophore (B, core fluorescence intensity) of LVs with (filled, colored) and without (black line) the core-fluorophore. The circles illustrate the LVs, including the position of the fluorophore-labels and their fluorescent colors. The black dotted line in A marks the trigger threshold value. The fluorescence intensities are in AU.

within the timeframe used for the MAP-LVs studies (Fig. S4A and B in SI).

2.3. Synthesis of MAPs

Having established that we can detect the LVs using flow cytometry based on their membrane-fluorophore fluorescence, and distinguish similar LVs with and without core-fluorophore, we aimed to study the effect of peptides on the LVs. For this, we synthesized the MAPs LL-37, melittin, magainin-2, macrolittin-70, Tat, and penetratin (Fig. 4), covering a range of different MAP-membrane interactions including membrane permeabilization, membrane solubilization, and potentially also vesicle aggregation.

All the peptides were prepared by microwave-assisted solid phase peptide synthesis using standard protocols [55]. Briefly, the peptides were synthesized on PAL-AM resin, TentaGel S RAM resin, or a preloaded Wang resin with diisopropylcarbodiimide as coupling reagent, and Oxyma as auxiliary nucleophile. After the final coupling and Fmoc removal, the peptides were cleaved and globally deprotected in trifluoroacetic acid, precipitated in diethyl ether, and purified by high- performance liquid chromatography (HPLC). Identification and purity of the peptides were assessed by mass spectrometry and analytical HPLC, respectively, see Fig. S10–S21 in SI.

2.4. Identifying different types of peptide-lipid membrane interactions

To identify different kinds of peptide-lipid membrane interactions, we mixed each of the six synthesized MAPs with LVs with core-fluorophore to a final MAP concentration of 10 μM and a final LV lipid concentration of 50 μM. The mixtures were incubated at 37 °C for 30–60 min to give the MAPs time to interact with the LVs. Subsequently, the solutions were diluted to a final lipid concentration of 500 nM so it was in the range for single LV detection by flow cytometry.

For magainin-2, macrolittin-70, LL-37, and melittin, the core MFI dropped from 104 ± 4 AU without MAP to 33–39 AU after incubation, which is similar to the core MFI for the LVs without core-fluorophore (core MFI = 28 ± 2 AU) (Fig. 5A). These data show almost complete release of the core-fluorophore when the LVs were exposed to these MAPs. The observations are consistent with these four peptides being known to induce a release of core-content from vesicles [3,24,44,56]. For Tat and penetratin, the core MFI increased about two-fold (Fig. 5A). This was likely due to a peptide-induced aggregation of the anionic LVs,

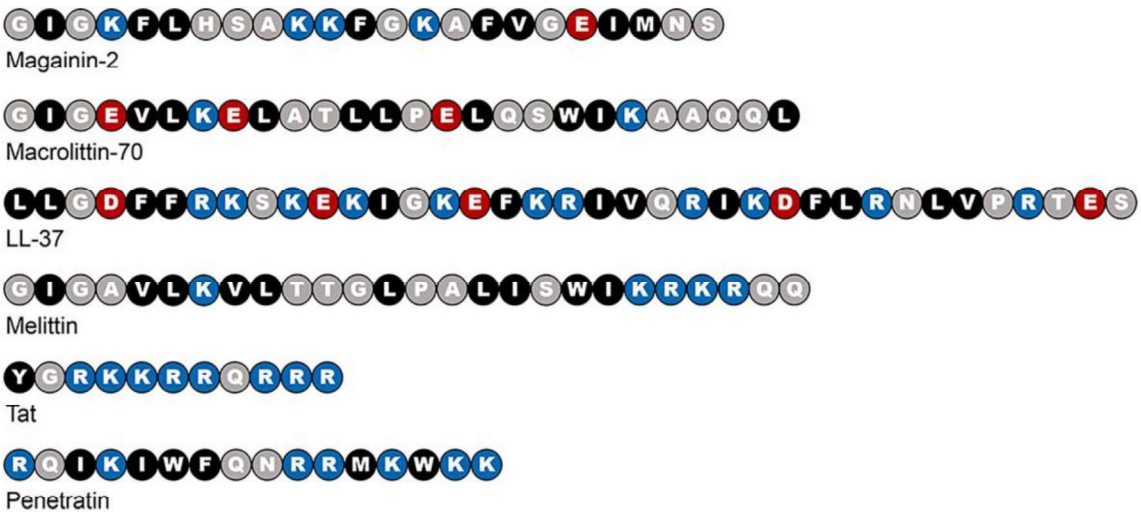

Fig. 4. Amino acid sequence of the synthesized membrane-active peptides (MAPs). Primary sequences, as described using the one letter code, of the MAPs used in this study. Hydrophobic residues are colored black, anionic residues red, cationic residues blue, and all other residues grey. Some of the MAPs are modified in the N- and C-

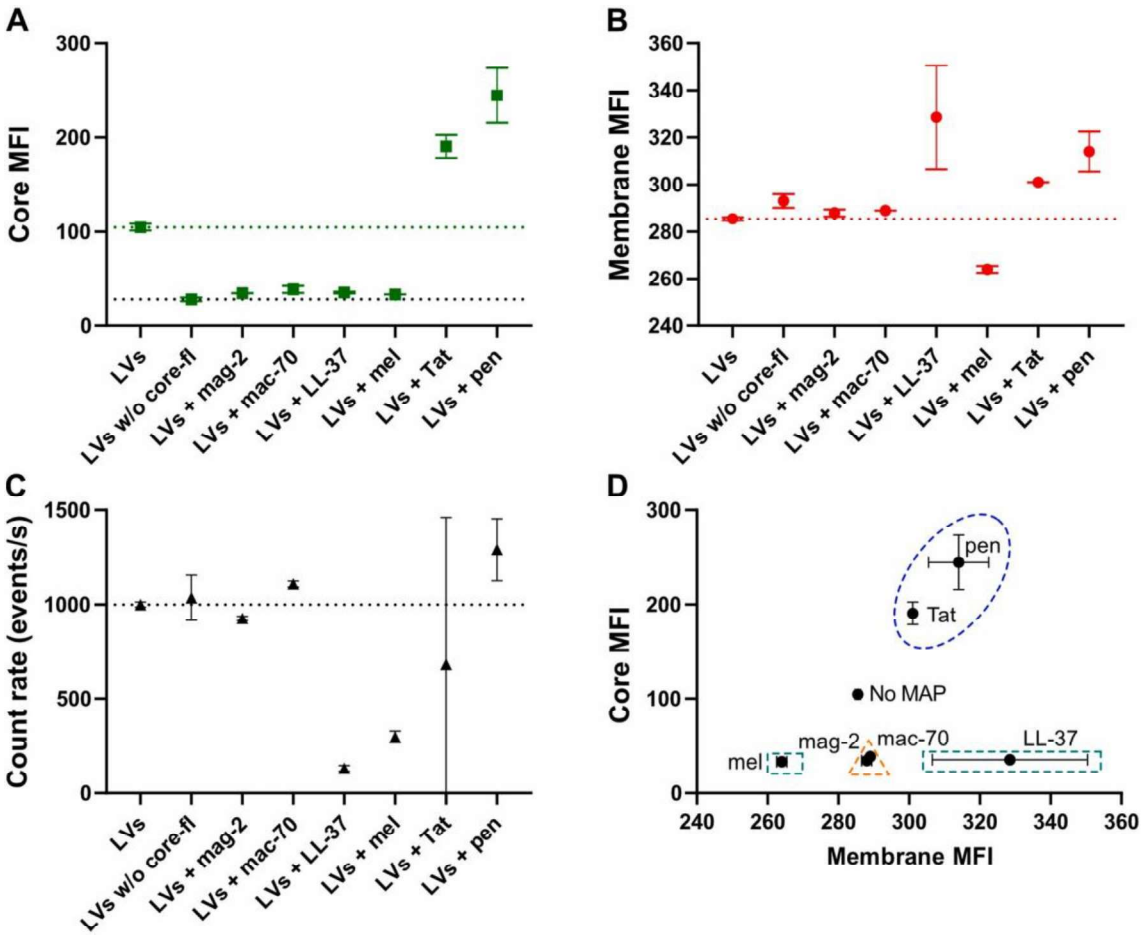

terminus (see Materials and methods section). The anionic and cationic classifications of the residues are based on their expected overall charge at the pH condition used in this study (pH 6.7).

Fig. 5. Flow cytometry measurements of LVs in the absence and presence of MAPs. Core MFI (A), membrane MFI (B), and count rate (C) for LVs with core- fluorophore in absence (LVs) or presence of MAPs (LVs + MAP) as well as for LVs without core-fluorophore (LVs w/o core-fl). (D) Scatter plot based on the membrane and core MFI values, with each point being labeled with the respective MAP. MAPs leading to core-fluorophore release without solubilization are marked with an orange triangle, MAPs leading to core-fluorophore release and solubilization are marked with a turquoise square, and MAPs leading to aggregation of the LVs are marked with a blue circle. The shown data are averages of two replicates and their standard deviation. mag-2: magainin-2, mac-70: macrolittin-70, mel: melittin, pen: penetratin. The MFI values are in arbitrary units.

as penetratin and Tat are both highly positively charged at the pH level used in this study (pH 6.7), as illustrated in Fig. 4. While it should be emphasized that the flow cytometry assay cannot distinguish between LV aggregation or fusion, previous studies support the notion that highly positively charged peptides can form aggregations of negatively charged vesicles [57,58].

To investigate the state of the LV membrane upon reaction with the MAPs, we studied the membrane MFI (Fig. 5B). The membrane MFI of the LVs did not differ much for the LVs exposed to magainin-2, macrolittin-70, or no MAP. This supports the interpretation that these MAPs led to increased membrane permeability without disrupting the LVs with respect to size, which is consistent with these MAPs forming pores as shown in the literature [3,59]. For melittin, however, the membrane MFI dropped, and for LL-37, the membrane MFI increased, indicating that the membrane was affected. In agreement with this, the count rate was almost unaffected for the LVs that were exposed to magainin-2 or macrolittin-70, and it decreased dramatically for the LVs that were exposed to LL-37 or melittin (Fig. 5C). This corroborates earlier finding using bulk assays [44,45] and suggests that LL-37 and melittin solubilize the membrane of a majority of the LVs. Ladokhin and White [45] found that melittin functions in a detergent-like manner for anionic vesicles, which supports our flow cytometry findings. For LL-37, the solubilization is consistent with the study by Sancho-Vaello et al. [44]. The increased membrane MFI with a dramatic drop in core MFI and drop in count rate could be a result of the LL-37 forming a few large aggregates with the membrane-fluorophore. It should be mentioned that LL-37 is a large amphipathic peptide comprised of 37 amino acids (Fig. 4). Hence, it is likely that it can form large LL-37-lipid aggregates.

For Tat and penetratin, both the core- and membrane MFI increased, supporting LV aggregation or fusion mediated by these highly cationic peptides (Fig. 5A and B). The corresponding count rate data may at first glance contradict our aggregation/fusion interpretation as the count rate clearly increased in the penetratin case (Fig. 5C). However, since we only detected a fraction of the LVs, the LVs that otherwise go undetected could, if they aggregate of fuse, get above the triggering threshold and thus add to the total count rate. The count rate data on Tat varied a lot (Fig. 5C). We therefore performed a separate quadruplicate flow cytometry study on Tat that clearly showed that the count rate of LVs + Tat was also increased compared to the bare LV control (Fig. S5 in SI) like in the penetratin case. Hence, all the measurable parameters support the assumption that highly positively charged peptides like Tat and penetratin likely form aggregates with the negatively charged LVs, and that they do not permeabilize the LVs.

To assign the mode of action for a given MAP, we plotted the core and membrane MFI values from the LVs as a scatter plot in Fig. 5D. This plot, together with the measured count rates, can help assign MAPs to the various known modes of action, including membrane per-

meabilization, membrane solubilization, and vesicle fusion/ aggregation. To ensure that our findings were reproducible on a day-to-day basis, we conducted the same kind of measurements on other days and got similar results (Fig. S4C-E in SI). We also showed that working at higher LV concentrations, i.e., studying a significant proportion of co- particle events, also lead to the same assigned modes of action (Fig. S6 in SI). The latter condition obviously gave rise to a higher signal, which can be useful if the signal-background resolution is low when studying single LV events. Along these lines, it is important to emphasize that the choice of LVs in terms of size and degree of fluorophore-labeling used for the flow cytometric assay depends to some extent on the sensitivity of the flow cytometer being used. To investigate whether attractive electrostatic interactions play a role in the formation of LV aggregates/ fusion, we performed a head-to-head experiment with Tat exposed to the negatively charged LVs containing POPS (the LVs used so far), and to neutral LVs without the negatively charged POPS (Fig. 6A). The relatively high membrane MFI value measured for the Tat-anionic LV mixture indicates that Tat forms larger aggregates with the negatively charged LVs than with the neutral LVs. It is known that LVs comprised of only zwitterionic phosphatidylcholine lipids (like in our case) are slightly negatively charged. This small negative surface might be enough for Tat to mediate some aggregation/fusion. Corresponding data based on the core-fluorophore supports that Tat forms the largest aggregates with the anionic LVs (Fig. S7A in SI).

Previous studies have shown that magainin-2 induces permeabilization in negatively charged vesicles, but not in neutral vesicles [60,61]. We confirmed these findings using the flow cytometric assay (Fig. 6B). It is clear that magainin-2 led to a decrease in the core MFI only for the negatively charged LVs. The complementary membrane-fluorophore data supports the interpretation that the decrease in core MFI is not due to solubilization of the LVs (Fig. S7B in SI).

We have successfully developed a flow cytometer assay that allowed us to distinguish between peptides that: (i) led to increased membrane permeability without solubilization (magainin-2 and macrolittin-70), (ii) led to solubilization of the LVs and release of core-fluorophore (LL-37 and melittin), and (iii) did not lead to core-fluorophore release, but rather aggregation of the LVs (Tat and penetratin) (Fig. 5D). In its current form, our assay cannot assess whether translocation of the CPPs Tat and penetratin takes place. Rather, our data highlight potential interactions or artifacts in peptide-lipid membrane studies when we use highly positively charged peptides in combination with negatively charged LVs.

It should be noted that the flow cytometric assay based on non-fluorophore-labeled MAPs have a few other limitations: It does not distinguish between MAPs that do not bind to LVs on the one hand, and MAPs that do bind and/or penetrate the LV membrane but do not lead to (i) release of the core-fluorophore (ii) and/or fusion and aggregation of LVs on the other. One way to overcome this binding issue is to fluorophore-label the MAP. One key feature of flow cytometry is its ability to analyze multiple different fluorescence parameters on single particles. Conventional flow cytometers can simultaneously measure and distinguish between fluorescence from 3 to 30 optically different fluorophore labels. That said, the aim with this project was to introduce a non-labeled MAP assay, as the introduction of fluorophore-labels can lead to alterations in the membrane interactions of MAPs [16–18].

2.5. Verifying our flow cytometry findings

To validate our observations from multi-parameter flow cytometry based on our chosen vesicle compositions, sizes, MAP: LV ratio and concentrations, we performed several complementary studies. This comparison is important, because certain MAPs can both permeabilize and solubilize vesicles [62]. Whether the former or latter mechanism takes place depends on the concentrations of the MAP and lipids/LVs.

To support our core-fluorophore release data based on flow cytometry, we performed the traditional calcein release assay on calcein- containing LVs (cLVs), using the same total lipid and MAP concentrations as in our flow cytometry studies. The calcein release assay is a bulk measurement that relies on vesicles loaded with calcein in the aqueous core, which are in a quenched state due to the high local calcein concentration. When calcein is released from the core of the vesicles to the surroundings, the fluorescence signal from the calcein increases due to dequenching. In the calcein release assay, 0% calcein release refers to the fluorescence intensity of the bare cLVs, and 100% calcein release refers to the fluorescence intensity for the cLVs solubilized by the Triton X-100 detergent. The calcein release was measured after 30 min. The calcein release (Fig. 7A) and the core-fluorophore release derived from flow cytometry (Fig. 5A) are very similar for magainin-2 and macrolittin-70. LL-37 and melittin show complete release, while no release was measured for Tat and penetratin (Fig. 7A). These results are also well aligned with the flow cytometry data (Fig. 5A). We also measured calcein release after 60 min and 120 min (Fig. S8 in SI). We found that the calcein release data at 30–60 min were similar to data obtained at 120 min. Therefore, measuring the mixtures on the flow cytometer after 30–60 min appears to be at, or close to, a steady-state condition for all the MAPs. Together, we observed a good agreement between the membrane activities derived from the flow cytometry

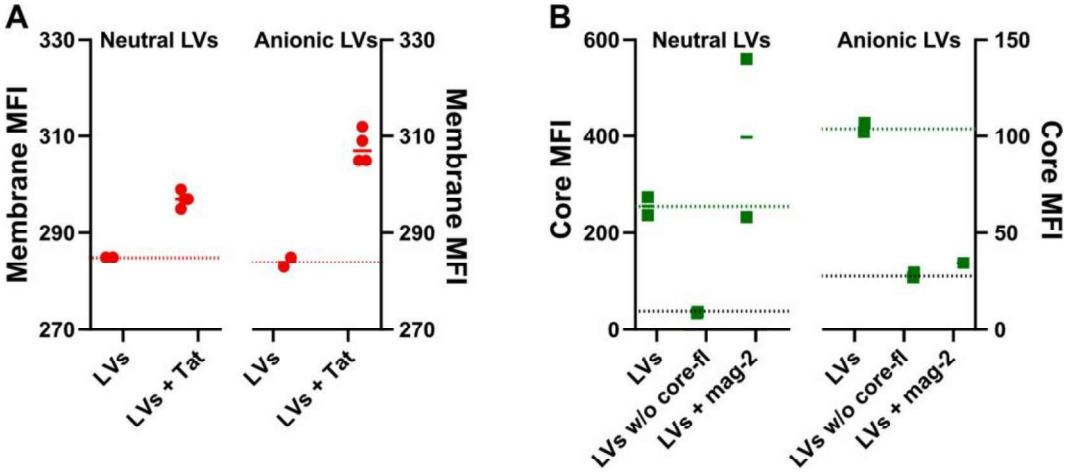

Fig. 6. Distinguishing MAP effects on neutral and anionic LVs. Membrane MFI (A) and core MFI (B) for LVs with core-fluorophore in absence (LVs) or presence (LVs + MAP) of a MAP, as well as for LVs without core-fluorophore (LVs w/o core-fl). The membrane of the LVs are either neutral (left) or negatively charged (right) in both (A) and (B). The short solid colored lines represent the average of the shown MFIs for LVs exposed to a MAP. The dotted, colored lines show the average of the MFI for the

neutral and charged LVs in the absence of a MAP. The dotted black lines are the average of the MFI for the neutral and charged LVs w/o core-fl. The MFI values are in arbitrary units.

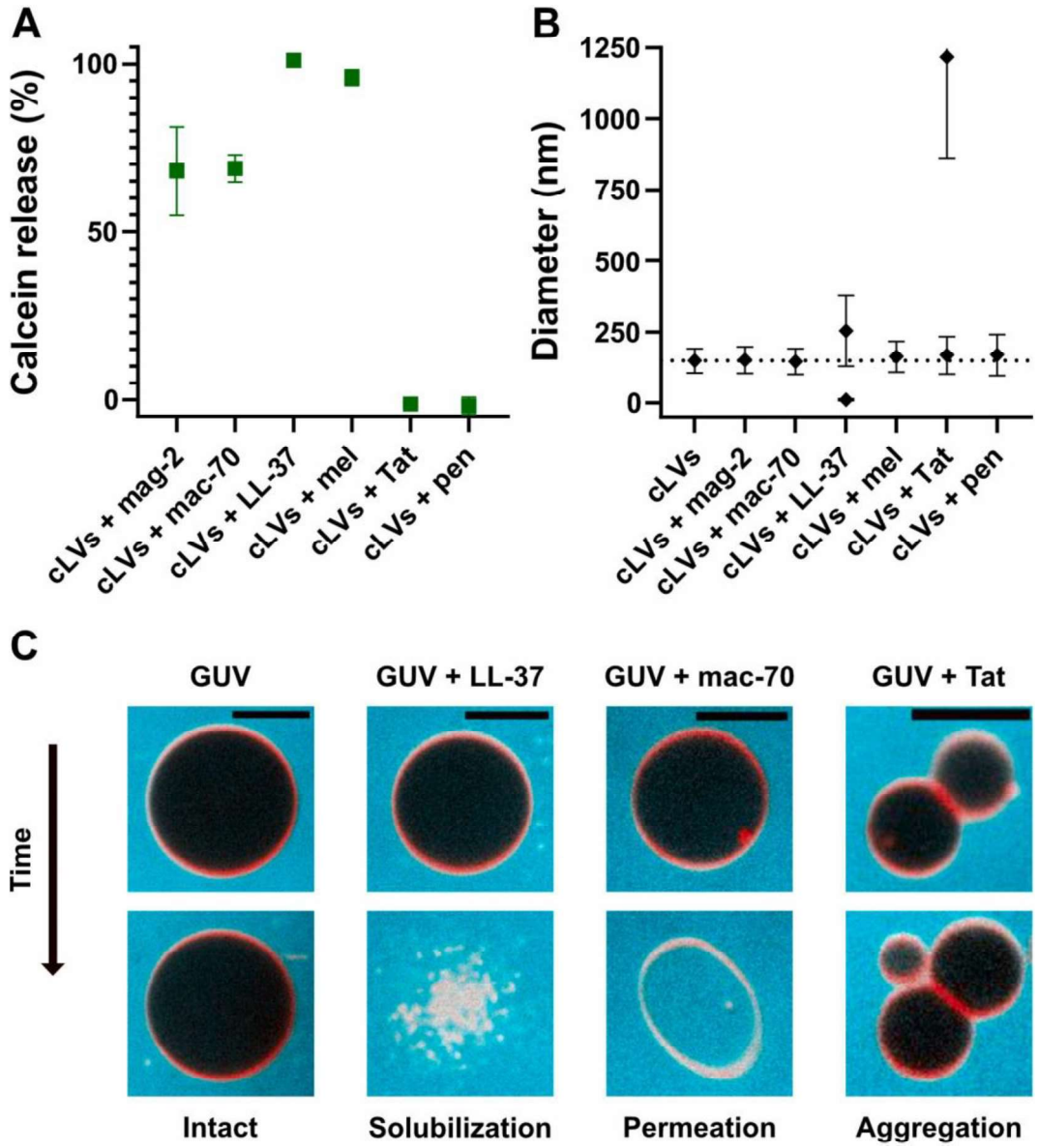

Fig. 7. Complementary data to verify our flow cytometry findings. (A) MAP-induced calcein release from cLVs after 30 min. 0% release is defined from the fluorescence intensity of bare cLVs, and 100% release is defined from the fluorescence intensity of cLVs solubilized by the Triton X-100 detergent. Each data point is the average of two independent measurements and their standard deviation. (B) Apparent diameter of cLVs in the presence of each of the MAPs as determined by DLS. Each data point represents the average of at least five measurements on two independent samples, and the corresponding standard deviation. The dotted line shows the bare cLVs. (C) MAP interactions with GUVs studied by fluorescence microscopy. Calcein is shown in cyan, and GUV membranes in red. A black GUV core indicates a tight non-leaking GUV membrane barrier. The first column from left displays a control GUV without peptide at 1:43 min:sec (top) and at 42:45 min:sec (bottom). The second column displays a GUV incubated with LL-37 at 6:40 min:sec (top) and at 6:55 min:sec (bottom). The third column display a GUV incubated with macrolittin-70 at 3:31 min:sec (top) and at 4:16 min:sec (bottom). The fourth column displays a GUV incubated with Tat at 3:27 min:sec (top) and at 31:56 min:sec (bottom). Scale bar: 10 µm. mag-2: magainin-2, mac-70: macrolittin-70, mel: melittin, pen: penetratin.

studies and the traditional calcein assay. That said, it should be noted that the flow cytometry assay provides information that is not accessible by the calcein assay, as it reveals the mechanisms behind the fluorophore leakage.

DLS data on the cLVs were used to investigate the integrity (with respect to size) of the cLVs upon MAP exposure in order to complement and verify the membrane fluorescence flow cytometry data. The magainin-2 and macrolittin-70 DLS data (Fig. 7B) are consistent with the flow cytometry, which shows that the LVs are intact (Fig. 5). In case of the LL-37, the DLS analysis gave rise to two size populations (Fig. 7B). One smaller (11 ± 3 nm) and one larger (253 ± 124 nm) than the 152 ± 46 nm for the untreated cLVs. A DLS analysis based on particle-volume that is less biased towards the larger particles, which scatter much more than small particles (data presented in Fig. 7B are based on the intensity- weighted analysis), showed that the population with the smaller size was the most abundant size-population (Fig. S9A in SI). This is in good agreement with our flow cytometry findings, including the count rate and membrane fluorescence data: LL-37 dissolves the LVs and form micelles (too small to be detected by flow cytometry) and a few larger aggregates (detected by flow cytometry). The DLS data on the CPPs Tat and penetratin are more ambiguous. In case of Tat, two populations were observed, one with a size similar to unaffected

vesicles, and another with a much larger size, and with a large variation, in line with potential vesicle aggregation taken place. This pattern is consistent for the DLS analysis based on volume (Fig. S9B in SI). The two size populations of Tat probably occurred because only vesicles with a sufficient amount of Tat bound are able to aggregate. The size of the cLVs exposed to penetratin indicates a slight increase compared to the non-treated cLVs, supporting the conclusion from flow cytometry that penetratin mediates vesicle aggregation/fusion.

Finally, we decided to perform a visual inspection of the proposed modes of action for the peptides by fluorescence microscopy. To do this, we prepared GUVs consisting of POPC, POPS and DOPE-Atto655 in a molar ratio of 79.5:20:0.5 (similar to the LV composition used for the flow cytometry studies) via electroformation using a sucrose solution for the formation protocol [63]. The GUVs were added to a glucose solution with 50 μM calcein in a BSA-passivated glass-bottom observation chamber. Lastly, the peptides were added and a time lapse recording was initiated with a temporal resolution of 15 s. We employed LL-37, macrolittin-70, and Tat for this study, as they represent LV solubilization, permeabilization, and aggregation/fusion modes of action, respectively. The upper row of images in Fig. 7C were recorded shortly after we added the MAPs to the observation chamber, while the images in the lower row show examples of how individual GUVs were modified due to their interaction with the MAPs at a later time point. It is clear that LL-37 solubilizes the GUV (within a 15 s timeframe), and that macrolittin-70 permeabilizes the GUV, as the surrounding calcein diffuse into the GUV core. The macrolittin-70 treated GUVs were solubilized at a later time point (Table S1 in SI). This observation shows that certain MAPs are able to both introduce permeability and to solubilize vesicles depending on the MAP and lipid concentrations. In the case of Tat, aggregation was immediately observed after addition (Fig. 7C, top row) and only increased over time (Fig. 7C, bottom row). It is evident from these studies that Tat does not mediate permeabilization of the GUVs, as the surrounding calcein stays outside the GUVs. These images are representative for the GUVs observed, and statistics for the GUVs are shown in Table S1. The GUV-studies confirmed the three different modes of action triggered by LL-37, macrolittin-70, and Tat that were derived from the flow cytometry analysis.

To sum up, the complementary studies, including the calcein release assay, DLS, and fluorescence microscopy on GUVs, support our flow cytometry findings, and thus verify that flow cytometry is a powerful technique to reveal how peptides interact with vesicles. Key advantages of the flow cytometry assay over the traditional methods include: (i) The flow cytometry assay is a high-throughput assay, unlike microscopy, and allowed us to detect 1000–2000 individual vesicles per second with limited time spent on sample preparation; (ii) label-free peptides can be used in this assay; (iii) detailed information about some of the most common modes of action between peptides and lipid membranes can be derived from the multi-readouts from individual LVs. Several other readouts/parameters can be added to the flow cytometric assay, including light scattering and additional fluorescence signals/probes. Further, the effects of lipid composition of the LV-based membrane- model system and time on the peptide-lipid membrane interactions can be studied with the flow cytometry-based assay. Finally, a detailed analysis of the fluorescence histograms may also provide insights into whether leakage is of a graded or all-or-none type [64]. Thus, the flow cytometry assay displays many of the same strengths as previous advanced fluorescence-based assays developed in our laboratory [65,66], but with the added benefit of requiring less specialized equipment, simpler work procedures, and non-customized data analysis software.

3. Conclusions

We have shown that flow cytometry can be used to identify different modes of action between membrane-active peptides and lipid membranes. These modes of action include membrane permeabilization, solubilization, and vesicle aggregation/fusion. The different mechanisms derived from the flow cytometry studies were confirmed by a bulk calcein release assay, DLS, and fluorescence microscopy studies on GUVs. Some of the attractive features of the presented flow cytometric assay are that: (i) it is a high-throughput assay (~2000 particle/s) with limited time spent on sample preparation, (ii) it can measure several parameters on single particles, including membrane-fluorophore fluorescence of LVs, core-fluorophore fluorescence of LVs and relative LV concentrations in our case, and (iii) flow cytometers are commonplace in many research laboratories, and thus accessible for many researchers. We believe that the flow cytometric assay presented here can be used for various types of peptide-membrane studies, e.g. to identify new antibiotics. Moreover, the assay can easily be expanded to derive additional valuable information.

4. Materials and methods

4.1. Materials

Calcein, sodium dihydrogen phosphate, sodium chloride (NaCl), dimethylformamide (DMF), piperidine, dichloromethane (DCM), trifluoroacetic acid (TFA), triisopropylsilane (TIPS), diethylether, acetonitrile (MeCN), resins (Fmoc-Ser(tBu)-Wang, Fmoc-Leu-Wang resin, Fmoc-Arg(Pbf)-Wang Fmoc-PAL-AM, TentaGel S RAM), bovine serum albumin (BSA), sucrose, D-(+)-glucose, phosphate buffered saline (PBS), and Triton X-100 were purchased from Sigma-Aldrich (St. Louis, MO, USA). Chloroform and methanol were purchased from VWR Chemicals (Radnor, PA, USA). 1-Palmitoyl-2-oleoyl-*sn*-glycero-3-phosphocholine (POPC) and 1-palmitoyl-2-oleoyl-*sn*-glycero-3-phospho-L-serine sodium salt (POPS) were purchased from Avanti Polar Lipids (Alabaster, AL, USA). 1,2-Dioleoyl-*sn*-glycero-3-phosphoethanolamine-Atto655 (DOPE- Atto655) was purchased from Atto-Tec (Siegen, Germany). Alexa Fluor 488 hydrazide (Alexa488) was purchased from Thermo Fisher Scientific (Waltham, MA, USA). Slurry for preparing Sepharose CL-4B columns was purchased from GE Healthcare (Little Chalfont, UK). Econo-Column glass chromatography column (dimensions 1.5 × 20 cm) was purchased from Bio-Rad (Hercules, CA, USA). Q-Max syringe filters with 0.22-μm cellulose acetate filtration membranes were purchased from Frisenette (Knebel, Denmark). Standard fluorenylmethoxycarbonyl (Fmoc)-protected amino acids, ethyl (hydroxyimino)cyanoacetate potassium salt (Oxyma) and diisopropylcarbodiimide (DIC) were purchased from Iris-Biotech (Marktredwitz, Germany). Micro-slide 8 well glass bottom was purchased from Ibidi (Grafelfing, Germany). All chemicals were of re¨ agent grade.

4.2. Vesicle preparation

We prepared the LVs for flow cytometry by dissolving the lipids in neat chloroform, mixed in the molar ratios mentioned in Table 1. The organic solvent was removed under a gentle nitrogen flow. Residual solvent was removed by placing the samples in vacuum (0.2–0.5 mbar) for approximately 2 h. Phosphate buffer (10 mM sodium phosphate, 100 mM NaCl, pH 6.7), filtered through a 0.22 μm sterile filter, with or without 80 μM Alexa488, as stated in Table 1, was added to the lipids, and the resulting lipid suspension was vortexed gently every 5 min over a period of 30 min and then subjected to five freeze-thaw cycles by alternate placement in a 70 °C water bath and a liquid nitrogen bath. Subsequently, the lipid suspension was extruded five times through a 400-nm polycarbonate membrane (Whatman, GE Healthcare) using a mini-extruder (Avanti Polar Lipids). For vesicle preparations containing Alexa488, excess Alexa488 was removed from the vesicles by size-exclusion chromatography using a Sepharose CL-4B column (dimensions 1.5 × 20 cm) eluted with phosphate buffer at a flow rate of 1 mL/min. For column-purified vesicles, the vesicles were added to

an Amicon Ultra-4 100 kDa centrifugal filter unit (Merck, Darmstadt, Germany) and concentrated by centrifuging at 2000 ×*g*.

Table 1
Name of vesicle formulation as used in this article, the corresponding lipid composition, fluorophore encapsulated in the core, and in which type of measurements the vesicles were used.

Sample name	Lipid composition (molar ratio)	Core-fluorophore	Measurement
Anionic LVs with core-fluorophore	POPC:POPS:DOPE-Atto655 (79:20:1)	80 μM Alexa488	Flow cytometry
Anionic LVs without core- fluorophore	POPC:POPS:DOPE-Atto655 (79:20:1)	No fluorophore	Flow cytometry
Neutral LVs with core-fluorophore	POPC:DOPE-Atto655 (99:1)	80 μM Alexa488	Flow cytometry
Neutral LVs without core- fluorophore	POPC:DOPE-Atto655 (99:1)	No fluorophore	Flow cytometry
cLVs	POPC:POPS (80:20)	60 mM calcein	Calcein release assay and DLS
GUVs	POPC:POPS:DOPE-Atto655 (79.5:20:0.5)	No fluorophore	Microscopy

cLVs were also prepared. This was done using a protocol similar to that described above for Alexa488-containing vesicles, except that (i) initial dissolution of the lipids was done using chloroform:methanol (9:1 V/V ratio), (ii) hydration of the lipids was done using a calcein solution (60 mM calcein, 10 mM sodium phosphate, pH 6.7 prepared using Milli- Q water filtered using a 0.22 μm sterile filter), (iii) extrusion was done 21 times through a 100-nm polycarbonate membrane (Whatman). GUVs were prepared via electroformation using a Digimess HUC65- 00 FG100 function generator using a procedure modified from Wheaten et al. [67]. The lipids (POPC:POPS:DOPE-Atto655) were mixed in a 79.5:20:0.5 molar ratio in chloroform (see Table 1) for a final concentration of 1 mM and stored at minus 20 °C until use. 20 μL of the chloroform solution was deposited equally on two platinum rods, which were connected to a custom-made Teflon support. Both the Teflon support and rods were kept in vacuum for at least 1 h to ensure efficient removal of chloroform. The GUVs were then produced by immersing the rods into a 226 mM sucrose solution and applying an AC field. To produce high quality GUVs, a constant sine wave shaped peak-to-peak voltage of 3.5 V was used in combination with three different frequency settings. First 10 Hz was used for 2 h, then 5 Hz for 10 min, and finally 1 Hz for 10 min. The GUVs were harvested using a 500 μL glass syringe (Hamilton Company, Bonaduz, Switzerland), kept at room temperature and used within 48 h.

The phosphorus concentration of the LV and cLV samples was determined using inductively coupled plasma mass spectrometry (ICP-MS, done on an iCAP Q ICP-MS, Thermo Fischer Scientific). The phospholipid concentration was then estimated by subtracting the contribution of the 10 mM phosphate buffer. Hence, the lipid concentration presented above refers to the phospholipid concentration measured by ICP-MS.

The LVs used for the flow cytometry measurements may be a mixture of uni- and multilamellar LVs. This does, however, not seem to affect our results, as our results are supported by complementary studies, including the calcein release assay and DLS data, which are based on LVs extruded through a 100 nm filter, and thus assumed to be unilamellar, and fluorescence microscopy on GUVs that are unilamellar.

4.3. Nanoparticle tracking analysis (NTA)

The samples under investigation were diluted to ~150 nM vesicles (concentration in terms of lipid) in phosphate buffer. The NTA measurements were performed using a ZetaView Particle PMX-220 TWIN 488/640 nm (Particle Metrix, Meerbusch, Germany). For the light scattering-based tracking a 640 nm laser was used. This laser was also used to excite/track the LVs based on the fluorescence from the membrane-fluorophore, while a 488 nm laser was used to excite and track the LVs based on the fluorescence from the core-fluorophore. Camera sensitivity of 75, 90, and 85 were used, respectively, and exposure times of 1/100 s, 1/70 s, and 1/100 s, respectively. The measurements were carried out at approximately 25 °C, for three cycles at 11 different positions, with a measurement rate of 30 frames/s. Data were analyzed using the ZetaView 8.04.02 software.

4.4. Synthesis and purification of MAPs

All peptides were synthesized at 0.2 mmol scale on a Biotage Initiator+ Alstra microwave-assisted peptide synthesizer using standard Fmoc-protected amino acids. Fmoc-deprotection was performed by addition of deprotection solution (20% piperidine in DMF, 0.1 M Oxyma) to the resin, heating at 75 °C for 2 min, drained and washed once with DMF. New deprotection solution was added, heating was repeated at 75 °C for 5 min, and the resin was drained and washed 5 times with DMF. Coupling of the amino acid was performed by addition of the required amino acid solution (5 eq. of Fmoc-amino acid, 5 eq. Oxyma in DMF, 0.3 M) and DIC solution (2 M DIC in DMF). The resin was heated at 75 °C for 10 min, drained and washed once with DMF, and the coupling was repeated. After the second coupling, the resin was washed 4 times with DMF. After deprotection of the final amino acid residue, the resin was washed 5 times with DMF, 5 times with DCM and dried by suction for 15 min. For arginine residues, the coupling times were 25 min and 5 min. For histidine residues the temperature was lowered to 50 °C.

The peptidyl-resin was suspended in cleavage cocktail (95% TFA, 2.5% water, 2.5% TIPS) for 1 to 4 h. The peptide-cleavage mixture was filtered off, and precipitated in cold diethylether, centrifuged, decanted and triturated (twice). The crude peptides were purified on a Dionex Ultimate 3000 reverse phase-high performance liquid chromatography (RP-HPLC) system equipped with a RQ variable wavelength detector and an automated fraction collector using a Phenomenex Gemini NX 5u, C18, 110 Å, 250 mm × 30 mm column at a 20 mL/min flow rate. RP- HPLC gradients were run using a solvent system consisting of solution A (H_2O + 0.1% TFA) and B (MeCN + 0.1% TFA). Pure fractions were combined and lyophilized. The purified peptides were analyzed on a Shimadzu NexeraX2 RP-HPLC system equipped with Shimadzu LC- 30AD pumps, a Shimadzu SIL-30AC autosampler, a CTO-20 AC column oven and a Shimadzu PDA detector (monitoring at 214 nm and 280 nm) using a Waters XBridge BEH C18, 2.5 μm 3.0 × 150 mm XP column at a flow rate of 0.5 mL/min. RP-HPLC gradients were run using a gradient from 0% to 50% of solution B over 10 min. The pure peptides were characterized by mass spectrometry using either a Bruker matrix assisted laser desorption ionization time of flight mass spectrometry (MALDI-TOF-MS) Autoflex speed or on a Waters Acquity Ultra Performance UPLC equipped with a QDa detector and an Acquity UPLC BEH C18, 1.7 μm, 2.1 × 50 mm column.

4.4.1. Characterization of the MAPs

4.4.1.1. Magainin-2. The magainin-2 sequence H-GIGKFLHSAKKFGKAFVGEIMNS-OH was synthesized on a pre-loaded Fmoc-Ser(tBu)- Wang resin (loading 0.63 mmol/g) using the synthesis procedure described above. After cleavage for 1 h, precipitation and RP-HPLC purification (10–40% B over 40 min) the desired peptide was obtained in 4% yield (Nanodrop (A214)) and 95% purity (HPLC) (Fig. S10 in SI). LC-MS (Electrospray ionization (ESI)) *m/z*: = $[M + 5H]^{5+}$ = 494.4 (calcd. 494.4), $[M + 4H]^{4+}$ = 617.8 (calcd. 617.7), $[M + 3H]^{3+}$ = 823.2 (calcd. 823.3) (Fig. S11 in SI).

4.4.1.2. Macrolittin-70. The macrolittin-70 sequence H-GIGEVLKELATLLPELQSWIKAAQQL-OH was synthesized on a pre-loaded Fmoc-Leu- Wang resin (loading 0.70 mmol/g) using the synthesis procedure described above. After cleavage for 1 h, precipitation and RP-HPLC purification (15–80% B over 40 min) the desired peptide was obtained in 23% yield (Nanodrop (A280)) and 91% purity (HPLC) (Fig. S12 in SI). MALDI-TOF- MS *m/z*: $[M + Na]^+$ = 2871.37 (calcd. 2871.35) (Fig. S13 in SI).

4.4.1.3. LL-37. The LL-37 sequence H-LLGDFFRKSKE-KIGKEFKRIVQRIKDFLRNLVPRTES-OH was synthesized on a pre-loaded Fmoc-Ser(tBu)-Wang resin (loading 0.63 mmol/g) using the synthesis procedure described above. After cleavage for 4 h, precipitation and RP- HPLC purification (20–50% B over 60 min) the desired peptide was obtained in 8% yield (Nanodrop (A214)) and 100% purity (HPLC) (Fig. S14 in SI). MALDI-TOF-MS *m/z*: $[M + H]^+$ = 4493.28 (calcd. 4493.34) (Fig. S15 in SI).

4.4.1.4. Melittin. The melittin sequence H-GIGAVLKVLTTGL PALISWIKRKRQQ-NH_2 was synthesized on TentaGel S RAM resin (loading 0.23 mmol/g) using the synthesis procedure described above. After cleavage for 4 h, precipitation and RP-HPLC purification (20–60% B over 40 min) the desired peptide was obtained in 4% yield (Nanodrop (A280)) and 99% purity (HPLC) (Fig. S16 in SI). LC-MS (ESI) *m/z*: = $[M + 6H]^{6+}$ = 475.4 (calcd. 475.4), $[M + 5H]^{5+}$ = 569.9 (calcd. 570.3), $[M + 4H]^{4+}$ = 712.3 (calcd. 712.6), $[M + 3H]^{3+}$ = 949.7 (calcd. 949.8) (Fig. S17 in SI).

4.4.1.5. Tat. The Tat sequence H-YGRKKRRQRRR-OH was synthesized on a pre-loaded Fmoc-Arg(Pbf)-Wang resin (loading 0.64 mmol/g) using the synthesis procedure described above. After cleavage in TFA-TIS-thioanisole-water (90%/2.5%/2.5%/5%) for 16 h, precipitation and RP-HPLC purification (1% B for 10 min then 1–50% over 33 min) the desired peptide was obtained in 3% yield (Nanodrop (A280)) and 99% purity (HPLC) (Fig. S18 in SI). LC-MS (ESI) *m/z*: = $[M + 5H]^{5+}$ = 312.9 (calcd. 313.0), $[M + 4H]^{4+}$ = 391.1 (calcd. 391.0), $[M + 3H]^{3+}$ = 521.1 (calcd. 521.0), $[M + 2H]^{2+}$ = 780.5 (calcd. 780.9) (Fig. S19 in SI).

4.4.1.6. Penetratin. The penetratin sequence H-RQIKIWFQNRR MKWKK-NH_2 was synthesized on Fmoc-PAL-AM resin (loading 0.61 mmol/g) using the synthesis procedure described above. After cleavage for 4 h, precipitation and RP-HPLC purification (10–40% B over 40 min) the desired peptide was obtained in 21% yield (Nanodrop (A280)) and 93% purity (HPLC) (Fig. S20 in SI). Liquid chromatography-MS (LC-MS)

(ESI) *m/z*: = $[M + 5H]^{5+}$ = 450.3 (calcd. 450.2), $[M + 4H]^{4+}$ = 562.4

(calcd. 562.6), $[M + 3H]^{3+}$ = 749.5 (calcd. 749.6), $[M + 2H]^{2+}$ = 1123.8 (calcd. 1123.9) (Fig. S21 in SI).

4.4.2. Quantification of MAPs

The absorption spectrum of the solubilized MAPs was measured using a NanoDrop 2000c spectrophotometer (NanoDrop Products, Thermo Fisher Scientific), and the exact MAP concentrations were calculated using Lambert-Beer's law with the following extinction coefficients: macrolittin-70, 5500 $M^{-1}cm^{-1}$ at 280 nm; melittin, 5500 $M^{-1}cm^{-1}$ at 280 nm; Tat, 1490 $M^{-1}cm^{-1}$ at 280 nm; penetratin, 11,000 $M^{-1}cm^{-1}$ at 280 nm; magainin-2, 42,783 $M^{-1}cm^{-1}$ at 214 nm; LL-37, 58,639 $M^{-1}cm^{-1}$ at 214 nm. The extinction coefficients for macrolittin-70, melittin, Tat, and penetratin were calculated using the work by Pace et al. [68], and the extinction coefficients for magainin-2 and LL-37, which contains no tryptophans or tyrosines, were calculated using the work by Kuipers and Gruppen [69].

4.5. Handling of MAPs

Freeze-dried MAPs were adjusted to room temperature, and phosphate buffer, filtered using a 0.22 μm sterile filter, was added to obtain an approximate MAP concentration of 500 μM. The solutions were vortexed gently for 10 s. The absorption spectrum of the solutions was then measured using a NanoDrop 2000c spectrophotometer, and the exact MAP concentrations were calculated using Lambert-Beer's law as described in Section 4.4.2.

4.6. Flow cytometry

The effect of MAPs on vesicles were measured by adding MAPs to vesicles to a final MAP concentration of 10 μM and a final lipid concentration of 50 μM. The solution was mixed by vortexing gently, and left to react for 30–60 min at 37 °C. Just before flow cytometry measurements, the solutions were diluted 100-fold to a final lipid concentration of 500 nM, and vortexed gently. Dilutions were done in phosphate buffer.

A BD LSRFortessa Flow cytometer (BD Biosciences, US) was used to study fluorophore-labeled vesicles and their interactions with MAPs (see Table 1). BD CS&T quality and control beads were used prior to the experiments to standardize the performance of the equipment. The measurements were run with a low flow rate (1 μL/min). The events were triggered by the fluorescence from DOPE-Atto655 fluorescence at a trigger value of 200, using a 640 nm laser. The emission from the Atto655 was detected at 655–685 nm. Alexa488 was excited using a 488 nm laser, and the emission detected at 515–545 nm. The applied voltages were chosen based on the signal from the anionic LVs with core- fluorophore. The voltage for the Atto655 detector was set to 280 V to detect a significant proportion of vesicles (800–2400 events/s for untreated vesicles) relative to the number of events from the buffer (typically <1 event/s). The voltage for the Alexa488 detector was set to 460 V. This value gave a rise to a relevant dynamic range of Alexa488 fluorescence in which the Alexa488 (core-fluorophore) loaded vesicles were measurable and distinguishable from empty vesicles. For measurements triggered on the core fluorescence, the trigger value was 200, using the 488 nm laser. The applied voltages were the same as for measurements triggered by the fluorescence from DOPE-Atto655. Events were recorded to a total of 50,000 events or at least 120 s, whichever came first.

The fluorescence intensities are reported by the height value from the recorded pulses because this has been reported to be the optimal read-out when studying submicron particles [70]. FlowJo v 10.7.2 was used to extract the median fluorescence intensities (MFIs) and the count rates and to generate the figures. All measurements were carried out at room temperature.

4.7. Calcein release assay

Stock samples with cLVs or MAPs were heated to 37 °C. The stock samples were mixed directly in black 96-well plates (Nunc, Thermo Fischer Scientific) to a final lipid concentration of 50 μM, a final MAP concentration of 10 μM, and a final volume of 150 μL. The mixtures were incubated for 30, 60, or 120 min at 37 °C. The fluorescence emission intensity, *F*, was measured using a Spark multimode microplate reader (Tecan, Mannedorf, Switzerland) with an excitation wavelength of 491 ¨ nm and an emission wavelength of 514 nm. The fluorescence emission intensity of intact cLVs, F_0, was measured using cLVs incubated without MAPs, and the fluorescence emission intensity for maximum calcein release, F_{max}, was measured using cLVs incubated with 0.5% Triton X- 100. The calcein release was calculated using the equation

$$\text{Calcein release (\%)} = \frac{F - F^0}{F_{max} - F_0} \times 100\%.$$

4.8. Dynamic light scattering (DLS)

cLVs were mixed with MAPs to a final lipid concentration of 50 μM and a final MAP concentration of 10 μM. The samples were incubated for 30–60 min at 37 °C before investigation by DLS using a Zetasizer Nano ZS (Malvern, Worcestershire, UK). The DLS measurements were performed at 37 °C. The number of runs per measurement were adjusted automatically by the Zetasizer. The acquired data were evaluated using an intensity-based size distribution analysis. Sizes representing ≤2% of the total intensity were not included in the final data representation. In a few cases, the volume-weighted size distributions were also presented.

4.9. Microscopy and image analysis

Imaging of GUVs was performed using a Nikon Ti2, Yokogawa CSU-W1 spinning disc confocal microscope equipped with a high numerical aperture 60× oil immersion objective and a Photometrics Prime 95B sCMOS detector. The images were acquired by alternating between exciting calcein and DOPE-Atto655 using 488 nm and 638 nm diode laser lines, respectively. The calcein emission was passed through a 520/ 28 Brightline HC filter set, while DOPE-Atto655 was passed through 600/50 ET Bandpass filter set. Ibidi micro-slide 8 wells were passivated with BSA by incubating 300 μL 1 g/L BSA in PBS in each well for a minimum of 30 min before washing each well 8 times with a 300 μL 226 mM glucose solution. The BSA passivated micro-slides were inserted into the microscope. 150 μL of a 226 mM glucose solution containing 50 μM calcein was added to the chamber. 25 μL of the GUV solution was hereafter added and incubated for 2 min before adding 150 μL 226 mM glucose solution containing 50 μM calcein and and 108 μM peptide. The final peptide concentration was 50 μM and the final calcein concentration was 46 μM. Imaging was performed for a minimum of 30 min and was initiated immediately after the last solution was added to the chamber. A temporal resolution of 15 s was applied. Presented images were sectioned and edited for brightness and contrast in ImageJ.

Declaration of competing interest

The authors declare that they have no known competing financial interests or personal relationships that could have appeared to influence the work reported in this paper.

Acknowledgement

We thank Bente Rotbøl for technical assistance with the flow cytometer and Jaco Botha and Nicolai Paulsen for critical reading of the manuscript. The work presented in this article is supported by Novo Nordisk Foundation grant NNF16OC0022166.

Appendix A. Supplementary data

Supplementary data to this article can be found online at https://doi.org/10.1016/j.bbamem.2021.183820.

References

[1] K. Matsuzaki, S. Yoneyama, K. Miyajima, Pore formation and translocation of melittin, Biophys. J. 73 (1997) 831–838, https://doi.org/10.1016/S0006-3495(97)78115-3.

[2] L. Gentilucci, A. Tolomelli, F. Squassabia, Peptides and peptidomimetics in medicine, surgery and biotechnology, Curr. Med. Chem. 13 (2006) 2449–2466, https://doi.org/10.2174/092986706777935041.

[3] S. Li, S.Y. Kim, A.E. Pittman, G.M. King, W.C. Wimley, K. Hristova, Potent macromolecule-sized poration of lipid bilayers by the macrolittins, a synthetically evolved family of pore-forming peptides, J. Am. Chem. Soc. 140 (2018) 6441–6447, https://doi.org/10.1021/jacs.8b03026.

[4] W.C. Wimley, K. Hristova, Antimicrobial peptides: successes, challenges and unanswered questions, J. Membr. Biol. 239 (2011) 27–34, https://doi.org/10.1007/s00232-011-9343-0.

[5] J. Xie, Y. Bi, H. Zhang, S. Dong, L. Teng, R.J. Lee, Z. Yang, Cell-penetrating peptides in diagnosis and treatment of human diseases: from preclinical research to clinical application, Front. Pharmacol. 11 (2020) 697, https://doi.org/10.3389/ fphar.2020.00697.

[6] Y. Li, H. Wu, P. Teng, G. Bai, X. Lin, X. Zuo, C. Cao, J. Cai, Helical antimicrobial sulfono-γ-AApeptides, J. Med. Chem. 58 (2015) 4802–4811, https://doi.org/10.1021/acs.jmedchem.5b00537.

[7] M.K. Kim, N. Kang, S.J. Ko, J. Park, E. Park, D.W. Shin, S.H. Kim, S.A. Lee, J.I. Lee, S.H. Lee, E.G. Ha, S.H. Jeon, Y. Park, Antibacterial and antibiofilm activity and mode of action of magainin 2 against drug-resistant Acinetobacter baumannii, Int. J. Mol. Sci. 19 (2018) 3041, https://doi.org/10.3390/ijms19103041.

[8] J.H. Choi, A.Y. Jang, S. Lin, S. Lim, D. Kim, K. Park, S.M. Han, J.H. Yeo, H.S. Seo, Melittin, a honeybee venom-derived antimicrobial peptide, may target methicillin- resistant Staphylococcus aureus, Mol. Med. Rep. 12 (2015) 6483–6490, https:// doi.org/10.3892/mmr.2015.4275.

[9] Y. Huan, Q. Kong, H. Mou, H. Yi, Antimicrobial peptides: classification, design, application and research progress in multiple fields, Front. Microbiol. 11 (2020) 582779, https://doi.org/10.3389/fmicb.2020.582779.

[10] S. Macchi, G. Signore, C. Boccardi, C. Di Rienzo, F. Beltram, F. Cardarelli, Spontaneous membrane-translocating peptides: influence of peptide self-aggregation and cargo polarity, Sci. Rep. 5 (2015) 16914, https://doi.org/10.1038/srep16914.

[11] A. Dinca, W.-M. Chien, M.T. Chin, Intracellular delivery of proteins with cell-penetrating peptides for therapeutic uses in human disease, Int. J. Mol. Sci. 17 (2016) 263, https://doi.org/10.3390/ijms17020263.

[12] H. Wang, J. Ma, Y. Yang, F. Zeng, C. Liu, Highly efficient delivery of functional cargoes by a novel cell-penetrating peptide derived from SP140-like protein, Bioconjug. Chem. 27 (2016) 1373–1381, https://doi.org/10.1021/acs.bioconjchem.6b00161.

[13] E.J.B. Nielsen, S. Yoshida, N. Kamei, R. Iwamae, E.S. Khafagy, J. Olsen, U. L. Rahbek, B.L. Pedersen, K. Takayama, M. Takeda-Morishita, In vivo proof of concept of oral insulin delivery based on a co-administration strategy with the cell- penetrating peptide penetratin, J. Control. Release 189 (2014) 19–24, https://doi. org/10.1016/j.jconrel.2014.06.022.

[14] M. Kristensen, H.M. Nielsen, Cell-penetrating peptides as tools to enhance non-injectable delivery of biopharmaceuticals, Tissue Barriers 4 (2016) e1178369, https://doi.org/10.1080/21688370.2016.1178369.

[15] J.B. Larsen, N. Taebnia, A. Dolatshahi-Pirouz, A.Z. Eriksen, C. Hjørringgaard, K. Kristensen, N.W. Larsen, N.B. Larsen, R. Marie, A.-K. Mündler, L. Parhamifar, A. J. Urquhart, A. Weller, K.I. Mortensen, H. Flyvbjerg, T.L. Andresen, Imaging therapeutic peptide transport across intestinal barriers, RSC Chem. Biol. 2 (2021) 1115–1143, https://doi.org/10.1039/d1cb00024a.

[16] S.F. Hedegaard, M.S. Derbas, T.K. Lind, M.R. Kasimova, M.V. Christensen, M. H. Michaelsen, R.A. Campbell, L. Jorgensen, H. Franzyk, M. Cardenas, H. ´ M. Nielsen, Fluorophore labeling of a cell-penetrating peptide significantly alters the mode and degree of biomembrane interaction, Sci. Rep. 8 (2018) 6327, https://doi.org/10.1038/s41598-018-24154-z.

[17] L.D. Hughes, R.J. Rawle, S.G. Boxer, Choose your label wisely: water-soluble fluorophores often interact with lipid bilayers, PLoS One 9 (2014), e87649, https://doi.org/10.1371/journal.pone.0087649.

[18] Z. Zhang, D. Yomo, C. Gradinaru, Choosing the right fluorophore for single-molecule fluorescence studies in a lipid environment, Biochim. Biophys. Acta Biomembr. 1859 (2017) 1242–1253, https://doi.org/10.1016/j.bbamem.2017.04.001.

[19] G. van den Bogaart, J.V. Guzman, J.T. Mika, B. Poolman, On the mechanism of ´ pore formation by melittin, J. Biol. Chem. 283 (2008) 33854–33857, https://doi.org/10.1074/jbc.M805171200.

[20] S. Rex, Pore formation induced by the peptide melittin in different lipid vesicle membranes, Biophys. Chem. 58 (1996) 75–85, https://doi.org/10.1016/0301-4622(95)00087-9.

[21] R.M. Epand, R.F. Epand, Liposomes as models for antimicrobial peptides, Methods Enzymol. 372 (2003) 124–133, https://doi.org/10.1016/S0076-6879(03)72007-2.

[22] C. Kayalar, N. Düzgüneçs, Membrane action of colicin E1: detection by the release of carboxyfluorescein and calcein from liposomes, Biochim. Biophys. Acta Biomembr. 860 (1986) 51–56, https://doi.org/10.1016/0005-2736(86)90497-9.

[23] S. Guha, J. Ghimire, E. Wu, W.C. Wimley, Mechanistic landscape of membrane-permeabilizing peptides, Chem. Rev. 119 (2019) 6040–6085, https://doi.org/10.1021/acs.chemrev.8b00520.

[24] K. Kristensen, J.R. Henriksen, T.L. Andresen, Applying fluorescence correlation spectroscopy to investigate peptide-induced membrane disruption, Methods Mol.
Biol. 1548 (2017) 159–180, https://doi.org/10.1007/978-1-4939-6737-7_11.
[25] R. Rathinakumar, W.C. Wimley, Biomolecular engineering by combinatorial design and high-throughput screening: small, soluble peptides that permeabilize membranes, J. Am. Chem. Soc. 130 (2008) 9849–9858, https://doi.org/10.1021/ ja8017863.
[26] A.L. Russell, A.M. Kennedy, A.M. Spuches, D. Venugopal, J.B. Bhonsle, R.P. Hicks, Spectroscopic and thermodynamic evidence for antimicrobial peptide membrane selectivity, Chem. Phys. Lipids 163 (2010) 488–497, https://doi.org/10.1016/j. chemphyslip.2010.03.009.
[27] W.C. Wimley, Determining the effects of membrane-interacting peptides on membrane integrity, Methods Mol. Biol. 1324 (2015) 89–106, https://doi.org/10.1007/978-1-4939-2806-4_6.
[28] H.M. Shapiro, Practical Flow Cytometry, Fourth edition, John Wiley Sons, Inc., 2003, https://doi.org/10.1002/0471722731.
[29] J.M. Freire, D. Gaspar, B.G. de la Torre, A.S. Veiga, D. Andreu, M.A.R.B. Castanho, Monitoring antibacterial permeabilization in real time using time-resolved flow cytometry, Biochim. Biophys. Acta Biomembr. 1848 (2015) 554–560, https://doi. org/10.1016/j.bbamem.2014.11.001.
[30] S.G. Patel, E.J. Sayers, L. He, R. Narayan, T.L. Williams, E.M. Mills, R.K. Allemann, L.Y.P. Luk, A.T. Jones, Y.-H. Tsai, Cell-penetrating peptide sequence and modification dependent uptake and subcellular distribution of green florescent protein in different cell lines, Sci. Rep. 9 (2019) 6298, https://doi.org/10.1038/s41598-019-42456-8.
[31] J.B. Simonsen, E.B. Kromann, Pitfalls and opportunities in quantitative fluorescence-based nanomedicine studies – a commentary, J. Control. Release 335 (2021) 660–667, https://doi.org/10.1016/j.jconrel.2021.05.041.
[32] K. Temmerman, W. Nickel, A novel flow cytometric assay to quantify interactions between proteins and membrane lipids, J. Lipid Res. 50 (2009) 1245–1254, https://doi.org/10.1194/jlr.D800043-JLR200.
[33] J.B. Simonsen, A liposome-based size calibration method for measuring microvesicles by flow cytometry, J. Thromb. Haemost. 14 (2016) 186–190, https://doi.org/10.1111/jth.13176.
[34] J.B. Simonsen, J.B. Larsen, C. Hempel, N. Eng, A. Fossum, T.L. Andresen, Unique calibrators derived from fluorescence-activated nanoparticle sorting for flow cytometric size estimation of artificial vesicles: possibilities and limitations, Cytometry A 95 (2019) 917–924, https://doi.org/10.1002/cyto.a.23797.
[35] S. Rex, Pore formation induced by the peptide melittin in different lipid vesicle membranes, Biophys. Chem. 58 (1996) 75–85, https://doi.org/10.1016/0301-4622(95)00087-9.
[36] Z. Yang, H. Choi, J.C. Weisshaar, Melittin-induced permeabilization, re-sealing, and re-permeabilization of E. coli membranes, Biophys. J. 114 (2018) 368–379, https://doi.org/10.1016/j.bpj.2017.10.046.
[37] K. Matsuzaki, O. Murase, K. Miyajima, Kinetics of pore formation by an antimicrobial peptide, magainin 2, in phospholipid bilayers, Biochemistry 34 (1995) 12553–12559, https://doi.org/10.1021/bi00039a009.
[38] Y. Imura, N. Choda, K. Matsuzaki, Magainin 2 in action: distinct modes of membrane permeabilization in living bacterial and mammalian cells, Biophys. J. 95 (2008) 5757–5765, https://doi.org/10.1529/biophysj.108.133488.
[39] U.H.N. Dürr, U.S. Sudheendra, A. Ramamoorthy, LL-37, the only human member of the cathelicidin family of antimicrobial peptides, Biochim. Biophys. Acta Biomembr. 1758 (2006) 1408–1425, https://doi.org/10.1016/j.bbamem.2006.03.030.
[40] D. Persson, P.E.G. Thoren, M. Herner, P. Lincoln, B. Nord´ en, Application of a novel ´ analysis to measure the binding of the membrane-translocating peptide penetratin to negatively charged liposomes, Biochemistry 42 (2003) 421–429, https://doi.org/10.1021/bi026453t.
[41] E. Dupont, A. Prochiantz, A. Joliot, Penetratin story: an overview, Methods Mol. Biol. 1324 (2015) 29–37, https://doi.org/10.1007/978-1-4939-2806-4_2.
[42] I.M. Kaplan, J.S. Wadia, S.F. Dowdy, Cationic TAT peptide transduction domain enters cells by macropinocytosis, J. Control. Release 102 (2005) 247–253, https:// doi.org/10.1016/j.jconrel.2004.10.018.
[43] C. Ciobanasu, J.P. Siebrasse, U. Kubitscheck, Cell-penetrating HIV1 TAT peptides can generate pores in model membranes, Biophys. J. 99 (2010) 153–162, https:// doi.org/10.1016/j.bpj.2010.03.065.
[44] E. Sancho-Vaello, P. François, E.-J. Bonetti, H. Lilie, S. Finger, F. Gil-Ortiz, D. Gil-Carton, K. Zeth, Structural remodeling and oligomerization of human cathelicidin on membranes suggest fibril-like structures as active species, Sci. Rep. 7 (2017) 15371, https://doi.org/10.1038/s41598-017-14206-1.
[45] A.S. Ladokhin, S.H. White, "Detergent-like" permeabilization of anionic lipid vesicles by melittin, Biochim. Biophys. Acta Biomembr. 1514 (2001) 253–260, https://doi.org/10.1016/S0005-2736(01)00382-0.
[47] S.A. Stoner, E. Duggan, D. Condello, A. Guerrero, J.R. Turk, P.K. Narayanan, J. P. Nolan, High sensitivity flow cytometry of membrane vesicles, Cytometry A 89 (2016) 196–206, https://doi.org/10.1002/cyto.a.22787.
[48] A. Wagner, K. Vorauer-Uhl, Liposome technology for industrial purposes, J. Drug Deliv. 2011 (2011) 591325, https://doi.org/10.1155/2011/591325.
[49] A.R. Karow, J. Gotzl, P. Garidel, Resolving power of dynamic light scattering for ¨ protein and polystyrene nanoparticles, Pharm. Dev. Technol. 20 (2015) 84–89, https://doi.org/10.3109/10837450.2014.910808.
[50] V. Filipe, A. Hawe, W. Jiskoot, Critical evaluation of nanoparticle tracking analysis (NTA) by NanoSight for the measurement of nanoparticles and protein aggregates, Pharm. Res. 27 (2010) 796–810, https://doi.org/10.1007/s11095-010-0073-2.
[51] W. Anderson, D. Kozak, V.A. Coleman, Å.K. Jamting, M. Trau, A comparative study ¨ of submicron particle sizing platforms: accuracy, precision and resolution analysis of polydisperse particle size distributions, J. Colloid Interface Sci. 405 (2013) 322–330, https://doi.org/10.1016/j.jcis.2013.02.030.
[52] K.B. Johnsen, J.M. Gudbergsson, T.L. Andresen, J.B. Simonsen, What is the blood concentration of extracellular vesicles? Implications for the use of extracellular vesicles as blood-borne biomarkers of cancer, Biochim. Biophys. Acta Rev. Cancer 1871 (2019) 109–116, https://doi.org/10.1016/j.bbcan.2018.11.006.
[53] A.H. Kunding, M.W. Mortensen, S.M. Christensen, D. Stamou, A fluorescence-based technique to construct size distributions from single-object measurements: application to the extrusion of lipid vesicles, Biophys. J. 95 (2008) 1176–1188, https://doi.org/10.1529/biophysj.108.128819.
[54] J.A. Welsh, E. Van Der Pol, G.J.A. Arkesteijn, M. Bremer, A. Brisson, F. Coumans, F. Dignat-George, E. Duggan, I. Ghiran, B. Giebel, A. Gorgens, A. Hendrix, ¨ R. Lacroix, J. Lannigan, S.F.W.M. Libregts, E. Lozano-Andr´es, A. Morales-Kastresana, S. Robert, L. De Rond, T. Tertel, J. Tigges, O. De Wever, X. Yan, R. Nieuwland, M.H.M. Wauben, J.P. Nolan, J.C. Jones, MIFlowCyt-EV: a framework for standardized reporting of extracellular vesicle flow cytometry experiments, J. Extracell. Vesicles 9 (2020) 1713526, https://doi.org/10.1080/20013078.2020.1713526.
[55] S.L. Pedersen, A.P. Tofteng, L. Malik, K.J. Jensen, Microwave heating in solid-phase peptide synthesis, Chem. Soc. Rev. 41 (2012) 1826–1844, https://doi.org/10.1039/c1cs15214a.
[56] G. Sessa, J.H. Freer, G. Colacicco, G. Weissmann, Interaction of a lytic polypeptide, melittin, with lipid membrane systems, J. Biol. Chem. 244 (1969) 3575–3582, https://doi.org/10.1016/s0021-9258(18)83408-1.
[57] J.E. Cummings, T.K. Vanderlick, Aggregation and hemi-fusion of anionic vesicles induced by the antimicrobial peptide cryptdin-4, Biochim. Biophys. Acta Biomembr. 1768 (2007) 1796–1804, https://doi.org/10.1016/j.bbamem.2007.04.016.
[58] M.-L. Jobin, P. Bonnafous, H. Temsamani, F. Dole, A. Gr´elard, E.J. Dufourc, I. D. Alves, The enhanced membrane interaction and perturbation of a cell penetrating peptide in the presence of anionic lipids: toward an understanding of its selectivity for cancer cells, Biochim. Biophys. Acta Biomembr. 1828 (2013) 1457–1470, https://doi.org/10.1016/j.bbamem.2013.02.008.
[59] K. Matsuzaki, O. Murase, N. Fujii, K. Miyajima, Translocation of a channel-forming antimicrobial peptide, magainin 2, across lipid bilayers by forming a pore, Biochemistry 34 (1995) 6521–6526, https://doi.org/10.1021/bi00019a033.
[60] K.T. Nguyen, S.V. Le Clair, S. Ye, Z. Chen, Molecular interactions between magainin 2 and model membranes in situ, J. Phys. Chem. B 113 (2009) 12358–12363, https://doi.org/10.1021/jp904154w.
[61] Y. Tamba, M. Yamazaki, Magainin 2-induced pore formation in the lipid membranes depends on its concentration in the membrane interface, J. Phys. Chem. B 113 (2009) 4846–4852, https://doi.org/10.1021/jp8109622.
[62] J.R. Henriksen, T.L. Andresen, Thermodynamic profiling of peptide membrane interactions by isothermal titration calorimetry: a search for pores and micelles, Biophys. J. 101 (2011) 100–109, https://doi.org/10.1016/j.bpj.2011.05.047.
[63] J.E. Faust, P.Y. Yang, H.W. Huang, Action of antimicrobial peptides on bacterial and lipid membranes: a direct comparison, Biophys. J. 112 (2017) 1663–1672, https://doi.org/10.1016/j.bpj.2017.03.003.
[64] S. Braun, S. Pokorn ˇ a, R. ´ Sachl, M. Hof, H. Heerklotz, M. Hoernke, Biomembrane ˇ permeabilization: statistics of individual leakage events harmonize the interpretation of vesicle leakage, ACS Nano 12 (2018) 813–819, https://doi.org/ 10.1021/acsnano.7b08184.
[65] K. Kristensen, J.R. Henriksen, T.L. Andresen, Quantification of leakage from large unilamellar lipid vesicles by fluorescence correlation spectroscopy, Biochim. Biophys. Acta Biomembr. 1838 (2014) 2994–3002, https://doi.org/10.1016/j. bbamem.2014.08.007.
[66] K. Kristensen, N. Ehrlich, J.R. Henriksen, T.L. Andresen, Single-vesicle detection and analysis of peptide-induced membrane permeabilization, Langmuir 31 (2015) 2472–2483, https://doi.org/10.1021/la504752u.
[67] S.A. Wheaten, F.D.O. Ablan, B.L. Spaller, J.M. Trieu, P.F. Almeida, Translocation of cationic amphipathic peptides across the membranes of pure phospholipid giant vesicles, J. Am. Chem. Soc. 135 (2013) 16517–16525, https://doi.org/10.1021/ ja407451c.
[68] C.N. Pace, F. Vajdos, L. Fee, G. Grimsley, T. Gray, How to measure and predict the molar absorption coefficient of a protein, Protein Sci. 4 (1995) 2411–2423, https:// doi.org/10.1002/pro.5560041120.
[69] B.J.H. Kuipers, H. Gruppen, Prediction of molar extinction coefficients of proteins and peptides using UV absorption of the constituent amino acids at 214 nm to enable quantitative reverse phase high-performance liquid

chromatography– mass spectrometry, J. Agric. Food Chem. 55 (2007) 5445–5451, https://doi.org/ 10.1021/jf070337l.

[70] P. Poncelet, S. Robert, N. Bailly, F. Garnache-Ottou, T. Bouriche, B. Devalet, J. H. Segatchian, P. Saas, F. Mullier, Tips and tricks for flow cytometry-based analysis and counting of microparticles, Transfus. Apher. Sci. 53 (2015) 110–126, https:// doi.org/10.1016/j.transci.2015.10.008.

Supplementary information

Applying flow cytometry to identify the modes of action of membrane-active peptides in a label-free and high-throughput fashion

Nanna Wichmann, Philip M. Lund, Morten B. Hansen, Claudia U. Hjørringgaard, Jannik B. Larsen, Kasper Kristensen, Thomas L. Andresen*, and Jens B. Simonsen*

Department of Health Technology, Center for Intestinal Absorption and Transport of Biopharmaceuticals, Technical University of Denmark, 2800 Kgs. Lyngby, Denmark

Table of contents:

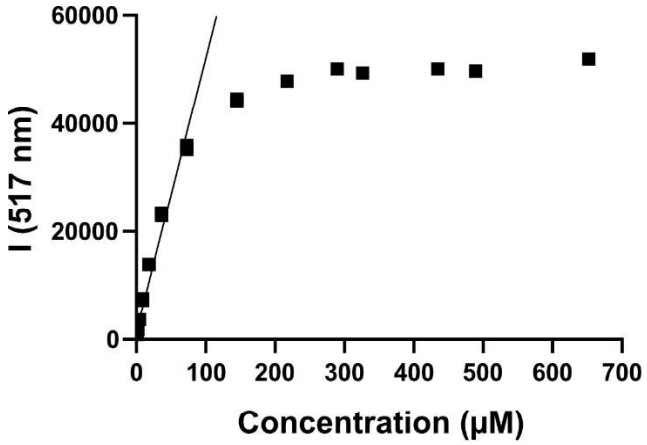

Figure S1. Studying the Alexa488 fluorescence intensity as a function of its concentration. The fluorescence emission intensity at 517 nm upon excitation at 488 nm of a dilution series of Alexa488 dissolved in phosphate buffer, measured in a black 96 well plate (Nunc, Thermo Fischer Scientific) using a Spark multimode microplate reader. The Alexa488 concentrations were calculated from absorbances

measured using a NanoDrop 2000c spectrophotometer assuming an extinction coefficient of 73000 M^{-1} cm^{-1} at a wavelength of 488 nm. The line is a linear fit derived from values between 0 and 80 µM.

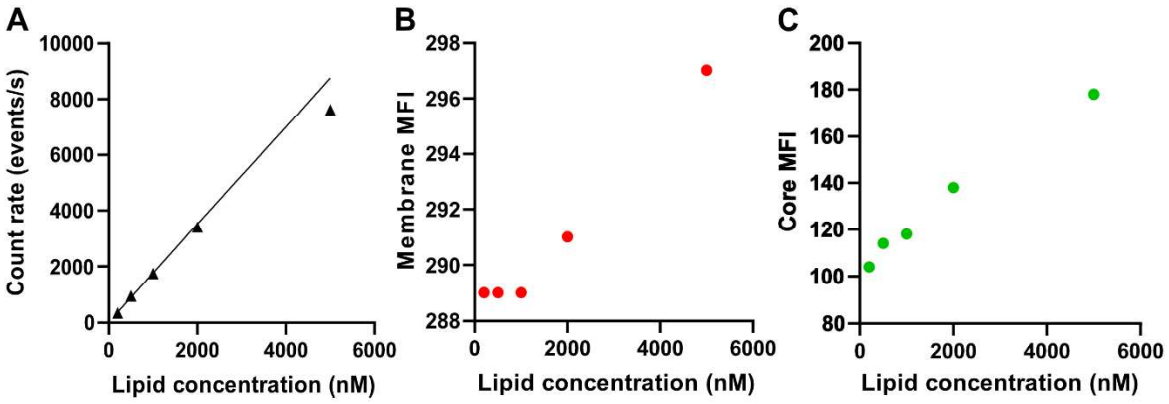

Figure S2. **Determining concentration range for single LV detection.** The count rate (A) and the membrane MFI (B) for various LV lipid concentrations of LVs with core-fluorophore. A linear fit to the data points for 250, 500, and 1000 nM is shown for the count rate. (C) Plot of the core MFI for various LV lipid concentrations of LVs with core-fluorophore. The small differences in the core MFI at low LV concentrations could be due to the four-fold higher relative standard deviation associated with the core MFI (3/104) measurements than the membrane MFI (2/287) measurements. These relative uncertainties are associated with the LV with core-fluorophore measurements. All measurements were triggered on membrane-fluorophore fluorescence. The MFI values are in arbitrary units.

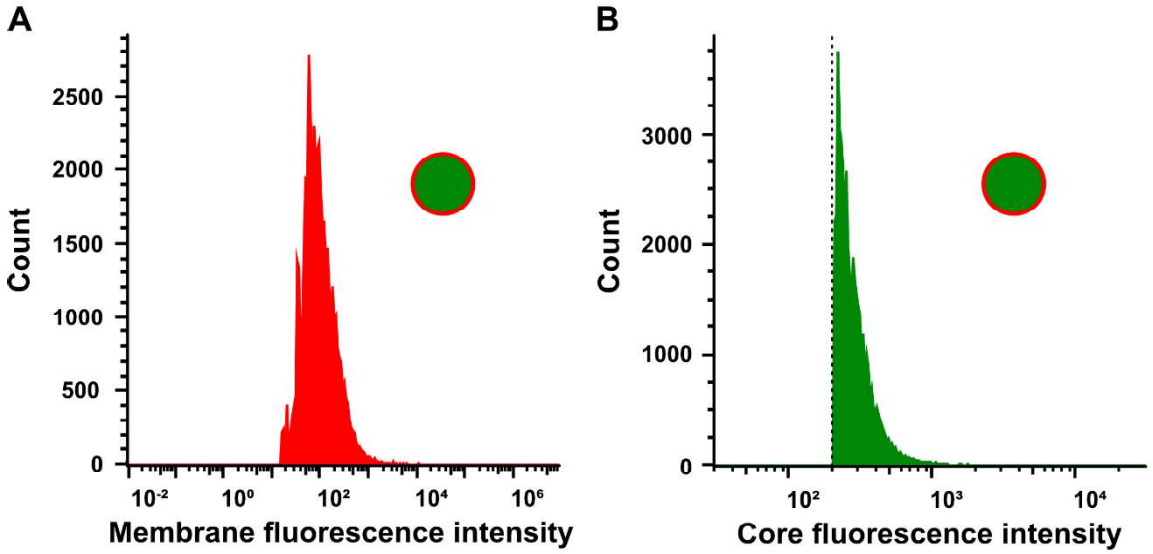

Figure S3. Flow cytometry data on LVs, triggered on the core-fluorophore fluorescence. Histograms of the membrane-fluorophore fluorescence intensities (A) and the core-fluorophore fluorescence intensities (B) of anionic, membrane-labeled LVs with core-fluorophore. The inserted circles illustrate the LVs including the position of the fluorophore-labels and their fluorescent colors. The black dotted line in B marks the trigger threshold value. All measurements were triggered on core-fluorophore fluorescence (200 AU).

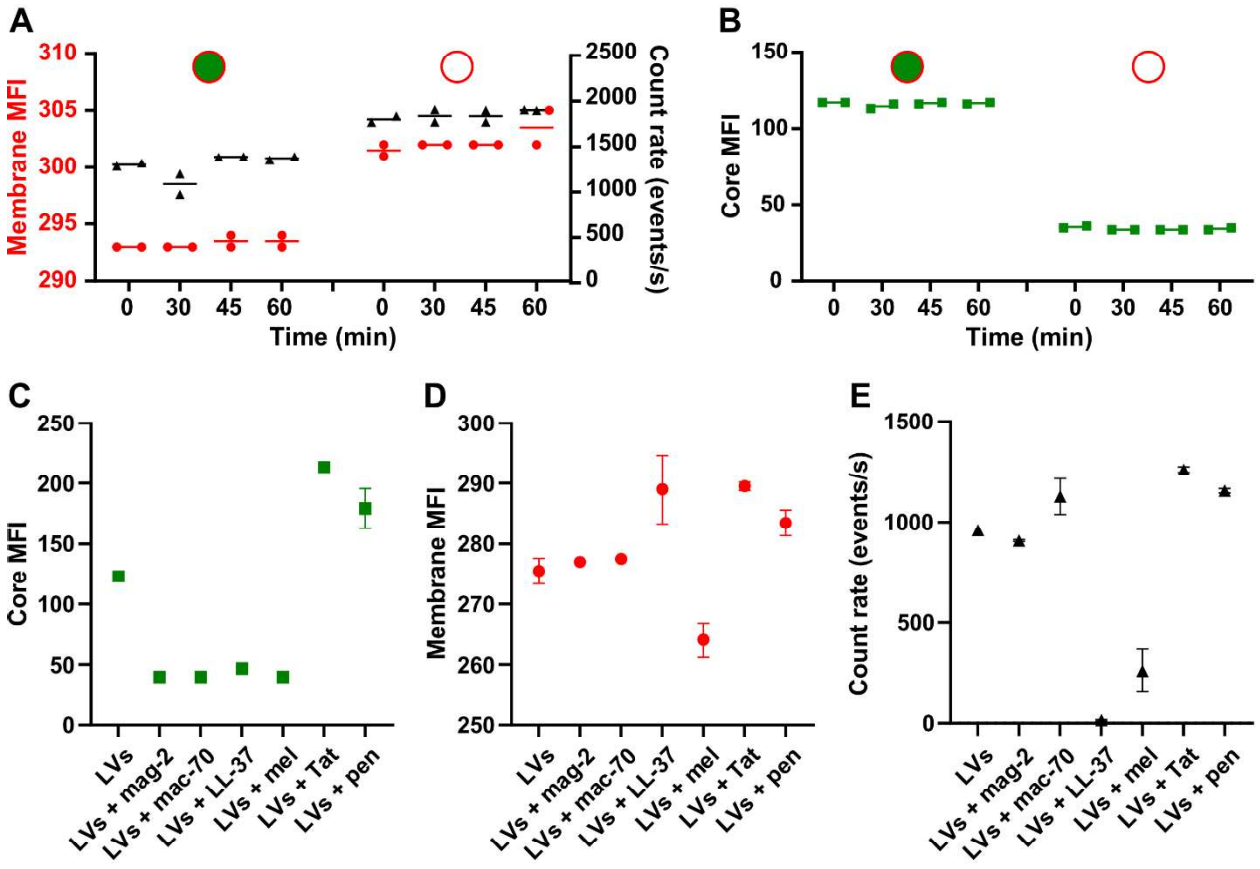

Figure S4. Robustness and reproducibility of the flow cytometry measurements. Top: Time dependence of the membrane MFI (red circles) and count rate (black triangles) (A) and of the core MFI (green squares) (B) for LVs with (left) or without (right) the core-fluorophores. The data represent the MFI for one replicate, and the lines the average of the replicates. Bottom: Core MFI (C), membrane MFI (D), and count rate (E) for LVs with core-fluorophore in the absence (LVs) or presence of a MAP (LVs + MAP), measured on another day than those shown in Figure 5. Data represent the average of two replicates and their standard deviation. All samples were incubated at 50 µM LV lipid concentration with and without MAP at 37 ˚C for 30-60 min, where no other time points are stated, and diluted to 500 nM lipid just prior to the measurements. All measurements were triggered on membrane fluorescence. mag-2: magainin-2, mac-70: macrolittin-70, mel: melittin, pen: penetratin. The MFI values are in arbitrary units.

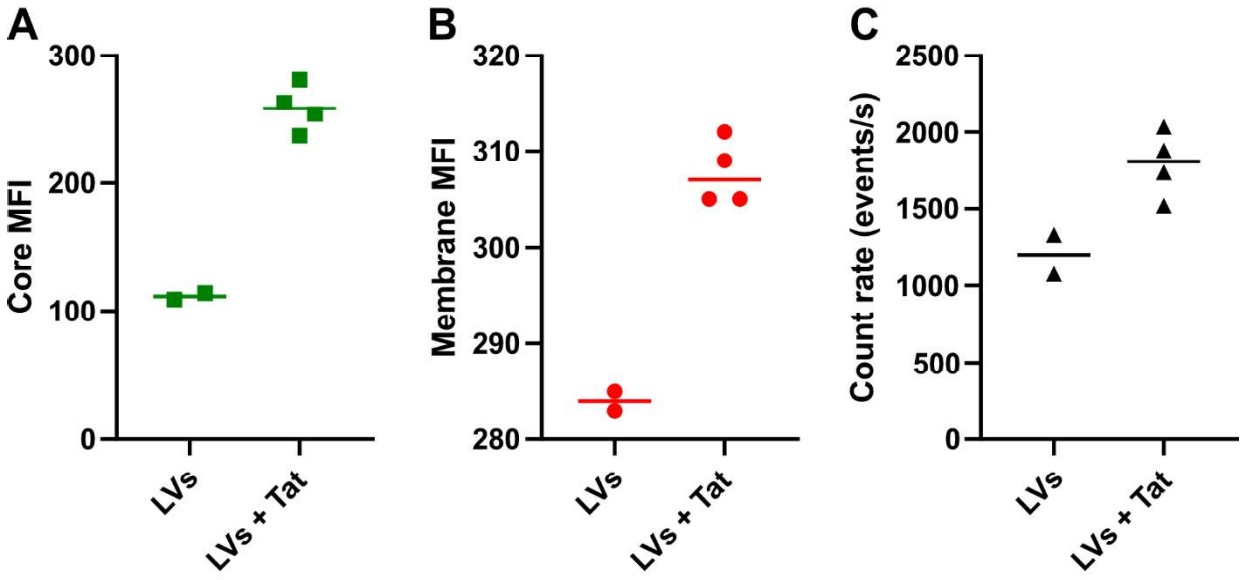

Figure S5. Replicates of flow cytometry measurements for Tat. Core MFI (A), membrane MFI (B), and count rate (C) for anionic LVs with core-fluorophore in the absence (LVs) or presence of Tat (LVs + Tat). Each point represents a replicate, and the line an average of the replicates. The MFI values are in arbitrary units.

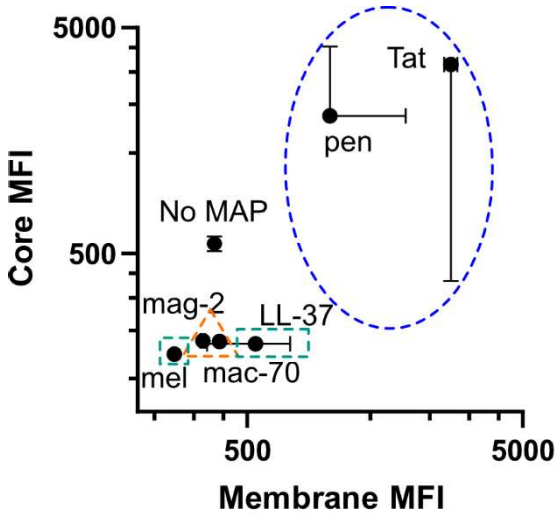

Figure S6. Core MFI vs Membrane MFI for LVs at 50 µM lipid. Core MFI vs membrane MFI for LVs with core-fluorophore in presence of the stated MAP. Measurements were performed after incubation at 37 ˚C for 30-60 min with a LV lipid concentration of 50 µM and 10 µM MAP without further dilution prior to the measurements. Data for MAPs leading to core-fluorophore release without solubilization are marked with an orange triangle, data for MAPs leading to core-fluorophore release and solubilization are marked with a turquoise square, and data for MAPs leading to aggregation of the LVs are marked with a blue circle. The shown data is an average of two replicates and the corresponding standard deviation. mag-2: magainin-2, mac-70: macrolittin-70, mel: melittin, pen: penetratin.

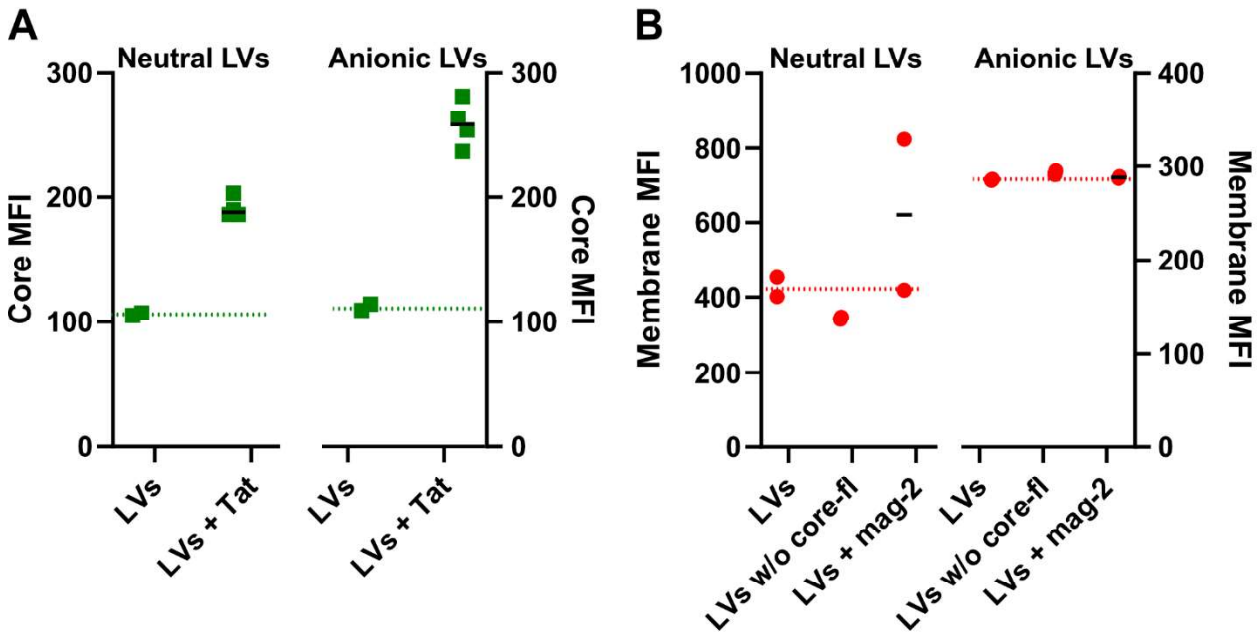

Figure S7. Effect of Tat and magainin-2 on neutral LVs and anionic LVs. A) Core MFI for LVs with the core-fluorophore in the absence (LVs) or presence of Tat (LVs + Tat), where the membrane of the LVs are either neutral (left) or negatively charged (right). The full black lines are the average of the shown MFIs for LVs exposed to Tat. The dotted, green lines are the average of the MFI for the neutral and charged LVs in the absence of a MAP. B) Membrane MFI for LVs with the core-fluorophore in the absence (LVs) or presence of magainin-2 (LVs + mag-2) as well as for LVs without core-fluorophore (LVs w/o core-fl), where the membrane of the LVs are either neutral (left) or negatively charged (right). The full black lines are the average of the shown MFIs for LVs exposed to magainin-2. The dotted, red lines are the average of the MFI for the neutral and charged LVs in the absence of a MAP. All measurements were triggered on membrane-fluorophore fluorescence.

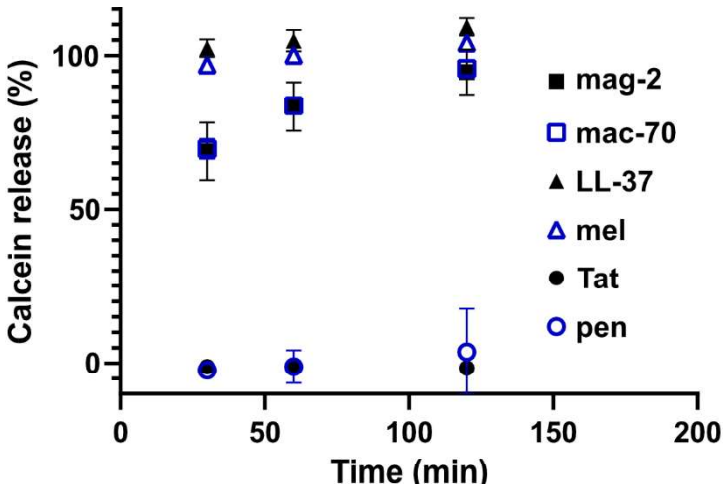

Figure S8. Calcein release kinetics. Calcein release from 50 μM (lipid-based concentration) anionic cLVs induced by 10 μM of one of the MAPs after incubation at 37 ˚C for the given time. Each data point is the average of two independent measurements and their standard deviation.

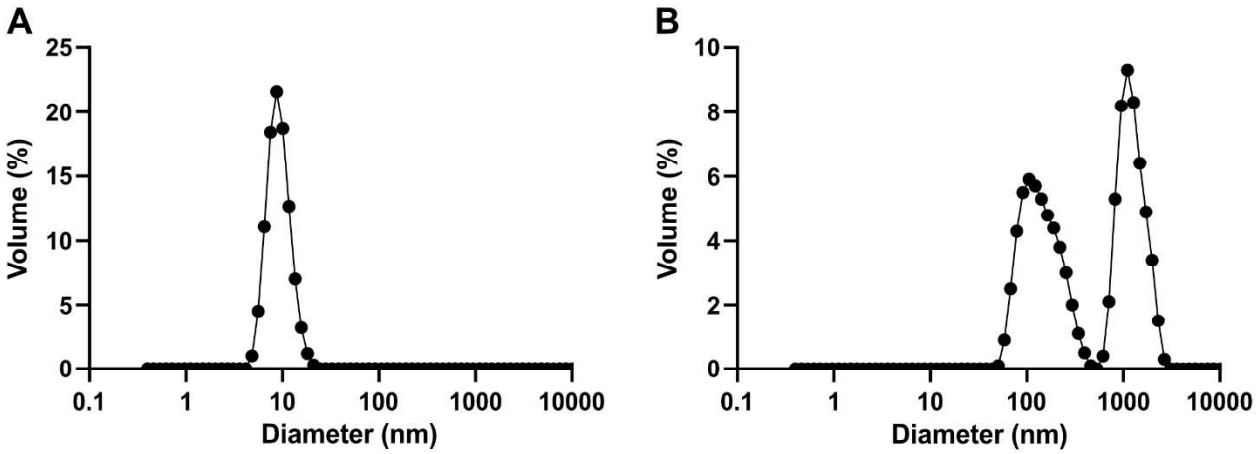

Figure S9. DLS derived size distribution of LVs in the presence of LL-37 (A) or Tat (B). Volume-weighted size distribution of 50 μM (lipid based concentration) anionic cLVs in the presence of 10 μM LL-37 (A) or Tat (B) after 30-60 min of incubation at 37 ˚C.

Table S1. Summary of MAP interaction with GUV data.

Number of GUVs observed throughout the recorded videos and classified in the various MAP interaction mechanisms. The MAP interactions with the GUVs were recorded for 30 min while control measurements with only GUVs were recorded for 45 min.

	Control	**LL-37**	**Mac-70**	**Tat**
Intact	123	0	0	32
Aggregation	0	0	0	73
Collapse (single GUVs collapse into a point)	0	0	0	3
Solubilization	0	30	0	0
Permeation	1	0	24	0
Permation leading to solubilzation	0	0	24	0
Total	**124**	**30**	**24**	**108**

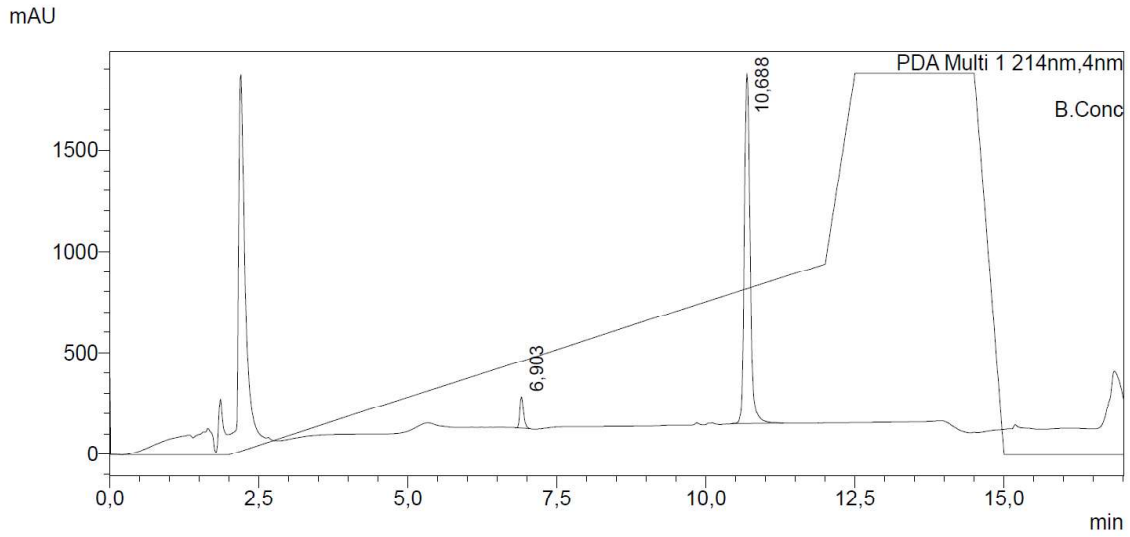

Figure S10. Magainin-2 purity. Analytical HPLC chromatogram.

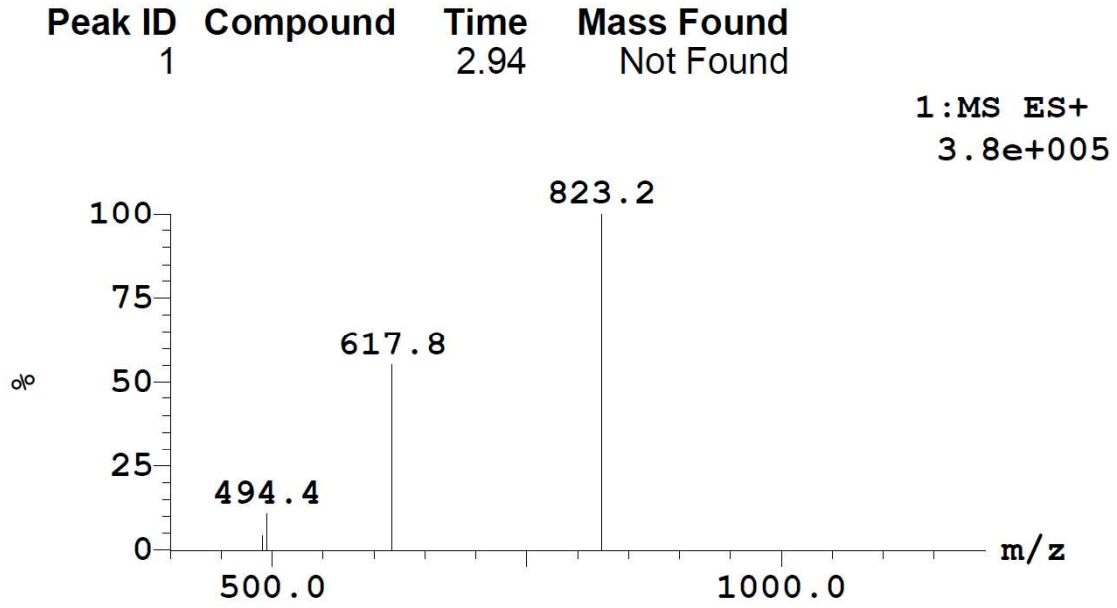

Figure S11. Identification of Magainin-2. ESI MS spectrum acquired via LC-MS.

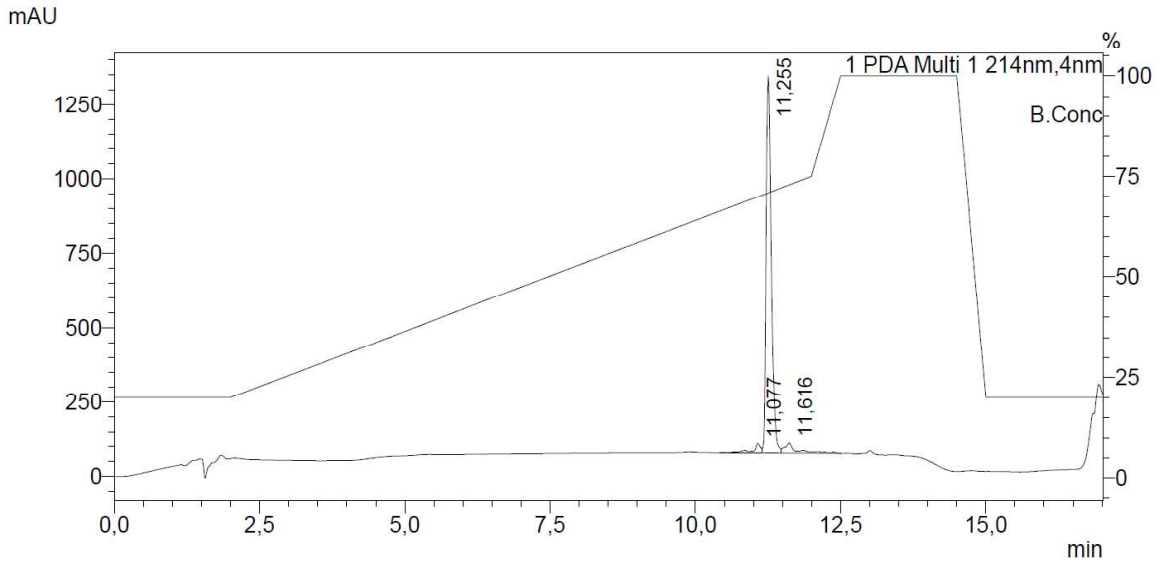

Figure S12. Macrolittin-70 purity. Analytical HPLC chromatogram.

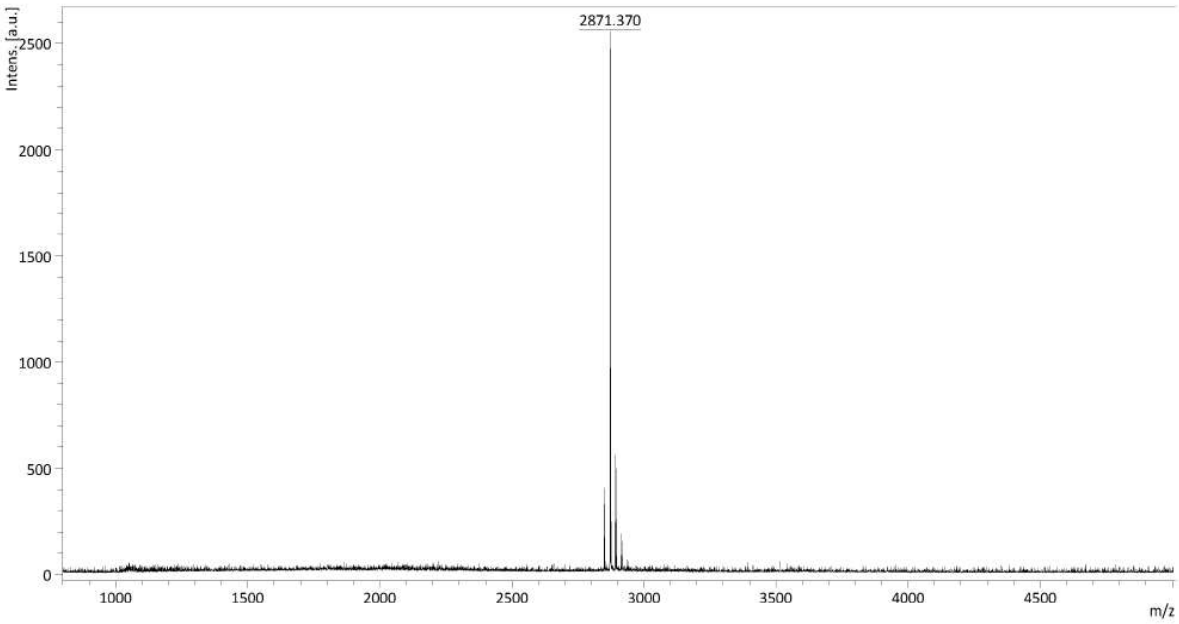

Figure S13. Identification of Macrolittin-70. MALDI-TOF.

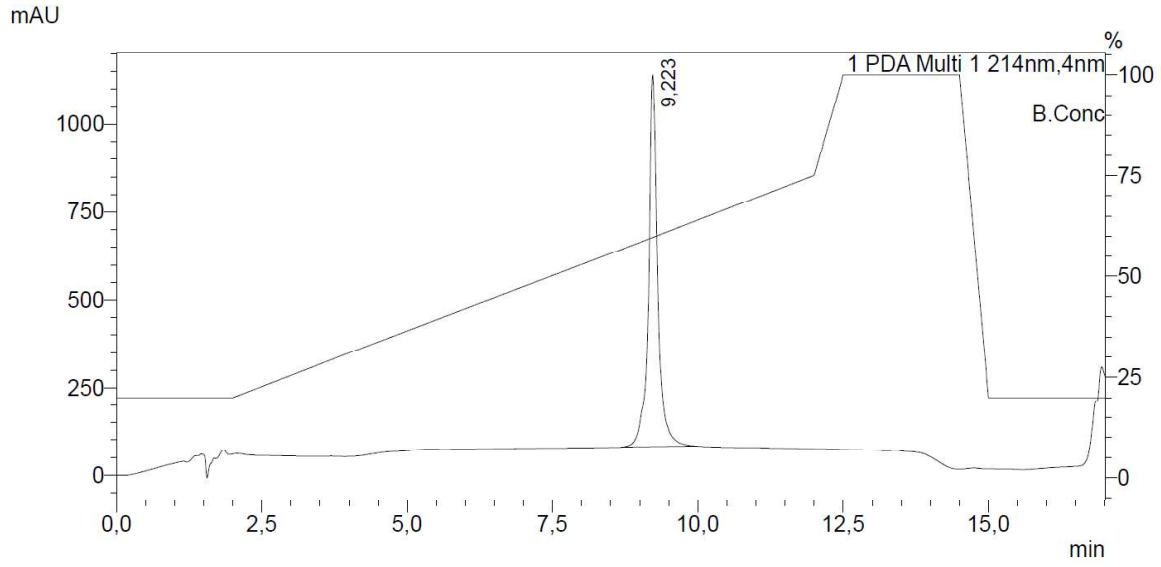

Figure S14. LL-37 purity. Analytical HPLC chromatogram.

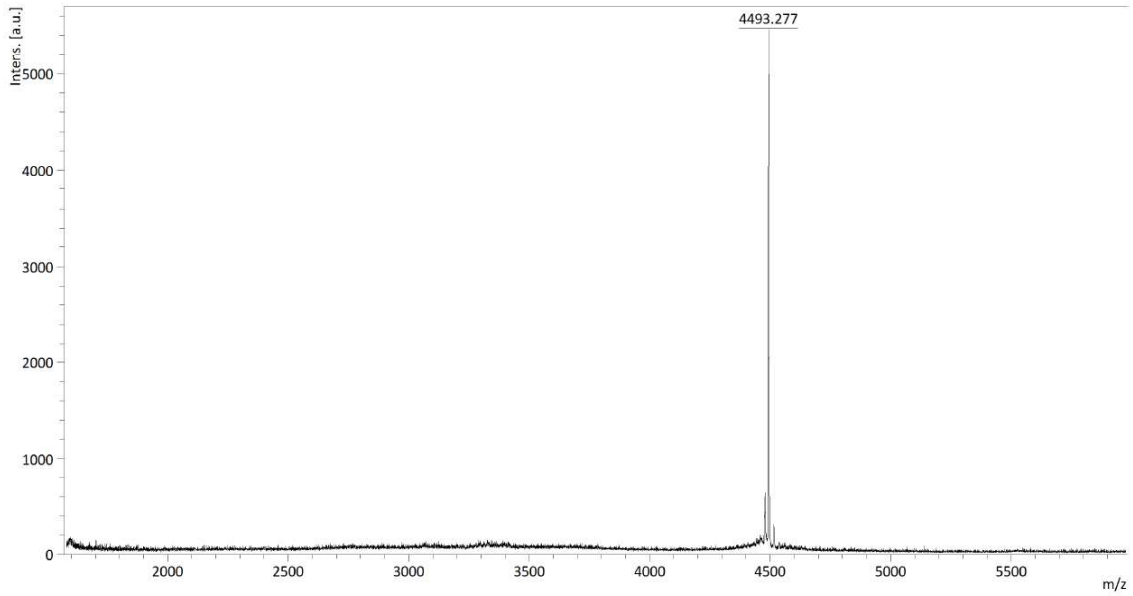

Figure S15. Identification of LL-37. MALDI-TOF.

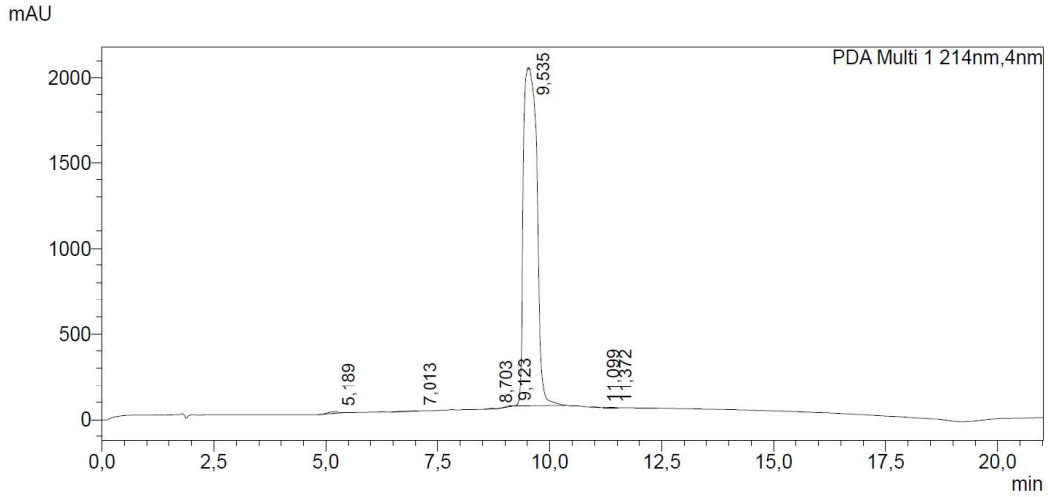

Figure S16. Melittin purity. Analytical HPLC chromatogram.

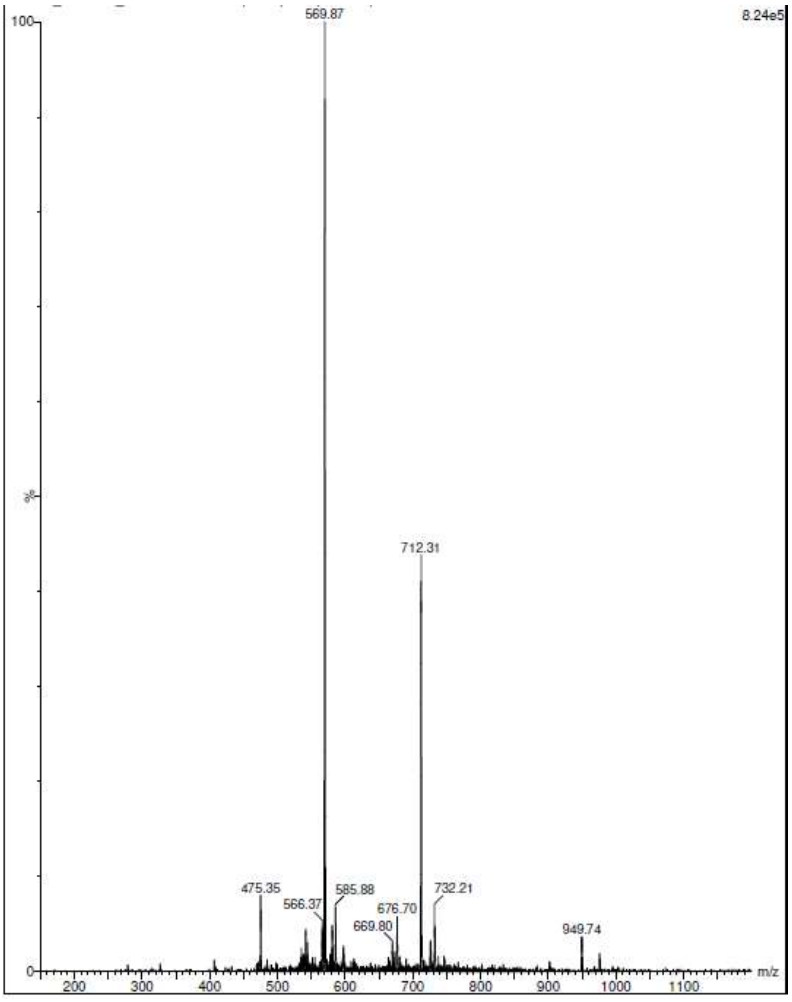

Figure S17. Identification of Melittin. ESI MS spectrum acquired via LC-MS.

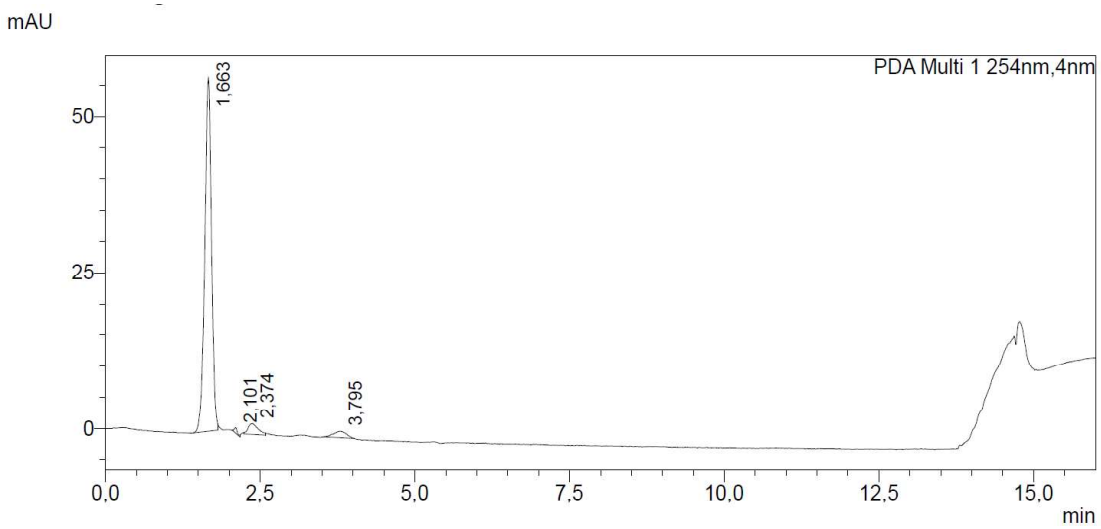

Figure S18. Tat purity. Analytical HPLC chromatogram.

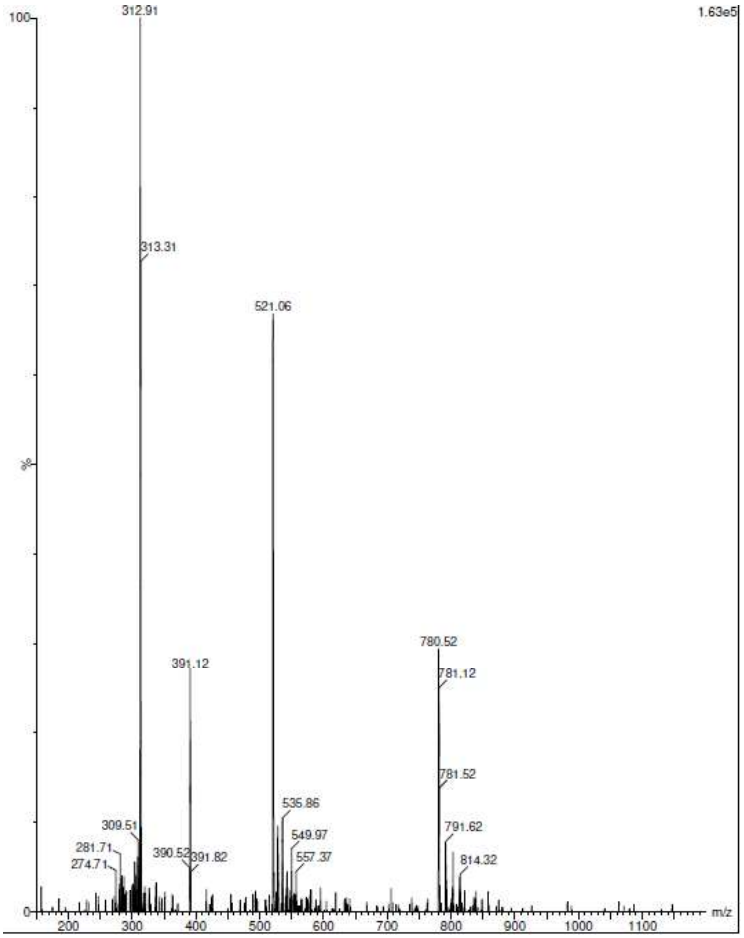

Figure S19. **Identification of Tat**. ESI MS spectrum acquired via LC-MS.

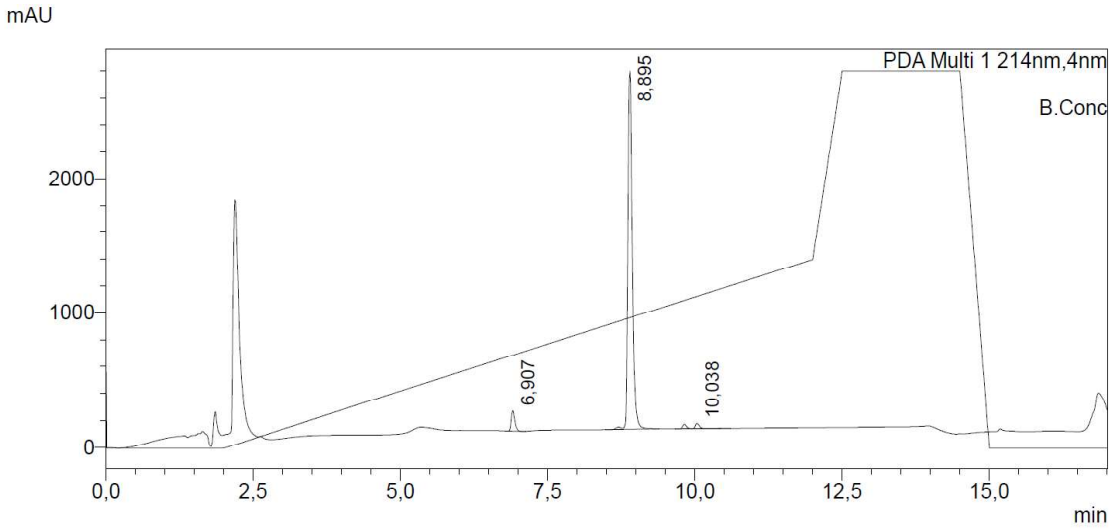

Figure S20. Penetratin purity. Analytical HPLC chromatogram.

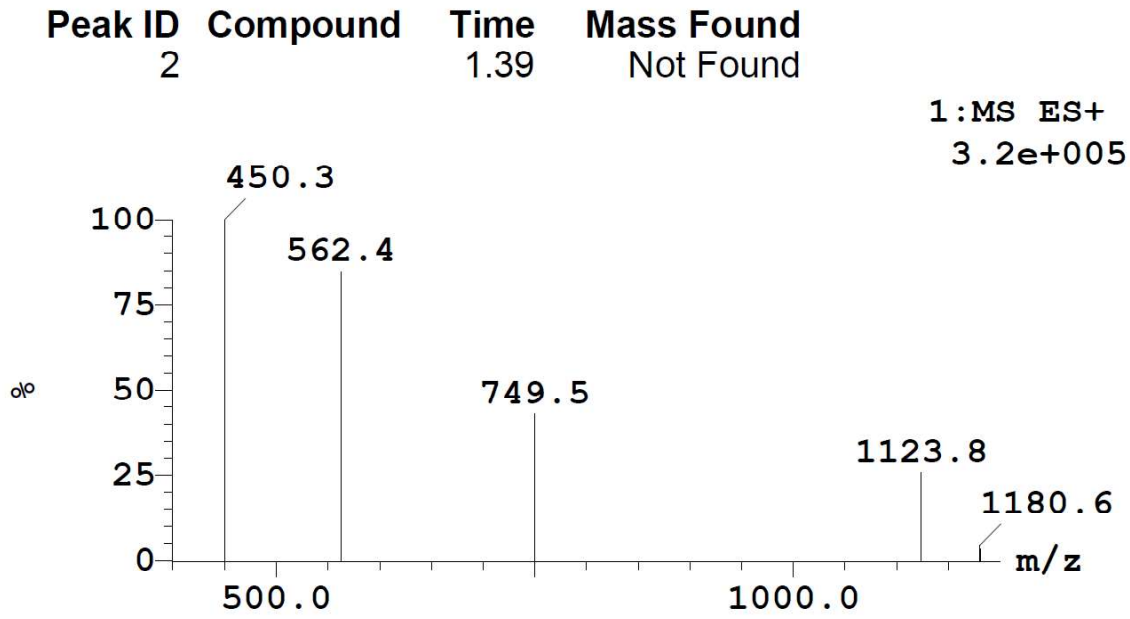

Figure S21. Identification of Penetratin. ESI MS spectrum acquired via LC-MS.

Chapter 6: Concluding remarks and perspectives

Peptides have many properties that makes them highly advantageous as drugs. They bind to their target with high specificity, they exhibit high potency and low toxicity. However, their intrinsic properties challenges their delivery through the desired oral route and result in low overall bioavailabilities upon oral delivery. The low bioavailability are in part due to their low membrane permeability, complicating their translocation across the enterocytes. Possibilities to enhance peptide translocation include enhancing the permeability of the membrane and enhancing the abilities of the peptides to translocate across a lipid membrane. An important aspect of these possibilities are membrane activity, either for the peptide itself or for permeation enhancers or combinations hereof. This thesis addresses membrane activity, mechanisms of membrane activity, and methods to study this for peptides and permeation enhancers in solutions with various biorelevance. It also addresses how various interactions may affect these mechanisms. The thesis provides novel perspectives and approaches to open new possibilities in oral peptide drug delivery.

There are currently not many studies of interactions of peptide drugs and permeation enhancers in the context of biological fluids. Potentially, the interplay between bile components, permeation enhancers, and peptide drugs can alter the bioavailability of the peptide drugs. In the first project of this thesis, we systematically characterized seven permeation enhancers and membrane active peptides (C10, DDM, NaC, SDS, SNAC, melittin, and penetratin) with respect to their self-aggregating properties and membrane activity. It was studied how the membrane activity was affected by interactions with either of the two peptide drugs insulin and sCT. The studies were carried out in solutions with properties mimicking the intestinal fluid with regards to pH and osmolality, and in the absence or presence of the bile components taurocholate and phospholipids. We were able to show that interactions with peptide drugs changed the membrane activity of permeation enhancers, and that this again was affected by the presence of taurocholate and phospholipids. Both increases and decreases of membrane activity was observed, potentially correlating with a modified bioavailability. This study underlines the importance of carrying out mechanistic studies of permeation enhancement in the presence of bile components, and to carefully choose the combination of permeation enhancer and peptide drug. Further studies are needed to investigate how changes in membrane activity relates to bioavailability, and if more systematic effects can be deduced from a larger set of peptide drug:permeation enhancer combinations, alternatively from more in-depth studies of the driving forces of the interactions. However, this study provides a new perspective to a field of emerging interest and broadens the mechanistic understanding of membrane activity in relation to peptide drugs and permeation enhancers targeting the small intestines.

In the second part of this thesis, a method was developed in which the mode of action of membrane active peptides, measuring the effect on the level of the individual liposome. The mode of action was investigated for six different membrane active peptides (penetratin, magainin-2, LL37, macrolittin 70, melittin, and Tat), and assigned as membrane permeabilization with or without solubilization, as well as aggregation of the liposomes. The membrane permeabilization with solubilization corresponds to a surfactant mode of action and the membrane permeabilization without solubilization corresponds to membrane-thinning or pore-formation. Furthermore, peptides inducing liposome-aggregation were identified. While no distinction of subpopulations were made in this work, it should be possible to expand the method to do this, which would enable the identification of eg. graded and all-or-none mechanisms.

Also, by including further fluorophores, eg. on the peptide drug, it may be possible to determine how the various mechanisms correlate with membrane association, all concurrently. This method thus provides the basis for new high-throughput mechanistic studies of membrane active species which can greatly contribute to the understanding of permeation enhancement of oral delivery of peptide drugs.

In summary, the studies here provides systematic insight into the mechanism of membrane activity as well as methods to perform such studies in high-throughput. Understanding mechanisms of permeation enhancement can aid in the development of oral peptide drugs and their formulations, and the work presented in this thesis can hence provide a basis for faster and more relevant understanding and screening of permeation enhancement, paving the way for successful oral peptide drug delivery.

Appendix: Review: Imaging therapeutic peptide transport across intestinal barriers

Review:

J. B. Larsen et al., “Imaging therapeutic peptide transport across intestinal barriers,” RSC Chem Biol, vol. 2, no. 4, pp. 1115–1143, Aug. 2021, doi: 10.1039/D1CB00024A.

RSC Chemical Biology

REVIEW

View Article Online
View Journal | View Issue

Cite this: *RSC Chem. Biol.*, 2021, 2, 1115

Imaging therapeutic peptide transport across intestinal barriers

Jannik Bruun Larsen, Nayere Taebnia, Alireza Dolatshahi-Pirouz, Anne Zebitz Eriksen, Claudia Hjørringgaard,† Kasper Kristensen, Nanna Wichmann Larsen, Niels Bent Larsen, Rodolphe Marie, Ann-Kathrin Mündler, Ladan Parhamifar,‡ Andrew James Urquhart, Arjen Weller, Kim I. Mortensen, Henrik Flyvbjerg and Thomas Lars Andresen*

Oral delivery is a highly preferred method for drug administration due to high patient compliance. However, oral administration is intrinsically challenging for pharmacologically interesting drug classes, in particular pharmaceutical peptides, due to the biological barriers associated with the gastrointestinal tract. In this review, we start by summarizing the pharmacological performance of several clinically relevant orally administrated therapeutic peptides, highlighting their low bioavailabilities. Thus, there is a strong need to increase the transport of peptide drugs across the intestinal barrier to realize future treatment needs and further development in the field. Currently, progress is hampered by a lack of understanding of transport mechanisms that govern intestinal absorption and transport of peptide drugs, including the effects of the permeability enhancers commonly used to mediate uptake. We describe how, for the past decades, mechanistic insights have predominantly been gained using functional assays with end-point read-out capabilities, which only allow indirect study of peptide transport mechanisms. We then focus on fluorescence imaging that, on the other hand, provides opportunities to directly visualize and thus follow peptide transport at high spatiotemporal resolution. Consequently, it may provide new and detailed mechanistic understanding of the interplay between the physicochemical properties of peptides and cellular processes; an interplay that determines the efficiency of transport. We review current methodology and state of the art in the field of fluorescence imaging to study intestinal barrier transport of peptides, and provide a comprehensive overview of the imaging-compatible *in vitro*, *ex vivo*, and *in vivo* platforms that currently are being developed to accelerate this emerging field of research.

Received 4th February 2021,
Accepted 9th June 2021

DOI: 10.1039/d1cb00024a

rsc.li/rsc-chembio

1. Introduction

Since the emergence of insulin therapy in the 1920s, peptides have been used extensively in medical practice.[1] Peptides are ideal drug candidates, since they may disrupt protein–protein interaction efficiently and serve as ligands for cell-surface receptors.[1,2] The worldwide market for peptide therapeutics has been estimated to more than double from 21.3 to 46.6 billion US$[1] between 2015 and 2024. Typically, therapeutic peptides are administrated by injection,[3] which limits the possibility for self-administration of the drug and lowers overall patient compliance.[4] Therefore, alternative routes of delivery are areas of strong focus.[5] Oral peptide delivery has received intense interest for decades.[6] In this context, bio-availabilities of peptides above a few percent have proven extremely difficult to achieve, due to the biochemical and physical barriers presented by the gastric and the intestinal environment.[7] The major obstacles include enzymatic peptide degradation and poor absorption through the epithelial cell layer.[8] Consequently, considerable efforts have been devoted to the development of various delivery systems and permeation enhancers (PEs), such as fatty acids, surfactants, and bile salts.[5] However, clinically approved delivery strategies for uptake *via* the gastro-intestinal tract remain scarce.[1,3,7]

In the quest for new peptide drugs and delivery systems, the quality of potential candidates is typically assessed using end-point bio-availability measurements (Fig. 1, left).[8] Positive hits are identified by their increased transport across experimental models of the physiological and cellular barriers of the intestine.[9] Such model systems span a vast range of technical

Center for Intestinal Absorption and Transport of Biopharmaceuticals, Department of Health Technology, Technical University of Denmark, DK-2800, Kgs., Lyngby, Denmark. E-mail: tlan@dtu.dk
† Current address: Patentgruppen A/S, DK-2200, Copenhagen, Denmark.
‡ Current address: AstraZeneca, World Trade Center Ballerup, DK-2750, Ballerup, Denmark.

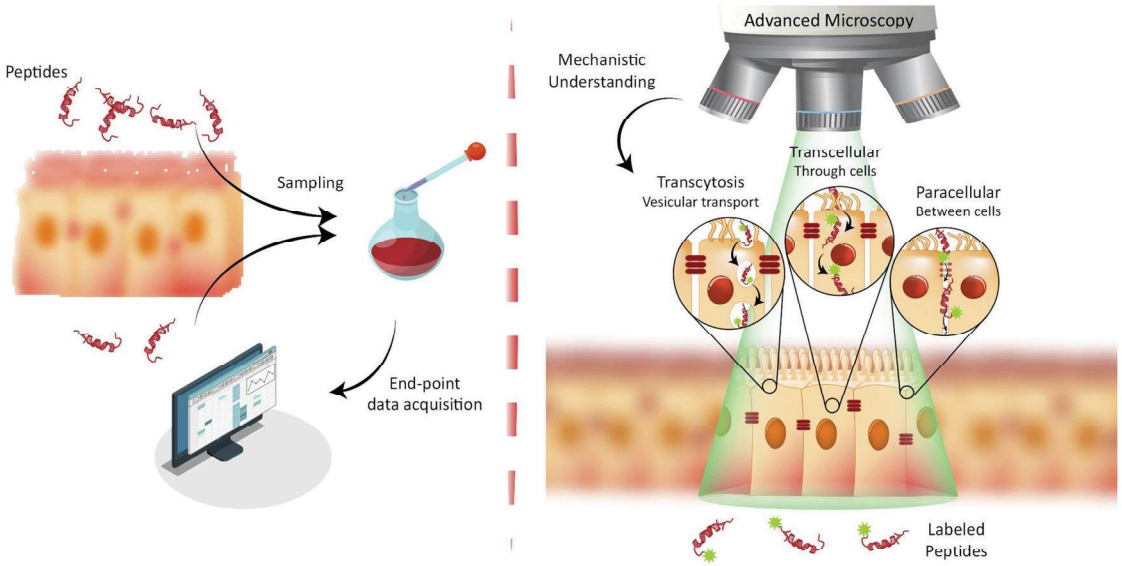

Fig. 1 Paradigms for studying peptide transport across intestinal barriers. (left) Traditionally, peptide transport across intestinal barriers has been studied using barrier model systems employing end-point assays offering only indirect mechanistic insight on peptide transport mechanisms. (right) Fluorescence live-cell imaging offers the ability to directly visualize and track peptide transport across intestinal barrier models allowing for determination of the transport mechanisms (such as transcytosis, transcellular and/or paracellular) governing peptide transport.

and biological complexities; they range from simple artificial membranes to tissue samples.[8] While the model systems do permit the quantification of pharmaceutical peptide transport across a biological barrier, they typically do not yield information about which cellular mechanisms that facilitated translocation. This approach was used, *e.g.*, in the development of the previously described array of PEs. Thus, many constructs and strategies have been tested, but their full biological mechanisms of action are complex and remain to be fully elucidated, which has led to concerns about the long-term use of PEs in chronic administration.[10,11]

The end-point screening methods applied for development of peptide drug candidates have recently been challenged by a community that has realized the importance of understanding the biological mechanisms governing drug delivery.[9,12] For transport studies on peptide translocation across the intestinal barrier, seminal mechanistic efforts focused on using pharmacological agents to modify tight junction (TJ) integrity or selectively disrupt endocytosis pathways.[8,13] Such studies have helped elucidate the major translocation pathways of the intestinal barrier employed by orally administrated small-molecule drugs and peptides.[1] These pathways include (Fig. 1, right) active transcytosis mediated vesicular transport, passive transcellular transport through epithelial cells, and paracellular transport between epithelial cells through the TJs. Despite the widespread use of pharmacological pathway inhibitors, their specificity has been disputed, as they have been shown to affect multiple endocytosis pathways simultaneously.[14–16] Therefore, more direct, rigorous mechanistic insight into peptide transport has been sought through other routes, most noticeably through the employment of fluorescence imaging.[13,17,18] The great advantage of this approach is the ability to directly track peptide transport in live-cell setups involving only a minimal disturbance of the cells' natural milieu (Fig. 1, right). Image-based transport studies should provide direct mechanistic information about the absorption and transport of peptides through and across the intestinal barriers. So far fluorescence-based methods have only routinely been used to study peptide transport in individual cells, as it is non-trivial to combine live-cell imaging with more realistic models of cellular barriers. However recent, significant strides in the field provide new and exciting opportunities for mechanistic studies of peptide transport across cellular barriers using more complex experimental setups and imaging modalities. The increase in mechanistic information should foster rationally design modifications to peptides and their delivery systems. Such guided modifications might optimize the bio-availability and end-point efficacy of orally delivered peptide pharmaceuticals dramatically.

Here, we briefly review what is known mechanistically about the modes of action of the clinically approved oral peptide and PE formulations as well as how conventional fluorescence imaging has aided to these ends. We then consider all steps involved in design and implementation of fluorescence image-based peptide-translocation studies: first, we discuss the choice of fluorescence imaging modality, the chemical considerations regarding choice of fluorescent probe and site of modification, and the biophysical characterization techniques used to monitor peptide stability and membrane interaction. Next we discuss the range of *in vitro* and *ex vivo* barrier models that are currently being developed to facilitate image-based studies and how *in vivo* imaging studies are emerging as an important method towards understanding peptide transport in the native environment. Finally, we briefly review the insights gained on how nanoparticle (NP) delivery systems made from peptides translocate across cellular barriers using imaging-based platforms.

2. Oral peptide drugs for systemic applications used in the clinic

Of all the classical non-invasive delivery routes, orally administrated pharmaceutical peptides had the largest share of clinical trials in 2019, emphasizing the strong effort in translating oral drugs to the clinic.[19] Nevertheless, only four peptide treatments designed for transport across the intestinal barrier have yet been approved by the FDA.[20] Despite earlier success with oral dosage forms of Cyclosporin A (CsA) and desmopressin in the 1980s, it has proven difficult to push other oral peptide drugs into the clinic. In fact, no other peptide drug for oral administration progressed beyond Phase II trials between 1987–2010.[21] Only very recently, did the field experience a resurgence with the FDA approval of oral semaglutide in 2019 and octreotide in 2020. The historical development of oral peptide drugs and the current status of candidates in end-stage clinical trials have been reviewed extensively recently.[5,21,22] Here we instead focus on the four peptide drugs currently approved for use in the clinic. We focus on the mechanisms involved in their successful transport across cell barriers and discuss instances where fluorescence imaging has helped elucidate these mechanisms.

2.1 Cyclosporin A

CsA is a cyclic undecapeptide used as an immunosuppressant to treat graft-versus-host disease in transplant patients. It was approved by the FDA for clinical use in 1983.[23] The case of CsA is unique due to its relatively high bioavailability (BA) (above 30%), which has spurred in-depth mechanistic studies aimed at elucidating the key structural features promoting the passive diffusion of CsA across cellular barriers.[24] Based on these studies, it was concluded that the efficient transport of CsA results from its ability to reduce its interactions with the aqueous solvent, driving the transport of CsA from the aqueous phase and through the cell membrane. Firstly, this relies on the presence of non-canonical N-methylated amino acids, which reduces hydrogen bond-mediated interactions with the aqueous solvent.[25] Secondly, conformational flexibility allows CsA to exist in an ''open'' conformation in aqueous solvents and a ''closed'' conformation when entering a lipid bilayer, thereby further modifying the hydrogen bonds available for interaction with the solvent.[24] Finally, the cyclic structure of CsA allows it to bury some of its polar backbone, thus concealing it from water.[21] Despite these unique features, CsA suffers from low solubility, and therefore the clinically approved product Neoral is formulated as a self-nanoemulsifying drug delivery system (SNEDDS) forming oil-droplets smaller than 150 nm. In addition to facilitating a rapid and uniform drug release, the fatty acid-based excipients in SNEEDS serve as PEs by directly leading to an increase in intestinal permeability as well as inhibiting *p*-glycoprotein efflux and cytochrome P450-3A4 mediated CsA metabolism.

2.2 Desmopressin

Oral Desmopressin acetate (DDVAP) is a nonapeptide with a six-amino acid ring structure that has been used for treatment of central diabetes insipidus and primary nocturnal enuresis since the 1980s.[5] DDVAP is a synthetically-made analog of arginine vasopressin with two modifications, a de-amination of the first amino acid and a substitution of the eighth amino acid replacing L-arginine by D-arginine. Both of these modifications strongly enhance the intestinal stability of DDVAP relative to native arginine vasopressin, mainly by reducing enzymatic degradation. DDVAP has been suggested to transport across the intestinal cell layer by passive permeation, most likely by the paracellular route,[26,27] however the oral BA of the commercial DDVAP product Minirin is only 0.17% in humans.[5] Its exceptional potency is the only reason why Minirin remains therapeutically viable at such an extremely low BA.

2.3 Oral semaglutide

Semaglutide is a 31-amino acid linear GLP-1 receptor agonist analog approved under the name Rybelsus in 2019 for treatment of Type 2 diabetes.[5] Facilitated by the addition of a di-acid C_{18}-acylation and substitution of strategic amino acids, semaglutide displays high potency, stability, and long circulating half-life.[21] These properties compensate for a BA of merely 0.4–1.0%.[28] However, the large market potential for Type 2 diabetes treatment has resulted in oral semaglutide being described as the most interesting peptide yet considered for oral delivery.[21] In Rybelsus, semaglutide is co-formulated with the PE salcaprozate sodium (SNAC) and was demonstrated to be exclusive absorbed across the gastric epithelial and thus not in the intestine.[29] It was shown that SNAC positively affected semaglutide uptake by locally lowering the gastric pH, hereby reducing peptide cleavage by pepsin, and shifting semaglutide towards a monomeric state better suited for transport. *Ex vivo* immunofluorescence imaging on canine gastric tissue was employed for an in-depth analysis of the transport mechanism of semaglutide (Fig. 2A).[29] An almost exclusive staining for semaglutide around the site of tablet identification strongly supported that close proximity of SNAC and semaglutide were essential for efficient transport (Fig. 2A top). Additional confocal microcopy imaging (see Section 4) revealed intracellular uptake of semaglutide in mucosal cells and staining of the TJ protein ZO-1 confirmed an intact TJ morphology (Fig. 2A bottom). That combined with *in vitro* assays displaying no effect on semaglutide transport upon introduction of TJ modulators like EDTA demonstrates that semaglutide is transported across the gastric epithelium through a transcellular mechanism. This mode of transport concurs with the known function of SNAC as a modulator of the transcellular pathway.[30]

2.4 Octreotide

Orally delivered octreotide is a cyclic octapeptide somatostatin-analog that binds with high affinity to somatostatin receptors, hereby blocking the production of growth hormone.[5] Very recently, octreotide was approved by the FDA (June 2020) for oral treatment of acromegaly under the name Mycappsa.[31] The Mycappsa delivery system relies on the ''Transient Permeation Enhancement'' (TPE) technology that solubilizes octreotide in an oily suspension, including the PE sodium caprylate (C_8).[21]

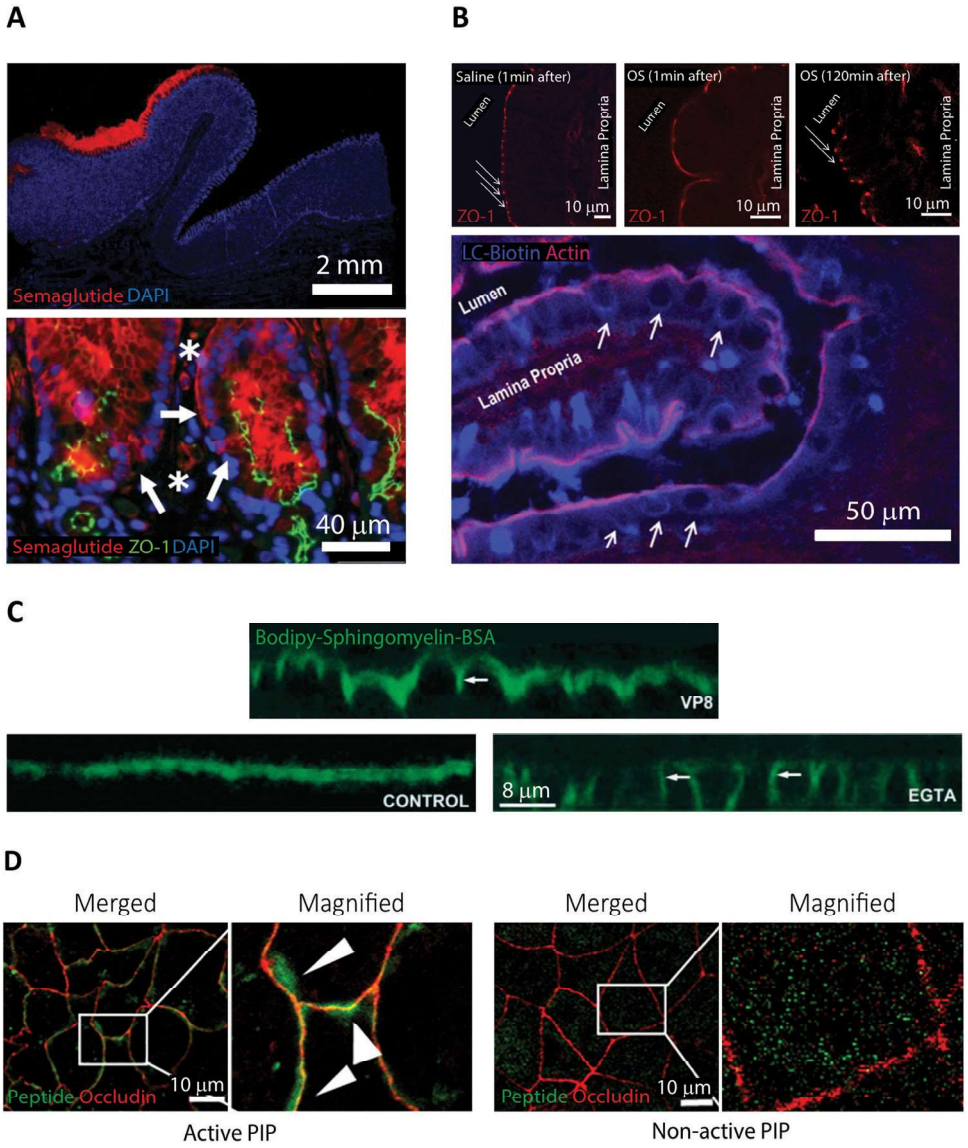

Fig. 2 Examples of fluorescence imaging used to elucidate peptide and PE transport mode of action. (A) Immunofluorescence imaging of canine gastric tissue uncovering a transcellular barrier transport mechanism of oral semaglutide. Top, semaglutide (red) and DNA (blue) stains reveal that peptide is predominantly localized to the region in and around of the Rybelsus tablet. Bottom, semaglutide (red) is shown to reside in the cytoplasm of mucosal epithelial cells (white arrows) with intact tight junctions depicted by ZO-1 (green) and DNA (blue). Semaglutide is also detected in capillaries under the epithelium marked by white asterisks. Reproduced from ref. 29 with permission from The American Association for the Advancement of Science, copyright 2018. (B) Immunofluorescence imaging of rat jejunum epithelium reveal that the ''Transient Permeation Enhancement'' (TPE) delivery technology employed for the octreotide system affects the paracellular permeability. Top, a transient disruption of ZO-1 (red) distribution is induced after one minute incubation with TPE (middle) as compared to saline (left). After 120 minutes incubation with TPE, the ZO-1 organization displays its normal puncta-like morphology (right). Bottom, paracellular flux of the tracer LC-biotin (blue) (white arrows) displayed after incubation with TPE, with the lateral membrane stained for actin (red). Reproduced from ref. 33 with permission from Springer Nature, copyright 2014. (C) Elucidating the ability of the microbial toxin VP8 and the Ca^{2+} chelator EGTA to affect the TJ fence function by imaging caco-2 cell monolayers. In control cells (lower left), imaging of the diffusion marker Bodipy-Sphingomyelin-BSA (green) revealed a staining restricted to the apical cell layer. After addition of either VP8 (top) or EGTA (lower right) clear baso-lateral membrane staining of Bodipy-Sphingomyelin-BSA is evident (see white arrows). Reproduced from ref. 35 with permission from The Company of Biologists Ltd, copyright 2004. (D) Distribution of PIP peptide analogs in caco-2 cell monolayers imaged after 45 min of apical incubation. Binding of Alexa488-streptavidin (green) to active biotinylated PIP peptides (left) or non-active biotinylated PIP peptides (right) reveal a strong colocalization with occluding (red) for active PIP, but a random cytosolic distribution for non-active PIP. Reproduced from ref. 39 with permission from Elsevier, copyright 2018.

Despite employing this multi-component delivery platform, the BA of octreotide remains at just 0.5%.[32] *Ex vivo* immunohistochemistry in combination with confocal microscopy were used to investigate the transport mechanisms employed by octreotide in this formulation (Fig. 2B).[33] Staining rat intestines for ZO-1 revealed a loss of TJ structural integrity within one minute of adding the TPE system and reversal of this effect after 120 minutes (Fig. 2B top). Additionally, using a fluorescently

labelled diffusion marker, it was shown that application of the TPE system leads to a paracellular flux (Fig. 2B bottom). This evidence supports that octreotide is transported across the intestinal barrier through paracellular transport *via* a TPE mediated TJ modulating mechanism, induced by C_8.

3. Elucidating permeation enhancers' modes of action using fluorescence imaging

A recurring obstacle for oral peptide delivery is the poor BAs that are reported in clinical trials to be in the low single digit percentages.[20] Therefore, there is a quest for discovery, design, and testing of new PEs that could increase the intestinal transport of peptide drugs. Until these endeavors prove successful, oral peptide delivery is restricted to rely on candidates that display elevated intrinsic permeability, high potency, stability, and/or long plasma-half-life. Here, we abstain from giving a comprehensive description of PEs and their use in ongoing clinical trials, since these subjects have been covered extensively in recent, excellent reviews.[5,20,34] Instead, we highlight some pivotal studies in which fluorescence imaging has been employed in an attempt to elucidate PE modes of action, paving the way for designing smarter and better PEs in the future (Fig. 2).

Traditionally, PEs are divided into classes based on the transport pathway that they affect, mainly paracellular or transcellular (Fig. 1).[20] However, it is well-established that many PEs affect numerous different pathways simultaneously, often making it hard to pin-point an exact mode of action. In general, paracellular PEs function by disrupting the TJ proteins that ensure a tight barrier between adjacent epithelial cells.[34] This class is further sub-divided into PEs that either directly affect the TJ proteins or target endogenous cell signaling cascades related to TJ function and integrity. Members of the first sub-group include microbial toxins, which disrupt TJ protein distribution, as shown using fluorescence imaging of *in vitro* cell monolayers.[35,36] This disruption induces an impairment of the TJ fence function evident from a loss of distinct apical or basolateral membrane staining of lipid reporter systems or membrane proteins (Fig. 2C, VP8). Despite the potent ability of microbial toxins to modulate TJ biology, their clinical use as PEs has remained sparse, mainly due to concerns about toxicity.[21] The most clinically advanced paracellular PEs are EDTA (ethylenediaminetetraacetic acid) and EGTA (ethylene glycol-bis(β-aminoethyl ether)-*N*,*N*,*N*′,*N*′-tetraacetic acid), which belong to the second sub-group affecting endogenous signaling pathways linked to TJ function.[20] Both EDTA and EGTA work by chelating extracellular Ca^{2+} ions, causing an efflux of intracellular Ca^{2+} leading to a disruption of TJ integrity. Fluorescence imaging in cell monolayers has shown a similar loss in TJ fence function induced by EGTA as compared to molecular toxins (Fig. 2C, EGTA).[35] A more directed approach homes in on a specific endogenous pathway, which is believed to reduce toxic off-target effects. One example is the phosphorylation state of the myosin light chain (MLC) complex, which dynamically controls whether the TJ complex is in an "open" or "closed" conformation.[37] The PIP decapeptide (Permeable Inhibitor of MLC Phosphatase) was developed to specifically prevent dephosphorylation of MLC, keeping the TJ complex in an open confirmation.[38] This detailed method of action was verified by imaging the intracellular localization of fluorescent PIP peptide in cell monolayers *in vitro*.[39] The active PIP analog displayed strong spatial colocalization with the TJ complex protein occludin, demonstrating its specific targeting to the site of MLC phosphatase action (Fig. 2D). Single amino acid replacements in control peptides was enough to completely abolish the occludin colocalization observed for native PIP.

Surfactants make up the most abundant group of PEs that potentially affect intestinal transport through the transcellular route.[20] This group contains fatty acids with intermediate chain lengths (C_8, C_{10}, and C_{12}) and acetylated amino acids (SNAC), which are the PEs most abundantly tested in humans.[5] Originally, these surfactants were believed to facilitate increased transcellular permeability through membrane-insertion-dependent reduction in plasma membrane packing density or through increased peptide hydrophobicity *via* complexation. More detailed method-of-action studies, in which fluorescence imaging has played a central part, have recently questioned the link between surfactants and the transcellular pathway. One example is the C_8-containing TPE technology (see Section 2.4) that facilitates uptake *via* the paracellular pathway, as shown by fluorescence imaging of rat intestines (Fig. 2B).[33] Also, a thorough description of the mode of action of C_{10} was recently performed to resolve previous ambiguity of C_{10} function.[30] The study included *in vitro* cell monolayer imaging of various TJ proteins, showing a clear C_{10} concentration-dependent loss in claudin-5 and occludin localization. Additionally, the authors performed a fluorescence imaging-based high-content analysis, where simultaneous multiplexed detection of fluorescent reporters for nuclear intensity, mitochondrial membrane potential, plasma membrane permeability, and intracellular calcium was achieved at the single-cell level. All evidence suggested that C_{10} increased paracellular permeability *via* a membrane-perturbation induced alteration in intracellular calcium levels, which leads to TJ opening through a MLC regulated mechanism.[30,40] Additionally, C_{10} has been shown to have a direct effect on membrane fluidity above its critical micelle concentration,[41] illustrating how PEs, like C_{10}, can affect numerous different pathways simultaneously.[21] The perceived mechanism of the main member of the acetylated amino acid class, SNAC, has also recently been updated. As described in Section 2.3 for the oral semaglutide formulation Rybelsus, SNAC was shown to display formerly unknown buffering and solubilizing effects.[29] Additionally, SNAC was also shown to facilitate transcellular transport of semaglutide as evident from *ex vivo* fluorescence imaging of canine gastric tissue (Fig. 2A). All the examples provided in this section illustrate how the field is only starting to reach consensus on the PE function, even for PEs extensively used in the clinic. Furthermore, it should be clear that fluorescence imaging is becoming a cornerstone for providing detailed insight, helping to usher in this increased focus on elucidating PE mode of action.

4. Fluorescence imaging modalities and single-particle data analysis

4.1 Fluorescence imaging modalities appropriate for studying peptide transport

Fluorescence imaging is widely used in the search for mechanistic insight into peptide transport across membrane- and cellular barriers. It is essential, however, to choose the right imaging modality among the following (ever growing) list of options[17,42] (Fig. 3):

(i) Wide-field microscopy (WFM) is the standard modality.[17] It is affordable and consequently broadly available. In wide-field microscopy, the entire sample is exposed to the illumination (bright-field or epi-fluorescence) and imaged with a camera. This mode does not provide resolution along the optical axis. Its achievable contrast is limited by a fluorescent background in samples that extend along the optical axis or when fluorescently tagged molecules of interest, say peptides, are present also in the solution surrounding the sample.

(ii) Total internal reflection fluorescence microscopy (TIRFM) uses an evanescent wave to confine the excitation light to within ~100 nm of the surface of a coverslip.[43] This enables single-molecule studies even in extended samples because most of the sample is not illuminated. For the same reason, TIRFM is limited to processes occurring in proximity of the coverslip surface, such as molecular motion in the plasma membrane and early steps of molecular uptake mechanisms.

(iii) Confocal laser scanning microscopy (CLSM) differs fundamentally from the above by scanning the sample with a focused spot of excitation light.[44] Emitted light is simultaneously collected with a photo detector, but only from the focused illuminated spot on the sample in the focal plane of the objective. All other light is blocked with a screen containing a 'pinhole' in the optically conjugate plane. Thus, spatial resolution here

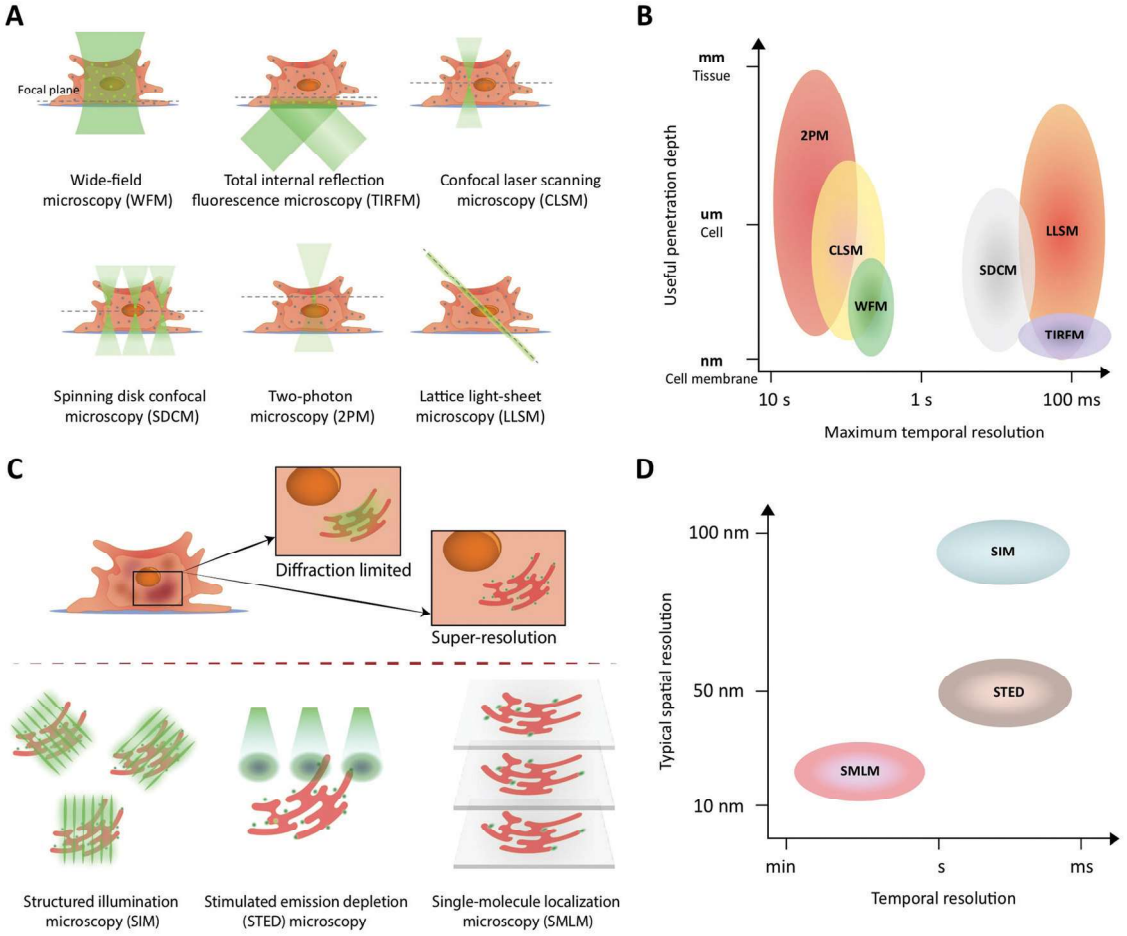

Fig. 3 Fluorescence imaging modalities applicable to study peptide transport across membranes and cellular barriers. (A) A schematic of the illumination strategies and the optical sectioning capabilities of different microscopy modalities. The illumination light (green) excites fluorophores in the sample and, effectively, light is collected from a modality-dependent subset of the fluorophores near the focal plane (green dots). (B) A schematic comparing different imaging modalities in terms of their performance with respect to useful imaging depth and maximum temporal resolution when used to image extended samples that are sparsely labeled. In low-light situations, modalities that rely on scanning (CLSM, 2PM) or do not yield efficient background rejection (WFM) are slower than camera-based methods (LLSM, SDCM, TIRFM) that collect light from all pixels in an image plane in parallel. WFM's poor rejection of fluorescence away from the focal plane strongly limits its useful penetration depth due to loss of contrast. (C) A schematic illustrating how the three major classes of super-resolution fluorescence imaging methods overcome the diffraction limit of conventional fluorescence imaging. (D) A schematic comparing the three super-resolution imaging modalities in terms of their typical performance in terms of temporal and lateral spatial resolution.

originates from the lateral scanning mode of the excitation combined with axial light selection by the pinhole. This also permits optical sectioning, thus providing three-dimensional (3D) spatial resolution in extended samples (~100 μm). Fast scanning modes are possible, but the modality suffers from high photobleaching rates, since the excitation light is not limited along the optical axis to the part of the sample from which light is collected.

(iv) Spinning disk confocal microscopy (SDCM) essentially parallelizes the confocal illumination and acquisition through multiple pinholes in a rotating disk, relying on a camera to collect the emitted light.[17] Compared to CLSM this modality has lower photobleaching rates and faster acquisition rates but lower effective penetration depth (~10 μm), limited by light-collection crosstalk between neighboring pinholes at deeper penetrations.[45]

(v) Two-photon microscopy (2PM) is the preferred modality for deep imaging (~1 mm) into tissue, model organisms, and on-chip model systems.[42,46] Here, the fluorescent label is simultaneously excited by two near-infrared photons. The longer excitation wavelength reduces scattering in the sample, while the non-linear multi-photon excitation process strongly confines the excited volume even in scattering samples. This makes pinholes redundant and suppresses the background. The light emitted is collected by a photodetector, which makes collection insensitive to moderate scattering of emission. The major drawback of the modality is its relatively low acquisition speed in practice.

(vi) Lattice light-sheet microscopy (LLSM) now offers prolonged intra-cellular imaging of single molecules. All light-sheet based microscopies uses a second objective to illuminate selectively a plane of interest in the sample.[47–49] In conjunction with a camera, these modalities allow imaging of an entire plane during each exposure. Recently, the lattice light-sheet microscope was developed to illuminate the sample with an ultra-thin light sheet. This effectively achieves extremely efficient background rejection in selected planes of living cells and optically transparent organisms.[50–52] This modality was recently combined with adaptive optics that permit correction for optical distortions created by the sample itself, which allows for deeper imaging (~100–200 μm) into tissues by tiling independently-acquired fields of view.

The choice of experiment, imaging modality,[17] and image analysis depends, obviously, on the scientific question at hand. This choice subsequently defines the resolution with which one can provide answers. Light scattering and background in thick samples, for example, are factors that determine the level of detail that can be imaged. Also, the working distance of the objective is an important parameter when imaging peptide transport across various models of the intestine. The physical dimensions of the model of interest (Fig. 4) determine the range of applicable objectives. The need for long working distance objectives to image traditional intestinal barrier models (see Sections 8 and 9) often prevents high-resolution imaging.[53] Oil-immersion objectives provide the highest numerical apertures (NAs), and hence the highest resolution, but typically have a working distance below 130 μm.[54,55] This leaves an effective depth of imaging around 100 μm in typical imaging conditions. Water-immersion objectives provide NAs up to 1.3 but offer a much larger range of working distances, up to 500 μm. If a cover glass can be omitted, water dipping objectives can provide very long working distances for high NAs (for example 60×/1.0 NA with 2.0 mm working distance). In all cases, the working distance increases if one can compromise on NA, magnification, and need for optical corrections. The choice of objective in turn determines the microscope modality and the magnification that can be used. Importantly, the temporal resolution in all modalities is either limited by the scanning speed of the microscope or the

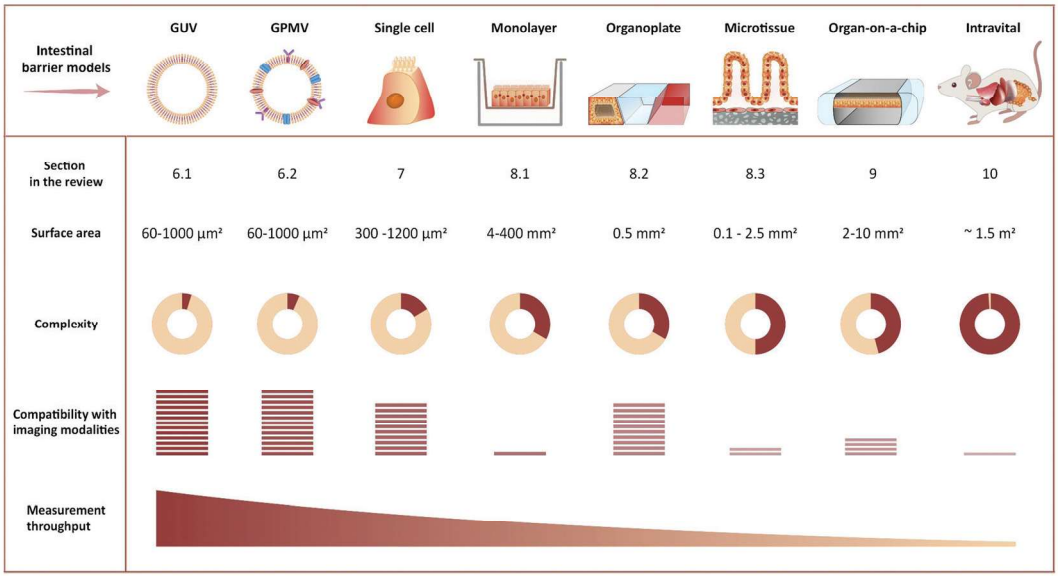

Fig. 4 Representative illustration of imaging-compatible biological models applicable to study peptide transport across the intestinal barrier. The pros and cons of various model systems are qualitatively compared with respect to complexity, compatibility with imaging modalities, and measurement throughput.

acquisition rate of the camera. When light is abundant, *e.g.* when imaging biological structures associated with bright or multiple fluorescent labels, the limited speed of the hardware limits time resolution. When light is scarce, *e.g.* when imaging single (peptide) molecules or structures labeled with a single or a few fluorophores, the rate at which photons are detected instead limits time resolution. In the latter case, recording with a camera (imaging sensor) in general yields better temporal resolution, provided that background fluorescence can be efficiently rejected (TIRFM, SDCM, LLSM), than scanning with a point detector (CLSM, 2PM), since all pixels in the image are acquired simultaneously and photons are usually collected with a higher quantum efficiency (Fig. 3B).

Phototoxicity is an important potential artifact, when using imaging modalities to study peptide transport in a live cell setup.[56] The excitation light used to illuminate the cells will react with naturally occurring compounds like flavin and porphyrin inside the cells.[57] These can then be degraded in a process creating reactive oxygen species that are detrimental to cell health and thus effect the experimental outcome. Reactive oxygen species can also be created when fluorophores undergo photobleaching. Some steps in the experimental setup can be taken to reduce phototoxicity: the detection scheme can be optimized to lower the effective illumination dose of the sample.[58] Additionally, modification of the buffer solution by adding antioxidants to scavenge reactive oxygen species or removing certain vitamins to reduce photobleaching have been demonstrated to reduce overall phototoxicity. Such specialized buffers for live cell imaging are commercially available.[57] However the most efficient way of reducing phototoxicity is to selectively only illuminate the currently imaged volume and not the entire depth of the sample. Selective illumination is a cornerstone in the emerging imaging methods TIRFM, 2PM and LLSM (Fig. 3A). Especially LLSM offers the possibility of only illuminating the focal plane, which is then scanned rapidly through the cell sample, allowing for time-dependent 3D imaging, often termed four-dimensional (4D) microscopy, with greatly reduced phototoxicity.[51]

4.2 How single-particle/molecule data analysis may be used to gain mechanistic insight on peptide transport

One path to mechanistic insight using fluorescence microscopy focuses on the detection and tracking of single molecules and/or particles. Tracking may enable quantification of heterogeneities in uptake pathways for individual particles. Heterogeneities may, in turn, identify the roadblocks in cases where transport of peptide drugs across a barrier is not complete, for example due to (partial) sequestering in endocytic pathways. The use of single-particle tracking in biophysical and pharmaceutical research has been reviewed on several occasions.[59–64] In the context of peptide translocation, single-particle tracking has predominantly been applied to study cell-penetrating peptides, both in artificial model membranes[65] (see also Section 6.1) and in live cells[66–68] (see also Section 7). In this way, the transport mechanisms of either the peptide itself or of its model delivery system have been elucidated.

Observation and analysis of the internalization, transport, and fate of individual peptides are desired to study uptake heterogeneities at the molecular level. Dynamic imaging of individual peptides is limited by only a single fluorescent molecule being present on each peptide (see Section 5). Despite continued progress in fluorophore development,[69] it remains a challenge to record a sufficient number of photons from the peptide with sufficient temporal resolution to follow its whereabouts. Single peptides diffuse fast, which results in motion blur during exposures long enough to record a supposedly sufficient number of photons. If stacks along the optical axis are required for full 4D resolution, the challenge is even bigger. On the other hand, a crowded cellular environment or interaction with the cell membrane or various organelles slows diffusion. Thus, single-peptide studies in such environments have their temporal extent limited by the fluorophore stability rather than by the acquisition speed of the microscope.

In case of sufficiently low (labeled) peptide density, LLSM allows 4D tracking of individual molecules/peptides in live-cells for extended durations. This modality should be particularly suited to study individual peptides in direct translocation across the membrane,[70–72] a process that is difficult to capture due to the limited number of photons available. On the other hand, endocytic uptake of multiple individual peptides or aggregates results in a high peptide density in the endosomes. This makes more photons available, as long as the fluorescent peptide remains in the compartment,[73] which enables single-particle (endosome) resolution in 4D using SDCM.

Successful analysis of single-particle/molecule tracking data relies on three main steps:

(i) Detection of spots and their linking into trajectories. This may be considered a precursor step to a single-particle/molecule analysis.[60,74–77]

(ii) Sub-pixel resolution location of the fluorophore(s) that caused the detected spot trajectories. Typically, this localization is done by fitting a 2D or 3D model for a spot's intensity distribution to the measured spots. The precision of the fluorophore's location that results from this localization analysis depends critically on the number of photons in the measured spot.[78,79] A plethora of packages for automated 2D and 3D localization analysis exist, and a large fraction of them have had their performances compared across a number of data sets.[80,81]

(iii) Characterization of the underlying motion at the single-object level based on the high-precision trajectories obtained.[59,60,82] Most approaches rely on the mean-squared displacement of particle trajectories, but simpler, more rigorous alternatives exist for particles that exhibit normal diffusion.[83,84]

In all steps, the automated analyses have obvious advantages in terms of ease-of-use. Unfortunately, one-size-fits-all tools may result in suboptimal localization analyses.[85] Care should be taken throughout, since choices made by the user in every step may affect conclusions.

Single-particle/molecule tracking is often conducted as co-localization studies, which allows real-time tracking of multiple objects. This may be quantified as correlations, *i.e.* synchronized motion, between spectrally separated images of a

drug/peptide and any labeled cellular entity of interest.[86,87] More detailed information is attainable by accurately correlating color channels over time in an experiment to provide relative positions of drug/peptide and carrier compartment, not just information on their colocalization.[88] Relative positions can potentially discriminate between the peptide being transported on the inside or the outside of a membrane of a compartment to further elucidate transport mechanisms after successful uptake.

Highly supervised data analysis is under pressure from the increased use of high-resolution fluorescence imaging. The large amounts of data produced cause a demand for automated analyses. Thus, machine learning strategies[89] towards analysis currently proliferate in many branches of science. In single-molecule based localization microscopy, such algorithms may well be used to automate and speed up analyses[90] when one knows what the machine should learn to look for, *e.g.* specific biological structures and/or dynamics.[89,91] However, in the exploratory phases of data analysis and improvements of experimental designs, their use seems limited.

4.3 Super-resolution fluorescence microscopy

The microscopy modalities described above are all limited by diffraction to a spatial resolution of a few hundred nanometers. Consequently, labelled structures and/or molecules that are separated by less than this distance cannot be discriminated in images, which occludes the nanoscale organization of biological structures. In the past two decades, however, this fundamental resolution limit has been surpassed by various super-resolution methods for optical microscopy. These methods have had a major impact on the visualization and quantification of biological structures and processes at the nanoscale, and, as a result, they have been reviewed on many occasions.[92–96] We refer the reader to these excellent reviews for a detailed account of the methods and their usages in various contexts. Here, we provide a brief overview of the classes of methods and highlight their strengths and limitations in the context of cellular transport. In this light, it is important to realize that these methods originally were conceived as tools to circumvent the diffraction limit in the imaging of structures, but more recent developments of the methods, however, also permit their use to probe dynamics. The different requirements of those two applications are important to be aware of when choosing a super-resolution fluorescence modality for an application. With that in mind, super-resolution microscopy has been applied to study many structures and processes that are relevant in the context of cellular transport. Examples are: the nanoscale architecture and dynamics of cellular organelles, such as endosomes, the heterogeneity and mobility of cell-membrane associated proteins, intra-cellular motion of proteins, and dynamics of internalization and cellular trafficking of nanoparticles.[92–98]

In general, super-resolution fluorescence methods can be divided into two main classes. The first class uses engineered illumination of the sample to circumvent the diffraction limit. The second class consists of various single-molecule localization-based methods, in which fluorophores are separated in space and/or time and then localized with nanometer resolution, using tools identical to those described above for single-molecule tracking (see Section 4.2).

(i) Structured illumination microscopy (SIM)[99,100] falls in the first class of methods. It exposes the sample to multiple high-spatial-frequency illumination structures, typically parallel lines that are phase-shifted and rotated relative to each other (Fig. 3C). This encodes sub-diffraction-limited features from the sample in the resulting images. A super-resolved image of the sample may then be obtained by deconvolution of the images. In its simplest implementation,[99,100] SIM essentially combines two diffraction-limited sources of information. Consequently, it results only in a doubling of resolution relative to conventional diffraction-limited imaging (Fig. 3D). SIM allows straightforward multiplexing with different colors of fluorophores, is compatible with live-cell imaging, since it does not require high illumination intensities, and does not require complicated sample preparation. The temporal resolution is in the millisecond-to-second range, limited by the number of structured illumination patterns necessary for reconstruction/deconvolution (Fig. 3D).

(ii) In stimulated emission depletion (STED) microscopy,[101,102] a super-resolution image is obtained by scanning the sample with an effectively sub-diffraction limited excitation spot. To this end, the conventional confocal excitation spot is scanned synchronously with a second, doughnut-shaped depletion spot (Fig. 3C). The latter beam depletes excited fluorophores before they decay to the ground state by emission of fluorescence. Sub-diffraction-limited resolution is achieved through the non-linear dependence of STED on intensity of the depletion light: Intensities above a certain threshold deplete all fluorophores. Thus, only fluorophores positioned in the middle of the "hole" in the doughnut will avoid depletion and hence emit fluorescence. Consequently, the spatial resolution of STED is determined by the sharpness of the doughnut around its minimum. Typically, a lateral resolution of $\sim$50 nm is achieved (Fig. 3D). Fluorophores should be chosen so they are compatible with both lasers of the STED setup. The large intensity required for the depletion laser may result in phototoxicity to the sample, which may hinder prolonged biological imaging with this modality. The temporal resolution is in the millisecond to second range and is limited by the need to scan the entire field of view (Fig. 3D).

(iii) Single-molecule localization microscopy (SMLM) is a class of methods that achieve sub-diffraction-limited resolution by precise localization of single fluorescent probes in a sample. To do this, the sample is imaged repeatedly, with only a sparse subset of fluorophores activated in each frame (Fig. 3C). Popular methods include (direct) stochastic optical reconstruction microscopy (STORM,[103,104] dSTORM[105]), photo-activated localization microscopy (PALM[106]), and point accumulation for imaging in nanoscale tomography (PAINT[107]), which primarily differ in the means by which they create the sparse subset of active fluorophores. In a given image, each active fluorophore is localized with a precision that is limited, in principle, only by the number of photons observed from it (see above). In practice, however, other factors, *e.g.* labelling density and sample stability, also influence the resolution. A final resolution of $\sim$20 nm is not uncommon for biological samples (Fig. 3D). The temporal

resolution is limited by the number of images required for sufficient coverage of the targeted structure, which typically takes seconds to minutes to acquire (Fig. 3D). Fluorophores must be chosen to be photo-switchable or have appropriate blinking dynamics in order to be compatible with the super-resolution method or, in the case of PAINT, be conjugated to molecules with appropriate binding kinetics relative to the structure of interest. All methods are compatible with various field-wide illumination schemes, such as WFM, TIRFM, and (L)LSM (see Section 4.1).

For studies of single-particle and single-molecule dynamics in live cells, both STED and the various SMLM methods may be combined with single-particle tracking (see Section 4.2) and dual-color labeling strategies for co-localization.[97,98,108] Due to its scanning nature, STED may achieve sufficiently high temporal resolution by compromising on the size of the field of view. On the other hand, SMLM methods, such as sptPALM (single-particle tracking PALM), simultaneously solve the two problems of sufficiently sparse labeling and replenishing of labels for imaging, since they only view a subset of the fluorescent molecules at the same time. This increases throughput by orders of magnitudes without any additional sample preparation steps. In this mode, SMLM is not limited by the number of images required for imaging of a structure, since only individual molecules are tracked through consecutive frames, until this tracking is repeated for another subset of molecules.

Recent methodological developments in microscopy have yielded a series of methods that essentially are hybrids of the different modalities described above. Notably, MINFLUX[109,110] uses multiple exposures of a doughnut-shaped illumination beam and the relative number of photons observed from a fluorophore to localize and track it. For given resolution, this requires an order of magnitude fewer photons than conventional single-molecule tracking, which enables MINFLUX to track individual molecules with unprecedented temporal resolution. Its scanning configuration, however, limits throughput. In its wake, a series of methods have emerged, which do not suffer from limited throughput. They use wide-field illumination structures (similar to those used in SIM) and thereby double the resolution of localization of individual molecules in 2D compared to what is achieved with uniform illumination.[111–113] Very recently, similar methods have been developed for improved axial localization using illumination structured along that dimension.[114,115] These wide-field methods are yet to be applied to imaging dynamics, however.

5. Fluorescent labeling and biophysical characterization of peptides

5.1 Potential artifacts introduced to peptide properties and behavior by fluorescent labeling

Fluorescence-based imaging studies of peptide transport across membranes and cellular barriers require the creation of a peptide–fluorophore construct.[116–120] Creating such constructs potentially changes the physiochemical properties of the peptide, which might affect the transport behavior as compared to the unlabeled peptide. Both the choice of fluorophore and conjugation strategy has been shown to influence the properties of the labeled peptide (Fig. 5).[121–124] Fluorophore size and hydrophobicity/hydrophilicity may influence the solubility, aggregation properties and partitioning coefficient of the labeled peptide (Fig. 5A).[121] The conjugation strategy such as the labeling position and conjugation chemistry may further impact amphipathicity and secondary structure of the labeled peptide (Fig. 5B).[122] A direct experimental artifact reported for some fluorescently labeled peptides is fluorophore mediated non-specific binding of peptides to glass surfaces or other substrates during microscopy, which can hamper single-molecule tracking and cause inaccuracies when using such setups to track peptide-membrane interactions.[125] It has been shown that the extent of fluorophore hydrophobicity (Fig. 5A) highly influences the extent of unspecific binding and caution should be exercised when choosing the respective fluorophore.[124–126] When employing fluorescently labeled peptides for studying transport across cellular barriers it is important to acknowledge that the fluorophore label has been shown to affect both the initial membrane interaction as well as the intracellular trafficking of peptides.[121,122,124] Based on a comprehensive screen of a wide range of commonly used fluorophores it was concluded that the fluorophore:membrane interaction propensity varied greatly. Thus, researchers should always strive to select fluorophores known to not drive the membrane interaction on its own. Once the peptide is taken up by the cell, the fluorophore can also influence the intracellular distribution of the conjugated peptides.[121] Depending on the size and shape of the fluorophore, different localization patterns were observed for the same peptide, demonstrating how fluorophore labeling can bias the interpretation of intracellular transport data.

In addition to phototoxicity during imaging, it has also been shown that the mere presence of the fluorophore conjugate can lead to an increased cellular toxicity.[121] A possible mechanism is a loss of membrane integrity due to the fluorophore mediated enhancement of peptide-membrane interactions supported by the physiochemical properties of the fluorophores having a direct influence on the extent of the cytotoxicity. Screening a selection of fluorophores determined that neutral hydrophobic fluorophores or negatively charged fluorophores conferred less cytotoxicity as compared positively charged, hydrophobic fluorophores.[121]

5.2 Strategies for fluorescent labeling of peptides

As outlined in the previous section, it is essential to understand the impact of the fluorophore on both the transport across membranes as well as the intracellular trafficking. This impact should, if at all possible, be evaluated in the context of the native peptide by performing a structure/activity analysis and mechanistic transport study. However for studies where fluorescence imaging is the sole experimental platform, any potentially detrimental effect of fluorophore conjugation can be delineated by comparing results from identical peptides labelled with chemically distinct fluorophores. Other factors for the choice of fluorophore depend on the experimental design, including the density of fluorescently-labeled peptides under study (see Section 4.1),

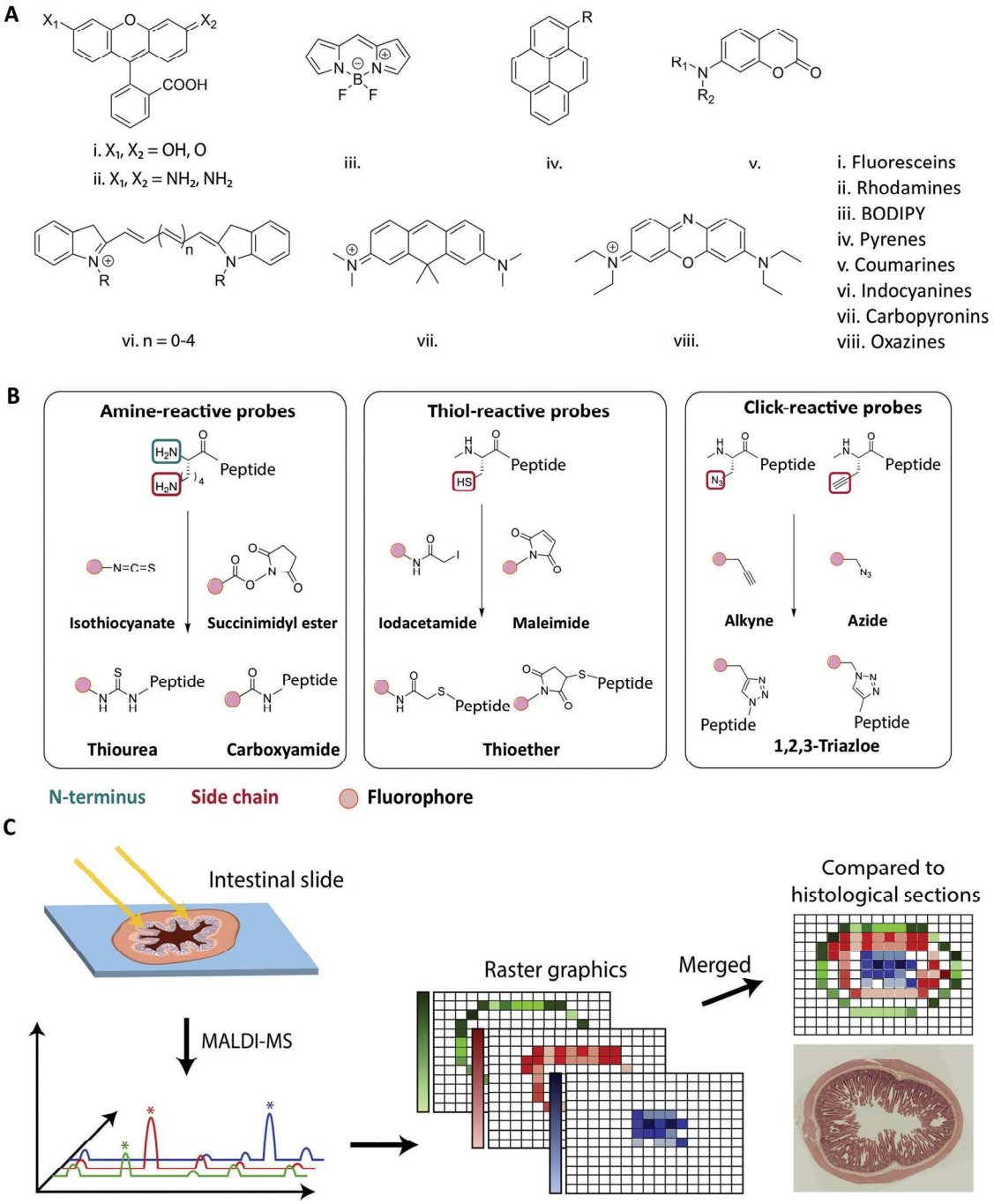

Fig. 5 Strategies for fluorescent labeling of peptides. (A) The chemical core structures of the most common and commercially available fluorophores. The properties of the fluorophore derivatives can be chemically tailored, by changing the substitution pattern of the respective core structures or by the addition of chemical moieties. This results in a great variety of different fluorophores available for many different applications. (B) The chemistry behind the commonly employed fluorophore conjugation techniques using either amine-, thiol- and click-reactive probes. Amine-reactive probes target amine groups like lysine residues or the N-terminus. A wide variety of different amine-reactive probes is available. This makes it an advantageous method, when labeling peptides during SPPS. Thiol-selective probes are advantageous, when labelling peptides in solution. Due to the low abundance of cysteine residues this conjugation techniques results in a high regioselectivity. Click-reactive probes offer the advantage of bioorthogonality, however, an unnatural amino acid with an alkyne or azide moiety needs to be incorporated into the peptide sequence. (C) Schematic overview of the MALDI-MSI method for the evaluation of peptide degradation or modification *in vivo*. A frozen intestinal section is first cryosliced and placed on a glass slide before a matrix is applied and the MALDI-MS is performed. For each pixel a mass spectrum is obtained allowing the creation of raster graphics which can be compared to histological sections. Reproduced from ref. 181 with permission from American Chemical Society, copyright 2021.

and should be made based on its spectroscopic properties, including absorption and emission spectra, the molar extinction coefficient, quantum yield, Stokes shift, and its propensity for quenching and bleaching.[127]

Traditionally, peptides are either produced by recombinant expression or synthesized using solid-phase peptide synthesis (SPPS).[128,129] The synthetic approach allows for full design-flexibility over the peptide sequence, enabling the introduction of chemically reactive handles available for bio-conjugation, such as the labeling with fluorophores. The conjugation of fluorophores to peptides[130,131] can be achieved by modifying the isolated peptide in solution, by adding the fluorescent label to side chain-protected polymer-bound peptides during SPPS[132,133] or by incorporating pre-labeled amino acids into the sequence.[134,135] When introduced in solution, the applied conjugation chemistry should be efficient, regio- and chemoselective, to ensure the formation of the desired product in high yield. When introduced during SPPS, the fluorophore should furthermore be compatible with deprotection- and cleavage conditions, as well as heating, if applied. In Fig. 5A the chemical core structures of the most commonly used fluorophores are depicted. By adding or changing the substitution pattern of functional groups, the properties of the respective fluorophores can be tailored. The most common commercially available fluorophores are derivatives of the shown core structures. For example, the widely used fluorophores fluorescein isothiocyanate (FITC) and carboxyfluorescein (CF) are built around the fluorescein core structure (i in Fig. 5A). The frequently used fluorophores Alexa Fluor 488, Atto 488 and 5-carboxytetramethylrhodamine (TAMRA) are all built around the rhodamine core structure (ii in Fig. 5A.). Bodipy and a number of derivates is designed around the main Bodipy structure (iii in Fig. 5A). Alexa Fluor 405 is built around the pyrene core structure (iv in Fig. 5A) and Alexa Fluor 350 or 430 are based on the coumarine core structure (v in Fig. 5A). The indocyanine core structure can be found in *e.g.* Cy5 or Alexa Fluor 647 (vi in Fig. 5A), Atto 610 builds around carbopyronin (vii in Fig. 5A) and Atto 655 represents a derivate of oxazines (viii in Fig. 5A). Many fluorophores, for example TAMRA and CF, contain reactive functional groups such as hydroxyl or amine groups. Consequently, the fluorophore preferably should be introduced in the final step, in order to avoid side-reactions during SPPS.[132,136] In cases where the fluorophore is in short supply due to cost or challenges in synthesis, the solution phase conjugation is a stoichiometric, cost-effective alternative to the SPPS approach, in which a larger excess of reagents is traditionally used.[137]

The most commonly used fluorophore conjugation chemistries utilize amine- and thiol-reactive probes and the alkyne/azide functionalized probes (Fig. 5B). The amine-reactive fluorophores are mainly acylating reagents such as activated esters[138] or isothiocyanates[139] (Fig. 5B, left). When they react with a peptidic amine, such as the N-terminus or a sidechain amino group, an amide bond or a thiourea will form. Although thioureas are less stable than amide bonds, isothiocyanates such as FITC and tetramethylrhodamine isothiocyanate (TRITC) are relatively cheap and thus are still widely used.[136,137,140] The thiol-reactive fluorophores are mainly alkylating reagents, such as iodoacetamides[141] or maleimides[142] (Fig. 5B, middle). The thiol-reactive fluorophores react with free cysteine residues forming a thioether bond, and the relatively low abundance of cysteine in in peptides makes regioselective fluorescent labeling possible. The majority of fluorescent dyes are commercially available as amine- and thiol-reactive probes. In an alternative bio-conjugation approach, alkyne- or azide-functionalized probes and peptides are used (Fig. 5B, right).[143,144] In the presence of a copper(I) catalyst, alkynes react with azides forming a very stable 1,4-substituted 1,2,3-triazole, often referred to as a "click" reaction.[145,146] It is biorthogonal, meaning that the reactants' chemical handles possess a unique reactivity that is orthogonal to naturally occurring functional groups.[144,147] The azide/alkyne moiety can be introduced into peptides by incorporating unnatural amino acids, either into the peptide sequence during synthesis[148] or by post-synthesis bio-conjugation of an azido/alkyne moiety.[149]

The broad range of commercially available fluorophores and their straightforward bio-conjugation and synthesis provide a high degree of flexibility in the peptide–fluorophore design. However, it is imperative to ensure that both the spectroscopic performance of the attached fluorescent dye and the basic functional properties of the peptide are minimally disturbed by the labeling process. Alternatively, any change should be characterized and understood. The next section details how to evaluate the effect fluorescent labeling infer on peptide properties and behavior and we outline the additional possibilities for peptide characterization offered by the fluorescent label, as well as the potential pitfalls associated with their use.

5.3 Basic characterization of fluorescently labeled peptides

While fluorescent labeling of peptides may give insight to the mechanistic pathway as they translocate across barriers (Fig. 1, right), the fluorescent labeling may directly affect a peptide's solubility,[150] conformational dynamics,[151] oligomerization and fibrillation behavior,[152–154] membrane interactions,[122] and receptor binding.[155] Before studying fluorescently labeled peptides in complex biological environments, it is thus important to evaluate the physicochemical properties of the peptides and how they compare to the unlabeled peptide.

In principle, fluorescently labeled peptides may be evaluated using common peptide characterization techniques,[156] including dynamic light scattering, size-exclusion chromatography with multi-angle light scattering, ultracentrifugation, circular dichroism, nuclear magnetic resonance, and fluorescence from extrinsic dyes (*e.g.* thioflavin T). However, for several of these techniques, there is a risk that the fluorophore attached to the peptide might disturb the measurement. For example, in assays with extrinsic fluorescent dyes, the peptide-attached fluorophore may obscure the signal of interest.[122] Likewise, the presence of a fluorophore may reduce the sensitivity and accuracy of light scattering-based techniques.[157] This calls for careful choice of the techniques used for characterization of fluorescently labeled peptides and execution in a manner compatible with the fluorophore.

Fluorescent labeling of peptides, however, also opens new opportunities for studying peptide properties, for instance investigation of the peptides with fluorescence fluctuation-based techniques.[158,159] An important example of this class of techniques is fluorescence correlation spectroscopy (FCS).[160] In FCS, the emission intensity of fluorescent molecules diffusing

in and out of a small confocal detection volume is recorded, and the temporal fluctuations of the intensity are analyzed to obtain information about the concentration and diffusion properties of the molecules. FCS may thus report on the oligomerization and aggregation of fluorescently labeled peptides, since multimeric peptide species have a smaller diffusion coefficient than monomeric peptides.[161] Similarly, FCS may reveal conformation changes of fluorescently labeled peptides in cases where these changes are associated with an altered diffusivity of the peptides.[162]

Fluorescent labeling may also provide the opportunity of studying peptides using Förster/fluorescence resonance energy transfer (FRET).[163] This non-radiant energy transfer process may take place between two fluorophores when the emission spectrum of the one fluorophore (the donor) overlaps with the excitation spectrum of the other fluorophore (the acceptor). The efficiency of the process depends on the spatial proximity and relative orientation of the donor and acceptor, and therefore, FRET may provide information about the relative nanometer scale distance of the two fluorophores. In samples with mixtures of peptides labeled with either a donor or an acceptor, it is possible to use this information to study peptide oligomerization and determine the stoichiometry of peptide complexes.[164,165] Additionally, if a given peptide is labeled with both a donor and an acceptor, it is possible to use the information to investigate the conformational state and dynamics of the peptide.[166]

Any research using fluorescently labeled peptides assumes that the fluorescence signal corresponds in space and time to the peptide of interest. Obviously, this is true only if the peptide–fluorophore construct is not degraded. Ensuring the absence of degradation is especially important in the design and study of peptide transport across the intestinal barrier, as the intestine is a particularly harsh environment.[7,8,167] The biochemical barrier is constituted by a range of peptide degrading enzymes including pancreatic proteases in the intestinal fluids, brush-border membrane peptidases at the cellular interface, and intracellular enzymes within the enterocytes.[168–170] Peptide degradation will in most cases not affect the fluorescent label. Consequently, the peptide's stability has to be assessed independently of the attached fluorophore. To this end, three alternative avenues are pursued: either (i) the peptide is incubated *in vitro*, simulating the intestinal environment; or (ii) the peptide is administrated *in vivo* and subsequently studied *ex vivo*, *e.g.*, by extracting blood samples; or (iii) the peptides are studied directly in the native intestinal environment. In option (i), researchers attempt to recreate the intestinal environment *in vitro* by incubating peptides in chemically simulated intestinal fluids (SIFs) that contain the naturally occurring pancreatic enzyme mixtures, bile acids, and phospholipids as well as having the relevant pH.[171,172] Another possibility is to incubate peptides in human aspirates from the upper gastro-intestinal tract, which mimics the *in vivo* environment closer but requires advanced sampling from human subjects.[173–175] Option (ii) exposes the peptide to the native intestinal environment prior to *ex vivo* analysis,[176,177] traditionally using the same analytical chemistry techniques as employed for studying peptides in option (i). These techniques most often include high-performance liquid chromatography- and/or mass-spectrometry-based analysis methods, which offer insight on peptide stability, potential chemical modifications as well as degradation kinetics.[178–180]

Options (i) and (ii) can indicate if the peptide of interest is still intact when exposing it to the environment of the intestine. However, they neglect the possibility of observing location dependent degradation or modification patterns (*e.g.* during transcytosis). For option (iii), techniques like matrix-assisted laser desorption/ionization mass-spectrometric imaging (MALDI-MSI), allows for visualization of the stability and distribution of peptides directly in the tissue, *e.g.*, across the small intestine.[181] This technique has been employed to elucidate how di-peptides were partially degraded by brush-border enzymes, providing an explanation for low *in vivo* absorptions (Fig. 5C).[182–184] The combination of MALDI-MSI and fluorescence imaging provides a powerful combination to verify the integrity of the peptide of interest but also opens up possibilities to learn about spatial degradation and modification mechanisms during peptide transport across the intestinal barrier.

Of relevance, the fluorescence-based techniques mentioned in Section 4 generally have in common that they allow for evaluation of the peptides not only in simple aqueous solutions but also in complex biological environments. Accordingly, they may be applicable for studying the behavior of peptides in the various experimental setups described in the following sections.

6. Membrane model systems

The cellular interaction of peptides starts at the level of the plasma membrane. The first step of deciphering the intestinal transport mechanisms of peptides is thus to understand their membrane interactions. Imaging-compatible membrane model systems represent a useful tool for shedding light on these interactions.

6.1 Image-based peptide–membrane interaction and translocation studies using artificial membrane models

The simplest approach to studying peptide–membrane interactions is to use artificial membrane models. To obtain free-standing artificial membranes compatible with imaging, giant unilamellar vesicles (GUVs) are often used (Fig. 4, GUV).[185–189] These vesicles are usually either formed by electroformation or by spontaneous swelling to be >5 μm in diameter, approximately the size of mammalian cells.[190] To ensure their biological relevance, the vesicles are typically prepared to consist of unsaturated phosphatidylcholines,[187–189] which is the most abundant type of phospholipid in mammalian plasma membranes.[191] Sometimes, they are also prepared with other lipid constituents to confer additional specific properties on the vesicles, for example, cholesterol to increase membrane rigidity[187] or phosphatidylglycerol to decrease membrane surface charge.[186,188,192]

GUVs are commonly used to study membrane binding and translocation of fluorescently labeled peptides. The translocation studies are frequently done with GUVs with enclosed inner vesicles, exploiting that peptides can only bind to an inner vesicle

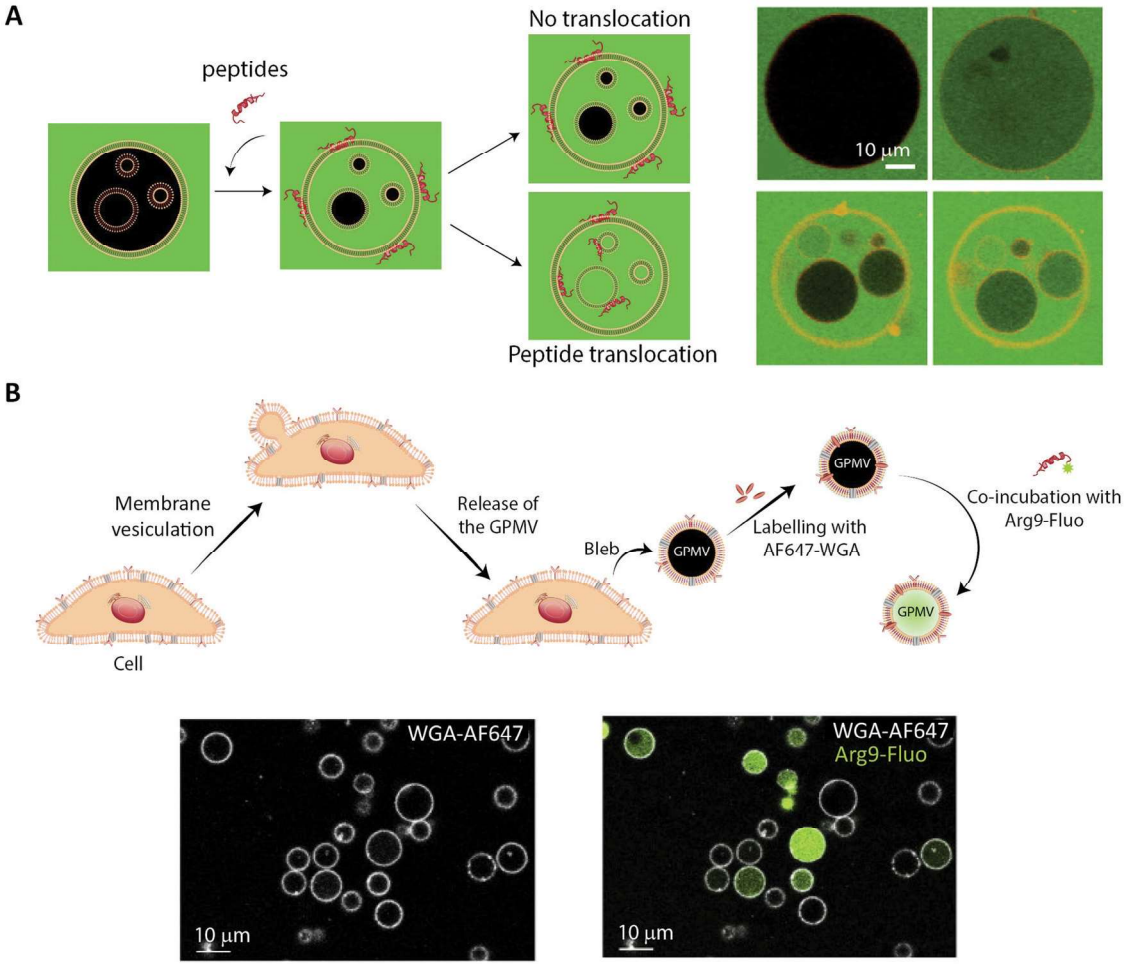

Fig. 6 Using membrane model systems to study peptide translocation. (A) Left, schematic illustration showing the concept of the peptide:membrane interaction and translocation experiment using the simplest membrane model system, GUVs. Influx of CF (green) in the inner GUVs constitutes a sensitive method for proving the ability of peptides to translocate across membranes. Right, studying the membrane translocation of fluorescent Transportan 10 analogs (Rhodamine-TP10W, red) using a microscopy-based multivesicular vesicle assay, employing CF influx into GUVs as a function of time (8.5, 14, 33, and 75 min). Reproduced from ref. 189 with permission from American Chemical Society, copyright 2013. (B) Top, schematic illustration of cell blebbing, GPMV formation and peptide transport experiment. Bottom, membrane translocation of the fluorescently labeled nona-arginine (Arg9, green) after 1 h, studied using GPMVs labeled with wheat germ agglutinin conjugated to Alexa Fluor 647 (WGA-AF64, white). Reproduced from ref. 204 with permission from Elsevier, copyright 2016.

if they have translocated across the outer membrane of the GUV (Fig. 6A).[186,188,189] By this principle, it is possible to determine the kinetics of peptide translocation across the outer membranes if the association to and dissociation from the membranes are not rate limiting.[189] Furthermore, by comparing the time course of the translocation process to the transport of non-permeable fluorophores across the outer membranes, it is possible to investigate whether or not the translocation process is coupled with membrane permeabilization.[185,187,189]

6.2 Using cell-derived giant plasma membrane vesicles for studying peptide membrane binding and translocation

While GUVs have been a steady work horse in the field of peptide translocation studies, they represent a completely artificial membrane system. Thus, their lipid composition are much simpler than that of a cell membrane, and they do not contain any of the membrane proteins making up roughly half the plasma membrane area in cells.[193] Thus, for more realistic quantitative biophysical peptide–membrane interaction studies, researchers have turned towards more native-like environments than classical synthetic liposomes.[194–196] Specifically, in recent years giant plasma membrane vesicles (GPMVs) have become increasingly popular (Fig. 4, GPMV). GPMVs are micron-sized single-bilayer structures, created by treating cells with chemicals that induce a controlled blebbing of the plasma membrane (Fig. 6B).[196] Initially GPMV production protocols relied on mixtures of the protein and lipid cross-linking agent formaldehyde and the reducing agent dithiothreitol (DTT) to weaken the interaction between the cytoskeleton and the plasma membrane followed by volume expansion driven by intracellular pressure.[197] Although much lower concentrations of formaldehyde is used than for regular cell fixation, this method was still believed to produce less than ideal mimics of the plasma membrane environment.[198] Less harmful protocols have been developed, including the use of

N-ethylmaleimide, which do not directly cross-link protein or reduce disulfide bridges.[196] Still, one needs to be aware that GPMV preparation processes have been reported to impose a lack of actin cytoskeleton, phosphorylated lipids, and strict lipid asymmetry between bilayer leaflets. The key advantage is that GPMVs maintain the diverse lipid and protein composition of the original cellular membrane.[199] This means that the GPMVs harbor a lipid complexity, which cannot be produced in purely artificial systems, and which can be modified by the choice of initial cell line.[197] Additionally, cell lines can be genetically modified to express fluorescently labelled plasma membrane proteins, giving the opportunity to use imaging modalities to track peptide:protein interactions in the produced GPMVs. Known regulators of peptide:cell interactions are the glycoproteins and glycolipids making up the pericellular matrix, known as the glycocalyx. Since GPMVs have been shown to retain the glycocalyx after isolation,[200] they offer the possibility to study how it affects peptide:membrane interactions in a controlled environment. Although GPMVs cannot be used to study the endocytic pathways of peptide uptake, they do represent a well-suited system for elucidating peptide–membrane interaction and direct translocation mechanisms. Thus GPMVs are believed to be a promising tool for peptide transport studies and have been used to study the translocation mechanism of therapeutic peptides,[201,202] cell-penetrating peptides[194,203,204] and bacterial toxins.[205]

7. Imaging-based studies on cellular uptake and transport of peptides using single-cell and cell-layer systems

While unique insight into peptide-membrane interaction and translocation can be gained using GUV and GPMVs, they are simplified model systems which lack key biological features that are central to cellular uptake and transport, such as an energy dependent uptake machinery. Therefore, single-cell systems in combination with fluorescence microscopy have been a cornerstone for studying cellular transport of peptides.[17,59,206–208] We note that such studies are compatible with many established and emerging imaging modalities (see Section 4.1) (Fig. 4, Single cell).

For some applications, conclusions may be made based on integrated intracellular levels of a fluorescently marked peptide and/or a rough cellular localization (with time-resolution) of peptides. In particular, such a simple data-analytic approach may be sufficient to provide evidence in favor of a particular peptide translocation mechanism[70–72,209] when combined with proper control experiments, biophysical assays and/or model calculations. For example, either immediate cytosolic delivery, resulting from direct translocation across the membrane, or endocytic uptake of GFP was readily observed to depend on the cell-penetrating peptide conjugated to the green fluorescent protein (GFP).[210] In this paradigm, one may maximize the temporal resolution of the imaging modality, since the signal from the fluorescent probes is typically not a limitation (see Section 4.1).

At the cellular level, mechanistic insight on uptake and translocation may be gained by the use of additional, organelle-specific markers that are spectrally separated from that of the peptide.[211,212] The extent of co-localization is typically assessed using simple image correlations.[60] Subcellular localization of peptides may also be revealed using other means, for example pH-sensitive probes.[211] Such environmental dependencies of fluorophores may however be a caveat in co-localization analysis. In particular, fluorescence quenching may conceal co-localization of peptides with the membrane of cells and/or organelles, which, however, may be leveraged by diluting labeled peptide with its unlabeled analogue.[213,214] In the presence of fluorescence quenching, care should be taken before integrated fluorescence intensities are used to quantify the density of peptides.

If peptide uptake in the cell does occur, fluorescence recovery after photobleaching (FRAP) can determine the mobile (free) and immobile (bound) fractions of molecules.[42,215,216] In this approach, intense, focused light bleaches a well-defined spatial region of a sample followed by observation of the recovery of fluorescence with time as surrounding fluorophores diffuse into the bleached region. Diffusion coefficients of various diffusers are subsequently estimated by employing a theoretical model for diffusion of a (heterogeneous) population of molecules.[216]

Assays based on single cell models can provide important knowledge on the cellular uptake and transport of peptides.[217] Simple intestinal barrier-like setups consisting of a confluent cell layer on a glass surface have added additional insights on barrier physiology[218,219] and peptide/protein transport.[220] However, neither single cells nor confluent cell layers on a glass surface recapitulate the complex three-dimensional characteristics and organization of fully differentiated cells making up an intestinal barrier. They fall short of accurately describing the chain of transport processes that the peptide experiences from one side of the intestinal barrier to the other in a polarized cell monolayer. This shortcoming makes physiologically relevant *in vitro* or *ex vivo* models of great interest, not only as endpoint screening platforms for investigating peptide permeability, but also for dynamic in-depth mechanistic studies of peptide transport across the intestinal barrier. To facilitate such studies, sophisticated physiologically relevant models that are compatible with live cell imaging are emerging. The following sections review them in detail.

8. *In vitro* and *ex vivo* models for studying peptide translocation across intestinal barriers

8.1 Peptide transport and translocation studied using *in vitro* intestinal barrier models

In vitro intestinal epithelial barrier models have traditionally been based on static 2D Transwell systems[221] utilizing the human-derived adenocarcinoma cell line Caco-2 that spontaneously differentiates into small intestine-like enterocytes after 17–21 days (Fig. 4, monolayer). To generate a model that more closely resembles the *in vivo* scenario, goblet-like cells HT29 MTX[222] and Raji B lymphocytes[223] have been employed to induce mucus expression and to implement immunological features, respectively. Efforts have

also been made to mimic the physiological villi-crypt structure of the small intestine by creating scaffolds made of porous poly(lactic-*co*-glycolic acid) (PLGA),[224] micromolded collagen[225,226] or silk fibroin proteins.[227] As an example, culturing human small intestinal cells on a collagen-derived scaffold and creating a chemical- and growth factor gradient across the cell layer (Fig. 7A, top) allowed the formation of a differentiated and polarized cellular compartment mimicking aspects of the *in vivo* scenario (Fig. 7A, bottom).

The Transwell technology uses a microporous diffusion-open polymer membrane as cell culture support to enable exposure to difference chemical environments on opposing sides of a cell layer. It has been a vital platform for investigating intestinal absorption of peptides[228] and has played a pivotal role in investigating passive paracellular/transcellular transport of peptides and the impact on their absorption profile upon various structural modifications.[229] A major limitation of Transwell-based models is that they are not designed for microscopy and thus offer no direct visual insight on transport mechanisms (Fig. 1, left). The main obstacle is the distance between the cell monolayer and the basolateral chamber, which is not compatible with the working distance of high magnification, high numerical aperture objectives (see Section 4.1).[53] Many studies circumvent this problem by chemically fixing the cell samples, excising the semi-permeable Transwell membrane, and placing it on a coverslip for imaging.[230] This approach provides static snap-shots of drug transport, but it falls short of capturing the dynamics of cellular transport of peptides and drugs inside cells and across the barrier.[230] In order to rectify these shortcomings, cells have been grown on the underside of the semi-permeable membrane, but the distance from the sample to the objective still remains a problem for high-magnification imaging.[53] Other studies have made use of a small-volume, closed-bath imaging chamber that allows live imaging with higher-magnification objectives.[231] However, this also requires a specialized microscope platform and stage adaptor, and the semi-permeable membrane must be cut out and placed in the chamber for imaging.[231]

8.2 Commercially available platforms for high-resolution live-cell imaging of peptide transport across intestinal barriers

More image-compatible cellular barrier systems than Transwells have been developed to facilitate high-end live cell imaging. The μ-Slide Membrane ibiPore Flow system (Ibidi, Germany) consists of two channels separated by a 0.3 μm-thick porous glass membrane and fluidic channels for inducing shear stress. The major advantage of this system is the highly transparent thin glass bottom (180 μm) and internal porous glass membrane, which gives access to real-time monitoring of drugs over time. However, the system is not designed for intestinal models and only allows liquid perfusion through the lower chamber. No intestinal transport studies have yet been reported with this system. Additional drawbacks of this single-chip system are the low throughput and the need for pumps, tubing systems, and related specialized equipment. In a recent development, an *in vitro* intestinal barrier model was established in the OrganoPlate (Mimetas, the Netherlands), a pump-free, microfluidic extracellular-matrix-based platform (Fig. 4, Organoplate) (Fig. 7B).[232] In forty parallel chips, Caco-2 cells differentiate into polarized, intact monolayers and form intestinal tubules. Due to continuous perfusion cell differentiation takes place in only 4 days.[232] In addition to the fast differentiation time and the lack of a physical membrane, the OrganoPlate is designed with three adjacent channels instead of the stacked topology of traditional models like the Transwell. This and its glass bottom strongly facilitate high-end live-cell imaging.[232]

8.3 *Ex vivo* barrier models offer increased biological complexity

Attempts to better preserve and recapitulate the biological complexity of the intestinal barrier have been made by the use of *ex vivo* intestinal models (Fig. 4, Microtissue). The Ussing chamber equipped with intestinal human or animal tissue[233] is one model that has been utilized vastly for determining drug permeability. However, the model suffers from short viability of the tissue segments, low-throughput, and incompatibility with live imaging.[233,234] A high-throughput alternative to the Ussing chamber is the InTESTine system (TNO, the Netherlands) that allows monitoring of 96 excised porcine tissue barriers simultaneously but also suffers from short tissue viability and imaging incompatibility issues.[234] The EpiIntestinal model (MatTek, MA) is a high-throughput, human primary cell-based, 3D microtissue model that can be kept in culture for up to a month (Fig. 7C).[235] The model demonstrates a higher correlation to human *in vivo* drug absorption profiles than classical Caco-2 Transwell systems[235] and has also been used in a multi-organ-chip system to recapitulate absorption.[236] As the EpiIntestinal model expresses many of the enzymes and transporters of the small intestine, peptide transport studies in this model could offer biologically relevant mechanistic insight. One promising approach for live-cell imaging of the model is 2PM, which can be employed for in-depth imaging of tissue samples, as explained in Section 4.1 (Fig. 3). The limitation of this approach is the compromise made on speed of imaging, resulting in limited information gained on dynamic intracellular processes. In addition to the more high-throughput solutions described above, the use of excised and fixed tissue sections for studying barrier transport is gaining more widespread use. Examples of this include the two recently FDA approved peptide formulations oral semaglutide (Section 2.3) and octreotide (Section 2.4).[29,33] Tissue fixation allows for the use of immunostaining, and tissue clearing greatly increasing the ability to image deep into tissue with high spatial resolution.[237] The main drawback of fixing excised tissue sections is the inability to perform live imaging and the potential artifacts introduced during fixation. The whole field of *ex vivo* barrier models is greatly benefitting from the emerging approaches enabling in-depth live imaging in tissues such as LLSM (see also Section 4.1) (Fig. 3). In combination with clearing techniques and adaptive optics, it has the possibility to revolutionize imaging deep into tissue samples with previously unseen levels of spatial and temporal resolution.[238]

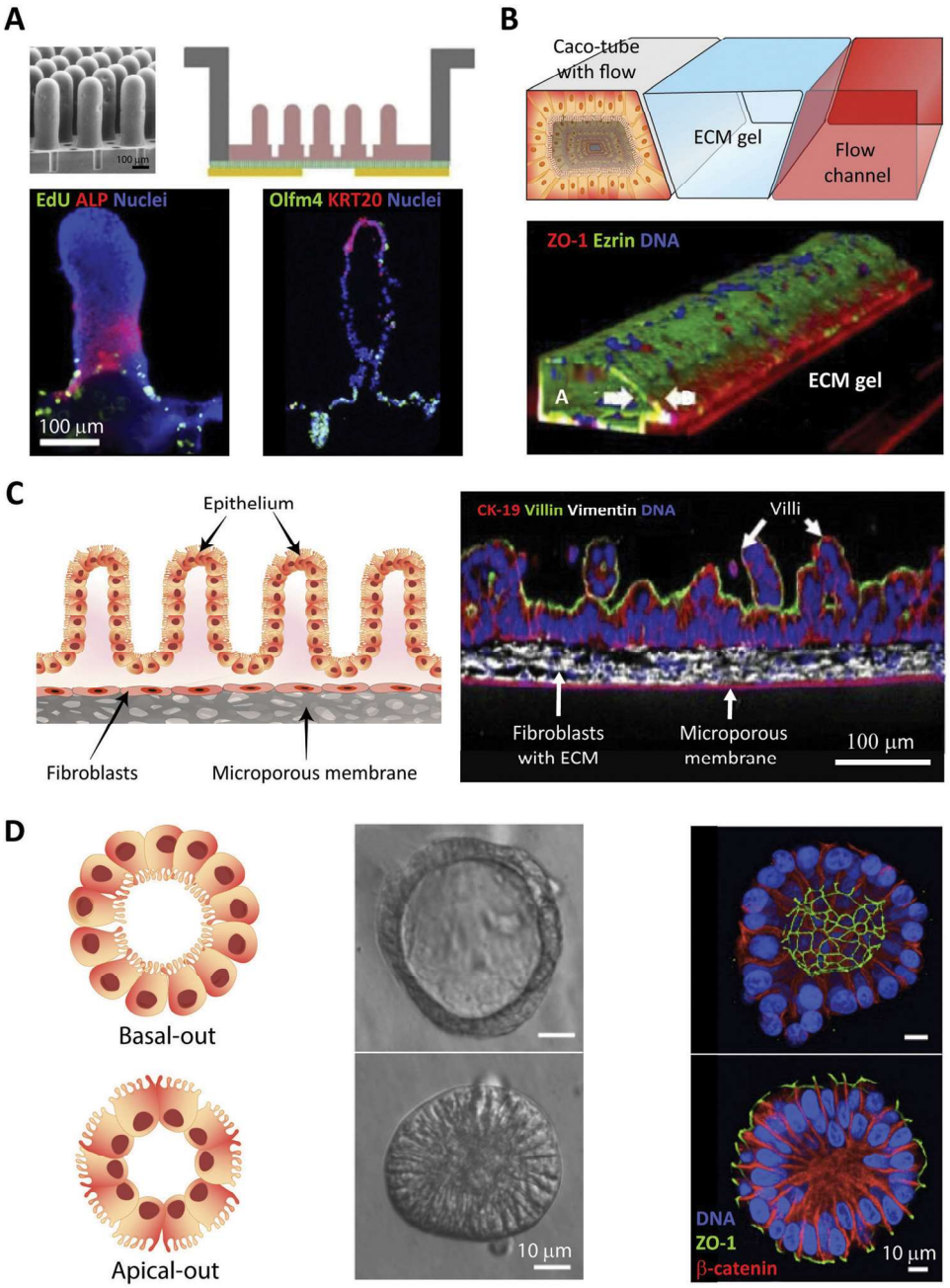

Fig. 7 Summary of *in vitro* and *ex vivo* intestinal barrier models for studying peptide transport. (A) Example of micro-engineered scaffolds to generate crypt-villus architecture of human small intestinal epithelium. Top left, an electron microscopy image of the PDMS stamp used to create, top right, a micromolded collagen scaffold in a modified Transwell insert; bottom, visualization of cellular differentiation and polarization using immunostaining. Left, absorptive enterocytes localized on the villi (ALP, red) and proliferative cells localized in the crypt (EdU, green). Right, terminally differentiated tissues of the intestine expressing human cytokeratin 20 localized on villi tips (KRT20, red) and stem cells localized to crypts and adjacent regions (Olfm4, green). Reproduced from ref. 226 with permission from Elsevier, copyright 2017. (B) Top, OrganoPlate by MIMETAS: schematic of the three lane system at the center of each channel network, consisting of a Caco-2 cell tubular lane, an extracellular matrix (ECM) gel lane, and a perfusion lane. Bottom, 3D reconstruction of a confocal z-stack showing the Caco-2 cell tubular morphology visualized by staining the tight junction protein ZO-1 (red), the brush border-protein Ezrin (green), and DNA (blue). White arrows indicate the apical (A) and basal sides (B). Reproduced from ref. 232 with permission from Springer Nature, copyright 2017. (C) EpiIntestinal™ model, an *ex vivo* model for studying drug absorption in the small intestine based on primary human cell-based organotypic small intestinal micro-tissues. Left, an illustration showing different types of cells and the microporous membrane underneath. Right, immmunostained cross-sections of the reconstructed microtissues showing cytokeratin-19 stained columnar epithelial cells (CK-19, red), villin stained apical surface of epithelium (green) and vimentin stained fibroblasts in the underlying ECM substrate (white). Reproduced from ref. 235 with permission from Springer Nature, copyright 2018. (D) Left, two types of organoid morphology, basal-out and apical-out, can be produced, with the latter potentially facilitating studies of peptide transport across the intestinal barrier from the apical to the basal side. Middle, organoids imaged using modulation contrast microscopy. Right, confocal microscopy images with nuclei in blue, ZO-1 (green) and β-catenin (red) illustrate how the orientation of the organoid organization is flipped when going from the basal-out to the apical-out system. Reproduced from ref. 252 with permission from Cell Press, copyright 2019.

Organoids are used as another tissue-mimicking model of the intestine, which is receiving increased interest in the field of drug delivery.[239] Organoids are multicellular organotypic 3D-clusters generated from either primary tissue, embryonic tissue, or induced pluripotent stem cells, closely resembling the structural build seen *in vivo* (Fig. 7D).[240–242] Organoids exhibit tissue-specific markers, with a self-renewal ability making them a complex and sophisticated model that is able to mimic a variety of organs (brain, liver, lung, gut, kidney, pancreas, and salivary gland). To date, however, intestinal organoids have primarily been used as disease models, for studying morphogenesis, or to investigate inflammatory host–pathogen interactions.[243–245] Thus, the use of organoids in the context of analyzing peptide trafficking across a cellular barrier have been limited, predominantly due to the traditional basolateral-side out orientation of intestinal organoids resulting in inaccessibility of the apical side.[240] To overcome this limitation, attempts have been made to use, *e.g.*, microinjections[246,247] or to dissociate intestinal organoids into single cells and culture them as 2D-monolayers in classical Transwells[248,249] or in more advanced organ-on a-chip systems.[250,251] Another approach to gain access to the apical side, while aiming at maintaining the 3D identity of intestinal organoids, rely on inverting organoid polarity by modifying the culturing conditions, resulting in so called apical-out organoids.[252] While these attempts show great potential, organoids must be fully verified as physiological relevant transport models, before they can emerge as a state-of-the art model system for studying peptide transport.

9. Imaging-compatible organ-on-a-chip microfluidic models

The most technically advanced cell-barrier models are the emerging organ-on-a-chip systems (Fig. 4, Organ-on-a-chip).[253,254] In these, researchers combine tissue engineering and lab-on-a-chip technology to create a platform that allows accurate and biologically relevant studies of both cellular barrier physiology and peptide transport. In recent years, micro-engineered devices have been used to establish tissue models that mimic physiological function and structural complexity of human organs such as lung,[255] intestine,[256,257] liver[258,259] and heart[260,261] *in vitro* (Fig. 8A). The intestine focused organ-on-a-chip systems represent minimal functioning units of the biological barrier providing a more native-like microenvironment within a micrometer-sized chamber as compared to their conventional counterparts, like Transwell- and 3D models (see Section 8.1). A major drawback of Transwell models is the absence of flow, which is an intrinsic feature of the native biological environment. With conventional 3D models, on the other hand, it is problematic to quantify transcellular transport, since sampling from the luminal content is challenging.[262,263] Additionally, these systems lack tissue–tissue interfaces, such as vascular endothelium and parenchymal cells.[254] The intestine-focused organ-on-a-chip systems combines living cells and continuous flow, creating a 3D model that exhibits key hallmarks of native tissues. Consequently, they offer the potential for more biologically accurate readouts of, *e.g.*, peptide transport across cellular barriers.

One strategy to recreate the multicellular interface of organs is to incorporate polymer membranes into the microfluidic channel of these devices.[264–269] Most commonly, poly(dimethylsiloxane) (PDMS) is used as fabrication material for such systems. PDMS is transparent and thus enables high-resolution microscopy of the developed intestinal barrier model.[256,257] This strategy has been widely employed to develop gut-on-a-chip systems and is popular among the researchers in the field. Another interesting approach uses microfluidic hydrogels with built-in microchannels, which are intrinsically highly permeable to biomolecules and therefore alleviate the need for micropores.[270–272] Moreover, microfabrication techniques, specifically 3D-printing, offer the possibility of creating complex microchannel networks and microarchitectures through a one-step procedure.[271,273–275] Recently the above-mentioned technologies were combined to develop a hybrid mini intestine, composed of an elastomeric PDMS-based frame and a hydrogel compartment for cell culture.[244] Exploiting the self-organization property of the intestinal stem cells, a tubular epithelium with similar spatial arrangement of crypt- and villus-like domains was generated as well as an accessible lumen. Horizontal orientation of the device—like most of the gut-on-a-chip systems in general – further facilitates monitoring of intercellular translocation by means of high-resolution imaging.[244,276–278] In contrast to other off-the-shelf solutions, such as living organs or macroscale 3D models, the chip-based models offer unique possibilities for high-resolution, real-time imaging of biological phenomena at the molecular scale within a 3D tissue model.[279,280] More specifically, integration of the mini-intestine chip with state-of-the-art microscopes and cameras enabled bright-field and fluorescence live imaging of the intestinal tissue development, regeneration, and parasite infection (Fig. 8B). Another interesting example of high-resolution imaging of organ-on-a-chip models is the implementation of stochastic optical reconstruction microscopy (STORM, see Section 4.3) on a simple and versatile microfluidic platform to visualize mitochondrial protein distribution in live cells.[281]

Besides cell orientation, the microfluidic platforms present several other advantages over their classical counterparts: They facilitate the required long-term high-resolution image acquisition by providing stable conditions for the cells, and, at the same time, they enable monitoring of cell growth and division.[244,282] This advantage has been utilized in the development of an integrated microfluidic device capable of real-time imaging of living cells with high signal-to-noise ratio under continuous perfusion.[283] Using TIRFM (see Section 4.1), the setup allows non-invasive *in situ* of the location of insulin granules in mouse pancreatic β-cells (Fig. 8C).[284] This is to date the most relevant study where advanced microscopy and organ-on-a-chip have joined forces to provide valuable insights into a biological translocation. However, it must be noted that organ-on-a-chip technology is in its infancy and many tissue characteristics still need to be engineered and integrated in a robust format to reach broad application. As mentioned, these microfluidic devices[256,257,285–289] have been

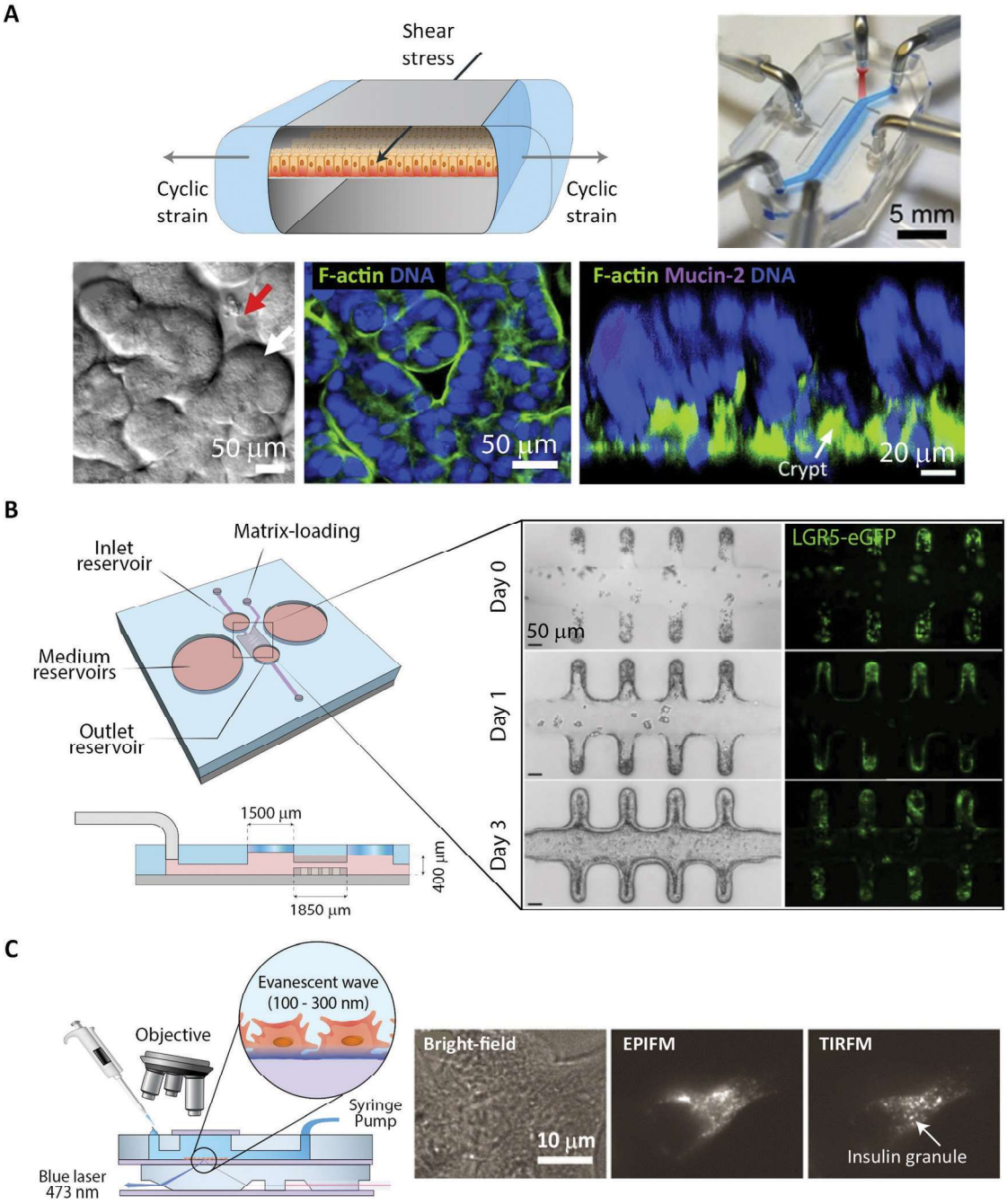

Fig. 8 Imaging cells in lab-on-a-chip platforms. (A) Schematic cross-section of a microfluidic organ-on-a-chip. Top, left, device showing cyclic mechanical strain using the two vacuum chambers, which creates a shear stress in the perpendicular direction. Top, right, photograph of the device with blue and red dyes representing upper and lower microchannels, respectively. Bottom left, a differential interference contrast micrograph showing intestinal crypt (red arrow) and villi (white arrow) formation for Caco-2 cells grown in the chip. Bottom center, confocal immunofluorescence image of horizontal cross-section of intestinal villi stained for F-actin (green) labelling the apical brush border of polarized intestinal epithelial cells and DNA (blue), reproduced from ref. 268 with permission from National Academy of Sciences, copyright 2016. Bottom right, confocal fluorescence image showing vertical cross section of an intestinal villi inside the chip, stained for F-actin (green), Mucin-2 (magenta), and DNA (blue). Reproduced from ref. 256 with permission from The Royal Society of Chemistry, copyright 2012. (B) Schematic of microfluidic platform of the mini-intestine, consisting of a hydrogel chamber in the center, fed by the two medium reservoirs, perspective and side view (left). Bright-field and fluorescence time-course experiments showing the real-time formation of epithelium in mini-intestine chip (right). Reproduced from ref. 244 with permission from Springer Naturee, copyright 2020. (C) Left, schematic of the integrated device for observation of insulin granules inside the adherent cells cultured under continuous medium perfusion. Right, microscopic images of the MIN6-m9/insulin-GFP cells captured on the integrated system with different illumination modes, bright-field, epifluorescence microscopy (EPIFM), and TIRFM. Reproduced from ref. 284 with permission from Springer Nature, copyright 2012.

successfully coupled with imaging setups for real-time imaging, which makes them candidates for providing detailed mechanistic understanding of complex biological phenomena, such as peptide transport across the intestinal barrier.

The organ-on-a-chip technology is rapidly growing. However, from a technological standpoint, several overarching considerations and operative challenges must be tackled to fully realize the potential of these micro-engineered devices and successfully translate them from proof-of-concept to practical screening platforms. One of the very basic issues arises from the material, PDMS, which is the most commonly used for fabrication. Albeit allowing high-resolution imaging, PDMS absorbs small hydrophobic compounds, including drug molecules,[290,291] which may hinder accurate evaluation of the parameters of interest. Furthermore, lack of a standardized automated fabrication process poses additional technical hurdles in terms of high-throughput operation and reproducibility. Another underdeveloped aspect of on-chip assays is the fact that high-end fluorescence imaging still relies mainly on fixed and immunostained samples. This is an end-point analysis, while current live-imaging techniques used in organ-on-a-chip platforms are mostly still limited to WFM modes, such as bright-field and epifluorescence imaging (see Section 4.1). Looking forward, one can envision highly automated systems integrating microfluidic devices, sophisticated built-in sensors,[292–294] and advanced multiplex imaging techniques.

10. *In vivo* imaging of transport across the intestinal barrier

Despite the immense amount of insight gained on the fundamental function of cellular barriers using *in vitro* and *ex vivo* models of various complexity, such systems are inherently limited and do not fully recapitulate the natural *in vivo* milieu. Consequently, within the last few decades, various *in vivo* imaging platforms have been developed.[295,296] They allow for continuous fluorescence imaging of a plethora of different living tissues, including the intestinal cellular barrier. Such intravital microscopy (IVM) setups allows for long-time measurements, ranging from hours to days, under minimally invasive conditions (Fig. 4, Intravital and Fig. 9). This circumvents the accelerated tissue degradation observed in, *e.g.*, explanted tissue models.[237,297] In contrast to whole-body *in vivo* imaging modalities like MRI and PET-CT, which typically have a spatial resolution in the millimeter range,[298,299] IVM allows for imaging with single-cell resolution, making it ideally suited for elucidating the molecular mechanisms governing peptide transport across cellular barriers.[299] The single-cell resolution of IVM also allows for quantitative measures of cellular barrier heterogeneities with respect to both physiology and transport processes.[295,299,300] The main limitations for employing IVM is the requirement for sophisticated equipment, both with respect to advanced microscopes and animal-handling setups, as well as specially trained and skilled personnel.[296,297] These technical requirements and the tedious data acquisition mean that IVM inherently is not a high through-put technique. Instead it offers an unmatched level of detail and biological accuracy.[295]

To facilitate IVM of the intestinal barrier, one method relies on an intestinal section being externalized from an anesthetized mouse and placed inside a glass-based imaging chamber (Fig. 9A).[297] The subcellular resolution provided by such setups has been used to determine *in vivo*, the molecular mechanism by which tumor necrosis factor α disrupts the intestinal barrier integrity through modification of TJ structure and function.[301] For transport studies, both peptides and proteins have been imaged crossing the intestinal barrier. This has offered unique insights on how specific epithelial- and immune cells coordinate the transport process *in vivo* (Fig. 9A and C).[302,303] In a drug-delivery context, the setup has been used to elucidate a clear dependency on NP size in both the amount and the route of transport across the intestinal barrier. Smaller particles displayed increased transport.[303] Finally, IVM was used to visualize how

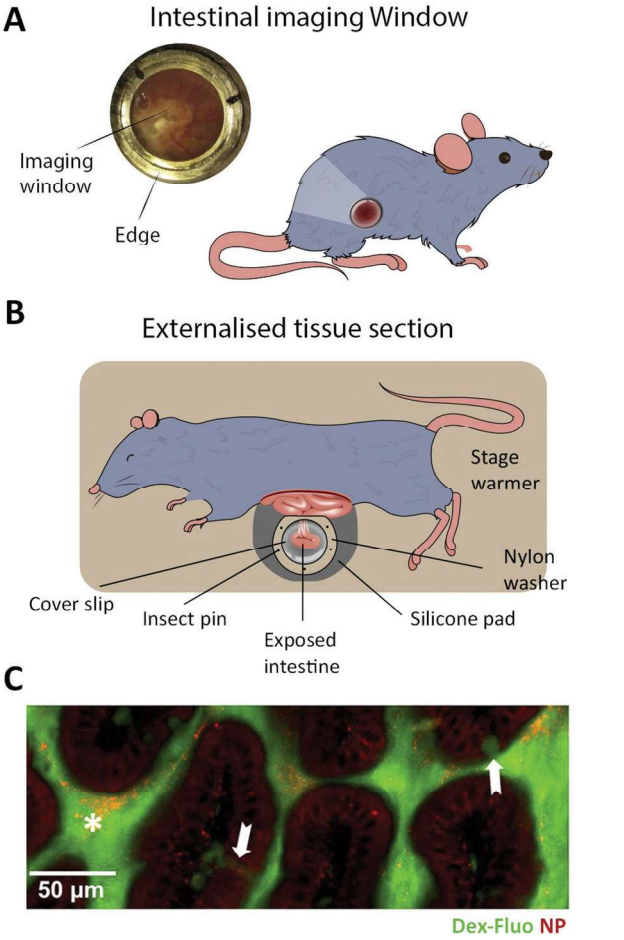

Fig. 9 *In vivo* imaging of the intestinal barrier. (A) An illustration showing a mouse with a surgically implanted imaging window allowing visualization of the small intestine. (B) A schematic showing an IVM setup where an intestinal section is externalized from an anesthetized mouse and placed inside a glass based imaging chamber. (C) An example of a IVM setup being used to demonstrate differential uptake of orally administered particles and antigens. Dextran-fluorescein (Dex-Fluo) (green) enters through Goblet cell-associated passageways (white arrows), while 20 nm polystyrene nanoparticles (NP) (red) enter *via* intestinal epithelial cells. Reproduced from ref. 303 with permission from Public Library of Science, copyright 2014.

NP-delivered insulin interacted with the microvilli of the intestine.[304] The molecular mechanism of the insulin absorption was revealed to depend on a direct interaction with the apical sodium-dependent bile acid transporter.

IVM may also be performed in conjunction with a surgical implantation of an imaging window through which the microscopy can be performed[295,305] (Fig. 9B). This methodology does not rely on tissue externalization and thus allows IVM to be performed on a larger range of cellular barriers. The main benefit of performing imaging window-based IVM is the ability to image tissue under near-native conditions and in its orthotopic position without this imaging being compromised by the detrimental optical distortions typically experienced when imaging non-superficial tissues.[306] Additionally, the technical advances in surgical procedures and window implementation now make it possible to image cellular barriers for extremely long periods (up to months), while maintaining subcellular resolution.[295,307] However, it is important to keep in mind that this technique requires highly specialized staff and sophisticated equipment. Also, it remains prone to trauma and contaminants introduced during the surgery and to damaging fluid accumulation over time. All of this limits the use of the technique to a restricted number of highly specialized groups.[307] Recently, surgically implanted imaging windows in the mouse abdomen have allowed researchers to perform IVM of living intestinal tissue.[306] This has facilitated novel insights on how the complex cellular architecture of the micro villi formations lining the intestinal barrier is produced and maintained.[300] These methods are still in their infancy and have, to our knowledge, not been employed for studying peptide transport across the cellular barrier. We envision, however, that such studies should be feasible with current setups. Overall, the unique ability of IVM to study biological processes and drug transport in conditions resembling the native environment will make IVM an increasingly important tool for reducing the translational gap between early drug development and clinical efficiency.[308,309]

11. Peptide-based nanoparticle delivery systems

The main focus of this review is on the transport across cellular barriers of peptides as individual entities. However, another appealing mode of delivering peptide and proteins is to assemble them into NPs. Here we define such peptide/protein NPs to be structures where the core element is the peptide/protein itself and thus not delivery vehicles where peptides/proteins are, *e.g.*, encapsulated. For a thorough discussion on the latter type of delivery system see the recent review by Brayden *et al.*[21] Making peptide/protein NPs can be done either through self-assembly, chemical cross linking, de-solvation, or a combination of approaches.[310] The benefits of NPs include: protection of the peptides/proteins against enzymatic degradation,[310] improved physicochemical properties compared to free peptide/protein, increased cellular uptake, reduced clearance from tissue microenvironments, the ability to bypass biological barriers (*e.g.*, mucus[8] and glycocalyx[311]), as well as the potential to deliver a high payload of biologically active molecules. The transport across intestinal barriers of NPs is highly dependent on the physicochemical properties of the particle.[312,313] Larger NPs (100–200 nm) are commonly endocytosed by clathrin- or caveolin-mediated endocytosis, while smaller (<100 nm in diameter) particles can be taken in by macro- or micropinocytosis. Some protein NPs will be endocytosed by interacting with the receptor of the free protein on the cell surface. For instance, albumin particles such as Abraxane, a 130 nm diameter bovine serum albumin particle loaded with the chemotherapeutic paclitaxel, has been shown to interact with the endothelial gp60 receptor to induce caveolin mediated endocytosis (similar to free albumin).[314] Unzueta *et al.* showed that 13 nm self-assembled NPs from GFP coupled to the peptide T22 interact with the CXCR4 receptor and lead to uptake into endosomes.[315] Interestingly, they found that the T22 peptide bound more weakly to the receptor than other peptides tested but that the T22-GFP NP was the only construct that lead to cellular uptake.[315] More detailed imaging might lead to a deeper understanding of the reason for the discrepancy between receptor-binding affinity and cell uptake. Estrada *et al.* also used GFP to formulate NPs. These chemically crossed-linked particles carrying β-galactosidase showed protection of the active enzyme in the biological environment as well as increased cellular uptake of the enzyme when delivered by the 283 nm negatively charged protein particles and compared to free enzyme in solution.[316] GFP has also been used to show protein encapsulation into Qβ-virus-like protein particles that helped to protect the encapsulated protein against thermal denaturation and degradation by proteases and lead to efficient uptake in $CD22^+$ cells.[317]

However, cellular uptake is not enough to cross epithelial barriers such as the ones found in the intestine, and knowledge about particle exocytosis and transcytosis is crucial.[318] Bramini *et al.* showed, using fluorescently labeled polystyrene NPs, how a Transwell setup and a combination of CLSM and TIRFM (see Section 4.1) (Fig. 3) can be used to evaluate transport of NPs through a tight epithelial barrier.[319] It would be interesting to see methods like these applied to peptide/protein particle systems, such as the ones described above, to gain more mechanistic insights on the transport and biological fates of these biodegradable systems after endocytosis. Different imaging techniques can also be utilized to evaluate NP interaction with mucosal barriers, such as particle tracking (see Section 4.2).[320] Surface charge of NPs has shown to have great impact on NP diffusion in mucus, with negatively and neutrally charged particles being able to diffuse through mucus while positively charged particles get trapped.[320] This interaction can possibly be utilized to ensure prolonged residence time of a NP system in the intestine allowing slow release of single proteins or peptides.[321] There are numerous examples of such prolonged NP interactions with biological barriers facilitating better delivery of vitamins[313,322] and hydrophobic drugs[323–325] and a few for delivery of active protein and peptides.[316,326] These highly biocompatible systems show great potential for improved drug targeting, availability, and enhanced patient compliance.

13. Conclusion

Poor predictive power of current preclinical drug testing results in major failures in clinical trials and consequently in high costs of research and development in the pharmaceutical industry.[308,327] To remedy this, it has been proposed to enhance the focus on understanding the biological mechanisms that facilitate drug uptake and transport.[9,12] This focus requires new barrier models and technical methods. Fluorescence imaging is poised to be part of the solution, and currently there is a rapid development of advanced intestinal barrier models that are compatible with high-end imaging modalities. This progress in model development coincides with the increased access to (L)LSM setups, both offering the imaging speed, sensitivity and low phototoxicity needed to implement 4D microscopy as a stable in peptide translocation studies. Here, we have provided an overview of the various aspects and possibilities one should consider before engaging in studies of peptide transport across the intestinal barrier using fluorescence microscopy. Overall, the endeavors reviewed here pave the way for cutting-edge, dynamic, high-resolution mechanistic transport studies in highly sophisticated barrier models that recapitulate the physiological features of the small intestine with enhanced precision. This should result in improved end-point efficacy in oral delivery and thereby bridge the translational gap between bench and bedside for peptide biopharmaceuticals.

Author contributions

Wrote or contributed to the writing of the manuscript: J. B. Larsen, Taebnia, Dolatshahi-Pirouz, Eriksen, Hjørringgaard, Kristensen, N. W. Larsen, N. B. Larsen, Marie, Mündler, Parhamifar, Urquhart, Weller, Mortensen, Flyvbjerg, Andresen.

Conflicts of interest

None.

Acknowledgements

This work was supported by the Novo Nordisk Foundation (Grant No. NNF16OC0022166).

References

1 A. F. B. Rader, M. Weinmuller, F. Reichart, A. Schumacher-Klinger, S. Merzbach, C. Gilon, A. Hoffman and H. Kessler, *Angew. Chem., Int. Ed.*, 2018, **57**, 14414–14438.
2 J. L. Lau and M. K. Dunn, *Bioorg. Med. Chem.*, 2018, **26**, 2700–2707.
3 S. Mitragotri, P. A. Burke and R. Langer, *Nat. Rev. Drug Discovery*, 2014, **13**, 655–672.
4 M. W. Tibbitt, J. E. Dahlman and R. Langer, *J. Am. Chem. Soc.*, 2016, **138**, 704–717.
5 D. J. Drucker, *Nat. Rev. Drug Discovery*, 2020, **19**, 277–289.
6 R. Ismail and I. Csoka, *Eur. J. Pharm. Biopharm.*, 2017, **115**, 257–267.
7 J. Renukuntla, A. D. Vadlapudi, A. Patel, S. H. S. Boddu and A. K. Mitra, *Int. J. Pharm.*, 2013, **447**, 75–93.
8 P. Lundquist and P. Artursson, *Adv. Drug Delivery Rev.*, 2016, **106**, 256–276.
9 *Nat. Biotechnol.*, 2014, **32**, 961.
10 M. Morishita and N. A. Peppas, *Drug Discovery Today*, 2006, **11**, 905–910.
11 F. McCartney, J. P. Gleeson and D. J. Brayden, *Tissue Barriers*, 2016, **4**, e1176822.
12 *Nat. Med.*, 2010, **16**, 347.
13 G. Sahay, D. Y. Alakhova and A. V. Kabanov, *J. Controlled Release*, 2010, **145**, 182–195.
14 A. I. Ivanov, in *Exocytosis and Endocytosis*, ed. A. I. Ivanov, Humana Press, Totowa, NJ, 2008, DOI: 10.1007/978-1-59745-178-9_2, pp. 15–33.
15 D. Vercauteren, R. E. Vandenbroucke, A. T. Jones, J. Rejman, J. Demeester, S. C. De Smedt, N. N. Sanders and K. Braeckmans, *Mol. Ther.*, 2010, **18**, 561–569.
16 R. Duncan and S. C. W. Richardson, *Mol. Pharmaceutics*, 2012, **9**, 2380–2402.
17 M. Gumbleton and D. J. Stephens, *Adv. Drug Delivery Rev.*, 2005, **57**, 5–15.
18 P. Watson, A. T. Jones and D. J. Stephens, *Adv. Drug Delivery Rev.*, 2005, **57**, 43–61.
19 A. C. Anselmo, Y. Gokarn and S. Mitragotri, *Nat. Rev. Drug Discovery*, 2019, **18**, 19–40.
20 S. Maher, C. Geoghegan and D. J. Brayden, *Expert Opin. Drug Delivery*, 2020, 1–28.
21 D. J. Brayden, T. A. Hill, D. P. Fairlie, S. Maher and R. J. Mrsny, *Adv. Drug Delivery Rev.*, 2020, **157**, 2–36.
22 T. D. Brown, K. A. Whitehead and S. Mitragotri, *Nat. Rev. Mater.*, 2020, **5**, 127–148.
23 G. Kolata, *Science*, 1983, **221**, 1273.
24 P. G. Dougherty, A. Sahni and D. H. Pei, *Chem. Rev.*, 2019, **119**, 10241–10287.
25 C. K. Wang and D. J. Craik, *Biopolymers*, 2016, **106**, 901–909.
26 S. Lundin and P. Artursson, *Int. J. Pharm.*, 1990, **64**, 181–186.
27 N. Pantzar, S. Lundin and B. R. Westrom, *J. Pharm. Sci.*, 1995, **84**, 1245–1248.
28 https://www.accessdata.fda.gov/drugsatfda_docs/label/2019/213051s000lbl.pdf.
29 S. T. Buckley, T. A. Baekdal, A. Vegge, S. J. Maarbjerg, C. Pyke, J. Ahnfelt-Ronne, K. G. Madsen, S. G. Scheele, T. Alanentalo, R. K. Kirk, B. L. Pedersen, R. B. Skyggebjerg, A. J. Benie, H. M. Strauss, P. O. Wahlund, S. Bjerregaard, E. Farkas, C. Fekete, F. L. Sondergaard, J. Borregaard, M. L. Hartoft-Nielsen and L. B. Knudsen, *Sci. Transl. Med.*, 2018, **10**, eaar7047.
30 C. Twarog, K. Liu, P. J. O'Brien, K. A. Dawson, E. Fattal, B. Illel and D. J. Brayden, *Eur. J. Pharm. Biopharm.*, 2020, **152**, 95–107.
31 https://ir.chiasma.com/news-releases/news-release-details/chiasma-announces-fda-approval-mycapssar-octreotide-capsules/.

32 S. Tuvia, J. Atsmon, S. L. Teichman, S. Katz, P. Salama, D. Pelled, I. Landau, I. Karmeli, M. Bidlingmaier, C. J. Strasburger, D. L. Kleinberg, S. Melmed and R. Mamluk, *J. Clin. Endocrinol. Metab.*, 2012, **97**, 2362–2369.
33 S. Tuvia, D. Pelled, K. Marom, P. Salama, M. Levin-Arama, I. Karmeli, G. H. Idelson, I. Landau and R. Mamluk, *Pharm. Res.*, 2014, **31**, 2010–2021.
34 S. Maher, D. J. Brayden, L. Casettari and L. Illum, *Pharmaceutics*, 2019, **11**, 41.
35 P. Nava, S. Lopez, C. F. Arias, S. Islas and L. Gonzalez-Mariscal, *J. Cell Sci.*, 2004, **117**, 5509–5519.
36 N. Sonoda, M. Furuse, H. Sasaki, S. Yonemura, J. Katahira, Y. Horiguchi and S. Tsukita, *J. Cell Biol.*, 1999, **147**, 195–204.
37 K. E. Cunningham and J. R. Turner, in *Barriers and Channels Formed by Tight Junction Proteins Ii*, ed. M. Fromm and J. D. Schulzke, 2012, vol. 1258, pp. 34–42.
38 A. Taverner, R. Dondi, K. Almansour, F. Laurent, S. E. Owens, I. M. Eggleston, N. Fotaki and R. J. Mrsny, *J. Controlled Release*, 2015, **210**, 189–197.
39 K. Almansour, A. Taverner, I. M. Eggleston and R. J. Mrsny, *J. Controlled Release*, 2018, **279**, 208–219.
40 D. J. Brayden, T. A. Hill, D. P. Fairlie, S. Maher and R. J. Mrsny, *Adv. Drug Delivery Rev.*, 2020, **157**, 2–36.
41 B. K. Yoon, J. A. Jackman, M. C. Kim, T. N. Sut and N.-J. Cho, *Langmuir*, 2017, **33**, 2750–2759.
42 N. S. White and R. J. Errington, *Adv. Drug Delivery Rev.*, 2005, **57**, 17–42.
43 D. Axelrod, T. P. Burghardt and N. L. Thompson, *Annu. Rev. Biophys. Bioeng.*, 1984, **13**, 247–268.
44 S. M. Nie, D. T. Chiu and R. N. Zare, *Science*, 1994, **266**, 1018–1021.
45 J. Jonkman and C. M. Brown, *J. Biomol. Tech.*, 2015, **26**, 54–65.
46 F. Helmchen and W. Denk, *Nat. Methods*, 2005, **2**, 932–940.
47 T. A. Planchon, L. Gao, D. E. Milkie, M. W. Davidson, J. A. Galbraith, C. G. Galbraith and E. Betzig, *Nat. Methods*, 2011, **8**, 417–423.
48 R. M. Power and J. Huisken, *Nat. Methods*, 2017, **14**, 360–373.
49 E. G. Reynaud, J. Peychl, J. Huisken and P. Tomancak, *Nat. Methods*, 2014, **12**, 30–34.
50 E. Betzig, G. H. Patterson, R. Sougrat, O. W. Lindwasser, S. Olenych, J. S. Bonifacino, M. W. Davidson, J. Lippincott-Schwartz and H. F. Hess, *Science*, 2006, **313**, 1642–1645.
51 B.-C. Chen, W. R. Legant, K. Wang, L. Shao, D. E. Milkie, M. W. Davidson, C. Janetopoulos, X. S. Wu, J. A. Hammer, Z. Liu, B. P. English, Y. Mimori-Kiyosue, D. P. Romero, A. T. Ritter, J. Lippincott-Schwartz, L. Fritz-Laylin, R. D. Mullins, D. M. Mitchell, A.-C. Reymann, J. N. Bembenek, R. Bohme, S. W. Grill, J. T. Wang, G. Seydoux, U. S. Tulu, D. P. Kiehart and E. Betzig, *Science*, 2014, **346**, 1257998.
52 W. R. Legant, L. Shao, J. B. Grimm, T. A. Brown, D. E. Milkie, B. B. Avants, L. D. Lavis and E. Betzig, *Nat. Methods*, 2016, **13**, 1–9.
53 Y. Wakabayashi, J. Chua, J. M. Larkin, J. Lippincott-Schwartz and I. M. Arias, *Histochem. Cell Biol.*, 2007, **127**, 463–472.
54 We note that the working distances given in this section represents typical values found for several commercially available microscope objectives from different manufacturers.
55 N. Ji, D. E. Milkie and E. Betzig, *Nat. Methods*, 2010, **7**, 141–147.
56 P. P. Laissue, R. A. Alghamdi, P. Tomancak, E. G. Reynaud and H. Shroff, *Nat. Methods*, 2017, **14**, 657–661.
57 J. Icha, M. Weber, J. C. Waters and C. Norden, *BioEssays*, 2017, **39**, 8.
58 K. L. Tosheva, Y. Yuan, P. M. Pereira, S. Culley and R. Henriques, *J. Phys. D: Appl. Phys.*, 2020, **53**, 163001.
59 N. Ruthardt, D. C. Lamb and C. Bräuchle, *Mol. Ther.*, 2011, **19**, 1199–1211.
60 B. S. Schuster, L. M. Ensign, D. B. Allan, J. S. Suk and J. Hanes, *Adv. Drug Delivery Rev.*, 2015, **91**, 70–91.
61 J. Suh, M. Dawson and J. Hanes, *Adv. Drug Delivery Rev.*, 2005, **57**, 63–78.
62 C. Manzo and M. F. Garcia-Parajo, *Rep. Prog. Phys.*, 2015, **78**, 124601.
63 M. P. Clausen and B. C. Lagerholm, *Curr. Protein Pept. Sci.*, 2011, **12**, 699–713.
64 J. Elf and I. Barkefors, in *Annual Review of Biochemistry*, ed. R. D. Kornberg, 2019, vol. 88, pp. 635–659.
65 C. Ciobanasu, J. P. Siebrasse and U. Kubitscheck, *Biophys. J.*, 2010, **99**, 153–162.
66 L. Parnaste, P. Arukuusk, E. Zagato, K. Braeckmans and U. Langel, *J. Drug Targeting*, 2016, **24**, 508–519.
67 Y. Suzuki, C. N. Roy, W. Promjunyakul, H. Hatakeyama, K. Gonda, J. Imamura, B. Vasudevanpillai, N. Ohuchi, M. Kanzaki, H. Higuchi and M. Kaku, *Mol. Cell. Biol.*, 2013, **33**, 3036–3049.
68 G. Ruan, A. Agrawal, A. I. Marcus and S. Nie, *J. Am. Chem. Soc.*, 2007, **129**, 14759–14766.
69 J. B. Grimm, A. K. Muthusamy, Y. Liang, T. A. Brown, W. C. Lemon, R. Patel, R. Lu, J. J. Macklin, P. J. Keller, N. Ji and L. D. Lavis, *Nat. Methods*, 2017, **14**, 987–994.
70 J. R. Marks, J. Placone, K. Hristova and W. C. Wimley, *J. Am. Chem. Soc.*, 2011, **133**, 8995–9004.
71 N. Nischan, H. D. Herce, F. Natale, N. Bohlke, N. Budisa, M. C. Cardoso and C. P. R. Hackenberger, *Angew. Chem., Int. Ed.*, 2015, **54**, 1950–1953.
72 R. Wallbrecher, T. Ackels, R. A. Olea, M. J. Klein, L. Caillon, J. Schiller, P. H. Bovée-Geurts, T. H. van Kuppevelt, A. S. Ulrich, M. Spehr, M. J. W. Adjobo-Hermans and R. Brock, *J. Controlled Release*, 2017, **256**, 68–78.
73 S. M. A. Tabei, S. Burov, H. Y. Kim, A. Kuznetsov, T. Huynh, J. Jureller, L. H. Philipson, A. R. Dinner and N. F. Scherer, *Proc. Natl. Acad. Sci. U. S. A.*, 2013, **110**, 4911–4916.
74 J. C. Crocker and D. G. Grier, *J. Colloid Interface Sci.*, 1996, **310**, 298–310.
75 Z. Püspöki, D. Sage, J. P. Ward and M. Unser, *Bioinformatics*, 2016, **32**, 1278–1280.

76 I. Smal, M. Loog, W. Niessen and E. Meijering, *IEEE Trans. Med. Imaging*, 2010, **29**, 282–301.
77 A. Sergé, N. Bertaux, H. Rigneault and D. Marguet, *Nat. Methods*, 2008, **5**, 687–694.
78 H. Deschout, F. Cella Zanacchi, M. Mlodzianoski, A. Diaspro, J. Bewersdorf, S. T. Hess and K. Braeckmans, *Nat. Methods*, 2014, **11**, 253–266.
79 K. I. Mortensen, L. S. Churchman, J. A. Spudich and H. Flyvbjerg, *Nat. Methods*, 2010, **7**, 377–381.
80 D. Sage, H. Kirshner, T. Pengo, N. Stuurman, J. Min, S. Manley and M. Unser, *Nat. Methods*, 2015, **12**, 717–724.
81 D. Sage, T.-A. Pham, H. Babcock, T. Lukes, T. Pengo, J. Chao, R. Velmurugan, A. Herbert, A. Agrawal, S. Colabrese, A. Wheeler, A. Archetti, B. Rieger, R. Ober, G. M. Hagen, J.-B. Sibarita, J. Ries, R. Henriques, M. Unser, S. Holden, R. Volum, R. Lateral, R. Axial, M. A. D. Volum, M. A. D. Lateral and M. A. D. Axial, *Nat. Methods*, 2019, **16**, 387–395.
82 A. S. Hansen, M. Woringer, J. B. Grimm, L. D. Lavis, R. Tjian and X. Darzacq, *eLife*, 2018, **7**, 1–33.
83 C. L. Vestergaard, P. C. Blainey and H. Flyvbjerg, *Phys. Rev. E: Stat., Nonlinear, Soft Matter Phys.*, 2014, **89**, 022726.
84 C. L. Vestergaard, J. N. Pedersen, K. I. Mortensen and H. Flyvbjerg, *Eur. Phys. J.-Spec. Top.*, 2015, **224**, 1151–1168.
85 C. L. Vestergaard, P. C. Blainey and H. Flyvbjerg, *Nucleic Acids Res.*, 2018, **46**, 2446–2458.
86 H. Deschout, T. Martens, D. Vercauteren, K. Remaut, J. Demeester, S. C. De Smedt, K. Neyts and K. Braeckmans, *Int. J. Mol. Sci.*, 2013, **14**, 16485–16514.
87 D. Vercauteren, H. Deschout, K. Remaut, J. F. J. Engbersen, A. T. Jones, J. Demeester, S. C. D. Smedt and K. Braeckmans, *ACS Nano*, 2011, **5**, 7874–7884.
88 K. I. Mortensen, J. Sung, H. Flyvbjerg and J. A. Spudich, *Nat. Commun.*, 2015, **6**, 8621.
89 W. Ouyang, A. Aristov, M. Lelek, X. Hao and C. Zimmer, *Nat. Biotechnol.*, 2018, **36**, 460–468.
90 P. Zelger, K. Kaser, B. Rossboth, L. Velas, G. J. Schutz and A. Jesacher, *Opt. Express*, 2018, **26**, 33166–33179.
91 E. Moen, D. Bannon, T. Kudo, W. Graf, M. Covert and D. V. Valen, *Nat. Methods*, 2019, **16**, 1233–1246.
92 J. Vangindertael, R. Camacho, W. Sempels, H. Mizuno, P. Dedecker and K. P. F. Janssen, *Methods Appl. Fluoresc.*, 2018, **6**, 022003.
93 B. Huang, M. Bates and X. Zhuang, *Annu. Rev. Biochem.*, 2009, **78**, 993–1016.
94 S. Pujals, N. Feiner-Gracia, P. Delcanale, I. Voets and L. Albertazzi, *Nat. Rev. Chem.*, 2019, **3**, 68–84.
95 A. M. Sydor, K. J. Czymmek, E. M. Puchner and V. Mennella, *Trends Cell Biol.*, 2015, **25**, 730–748.
96 D. Baddeley and J. Bewersdorf, *Annu. Rev. Biochem.*, 2018, **87**, 965–989.
97 N. Li, R. Zhao, Y. Sun, Z. Ye, K. He and X. Fang, *Natl. Sci. Rev.*, 2017, **4**, 739–760.
98 J. Yu, *Annu. Rev. Phys. Chem.*, 2016, **67**, 565–585.
99 R. Heintzmann and T. Huser, *Chem. Rev.*, 2017, **117**, 13890–13908.
100 M. G. L. Gustafsson, *J. Microsc.*, 2000, **198**, 82–87.
101 S. W. Hell and J. Wichmann, *Opt. Lett.*, 1994, **19**, 780–782.
102 H. Blom and J. Widengren, *Chem. Rev.*, 2017, **117**, 7377–7427.
103 B. Huang, S. A. Jones, B. Brandenburg and X. Zhuang, *Nat. Methods*, 2008, **5**, 1047–1052.
104 M. J. Rust, M. Bates and X. Zhuang, *Nat. Methods*, 2006, **3**, 793–796.
105 M. Heilemann, S. van de Linde, M. Schüttpelz, R. Kasper, B. Seefeldt, A. Mukherjee, P. Tinnefeld and M. Sauer, *Angew. Chem., Int. Ed.*, 2008, **47**, 6172–6176.
106 E. Betzig, G. H. Patterson, R. Sougrat, O. W. Lindwasser, S. Olenych, J. S. Bonifacino, M. W. Davidson, J. Lippincott-Schwartz and H. F. Hess, *Science*, 2006, **313**, 1642.
107 A. Sharonov and R. M. Hochstrasser, *Proc. Natl. Acad. Sci. U. S. A.*, 2006, **103**, 18911.
108 M. Miyake, T. Koga, S. Kondo, N. Yoda, C. Emoto, T. Mukai and H. Toguchi, *Eur. J. Pharm. Sci.*, 2017, **96**, 373–380.
109 K. C. Gwosch, J. K. Pape, F. Balzarotti, P. Hoess, J. Ellenberg, J. Ries and S. W. Hell, *Nat. Methods*, 2020, **17**, 217–224.
110 F. Balzarotti, Y. Eilers, K. C. Gwosch, A. H. Gynnå, V. Westphal, F. D. Stefani, J. Elf and S. W. Hell, *Science*, 2017, **355**, 606.
111 M. Schmidt, A. C. Hundahl, H. Flyvbjerg, R. Marie and K. I. Mortensen, *Commun. Phys.*, 2021, **4**, 41.
112 J. Cnossen, T. Hinsdale, R. Thorsen, M. Siemons, F. Schueder, R. Jungmann, C. S. Smith, B. Rieger and S. Stallinga, *Nat. Methods*, 2020, **17**, 59–63.
113 L. Gu, Y. Li, S. Zhang, Y. Xue, W. Li, D. Li, T. Xu and W. Ji, *Nat. Methods*, 2019, **16**, 1114–1118.
114 P. Jouchet, C. Cabriel, N. Bourg, M. Bardou, C. Poüs, E. Fort and S. Lévêque-Fort, *Nat. Photonics*, 2021, **15**, 297–304.
115 L. Gu, Y. Li, S. Zhang, M. Zhou, Y. Xue, W. Li, T. Xu and W. Ji, *Nat. Methods*, 2021, **18**, 369–373.
116 P. M. Fischer, N. Z. Zhelev, S. Wang, J. E. Melville, R. Fahraeus and D. P. Lane, *J. Pept. Res.*, 2000, **55**, 163–172.
117 R. Fischer, T. Waizenegger, K. Köhler and R. Brock, *Biochim. Biophys. Acta, Biomembr.*, 2002, **1564**, 365–374.
118 M. Hällbrink, A. Florén, A. Elmquist, M. Pooga, T. Bartfai and Ü. Langel, *Biochim. Biophys. Acta, Biomembr.*, 2001, **1515**, 101–109.
119 M. Hällbrink, J. Oehlke, G. Papsdorf and M. Bienert, *Biochim. Biophys. Acta, Biomembr.*, 2004, **1667**, 222–228.
120 S. Al-Taei, N. A. Penning, J. C. Simpson, S. Futaki, T. Takeuchi, I. Nakase and A. T. Jones, *Bioconjugate Chem.*, 2006, **17**, 90–100.
121 D. Birch, M. V. Christensen, D. Staerk, H. Franzyk and H. M. Nielsen, *Biochim. Biophys. Acta, Biomembr.*, 2017, **1859**, 2483–2494.
122 S. F. Hedegaard, M. S. Derbas, T. K. Lind, M. R. Kasimova, M. V. Christensen, M. H. Michaelsen, R. A. Campbell, L. Jorgensen, H. Franzyk, M. Cárdenas and H. M. Nielsen, *Sci. Rep.*, 2018, **8**, 1–14.
123 J. D. Ochocki, D. G. Mullen, E. V. Wattenberg and M. D. Distefano, *Bioorg. Med. Chem. Lett.*, 2011, **21**, 4998–5001.

124 L. D. Hughes, R. J. Rawle and S. G. Boxer, *PLoS One*, 2014, **9**, e87649.
125 L. C. Zanetti-Domingues, C. J. Tynan, D. J. Rolfe, D. T. Clarke and M. Martin-Fernandez, *PLoS One*, 2013, **8**, e74200.
126 L. C. Zanetti-Domingues, M. L. Martin-Fernandez, S. R. Needham, D. J. Rolfe and D. T. Clarke, *PLoS One*, 2012, **7**, e45655.
127 X. Liu, Z. Xu and J. M. Cole, *J. Phys. Chem. C*, 2013, **117**, 16584–16595.
128 V. Mäde, S. Els-Heindl and A. G. Beck-Sickinger, *Beilstein J. Org. Chem.*, 2014, **10**, 1197–1212.
129 *Fmoc solid phase peptide synthesis*, ed. W. Chan and P. White, a practical approach, Oxford University Press, 2000.
130 N. Stephanopoulos and M. B. Francis, *Nat. Chem. Biol.*, 2011, **7**, 876–884.
131 J. Kalia and R. T. Raines, *Curr. Org. Chem.*, 2010, **14**, 138–147.
132 R. Fischer, O. Mader, G. Jung and R. Brock, *Bioconjugate Chem.*, 2003, **14**, 653–660.
133 C. N. Carrigan and B. Imperiali, *Anal. Biochem.*, 2005, **341**, 290–298.
134 M. Sainlos and B. Imperiali, *Nat. Protoc.*, 2007, **2**, 3210–3218.
135 M. Eugenio Vázquez, D. M. Rothman and B. Imperiali, *Org. Biomol. Chem.*, 2004, **2**, 1965–1966.
136 A. Chersi, S. Giommi and L. Rosanò, *Biochim. Biophys. Acta, Gen. Subj.*, 2000, **1474**, 196–200.
137 D. Boturyn, J. L. Coll, E. Garanger, M. C. Favrot and P. Dumy, *J. Am. Chem. Soc.*, 2004, **126**, 5730–5739.
138 P. Hoogerhout, K. J. Stittelaar, H. F. Brugghe, J. A. M. Timmermans, G. J. Ten Hove, W. Jiskoot, J. H. G. Hoekman and P. J. M. Roholl, *J. Pept. Res.*, 1999, **54**, 436–443.
139 M. Dettin, C. Scarinci, C. Zanotto, A. Cabrelle, A. Rossi and C. Bello, *J. Pept. Res.*, 2009, **51**, 110–115.
140 A. Song, X. Wang, J. Zhang, J. Mařík, C. B. Lebrilla and K. S. Lam, *Bioorg. Med. Chem. Lett.*, 2004, **14**, 161–165.
141 M. Miki and C. G. D. Remedios, *J. Biochem.*, 1988, **104**, 232–235.
142 J. S. Nanda and J. R. Lorsch, *Methods Enzymol.*, 2014, **536**, 79–86.
143 M. D. Best, *Biochemistry*, 2009, **48**, 6571–6584.
144 N. K. Devaraj, *ACS Cent. Sci.*, 2018, **4**, 952–959.
145 V. V. Rostovtsev, L. G. Green, V. V. Fokin and K. B. Sharpless, *Angew. Chem., Int. Ed.*, 2002, **41**, 2596–2599.
146 M. Meldal and C. W. Tornøe, *Chem. Rev.*, 2008, **108**, 2952–3015.
147 E. M. Sletten and C. R. Bertozzi, *Angew. Chem., Int. Ed.*, 2009, **48**, 6974–6998.
148 J. Marik and J. L. Sutcliffe, *Tetrahedron Lett.*, 2006, **47**, 6681–6684.
149 P. Kele, G. Mezö, D. Achatz and O. S. Wolfbeis, *Angew. Chem., Int. Ed.*, 2009, **48**, 344–347.
150 M. K. Quinn, N. Gnan, S. James, A. Ninarello, F. Sciortino, E. Zaccarelli and J. J. McManus, *Phys. Chem. Chem. Phys.*, 2015, **17**, 31177–31187.
151 M. P. Luitz, A. Barth, A. H. Crevenna, R. Bomblies, D. C. Lamb and M. Zacharias, *PLoS One*, 2017, **12**, e0177139.
152 L. M. Jungbauer, C. Yu, K. J. Laxton and M. J. LaDu, *J. Mol. Recognit.*, 2009, **22**, 403–413.
153 M. Mučibabić, M. M. Apetri, G. W. Canters and T. J. Aartsma, *Biochim. Biophys. Acta, Proteins Proteomics*, 2016, **1864**, 1419–1427.
154 J. Wägele, S. De Sio, B. Voigt, J. Balbach and M. Ott, *Biophys. J.*, 2019, **116**, 227–238.
155 L. Yin, W. Wang, S. Wang, F. Zhang, S. Zhang and N. Tao, *Biosens. Bioelectron.*, 2015, **66**, 412–416.
156 S. M. D'Addio, J. R. Bothe, C. Neri, P. L. Walsh, J. Zhang, E. Pierson, Y. Mao, M. Gindy, A. Leone and A. C. Templeton, *J. Pharm. Sci.*, 2016, **105**, 2989–3006.
157 D. Geissler, C. Gollwitzer, A. Sikora, C. Minelli, M. Krumrey and U. Resch-Genger, *Anal. Methods*, 2015, **7**, 9785–9790.
158 A. Kitamura and M. Kinjo, *Int. J. Mol. Sci.*, 2018, **19**, 964.
159 S. Macchi, G. Signore, C. Boccardi, C. Di Rienzo, F. Beltram and F. Cardarelli, *Sci. Rep.*, 2015, **5**, 16914.
160 J. Ries and P. Schwille, *BioEssays*, 2012, **34**, 361–368.
161 L. O. Tjernberg, A. Pramanik, S. Björling, P. Thyberg, J. Thyberg, C. Nordstedt, K. D. Berndt, L. Terenius and R. Rigler, *Chem. Biol.*, 1999, **6**, 53–62.
162 M. Schneider, S. Walta, C. Cadek, W. Richtering and D. Willbold, *Sci. Rep.*, 2017, **7**, 2154.
163 H. Sahoo, *J. Photochem. Photobiol., C*, 2011, **12**, 20–30.
164 A. S. Khadria and A. Senes, *Biopolymers*, 2015, **104**, 247–264.
165 V. Raicu, *J. Biol. Phys.*, 2007, **33**, 109–127.
166 B. Schuler, *J. Nanobiotechnol.*, 2013, **11**(suppl. 1), S2.
167 B. Wang, N. Xie and B. Li, *J. Food Biochem.*, 2019, **43**, e12571.
168 M. D. Sitrin, in *The Gastrointestinal System: Gastrointestinal, Nutritional and Hepatobiliary Physiology*, ed. P. S. Leung, Springer, Netherlands, Dordrecht, 2014, DOI: 10.1007/978-94-017-8771-0_6, pp. 137–158.
169 A. Bernkop-Schnürch, *Oral Delivery of Macromolecular Drugs: Barriers, Strategies and Future Trends*, Springer, New York, 2009.
170 J. F. Woodley, *Crit. Rev. Ther. Drug Carrier Syst.*, 1994, **11**, 61–95.
171 A. Bernkop-Schnürch, *J. Controlled Release*, 1998, **52**, 1–16.
172 E. Galia, E. Nicolaides, D. Hörter, R. Löbenberg, C. Reppas and J. B. Dressman, *Pharm. Res.*, 1998, **15**, 698–705.
173 L. Kalantzi, K. Goumas, V. Kalioras, B. Abrahamsson, J. B. Dressman and C. Reppas, *Pharm. Res.*, 2006, **23**, 165–176.
174 A. Lindahl, A.-L. Ungell, L. Knutson and H. Lennernäs, *Pharm. Res.*, 1997, **14**, 497–502.
175 M. Perez de la Cruz Moreno, M. Oth, S. Deferme, F. Lammert, J. Tack, J. Dressman and P. Augustijns, *J. Pharm. Pharmacol.*, 2006, **58**, 1079–1089.

176 W. H. Shen and R. J. Xu, *Comp. Biochem. Physiol., Part A: Mol. Integr. Physiol.*, 2000, **125**, 389–401.
177 M. Foltz, E. E. Meynen, V. Bianco, C. van Platerink, T. M. M. G. Koning and J. Kloek, *J. Nutr.*, 2007, **137**, 953–958.
178 J. Wang, V. Yadav, A. L. Smart, S. Tajiri and A. W. Basit, *Mol. Pharmaceutics*, 2015, **12**, 966–973.
179 M. M. Frigault, J. Lacoste, J. L. Swift and C. M. Brown, *J. Cell Sci.*, 2009, **122**, 753–767.
180 A. Fjellestad-Paulsen, C. Söderberg-Ahlm and S. Lundin, *Peptides*, 1995, **16**, 1141–1147.
181 S. Strindberg, J. Plum, C. Bagger, C. Janfelt and A. Müllertz, *Mol. Pharmaceutics*, 2021, **18**, 2189–2197.
182 M. Tanaka, S. M. Hong, S. Akiyama, Q. Q. Hu and T. Matsui, *Mol. Nutr. Food Res.*, 2015, **59**, 1541–1549.
183 S. M. Hong, M. Tanaka, S. Yoshii, Y. Mine and T. Matsui, *Anal. Chem.*, 2013, **85**, 10033–10039.
184 J. Kovacs-Nolan, P. Rupa, T. Matsui, M. Tanaka, T. Konishi, Y. Sauchi, K. Sato, S. Ono and Y. Mine, *J. Agric. Food Chem.*, 2014, **62**, 9499–9506.
185 P. E. G. Thorén, D. Persson, M. Karlsson and B. Nordén, *FEBS Lett.*, 2000, **482**, 265–268.
186 M. Z. Islam, H. Ariyama, J. M. Alam and M. Yamazaki, *Biochemistry*, 2014, **53**, 386–396.
187 B. Apellániz, J. L. Nieva, P. Schwille and A. J. García-Sáez, *Biophys. J.*, 2010, **99**, 3619–3628.
188 J. He, K. Hristova and W. C. Wimley, *Angew. Chem., Int. Ed.*, 2012, **51**, 7150–7153.
189 S. A. Wheaten, F. D. O. Ablan, B. L. Spaller, J. M. Trieu and P. F. Almeida, *J. Am. Chem. Soc.*, 2013, **135**, 16517–16525.
190 P. Meleard, L. A. Bagatolli and T. Pott, in *Methods in Enzymology Liposomes*, ed. N. Duzgunes and G. Pt, 2009, vol. 465, pp. 161–176.
191 G. van Meer, D. R. Voelker and G. W. Feigenson, *Nat. Rev. Mol. Cell Biol.*, 2008, **9**, 112–124.
192 Y. Tamba, H. Ariyama, V. Levadny and M. Yamazaki, *J. Phys. Chem. B*, 2010, **114**, 12018–12026.
193 B. Alberts, *Molecular Biology of the Cell*, Garland Science, 2002.
194 P. Saalik, A. Niinep, J. Pae, M. Hansen, D. Lubenets, U. Langel and M. Pooga, *J. Controlled Release*, 2011, **153**, 117–125.
195 K. R. Levental and I. Levental, in *Lipid Domains*, ed. A. K. Kenworthy, 2015, vol. 75, pp. 25–57.
196 E. Sezgin, H. J. Kaiser, T. Baumgart, P. Schwille, K. Simons and I. Levental, *Nat. Protoc.*, 2012, **7**, 1042–1051.
197 B. Bauer, M. Davidson and O. Orwar, *Angew. Chem., Int. Ed.*, 2009, **48**, 1656–1659.
198 K. R. Levental and I. Levental, in *Current Topics in Membranes*, ed. A. K. Kenworthy, Academic Press, 2015, vol. 75, pp. 25–57.
199 E. Sezgin, I. Levental, S. Mayor and C. Eggeling, *Nat. Rev. Mol. Cell Biol.*, 2017, **18**, 361–374.
200 D. A. Costello, C.-Y. Hsia, J. K. Millet, T. Porri and S. Daniel, *Langmuir*, 2013, **29**, 6409–6419.
201 A. Moutal, L. Francois-Moutal, J. M. Brittain, M. Khanna and R. Khanna, *Front. Cell. Neurosci.*, 2015, **8**, 471.
202 C. Lepinoux-Chambaud and J. Eyer, *Int. J. Pharm.*, 2013, **454**, 738–747.
203 J. Pae, P. Saalik, L. Liivamagi, D. Lubenets, P. Arukuusk, U. Langel and M. Pooga, *J. Controlled Release*, 2014, **192**, 103–113.
204 J. Pae, L. Liivamagi, D. Lubenets, P. Arukuusk, U. Langel and M. Pooga, *Biochim. Biophys. Acta, Biomembr.*, 2016, **1858**, 1860–1867.
205 M. M. Manni, J. Sot and F. M. Goni, *Biochim. Biophys. Acta, Biomembr.*, 2015, **1848**, 797–804.
206 B. N. G. Giepmans, S. R. Adams, M. H. Ellisman and R. Y. Tsien, *Science*, 2006, **312**, 217–224.
207 C. Bechara and S. Sagan, *FEBS Lett.*, 2013, **587**, 1693–1702.
208 N. J. Yang and M. J. Hinner, *Methods Mol. Biol.*, 2015, **1266**, 29–53.
209 H. D. Herce, A. E. Garcia and M. C. Cardoso, *J. Am. Chem. Soc.*, 2014, **136**, 17459–17467.
210 N. Nischan, H. D. Herce, F. Natale, N. Bohlke, N. Budisa, M. C. Cardoso and C. P. R. Hackenberger, *Angew. Chem., Int. Ed.*, 2015, **54**, 1950–1953.
211 A. Méndez-Ardoy, I. Lostalé-Seijo and J. Montenegro, *ChemBioChem*, 2019, **20**, 488–498.
212 P. Watson, A. T. Jones and D. J. Stephens, *Adv. Drug Delivery Rev.*, 2005, **57**, 43–61.
213 F. Illien, N. Rodriguez, M. Amoura, A. Joliot, M. Pallerla, S. Cribier, F. Burlina and S. Sagan, *Sci. Rep.*, 2016, **6**, 1–13.
214 J.-M. Swiecicki, F. Thiebaut, M. Di Pisa, S. Gourdin-Bertin, J. Tailhades, C. Mansuy, F. Burlina, S. Chwetzoff, G. Trugnan, G. Chassaing and S. Lavielle, *Sci. Rep.*, 2016, **6**, 20237.
215 S. C. De Smedt, K. Remaut, B. Lucas, K. Braeckmans, N. N. Sanders and J. Demeester, *Adv. Drug Delivery Rev.*, 2005, **57**, 191–210.
216 H. Deschout, K. Raemdonck, J. Demeester, S. C. De Smedt and K. Braeckmans, *Pharm. Res.*, 2014, **31**, 255–270.
217 S. G. Patel, E. J. Sayers, L. He, R. Narayan, T. L. Williams, E. M. Mills, R. K. Allemann, L. Y. P. Luk, A. T. Jones and Y. H. Tsai, *Sci. Rep.*, 2019, **9**, 6298.
218 C. A. Thaiss, M. Levy, I. Grosheva, D. Zheng, E. Soffer, E. Blacher, S. Braverman, A. C. Tengeler, O. Barak, M. Elazar, R. Ben-Zeev, D. Lehavi-Regev, M. N. Katz, M. Pevsner-Fischer, A. Gertler, Z. Halpern, A. Harmelin, S. Aamar, P. Serradas, A. Grosfeld, H. Shapiro, B. Geiger and E. Elinav, *Science*, 2018, **359**, 1376–1383.
219 M. Aguilar-Aragon, A. Elbediwy, V. Foglizzo, G. C. Fletcher, V. S. W. Li and B. J. Thompson, *Cell Rep.*, 2018, **22**, 1639–1646.
220 X. Liu, S. Zheng, Y. Qin, W. Ding, Y. Tu, X. Chen, Y. Wu, L. Yanhua and X. Cai, *Front. Pharmacol.*, 2017, **8**, 781.
221 A. R. Hilgers, R. A. Conradi and P. S. Burton, *AAPS J.*, 1990, **7**, 902–910.
222 N. Navabi, M. A. McGuckin and S. K. Lindén, *PLoS One*, 2013, **8**, e68761.
223 F. Antunes, F. Andrade, F. Araújo, D. Ferreira and B. Sarmento, *Eur. J. Pharm. Biopharm.*, 2013, **83**, 427–435.
224 C. M. Costello, J. Hongpeng, S. Shaffiey, J. Yu, N. K. Jain, D. Hackam and J. C. March, *Biotechnol. Bioeng.*, 2014, **111**, 1222–1232.

225 J. Yu, S. Peng, D. Luo and J. C. March, *Biotechnol. Bioeng.*, 2012, **109**, 2173–2178.
226 Y. Wang, D. B. Gunasekara, M. I. Reed, M. DiSalvo, S. J. Bultman, C. E. Sims, S. T. Magness and N. L. Allbritton, *Biomaterials*, 2017, **128**, 44–55.
227 Y. Chen, Y. Lin, K. M. Davis, Q. Wang, J. Rnjak-Kovacina, C. Li, R. R. Isberg, C. A. Kumamoto, J. Mecsas and D. L. Kaplan, *Sci. Rep.*, 2015, **5**, 13708.
228 R. A. Conradi, A. R. Hilgers, N. F. H. Ho and P. S. Burton, *Pharm. Res.*, 1991, **8**, 1453–1460.
229 J. H. Hamman, G. M. Enslin and A. F. Kotze, *BioDrugs*, 2005, **19**, 165–177.
230 W. Hua, D. Sheff, D. Toomre and I. Mellman, *J. Cell Biol.*, 2006, **172**, 1035.
231 K. A. Toops, L. X. Tan and A. Lakkaraju, *Exp. Eye Res.*, 2014, **124**, 74–85.
232 S. J. Trietsch, E. Naumovska, D. Kurek, M. C. Setyawati, M. K. Vormann, K. J. Wilschut, H. L. Lanz, A. Nicolas, C. P. Ng, J. Joore, S. Kustermann, A. Roth, T. Hankemeier, A. Moisan and P. Vulto, *Nat. Commun.*, 2017, **8**, 262.
233 V. Rozehnal, D. Nakai, U. Hoepner, T. Fischer, E. Kamiyama, M. Takahashi, S. Yasuda and J. Mueller, *Eur. J. Pharm. Sci.*, 2012, **46**, 367–373.
234 J. Westerhout, E. Van De Steeg, D. Grossouw, E. E. Zeijdner, C. A. M. Krul, M. Verwei and H. M. Wortelboer, *Eur. J. Pharm. Sci.*, 2014, **63**, 167–177.
235 S. Ayehunie, T. Landry, Z. Stevens, A. Armento, P. Hayden and M. Klausner, *Pharm. Res.*, 2018, **35**, 72.
236 I. Maschmeyer, A. K. Lorenz, K. Schimek, T. Hasenberg, A. P. Ramme, J. Hubner, M. Lindner, C. Drewell, S. Bauer, A. Thomas, N. S. Sambo, F. Sonntag, R. Lauster and U. Marx, *Lab Chip*, 2015, **15**, 2688–2699.
237 M. A. Miller and R. Weissleder, *Nat. Rev. Cancer*, 2017, **17**, 399–414.
238 J. M. Girkin and M. T. Carvalho, *J. Opt.*, 2018, **20**, 053002.
239 K. G. Chen, B. S. Mallon, K. Park, P. G. Robey, R. D. G. McKay, M. M. Gottesman and W. Zheng, *Trends Mol. Med.*, 2018, **24**, 805–820.
240 A. Fatehullah, S. H. Tan and N. Barker, *Nat. Cell Biol.*, 2016, **18**, 246–254.
241 X. Yin, B. E. Mead, H. Safaee, R. Langer, J. M. Karp and O. Levy, *Cell Stem Cell*, 2016, **18**, 25–38.
242 H. Clevers, *Cell*, 2016, **165**, 1586–1597.
243 K. G. Chen, B. S. Mallon, K. Park, P. G. Robey, R. D. G. McKay, M. M. Gottesman and W. Zheng, *Trends Mol. Med.*, 2018, **24**, 805–820.
244 M. Nikolaev, O. Mitrofanova, N. Broguiere, S. Geraldo, D. Dutta, Y. Tabata, B. Elci, N. Brandenberg, I. Kolotuev, N. Gjorevski, H. Clevers and M. P. Lutolf, *Nature*, 2020, **585**, 574–578.
245 D. Dutta and H. Clevers, *Curr. Opin. Immunol.*, 2017, **48**, 15–22.
246 S. Bartfeld and H. Clevers, *J. Visualized Exp.*, 2015, **105**, 53359.
247 D. R. Hill, S. Huang, Y. H. Tsai, J. R. Spence and V. B. Young, *J. Visualized Exp.*, 2017, **130**, 56960.
248 K. Kozuka, Y. He, S. Koo-McCoy, P. Kumaraswamy, B. Nie, K. Shaw, P. Chan, M. Leadbetter, L. He, J. G. Lewis, Z. Zhong, D. Charmot, M. Balaa, A. J. King, J. S. Caldwell and M. Siegel, *Stem Cell Rep.*, 2017, **9**, 1976–1990.
249 G. Altay, E. Larrañaga, S. Tosi, F. M. Barriga, E. Batlle, V. Fernández-Majada and E. Martínez, *Sci. Rep.*, 2019, **9**, 10140.
250 M. Kasendra, A. Tovaglieri, A. Sontheimer-Phelps, S. Jalili-Firoozinezhad, A. Bein, A. Chalkiadaki, W. Scholl, C. Zhang, H. Rickner, C. A. Richmond, H. Li, D. T. Breault and D. E. Ingber, *Sci. Rep.*, 2018, **8**, 2871.
251 E. Naumovska, G. Aalderink, C. Wong Valencia, K. Kosim, A. Nicolas, S. Brown, P. Vulto, K. S. Erdmann and D. Kurek, *Int. J. Mol. Sci.*, 2020, **21**, 4964.
252 J. Y. Co, M. Margalef-Català, X. Li, A. T. Mah, C. J. Kuo, D. M. Monack and M. R. Amieva, *Cell Rep.*, 2019, **26**, 2509–2520.
253 E. W. Esch, A. Bahinski and D. Huh, *Nat. Rev. Drug Discovery*, 2015, **14**, 248–260.
254 B. Zhang, A. Korolj, B. F. L. Lai and M. Radisic, *Nat. Rev. Mater.*, 2018, **3**, 257–278.
255 D. Huh, B. D. Matthews, A. Mammoto, M. Montoya-Zavala, H. Y. Hsin and D. E. Ingber, *Science*, 2010, **328**, 1662–1668.
256 H. J. Kim, D. Huh, G. Hamilton and D. E. Ingber, *Lab Chip*, 2012, **12**, 2165–2174.
257 H. J. Kim and D. E. Ingber, *Integr. Biol.*, 2013, **5**, 1130–1140.
258 A. Carraro, W.-M. Hsu, K. M. Kulig, W. S. Cheung, M. L. Miller, E. J. Weinberg, E. F. Swart, M. Kaazempur-Mofrad, J. T. Borenstein, J. P. Vacanti and C. Neville, *Biomed. Microdevices*, 2008, **10**, 795–805.
259 P. J. Lee, P. J. Hung and L. P. Lee, *Biotechnol. Bioeng.*, 2007, **97**, 1340–1346.
260 A. Agarwal, J. A. Goss, A. Cho, M. L. McCain and K. K. Parker, *Lab Chip*, 2013, **13**, 3599–3608.
261 A. Grosberg, P. W. Alford, M. L. McCain and K. K. Parker, *Lab Chip*, 2011, **11**, 4165–4173.
262 R. Mroue and M. J. Bissell, in *Epithelial Cell Culture Protocols*, ed. S. H. Randell and M. L. Fulcher, Humana Press, Totowa, NJ, 2nd edn, 2013, pp. 221–250.
263 T. Sato and H. Clevers, *Science*, 2013, **340**, 1190–1194.
264 K. H. Benam, R. Villenave, C. Lucchesi, A. Varone, C. Hubeau, H.-H. Lee, S. E. Alves, M. Salmon, T. C. Ferrante and J. C. Weaver, *Nat. Methods*, 2016, **13**, 151.
265 D. E. Ingber, *FASEB J.*, 2006, **20**, 811–827.
266 D. Huh, D. C. Leslie, B. D. Matthews, J. P. Fraser, S. Jurek, G. A. Hamilton, K. S. Thorneloe, M. A. McAlexander and D. E. Ingber, *Sci. Transl. Med.*, 2012, **4**, 147–159.
267 D. Huh, H. J. Kim, J. P. Fraser, D. E. Shea, M. Khan, A. Bahinski, G. A. Hamilton and D. E. Ingber, *Nat. Protoc.*, 2013, **8**, 2135.
268 H. J. Kim, H. Li, J. J. Collins and D. E. Ingber, *Proc. Natl. Acad. Sci. U. S. A.*, 2016, **113**, 7–15.
269 R. Villenave, S. Q. Wales, T. Hamkins-Indik, E. Papafragkou, J. C. Weaver, T. C. Ferrante, A. Bahinski, C. A. Elkins, M. Kulka and D. E. Ingber, *PLoS One*, 2017, **12**, e0169412.

270 S. Trkov, G. Eng, R. Di Liddo, P. P. Parnigotto and G. Vunjak-Novakovic, *J. Tissue Eng. Regener. Med.*, 2010, **4**, 205–215.
271 N. W. Choi, M. Cabodi, B. Held, J. P. Gleghorn, L. J. Bonassar and A. D. Stroock, *Nat. Mater.*, 2007, **6**, 908.
272 Y. Zheng, J. Chen, M. Craven, N. W. Choi, S. Totorica, A. Diaz-Santana, P. Kermani, B. Hempstead, C. Fischbach-Teschl, J. A. López and A. D. Stroock, *Proc. Natl. Acad. Sci. U. S. A.*, 2012, **109**, 9342–9347.
273 J. B. Leach and C. E. Schmidt, *Biomaterials*, 2005, **26**, 125–135.
274 G. Ligresti, R. J. Nagao, J. Xue, Y. J. Choi, J. Xu, S. Ren, T. Aburatani, S. K. Anderson, J. W. MacDonald and T. K. Bammler, *J. Am. Soc. Nephrol.*, 2016, **27**, 2370–2381.
275 R. J. Zhang and N. B. Larsen, *Lab Chip*, 2017, **17**, 4273–4282.
276 N. LiáJeon, *Lab Chip*, 2015, **15**, 3984–3988.
277 I. K. Zervantonakis, S. K. Hughes-Alford, J. L. Charest, J. S. Condeelis, F. B. Gertler and R. D. Kamm, *Proc. Natl. Acad. Sci. U. S. A.*, 2012, **109**, 13515–13520.
278 A. Sobrino, D. T. Phan, R. Datta, X. Wang, S. J. Hachey, M. Romero-López, E. Gratton, A. P. Lee, S. C. George and C. C. Hughes, *Sci. Rep.*, 2016, **6**, 31589.
279 C.-C. Hsieh, S.-B. Huang, P.-C. Wu, D.-B. Shieh and G.-B. J. B. M. Lee, *Biomed. Microdevices*, 2009, **11**, 903–913.
280 V. Vickerman, J. Blundo, S. Chung and R. Kamm, *Lab Chip*, 2008, **8**, 1468–1477.
281 J. Tam, G. A. Cordier, Š. Bálint, Á. Sandoval Álvarez, J. S. Borbely and M. Lakadamyali, *PLoS One*, 2015, **9**, e115512.
282 E. K. Sackmann, A. L. Fulton and D. J. Beebe, *Nature*, 2014, **507**, 181–189.
283 L. K. Chin, C.-H. Lee and B.-C. Chen, *Lab Chip*, 2016, **16**, 2014–2024.
284 R. Yokokawa, Y. Kitazawa, K. Terao, A. Okonogi, I. Kanno and H. Kotera, *Biomed. Microdevices*, 2012, **14**, 791–797.
285 B. Prabhakarpandian, M.-C. Shen, J. B. Nichols, I. R. Mills, M. Sidoryk-Wegrzynowicz, M. Aschner and K. Pant, *Lab Chip*, 2013, **13**, 1093–1101.
286 L. Griep, F. Wolbers, B. De Wagenaar, P. M. ter Braak, B. Weksler, I. A. Romero, P. Couraud, I. Vermes, A. D. van der Meer and A. van den Berg, *Biomed. Microdevices*, 2013, **15**, 145–150.
287 A. K. H. Achyuta, A. J. Conway, R. B. Crouse, E. C. Bannister, R. N. Lee, C. P. Katnik, A. A. Behensky, J. Cuevas and S. S. Sundaram, *Lab Chip*, 2013, **13**, 542–553.
288 R. Booth and H. Kim, *Lab Chip*, 2012, **12**, 1784–1792.
289 T.-E. Park, N. Mustafaoglu, A. Herland, R. Hasselkus, R. Mannix, E. A. FitzGerald, R. Prantil-Baun, A. Watters, O. Henry, M. Benz, H. Sanchez, H. J. McCrea, L. C. Goumnerova, H. W. Song, S. P. Palecek, E. Shusta and D. E. Ingber, *Nat. Commun.*, 2019, **10**, 2621.
290 E. Berthier, E. W. Young and D. Beebe, *Lab Chip*, 2012, **12**, 1224–1237.
291 A. D. van der Meer and A. van den Berg, *Integr. Biol.*, 2012, **4**, 461–470.
292 B. M. Maoz, A. Herland, O. Y. Henry, W. D. Leineweber, M. Yadid, J. Doyle, R. Mannix, V. J. Kujala, E. A. FitzGerald and K. K. Parker, *Lab Chip*, 2017, **17**, 2294–2302.
293 O. Y. Henry, R. Villenave, M. J. Cronce, W. D. Leineweber, M. A. Benz and D. E. Ingber, *Lab Chip*, 2017, **17**, 2264–2271.
294 A. D. Ávan der Meer, H. Jungá-Kim, M. W. Ávan der Helm and A. den Berg, *Lab Chip*, 2015, **15**, 745–752.
295 M. J. Pittet and R. Weissleder, *Cell*, 2011, **147**, 983–991.
296 I. M. Schiessl and H. Castrop, *Pflügers Arch.*, 2016, **468**, 1505–1516.
297 M. Kolesnikov, J. Farache and G. Shakhar, *J. Immunol. Methods*, 2015, **421**, 73–80.
298 P. R. Contag, *Drug Discovery Today*, 2002, **7**, 555–562.
299 M. A. Miller and R. Weissleder, *Adv. Drug Delivery Rev.*, 2017, **113**, 61–86.
300 L. Ritsma, S. I. J. Ellenbroek, A. Zomer, H. J. Snippert, F. J. de Sauvage, B. D. Simons, H. Clevers and J. van Rheenen, *Nature*, 2014, **507**, 362–365.
301 A. M. Marchiando, L. Shen, W. V. Graham, C. R. Weber, B. T. Schwarz, J. R. Austin, D. R. Raleigh, Y. Guan, A. J. M. Watson, M. H. Montrose and J. R. Turner, *J. Cell Biol.*, 2010, **189**, 111–126.
302 J. R. McDole, L. W. Wheeler, K. G. McDonald, B. Wang, V. Konjufca, K. A. Knoop, R. D. Newberry and M. J. Miller, *Nature*, 2012, **483**, 345–349.
303 S. E. Howe, D. J. Lickteig, K. N. Plunkett, J. S. Ryerse and V. Konjufca, *PLoS One*, 2014, **9**, e86656.
304 W. W. Fan, D. N. Xia, Q. L. Zhu, X. Y. Li, S. F. He, C. L. Zhu, S. Y. Guo, L. Hovgaard, M. S. Yang and Y. Gan, *Biomaterials*, 2018, **151**, 13–23.
305 J. R. W. Conway, N. O. Carragher and P. Timpson, *Nat. Rev. Cancer*, 2014, **14**, 314–328.
306 L. Ritsma, E. J. A. Steller, S. I. J. Ellenbroek, O. Kranenburg, I. Rinkes and J. van Rheenen, *Nat. Protoc.*, 2013, **8**, 583–594.
307 C. Prunier, N. Chen, L. Ritsma and N. Vrisekoop, *Methods*, 2017, **128**, 52–64.
308 S. M. Paul, D. S. Mytelka, C. T. Dunwiddie, C. C. Persinger, B. H. Munos, S. R. Lindborg and A. L. Schacht, *Nat. Rev. Drug Discovery*, 2010, **9**, 203.
309 P. Lang, K. Yeow, A. Nichols and A. Scheer, *Nat. Rev. Drug Discovery*, 2006, **5**, 343–356.
310 L. P. H. Estrada and J. A. Champion, *Biomater. Sci.*, 2015, **3**, 787–799.
311 M. J. Cheng, R. Kumar, S. Sridhar, T. J. Webster and E. E. Ebong, *Int. J. Nanomed.*, 2016, **11**, 3305–3315.
312 P. Foroozandeh and A. A. Aziz, *Nanoscale Res. Lett.*, 2018, **13**, 339.
313 G. Y. Liu, Y. Zhou and L. Y. Chen, *Acta Pharm. Sin. B*, 2019, **9**, 87–96.
314 N. Desai, V. Trieu, Z. W. Yao, L. Louie, S. Ci, A. Yang, C. L. Tao, T. De, B. Beals, D. Dykes, P. Noker, R. Yao, E. Labao, M. Hawkins and P. Soon-Shiong, *Clin. Cancer Res.*, 2006, **12**, 1317–1324.
315 U. Unzueta, M. V. Cespedes, N. Ferrer-Miralles, I. Casanova, J. Cedano, J. L. Corchero, J. Domingo-Espin,

A. Villaverde, R. Mangues and E. Vazquez, *Int. J. Nanomed.*, 2012, **7**, 4533–4544.
316 L. H. Estrada, S. Chu and J. A. Champion, *J. Pharm. Sci.*, 2014, **103**, 1863–1871.
317 J. K. Rhee, M. Hovlid, J. D. Fiedler, S. D. Brown, F. Manzenrieder, H. Kitagishi, C. Nycholat, J. C. Paulson and M. G. Finn, *Biomacromolecules*, 2011, **12**, 3977–3981.
318 N. Oh and J. H. Park, *Int. J. Nanomed.*, 2014, **9**, 51–63.
319 M. Bramini, D. Ye, A. Hallerbach, M. Nic Raghnaill, A. Salvati, C. Åberg and K. A. Dawson, *ACS Nano*, 2014, **8**, 4304–4312.
320 J. S. Crater and R. L. Carrier, *Macromol. Biosci.*, 2010, **10**, 1473–1483.
321 Y. Yun, Y. W. Cho and K. Park, *Adv. Drug Delivery Rev.*, 2013, **65**, 822–832.
322 M. Haham, S. Ish-Shalom, M. Nodelman, I. Duek, E. Segal, M. Kustanovich and Y. D. Livney, *Food Funct.*, 2012, **3**, 737–744.
323 M. Bar-Zeev, Y. G. Assaraf and Y. D. Livney, *Oncotarget*, 2016, **7**, 23322–23334.
324 A. Shapira, Y. G. Assaraf and Y. D. Livney, *J. Nanomed. Nanotechnol.*, 2010, **6**, 119–126.
325 T. T. Lin, P. F. Zhao, Y. F. Jiang, Y. S. Tang, H. Y. Jin, Z. Z. Pan, H. N. He, V. C. Yang and Y. Z. Huang, *ACS Nano*, 2016, **10**, 9999–10012.
326 E. Y. Chuang, K. J. Lin, F. Y. Su, F. L. Mi, B. Maiti, C. T. Chen, S. P. Wey, T. C. Yen, J. H. Juang and H. W. Sung, *J. Controlled Release*, 2013, **172**, 513–522.
327 J. W. Scannell, A. Blanckley, H. Boldon and B. Warrington, *Nat. Rev. Drug Discovery*, 2012, **11**, 191.